Investigating the emergence of electronic and atomic structure during the synthesis of transition-metal sulfides

Dissertation
zur Erlangung des Doktorgrades
and der Fakultät für Mathematik, Informatik und Naturwissenschaften
Fachbereich Physik
Der Universität Hamburg

vorgelegt von

Lars Klemeyer

Hamburg
2025

Gutachter/innen der Dissertation (Supervisor)	Prof. Dr. Dorota Koziej Prof. Dr. Wolfgang J. Parak
Zusammensetzung der Prüfungskommission (Examination Board)	Prof. Dr. Dorota Koziej Prof. Dr. Wolfgang J. Parak Prof. Dr. Daniela Pfannkuche Prof. Dr. Gabriel Bester Dr. Florian Schulz
Vorsitzende/r der Prüfungskommission (Head of Examination Board)	Prof. Dr. Daniela Pfannkuche
Datum der Disputation (Date of Disputation)	21.05.2025
Vorsitzender des Fach-Promotionsausschusses PHYSIK (Chairman of the Doctoral Committee Physics)	Prof. Dr. Wolfgang J. Parak
Leiter des Fachbereichs PHYSIK (Chairman of the Faculty Physics)	Prof. Dr. Markus Drescher
Dekan der Fakultät MIN (Dean of the MIN-Faculty)	Prof. Dr.-Ing. Norbert Ritter

Abstract

The synthesis of nanomaterials in solution often involves multiple intermediate steps from the precursor to the final product, as outlined in the non-classical nucleation theory. The first step in a one-pot reaction typically begins with the dissolution of the precursors in a solvent, often promoted by the coordination of metal ions with specific ligands. Upon heating, a series of chemical reactions are triggered, leading to the nucleation and growth of the desired nanoparticles. Understanding all steps in the synthesis of nanomaterials is essential for controlling and designing their formation mechanism.

Especially transition metal oxide and sulfide nanomaterials are used in a variety of applications. While mechanistic studies are often reported for the case of metal oxides, the key reaction pathways influencing the synthesis of many transition metal sulfides are still under debate. This thesis elucidates the formation of ZnS nanomaterials in solvothermal reactions through *in situ* X-ray spectroscopy and scattering techniques as a benchmark and shows preliminary characterization of Fe_xS_y nanomaterial synthesis.

We utilized *in situ* valence-to-core X-ray emission spectroscopy (vtc-XES) combined with *in situ* high-energy-resolution fluorescence-detected X-ray absorption spectroscopy (HERFD-XAS) supported by density functional theory (DFT) calculations to resolve the metal-ligand coordination during the synthesis of sphalerite ZnS nanorods (s-ZnS). The study elucidates the dissolution of $Zn(Ac)_2$ in oleylamine (OA), proposing $[Zn(OA)_4]^{2+}$ and $[Zn(OA)_6]^{2+}$ complexes, and detailing the ligand exchange towards oleylthioamide (SOA) upon the addition of elemental sulfur to the reaction mixture at room temperature. Throughout the synthesis of s-ZnS, *in situ* vtc-XES and HERFD-XAS analyses were employed to calculate an *in situ* HOMO/LUMO gap, showing the emergence of a band structure during the synthesis of s-ZnS. This enables the size prediction of the intermediate structure, the ZnS nanoparticle in the wurtzite phase (w-ZnS), based on their band gap. Complementary *in situ* powder X-ray diffraction (PXRD) and small angle X-ray scattering (SAXS) analysis confirm the identity of w-ZnS and s-ZnS and provide additional information about their size and morphology.

We also propose and study the synthesis of ZnS nanoparticles using a two-phase water-toluene solvothermal reaction. The method allows the obtaining of colloidally stable monodispersed ZnS nanoparticles in the sphalerite phase. The diffusion of Zn^{2+} ions at the water-toluene interface was monitored by spatially resolved HERFD-XAS analysis, where the coordination of Zn^{2+} ions in each phase was resolved using DFT calculations. The dissolution of $Zn(Ac)_2$ in water leads to the formation of a $[Zn(H_2O)_6]^{2+}$ complex. The Zn^{2+} ion diffuses into the toluene

phase already at room temperature, forming a $[Zn(OA)_6]^{2+}$ complex. *In situ* HERFD-XAS during the heating of the reaction solution up to 155°C reveals the formation of ZnS nanoparticles in the sphalerite phase, undergoing a $[Zn(RS)_4]^{2+}$ cluster and ZnS nuclei as intermediate structures. The findings were complemented by *in situ* PXRD and total X-ray scattering (TS) analysis, which verified the occurrence of these intermediates and assigned domain sizes to them. To validate the versatility of the method, we applied the complementary analysis to understand the formation of Fe_3S_4 nanomaterials in a solvothermal reaction. Since the reaction of $Fe(acac)_3$ with elemental sulfur and oleylamine dissolved in toluene failed to achieve the required reaction temperature (180°C) to yield Fe_3S_4 nanomaterials, the solvent was exchanged to benzyl alcohol (BA) and the sulfur source to thioacetamide. In this reaction, no addition of oleylamine was required. BA is well known as a solvent that promotes the formation of ultrasmall and monodisperse nanoparticles.

The preliminary analysis of *in situ* HERFD-XAS and vtc-XES data of the synthesis of Fe_3S_4 nanomaterials uncovers the formation of an intermediate structure above 50°C, which can be attributed to the coordination of $Fe(acac)_3$ by BA under the formation of a $[Fe(acac)_2(BA)_2]$ complex, as resolved by HERFD-XAS analysis and supported by DFT calculations. Furthermore, the formation of Fe_3S_4 nanocrystals undergoes an intermediate formation of FeS nanocrystals, as revealed by combined HERFD-XAS and FEFF analysis.

The *in situ* approach of vtc-XES reveals changes in donor orbitals during the first 50 minutes of the reaction, confirming the emergence of the $[Fe(acac)_2(BA)_2]$ complex. Through complementary *in situ* PXRD analyses, we identified the formation of FeS nanosheets and their conversion into Fe_3S_4 nanocrystals, which are approximately 22 nm in size.

This thesis presents an analysis of the coordination chemistry and structural evolution during the synthesis of ZnS and Fe_xS_y nanomaterials. It aims to propose reaction mechanisms for transition metal sulfides under solvothermal conditions by combining *in situ* X-ray spectroscopy and scattering analysis with quantum-mechanical calculations. This complementary approach offers insights into the formation of transition metal sulfide molecular clusters, the emergence of transition metal sulfide nuclei, and the crystallization processes of transition metal sulfide nanoparticles, nanorods, and nanosheets.

Zusammenfassung

Die Synthese von Nanomaterialien in Lösung umfasst oft mehrere Zwischenschritte vom Vorläufer bis zum Endprodukt, wie es die nicht-klassische Nukleationstheorie beschreibt. Der erste Schritt in einer One-Pot-Reaktion beginnt typischerweise mit der Auflösung der Vorläufer in einem Lösungsmittel, was oft durch die Koordination von Metallionen mit spezifischen Liganden gefördert wird. Beim Erhitzen wird eine Reihe von chemischen Reaktionen ausgelöst, die zur Nukleation und zum Wachstum der gewünschten Nanopartikel führen. Das Verständnis aller Schritte bei der Synthese von Nanomaterialien ist entscheidend für die Kontrolle und Anpassung ihres Formationsmechanismus. Übergangsmetalloxide und -sulfide werden in einer Vielzahl von Anwendungen eingesetzt. Während zahlreiche mechanistische Studien für Metalloxide in der Literatur verfügbar sind, ist der Reaktionsmechanismus, der Herstellung vieler Übergangsmetallsulfide, noch nicht im Detail verstanden. Diese Dissertation beleuchtet die Bildung von ZnS-Nanomaterialien in solvothermalen Reaktionen durch *in situ* Röntgenspektroskopie und Streutechniken als Blaupause für andere Syntheserouten und zeigt eine vorläufige Charakterisierung der Fe_xS_y-Nanomaterial-Synthese.

Wir nutzten *in situ* Valenz-zu-Kern-Röntgenemissionsspektroskopie (vtc-XES) kombiniert mit *in situ* hochenergetischer Fluoreszenz-detektierten Röntgenabsorptionsspektroskopie (HERFD-XAS), unterstützt durch Dichtefunktionaltheorie (DFT)-Berechnungen, um die Metall-Ligand-Koordination während der Synthese von Sphalerit ZnS-Nanorods (s-ZnS) aufzuklären. Die Studie erläutert die Auflösung von $Zn(Ac)_2$ in Oleylamin (OA) und schlägt die Bildung von $[Zn(OA)_4]^{2+}$ und $[Zn(OA)_6]^{2+}$ Komplexen vor, sowie den Ligandenaustausch zu Oleylthioamid (SOA) bei Zugabe von elementarem Schwefel zur Reaktionsmischung bei Raumtemperatur. Während der Synthese von s-ZnS wurden *in situ* vtc-XES und HERFD-XAS Analysen eingesetzt, um eine *in situ* HOMO/LUMO-Lücke zu berechnen, welche das Entstehen einer Bandstruktur während der Synthese von s-ZnS aufzeigt und die Größenbestimmung der Zwischenstruktur, des ZnS-Nanopartikels in der Wurtzit-Phase (w-ZnS), basierend auf ihrer Bandlücke ermöglicht. Ergänzende *in situ* Pulverdiffraktometrie (PXRD) und Kleinwinkel-Röntgenstreuungsanalysen (SAXS) bestätigen die Identität von w-ZnS und s-ZnS und liefern zusätzliche Informationen über deren Größe und Morphologie.

Wir entwickelten außerdem die Synthese von ZnS-Nanopartikeln in einer Wasser-Toluol-Solvothermalsynthese und untersuchen diese. Die Methode ermöglicht es, kolloidal stabile

monodisperse ZnS-Nanopartikel in der Sphalerit-Phase zu erhalten. Die Diffusion von Zn^{2+}-Ionen an der Wasser-Toluol-Grenzfläche wurde durch ortsaufgelöste HERFD-XAS-Analysen untersucht, wobei die Koordination der Zn^{2+}-Ionen in jeder Phase mithilfe von DFT-Berechnungen aufgelöst wurde. Die Auflösung von $Zn(Ac)_2$ in Wasser führt zur Bildung eines $[Zn(H2O)_6]^{2+}$-Komplexes. Die Zn^{2+}-Ion wandern bereits bei Raumtemperatur in die Toluol-Phase und bilden einen $[Zn(OA)_6]^{2+}$-Komplex. *In situ* HERFD-XAS während des Erhitzens der Reaktionslösung bis zu 155°C zeigt die Bildung von ZnS-Nanopartikeln in der Sphalerit-Phase, die ein $[Zn(RS)_4]^{2+}$-Cluster und ZnS Nukleationskeime als Zwischenstrukturen durchlaufen. Die Erkenntnisse wurden durch *in situ* PXRD und Totalen Streuungsanalyse (TS) ergänzt, die das Auftreten dieser Zwischenstrukturen bestätigen und ihnen Domänengrößen zuweisen. Um die Vielseitigkeit der Methode zu validieren, wendeten wir die komplementäre Analyse an, um die Bildung von Fe_3S_4-Nanomaterialien in einer solvothermalen Reaktion zu verstehen. Da die Reaktion von $Fe(acac)_3$ mit elementarem Schwefel und in Toluol gelöstem Oleylamin die erforderliche Reaktionstemperatur (180°C) zur Erzeugung von Fe_3S_4-Nanomaterialien nicht erreichte, wurde das Lösungsmittel durch Benzylalkohol (BA) und die Schwefelquelle durch Thioacetamid ersetzt. In dieser Reaktion war keine Zugabe von Oleylamin erforderlich. BA ist bekannt als Lösungsmittel, das die Bildung kleiner und monodisperse Nanopartikel fördert.

Die vorläufige Analyse von *in situ* HERFD-XAS und vtc-XES Daten der Synthese von Fe_3S_4-Nanomaterialien deckt die Bildung einer Zwischenstruktur oberhalb von 50°C auf, die der Koordination von $Fe(acac)_3$ durch BA mit der Bildung eines $[Fe(acac)_2(BA)_2]$-Komplexes zugeschrieben werden kann, wie durch HERFD-XAS-Analyse aufgelöst und durch DFT-Berechnungen unterstützt. Darüber hinaus durchläuft die Bildung von Fe_3S_4-Nanokristallen eine Zwischenbildung von FeS-Nanokristallen, wie durch kombinierte HERFD-XAS und FEFF-Analyse aufgezeigt. Der *in situ* Ansatz von vtc-XES zeigt Änderungen in den Donor-Orbitalen während der ersten 50 Minuten der Reaktion, was das Auftreten des $[Fe(acac)_2(BA)_2]$-Komplexes bestätigt. Durch ergänzende *in situ* PXRD-Analysen identifizierten wir die Bildung von FeS-Nanosheets und deren Umwandlung in Fe_3S_4-Nanokristalle, die ungefähr 22 nm groß sind.

Diese Arbeit präsentiert eine Analyse der Koordinationschemie und der strukturellen Evolution während der Synthese von ZnS- und Fe_xS_y-Nanomaterialien. Ziel ist es, Reaktionsmechanismen für Übergangsmetallsulfide unter solvothermalen Bedingungen vorzuschlagen, indem *in situ* Röntgenspektroskopie und Streuanalyse mit quantenmechanischen Berechnungen kombiniert werden. Dieser komplementäre Ansatz bietet Einblicke in die Bildung von Übergangsmetall-Sulfid-Molekülclustern, das Entstehen von Übergangsmetall-Sulfid-Kernen und die Kristallisationsprozesse von Übergangsmetall-Sulfid-Nanopartikeln, -Nanorods und -Nanosheets.

Table of Content

1 Introduction

Controlling physical key parameters of materials, such as size, shape, composition, and atomic structure, is the foundation for influencing their electronic properties. The group of nanomaterials, materials in the site range between ∼1-100 nm, exhibit advanced physicochemical properties due to confinement effects and their large surface-to-volume ratio.[1, 2]

By confining the size in 0D (nanospheres)[3], 1D (nanorods)[4, 5], or 2D (nanosheets)[6], the quantum confinement effect can be used to access distinct optical or electronic properties.

Limited access on earth calls for scientists to establish abundant alternatives to noble metal nanoparticles. Transition metal oxides,[7, 8] nitrides,[9] selenides,[10-12] or sulfides[13, 14] can cover the range of metallic to large band gap semiconductors, enabling them to be used for a broad range of applications. Transition metal sulfides are a promising class of materials due to their chemical stability, low-cost fabrication, and high abundance. Especially the formation of ZnS nanomaterials in solvothermal reactions is often chosen to achieve wide band gap semiconducting quantum dots. The reaction of $Zn(Ac)_2$ with elemental sulfur and oleylamine is widely used to synthesize ZnS nanomaterials in different shapes and morphologies, although the role of oleylamine during the synthesis is poorly understood.[15]

The metal-ligand coordination in the reaction solution and the arrangement of atoms in the nanoparticle define the orbital composition and mixing and directly correlate with the electronic properties of materials at each step in the reaction.[8] Therefore, resolving the emergence of electronic and atomic structures during the synthesis of nanomaterials provides the knowledge to tune them. Often, the orbital composition is probed by exciting electrons from the highest occupied orbitals (valence band in crystals, HOMO in molecules) to the lowest unoccupied orbitals (conduction band in crystals, LUMO in molecules), e.g., by UV-Vis absorbance spectroscopy.[16] Especially for large band gap semiconductors, these excitation energies are moved to higher energies, where the signals can interfere with electronic structures of organic components, like ligands and solvents. This lack of sensitivity to the material of interest makes these methods not applicable to probing the emergence of the orbital compositions during the synthesis of large band gap semiconductors.

Synchrotron-based analysis techniques, such as X-ray scattering and spectroscopy, have been utilized over the past few decades as powerful tools for analyzing the atomic and electronic structures of nanomaterials during their synthesis.[17-20] Hard X-ray radiation offers, due to its small wavelength, a high penetration depth, and the ability to test complex sample environments. While total scattering analysis records all equipment and substances in the beam path and therefore relies on adequate background subtraction, X-ray spectroscopy provides element-specific sensitivity due to excitation or recombination at distinct element-specific absorption or emission lines. While X-ray scattering is a powerful technique to resolve the atomic structure of crystals (PXRD) and nano-crystalline materials (PDF), [21] X-ray spectroscopy experimentally accesses the electronic structure of the absorbing atom by probing the excitation of a core electron into the LUMO (XANES) or the recombination of a valence-electron to the core (vtc-XES).[22] XANES is extremely sensitive to metal-ligand coordination, giving rise to coordination numbers, geometries, and oxidation states. Vtc-XES provides detailed information about the identity of the ligands and their oxidation states. The analysis of nanomaterials can be complemented by SAXS experiments, where the signal gives rise to the shape and size of nanomaterials, as well as their assembly in solution. Combining multiple X-ray scattering and spectroscopic techniques during the synthesis of nanomaterials (*in situ*) can provide a comprehensive understanding of the reaction mechanism, nucleation and growth phases, and changes in morphology during solvothermal reactions.

1.1 Scope of this thesis

This thesis aims to employ combined X-ray scattering and X-ray spectroscopy analysis to investigate the formation of ZnS nanomaterials *in situ*. The first step of one-pot solvothermal synthesis is the dissolution and coordination of precursors and ligands. Therefore, we utilized HERFD-XAS, vtc-XES, and DFT analysis to clarify the dissolution and coordination of $Zn(Ac)_2$ and sulfur with oleylamine (Chapter 4.3.1).
This thesis overcomes temporal limitations in collecting vtc-XES data *in situ*, enabling monitoring changes in vtc-XES during the synthesis of transition metal sulfides. The obtained vtc-XES data provides experimental access to the electronic structure by revealing the *in situ* HOMO/LUMO gap during the formation of ZnS nanorods (Chapter 4.3.2). The element-specific X-ray spectroscopic methods facilitate studying the formation of large band gap semiconductor nanoparticles without signal interferences from present organic molecules. Combining X-ray spectroscopy analysis with in situ X-ray scattering results in a comprehensive analysis of the reaction mechanism, resolving the identity of intermediate states (Chapter 4.3.2). The investigation of the electronic structure was complemented by following the emergence of the atomic structure by *in situ* PXRD and SAXS analysis, also providing the size and shape evolution of w-ZnS and s-ZnS throughout the reaction (Chapter 4.3.3).

Those findings allow for the development of a novel synthesis protocol for yielding ZnS nanoparticles (Chapter 5). The formation of ZnS at the water-toluene interface aimed to enhance the solubility of precursors in the reaction solution. The diffusion of Zn^{2+} ions through the water-toluene interface was investigated using HERFD-XAS and DFT calculations (Chapter 5.3). The combination of *in situ* HERFD-XAS with *in situ* PXRD and PDF analysis reveals the formation of ZnS clusters, the Zn-S-Zn bond formation, as well as the crystallization into ZnS nanoparticles (Chapter 5.3).

Further, the preliminary analysis of small band gap semiconducting iron sulfide nanomaterials is presented (Chapter 6). To reveal the coordination of $Fe(acac)_3$ with thioacetamide in BA, we applied *in situ* vtc-XES and HERFD-XAS analysis, showcasing the versatility of the methods. The *in situ* vtc-XES, supported by DFT calculations, revealed changes in donor orbitals at the start of the reaction, which were linked to the solvent coordination of benzyl alcohol on $Fe(acac)_3$ (Chapter 6.2.3). Combining *in situ* HERFD-XAS, vtc-XES, and PXRD analysis reveals the formation of FeS nanosheets as intermediates in the reaction, offering insights into the phase transformation to Fe_3S_4 nanoparticles.

2 Nucleation and growth of transition metal sulfides.

This section is partly paraphrased from Thomson et al. [15]*, and from the PhD thesis from D. Derelli*[23] *and L. Grote.*[24]

2.1 Role of oleylamine in the synthesis of nanostructured transition metal sulfides.

Oleylamine (OA) is a highly versatile reagent for the colloidal synthesis of various nanoscale materials, owing to its capacity to simultaneously function as a solvent, a surfactant, and a mild reducing agent. OA is a long-chain primary alkylamine, similar to octadecylamine (ODA) or hexadecylamine (HDA), which acts as an electron donor at elevated temperatures. OA is liquid at room temperature, potentially simplifying the washing procedures which usually performed after the nanoparticle synthesis. An additional distinctive feature of this compound is the double bond (C═C) located in the middle of the molecule. Specifically, although ODA and OA have similar basicity and affinity for metals due to their NH_2 functional group, the morphology and crystallinity of nanoparticles produced with these amines can differ significantly.

Often, in nanoparticle synthesis, OA was mainly expected to impact the crystallization, assembly, and shape formation of the particle. In the case of the synthesis of transition metal sulfides, where OA-containing routes are often chosen,[25] the OA also actively contributes to the chemical reaction by, e.g., reacting with elemental sulfide before the reaction. It has been proposed that this reaction, also called ‘solubilization’ of elemental sulfur in OA, is critical for the formation of transition metal sulfides via the sulfur-OA route.[15]

It is important to note that sulfur predominantly exists as S_8 rings.[26] In Reaction 1 depicted in **Figure 2.1.**, a direct nucleophilic attack by nitrogen on the S_8 molecule occurs, leading to the ring-opening and subsequent formation of an open-chain alkylammonium N-polythioamine salt, forming an N−S bond.[27] The second reaction, illustrated in Reaction 2, results in the generation of hydrogen sulfide and an N,N′-polythiobisamine, which contains two N−S bonds.[28] The characterization of these products was limited to elemental analysis[28] and electron spin resonance (ESR).[29]

While Reaction 2 leads directly to the formation of H_2S, it also has been proposed that H_2S can also be generated through the reaction of sulfur with the methylene protons located α to the nitrogen, resulting in the formation of a thioamide (as illustrated in Reaction 3).[27] In both studies, it is suggested that H_2S subsequently reacts with S_8 to yield alkylammonium polysulfides, as outlined in Reaction 4. Alkylammonium polysulfides have been isolated in reactions involving ethylenediamine and benzylamine, and their presence has been proposed to contribute to enhanced solution conductivity in other amines.[30-32]

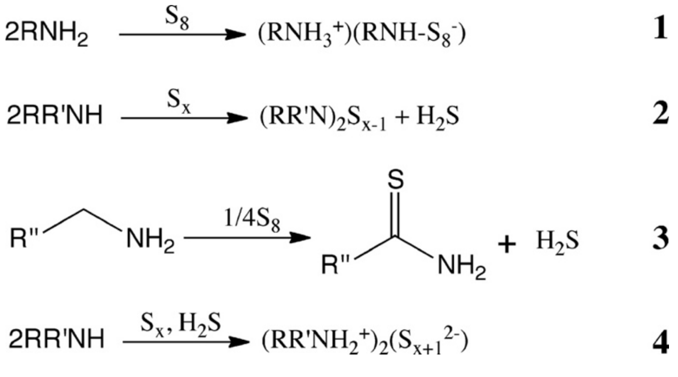

Figure 2.1: Reactions of Sulfur with Amines. Collection of proposed reactions of elemental Sulfur (S_8) with amines from literature. Used with permission from Thomson et.al.[15] Copyright 2011, American Chemical Society.

The literature does not describe which of the possible sulfides will react during the synthesis of transition metal sulfides. Chapter 4 describes the formation of an oleylthioamide at room temperature and its coordination with Zn^{2+} ions in an oleylamine solution.

2.2 Classical and non-classical nucleation

Nanostructures' chemical and physical properties depend highly on their composition, crystal structure, size, and morphology. The key to understanding and influencing the emergence of these properties is to control the synthesis of nanomaterials to gain control over them. There are two main theoretical approaches to describe the nucleation of nanoparticles in solution, the classical nucleation and the non-classical nucleation theory. The classical nucleation theory provides a framework for understanding the formation of nanoparticles in a supersaturated solution by incorporating individual atoms, ions, or molecules. This theory posits that the crystallization of nanoparticles commences from small stable nuclei that develop in the solution when the concentration of the active species pertinent to the nucleation process, commonly referred to as monomers, surpasses a specific critical threshold.[33, 34]

Nuclei can arise through homogeneous nucleation, which occurs due to random collisions among monomers, or through heterogeneous nucleation, which involves interactions between monomers and an external seed.

Following nucleation, the growth of a crystalline nanoparticle proceeds through a layer-by-layer addition of additional monomers from the solution onto the nucleus. This straightforward model is now known as classical nucleation theory. By examining the Gibbs free energy associated with the nucleation process, one can quantitatively determine the size of a stable nucleus. The Gibbs equation is shown in Equation 2.1:[35]

$$\Delta G(r) = \frac{4}{3}\pi r^3 \Delta G_V + 4\pi r^2 \gamma \tag{2.1}$$

In this context, ΔG_V represents the free energy per unit volume of the crystal, and γ represents the surface free energy per unit area. Equation 2.1 describes a balance between the reduction in energy resulting from the formation of chemical bonds within the bulk of the nanoparticles and the increase in energy arising from the unfavorable formation of a solid-liquid interface. For small radii, the destabilizing surface energy predominates, leading to the re-dissolution of the nucleus in solution. In contrast, nuclei with radii larger than a certain critical radius r_c are stable against dissolution and continue to grow. The relationship between free energy and particle radius is depicted in **Figure 2.2**.

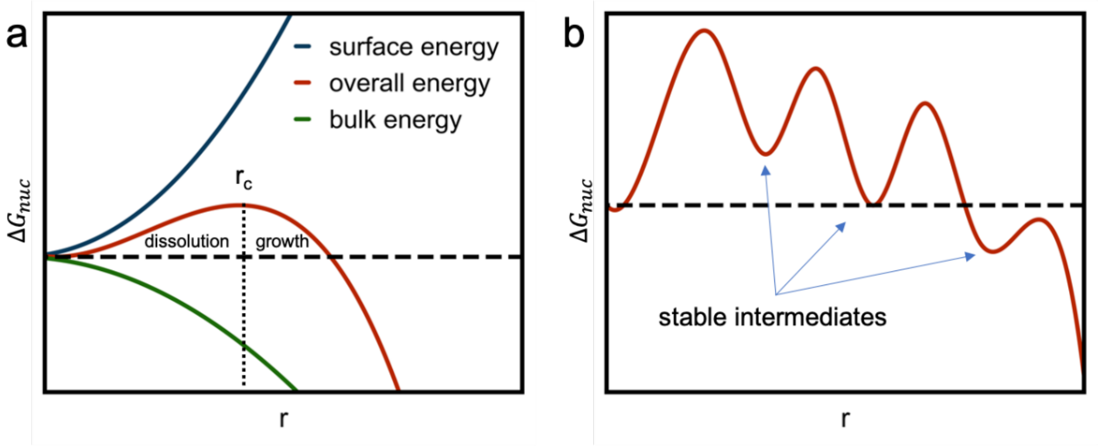

Figure 2.2: Plot of the Gibbs free energy for the classical (a) and the non-classical (b) nucleation pathway. The r_c mark the critical radius, above where a nuclei are stable in solution. The non-classical nucleation pathways describe the formation of stable intermediates, corresponding to local minima in the energy profile.

Within classical nucleation theory, the degree of supersaturation S is the primary parameter influencing the nucleation and growth of nanoparticles. Here, is defined as the ratio

[M]/[M]₀, where *[M]* represents the monomer concentration in solution and *[M]₀* denotes its equilibrium concentration with the solid phase. **Figure 2.3** presents the LaMer diagram, illustrating the changes in the supersaturation profile during nanoparticle synthesis.[33] Three distinct stages are observable throughout the process. Initially, the nanoparticle precursor transforms into the active monomer, accumulating in the solution. Homogeneous nucleation occurs when the monomer concentration exceeds a critical supersaturation level S_c. During this phase, monomer species are consumed, reducing the supersaturation level below S_c. At this point, further nucleation is suppressed, and the existing nuclei grow by incorporating the remaining monomers in the solution.

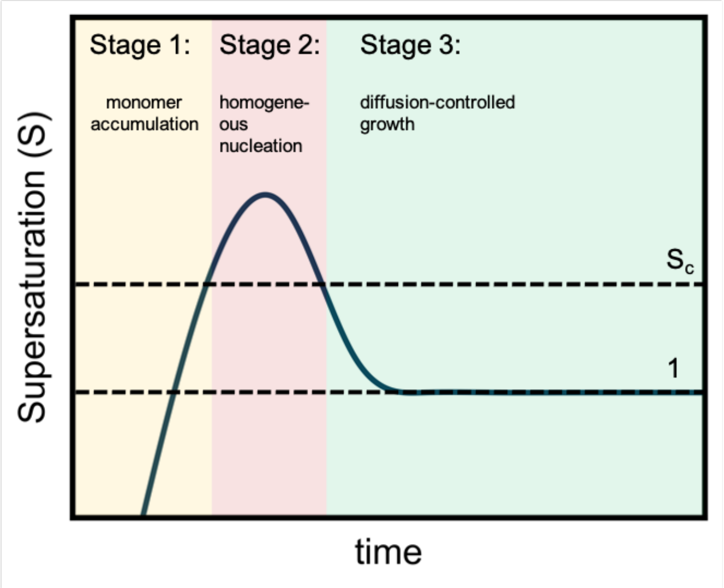

Figure 2.3: LaMer diagram. Sc marks the critical supersaturation, while S = 1 indicates that the monomer concentration in solution is in equilibrium with the nanoparticle. Once S is above Sc, nucleation occurs, which reduces the monomer concentration in the solution until equilibrium is achieved. Conducting a nucleation reaction at a solvent-solvent interface, where there is a constant diffusion of monomer to the reaction phase, can extend the nucleation phase, allowing the nucleation and growth phases to overlap.

The LaMer diagram offers a highly simplified representation of nanoparticle nucleation; however, it is a valuable model for understanding the size distribution of nanoparticles produced via various synthetic methods.[36, 37] For example, the theory suggests that if the nucleation phase is extremely brief, all nanoparticle nuclei form simultaneously, allowing the growth process to occur over the same duration for all nuclei. Consequently, this results in a collection of nanoparticles with uniform size. This principle underlies two prevalent synthetic techniques:

the hot-injection and heat-up methods.[38] During the hot-injection method, one inject rapidly a stock solution containing reactive precursors into a preheated reaction solution including surfactants.[39, 40] The elevated temperatures and high local supersaturation levels induce immediate and rapid nanoparticle nucleation. During formation, surfactants attach to the nanoparticle surfaces, preventing aggregation.

Conversely, the heat-up method differs fundamentally from hot injection.[41] In this technique, a precursor solution is initially prepared at a low temperature and subsequently heated to a higher temperature, triggering the nanoparticle formation.[42, 43] If the heating rate is sufficiently rapid, the temperature quickly surpasses the reaction's activation threshold, leading to a nucleation burst.[44] Nonetheless, monodisperse nanoparticles can also be synthesized using the heat-up method by employing comparatively slow temperature increases.[43, 45] These findings indicate that autocatalytic reactions, not accounted for in the classical model, can significantly influence the kinetics of nanoparticle nucleation, as corroborated by numerical simulations.[46] By establishing a reaction with a solvent-solvent interface, the diffusion of monomers through this interface can further impact the nucleation process. If monomers diffuse into the reaction phase after nucleation begins, the LaMer diagram may display multiple maxima corresponding to several nucleation phases or a prolonged nucleation phase, which result in simultaneous nucleation and growth.[47] In this case, where the diffusion impacts the nucleation rate, the reaction at a solvent-solvent interface behaves similarly to a reaction with the constant addition of monomer. In Chapter 5, the diffusion of Zn^{2+} ions through the water-toluene interface achieves equilibrium prior to the nucleation of ZnS nuclei. Therefore, the nucleation in this reaction should behave similarly to a single phase heating up reaction.

Classical nucleation theory typically explains nanoparticle growth as the result of individual atoms, ions, or molecules adding to a nucleus. However, it does not work for synthesizing nanoparticles with complex geometries, polycrystalline structures, and organic-inorganic hybrids, which are commonly produced. Investigations using electron microscopy and X-ray techniques have revealed synthetic pathways not anticipated by the classical model.[23, 24] In non-classical pathways, particle nucleation involves a multi-step process that includes amorphous intermediates such as droplets, complexes, clusters, and oligomers.[48] These intermediates are moderately stable in solution and reduce the overall energy barrier for forming stable solids, as depicted in **Figure 2.2b**.[49-51] Pre-nucleation clusters can develop into final nanoparticles through various routes, some of which are schematically presented in **Figure 2.4**. Once primary stable nanoparticles form, they can grow into single crystalline nanoparticles via monomer addition, consistent with classical nucleation theory (**Figure 2.4a**). Alternatively, primary particles may assemble into aggregates with a standard crystallographic orientation, known as mesoscale assemblies (**Figure 2.4b**), which can further merge into single-crystalline particles through processes like oriented attachment.[52, 53] Primary particles stabilized with organic ligands can also self-assemble with a shared crystallographic orientation to form mesocrystals (**Figure 2.4c**)[54, 55]. Pre-nucleation clusters might also follow distinct pathways that lead to the formation of intermediate dense liquid droplets or amorphous phases through the aggregation of individual clusters or oligomers (**Figure 2.4d**).[56-58] These intermediates further evolve through aggregation and crystallization, resulting in polycrystals with intricate shapes.

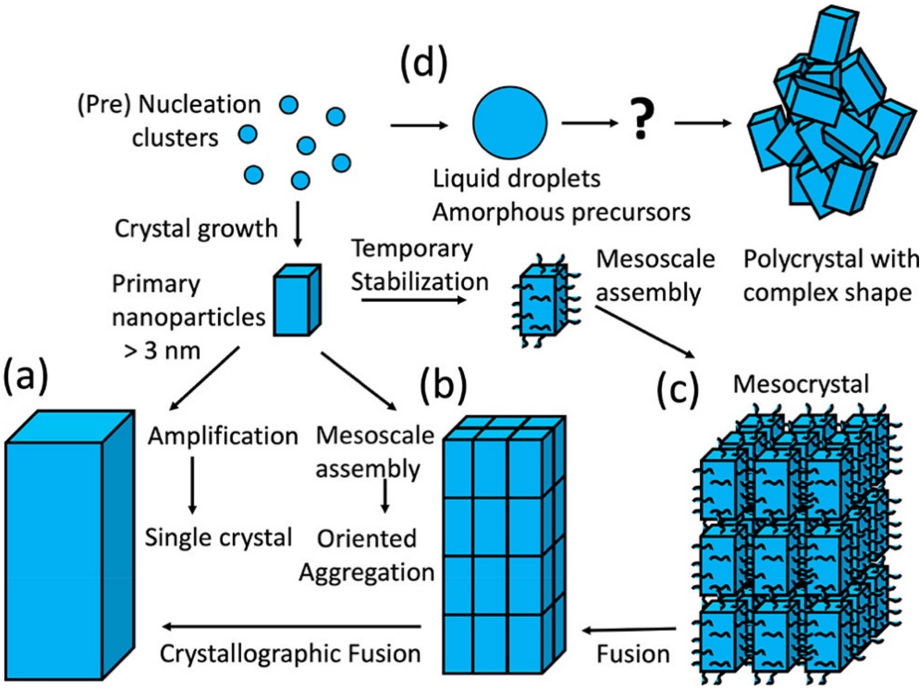

Figure 2.4: Illustration of non-classical crystallization pathways. Classical nucleation results in a single crystal formation (a). Oriented attachment of non-stabilized primary particles results in mesoscale assemblies (b) while stabilized primary particles by organic surfactants self-assemble into mesocrystals (c). The formation of a liquid droplet or amorphous precursor before the nucleation of a polycrystal particle with a complex shape is described as a Pre-nucleation cluster (d). Used with permission from[59] Copyright 2019, American Chemical Society.

A comprehensive model for particle nucleation does not currently exist. The complexity of these processes necessitates moving from a "one model fits all" approach to a chemistry-based understanding of nucleation and crystallization phenomena. X-ray techniques effectively elucidate the chemical and structural changes involved in nanoparticle formation.

3 Fundamentals of X-ray-based methods

This section is partly paraphrased from the textbooks by Als-Nielsen and McMorrow,[60] *Egami and Billinge,*[61] *and Juhin and Glatzel,*[62] *and from F. Neese et.al.,*[63]*, Cutsail III et.al,*[64] *and from the PhD thesis from D. Derelli*[23] *and L. Grote.*[24]

Material properties, like chemical, electronical and structural material properties, can be resolved by the materials interaction with X-rays. This chapter introduces X-ray analytical techniques, highlighting their strengths and weaknesses in observing various nanomaterial formation and transformation stages. It will become evident that these methods are often used complementary, and combining them in multimodal experiments provides the most comprehensive understanding of a synthesis.

At the most fundamental level, the interaction of an X-ray wave with an electron is considered. Classically, the incident electromagnetic wave accelerates the electron, emitting radiation at the same frequency, an effect known as Thomson scattering. For all the electrons in an atom, this scattering is described by the atomic form factor $f^0(\boldsymbol{q})$, which depends on the scattering vector $\boldsymbol{q} = \boldsymbol{k_i} - \boldsymbol{k_f}$, where $\boldsymbol{k_i}$ and $\boldsymbol{k_f}$ are the incident and outgoing wavevectors, respectively.

Electrons bound to an atomic nucleus cannot freely follow the incident electromagnetic wave. Classically, a bound electron interacting with the wave can be considered a forced damped oscillator. This concept consequently results in a decrease in the atom's scattering length, described by an additional term $f'(\omega)$ in the atomic form factor. Furthermore, an imaginary term $if''(\omega)$ must be included to account for damping in the oscillator, which describes X-ray absorption. Therefore, the complete atomic form factor is given by:

$$f(\boldsymbol{q},\omega) = f^0(\boldsymbol{q}) + f'(\omega) - if''(\omega) \tag{3.1}$$

Loosely bound electrons primarily influence the scattering term $f^0(\boldsymbol{q})$ in high energy levels. In contrast, the behavior of the correction terms $f'(\omega)$ and $f''(\omega)$ is determined by core-level electrons with binding energies similar to typical X-ray photon energies. These correction terms depend on the frequency ω of the incident X-rays but are independent of $\boldsymbol{q}$. They reach maximum values when the photon energy matches the binding energy of a core-level electron.

3.1 Photon-in photon-out spectroscopy:

Photon spectroscopy investigates the inelastic interaction between electromagnetic radiation and matter. The radiation induces excitations within the system, leading to the formation of excited states. Spectroscopy measures the energies associated with these excited states and the probability of their formation, known as spectral intensities. This methodology enables spectroscopists to characterize the atomic and electronic structure of the system, ideally corroborated by quantum mechanical calculations.[62]

This chapter describes the fundamental theoretical background of photon-in photon-out spectroscopy. In **Figure 3.1** the main transitions of interest, probed with resonant excitation (right) and non-resonant excitation (left) are summarized. Zn is a special case in X-ray spectroscopy since the excitation of a core electron 1s to 3d orbitals is inhibited by the saturated d-orbitals. In contrast to the XAS analysis of Zn compounds, the XAS analysis of Fe compounds also gives rise to d-orbitals when focusing on the pre-edge.[19] The pre-Edge of Iron is well known for its sensitivity to coordination number, ligand identity, bond angles between Fe and ligand.

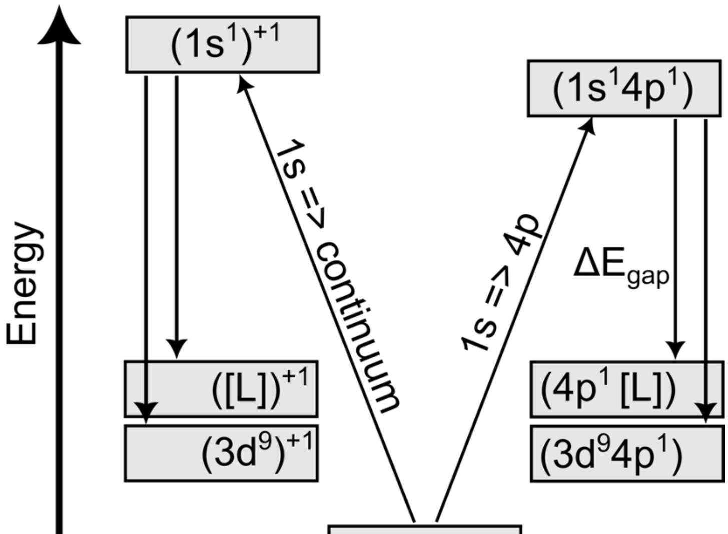

Figure 3.1: Electron transitions diagram. Showing non-resonant (left) and resonant (right) excitations in Zn. Adapted with permission from *Klemeyer et. al.* [65] Copyright 2024, American Chemical Society.

All shown X-ray spectroscopic data are collected at the ESRF beamlines ID24 and ID26, where a Johann-Type spectrometer is installed between sample and detector. A drawing of this setup is shown in **Figure 3.2.**

The movable spherical bent analyzing crystals work like reflective prisms which divide the emitted x-rays from the sample within energy operation range of a crystal, into an Bragg-angle specific energy.[66] Therefore, these crystals work as a monochromator where the energy can be scanned by varying the angle between sample, crystal and monochromator.[67-69]

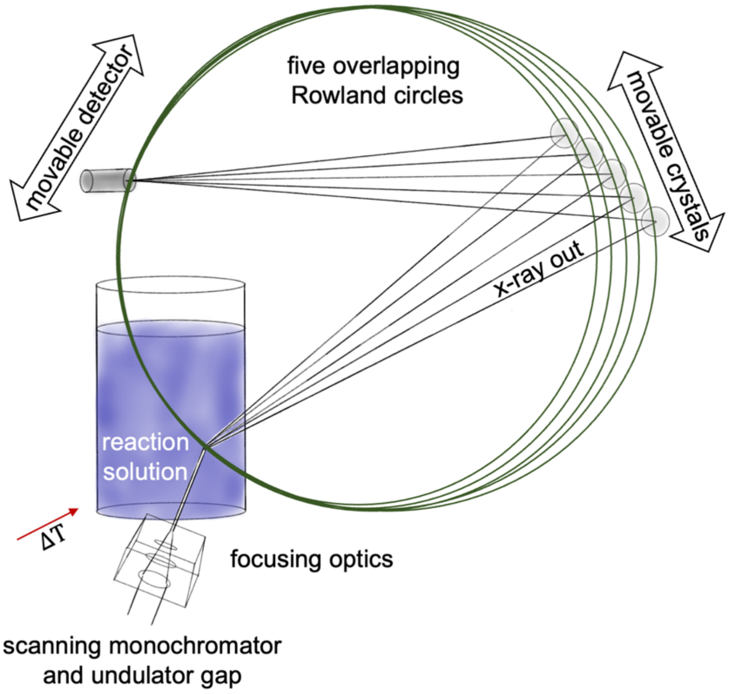

Figure 3.2: Johann-type spectrometer at ESRF Beamlines ID24 and ID26. Five spherical bent analyzing crystals with overlapping Rowland circles are installed between the reaction solution and the SDD detector. The crystals and the detector are moveable on the Rowland circle enables to probe different emission energies. The reaction solution can now be heated to collect *in situ* HERFD-XAS or *in situ* vtc-XES data during the reaction.

With this spectrometer, it is possible to collect the X-ray emission spectra at different excitation energies, which result in a two-dimensional map testing the resonant inelastic X-ray scattering (RIXS) properties of the sample. This map give rise to the energy-loss depended on the incident X-ray energy. A theoretical $1s2p_{3/2}$ RIXS map of Fe^{2+} is shown in **Figure 3.3**. This method is very sensitive to quadrupole transitions and often applied for elements with pre-Edge features in XAS. The RIXS analysis of pre-edge features provide enhanced sensitivity to oxidation states, spin states and coordination geometries.[62] Line profiles in this RIXS maps, indicated by CTE, CIE or CEE in **Figure 3.3**, result in different kind of X-ray spectra. The constant incident energy (CIE) spectra, a vertical cross section at fixed excitation energy (here 7112 eV) relates to a resonant X-ray emission spectrum. The horizontal cross section relates to the constant transferred energy (CTE) spectra, which probe all excitations into the same final states. The constant emission energy (CEE) spectra correspond to lifetime suppressed HERFD-XAS spectra.[70] In this work, we are mainly focused on the HERFD-XAS (CEE) at the Zn and Fe K-edge, which probes the 1s to 4p transition, and on non-resonant Kβ valence-to-core X-ray emission spectroscopy (vtc-XES).

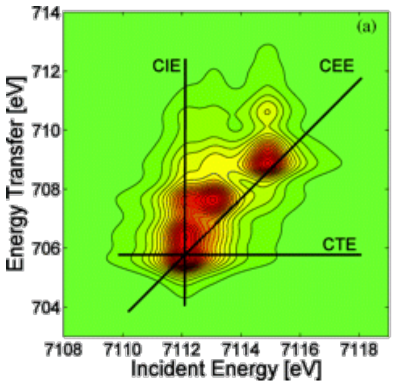

Figure 3.3: Simulated RIXS map of Fe^{2+}. Two-dimensional contour plot of a theoretical 1s2p$_{3/2}$ RIXS spectrum for Fe^{II} using an experimental broadening of 0.3 eV for both the monochromator and the detector resolution. The contour plot indicates lines of equal intensity where the dark (red) areas have the highest intensity. Adapted with permission from *de Groot. al.*[70] Copyright 2005, American Chemical Society.

To collect HERFD-XAS spectra without collecting RIXS maps, the crystals were set to collect the intensity of the Kα1 emission line of Zn and Fe, respectively. The intensity of the emission is directly proportional to the absorbance of the sample. Therefore, scanning the incident X-ray energy while collecting the emission intensity of the Kα1 Line result in a HERFD-XAS spectra. More details about the HERFD-XAS method are provided in **Chapter 3.1.1.**

By fixing the incident X-ray energy above the resonant excitation, one can scan the angle between sample, crystal and detector to acquire an non resonant emission spectra of the sample. These was used to collect vtc-XES data in this thesis. More details about the vtc-XES method are provided in **Chapter 3.1.2.**

3.1.1 X-ray Absorption Spectroscopy (XAS):

X-ray absorption spectroscopy utilizes the frequency dependence of the absorption term f'' in the atomic form factor (Equation 3.1). This technique provides element-specific chemical information about the absorbing atom, such as its oxidation state, and details about ligands in the local chemical environment. XAS spectra also contain short-range structural information.

The simple model of a forced damped oscillator is inadequate for accurately describing the absorption of X-rays by bound electrons. A quantum mechanical approach that describes electronic transitions, which considers the chemical environment of the absorber, would be necessary for a more precise description. This subchapter will address the subject from an experimental standpoint, using the Lambert-Beer law to describe X-ray absorption:[71]

$$I = I_0 * e^{-\mu d} \tag{3.2}$$

where I_0 and I are the incident and transmitted intensities, respectively, d is the thickness of the sample, and μ represents the linear absorption coefficient. The absorption coefficient μ is related to f'' by:

$$\mu = 2\rho_{at} r_0 \lambda f'' \tag{3.2}$$

where ρ_{at} is the average atomic number density, r_0 is the Thomson scattering length, and λ is the X-ray wavelength. An absorption spectrum is obtained by measuring how μ varies with the incident photon energy E.

When E exceeds the binding energy of a core-level electron, there is an observable jump in μ due to the photo-absorption of the photon that excites the electron. This is referred to as an absorption edge. The naming of absorption edges uses capital letters (K, L, M, etc.) to indicate the principal atomic quantum number n of the initial state, with additional indexes denoting the azimuthal quantum number l and differentiating the high spin-orbit split of the core states. For instance, the excitation of a 1s electron results in the K edge, whereas the excitation of a 2s electron corresponds to the L_1 edge, and excitations from the $2p_{1/2}$ and $2p_{3/2}$ levels correspond to the L_2 and L_3 edges, respectively. The position of the edge can also shift depending on the oxidation state of the absorber. As the oxidation state increases, the binding energy of core-level electrons slightly rises, causing the edge to shift to higher incident energies.[71]

In some cases, for example, in high-absorbing samples or in low-concentration samples, one could use the secondary process of fluorescence to probe the absorption of the element of interest. The fluorescence lines are consequences of the core-hole creation during the absorption process, and their intensity is directly proportional to the absorption process. Using a spectrometer, like a Johann-type spectrometer,[72] one could selectively focus on the intensity of specific fluorescence lines while scanning the incident X-ray energy around the K-Edge, significantly reducing the impact of core-hole lifetime broadening on the XAS spectra. Due to the increased energy resolution of those XAS spectra, those are often called high energy resolution fluorescence detected XAS (HERFD-XAS). Due to the improved energy resolution, the sensitivity to weak contributions to the XAS spectra, like solvent coordination, is enhanced. By excitation above the K-edge, and scanning the energy of the emitted fluorescence, one can acquire X-ray emission spectra, which is explained in the next section.

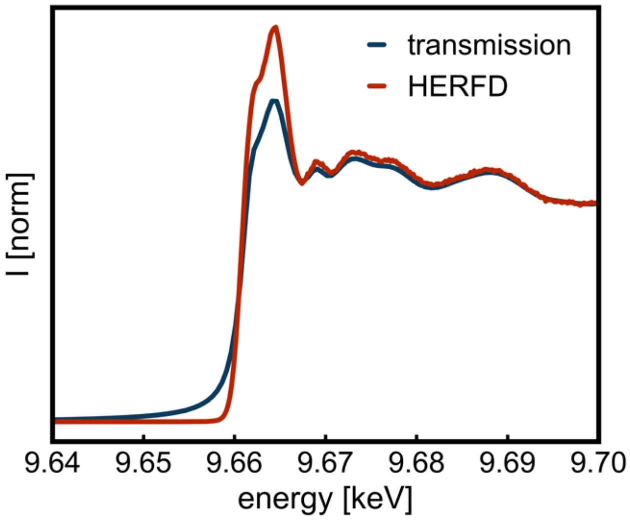

Figure 3.4: XAS in transmission and in HERFD mode. Comparing XAS spectra of sphalerite ZnS nanoparticles in toluene, measured in transmission (blue) and HERFD-XAS mode (red).

The applicability of HERFD-XAS extends beyond merely attaining higher resolution spectra. An additional advantage of utilizing Johann-type spectrometer is its capacity to effectively suppress and eliminate potential background signals. The configuration of the Johann-type spectrometer, which includes the spatial arrangement of the sample, optical components, and detectors, is specifically designed to detect narrow emission energy defined by their Bragg angle. Consequently, the spectrometer naturally rejects extraneous background signals originating from locations in space other than the sample itself, such as cryostat walls, windows, and beamline components.[73]

HERFD-XAS has enabled the acquisition of well-resolved pre-edge features for various transition metals. The enhanced resolution of the experimental spectra, combined with time-dependent density functional theory (TDDFT) calculations, has facilitated a more comprehensive understanding of the electronic and geometric structures, also of e.g., numerous enzymatic active sites. For example, probing the heterometal molybdenum (Mo) within the nitrogenase active site through X-ray absorption necessitates an incident beam energy of approximately 20 keV. Conventional methods for obtaining XAS spectra of Mo complexes yield broad profiles, thereby constraining the chemical information that can be derived. Mo Kα HERFD-XAS presents a viable approach to achieving higher resolution spectra in which the pre-edge and rising edge features are distinctly resolved.[74] The exceptional alignment between the Mo Kα HERFD-XAS pre-edges and the corresponding TDDFT-calculated spectra of various Mo model complexes build the foundation for further exploration of the biological catalytic center of nitrogenase.[75] Augmented by broken symmetry quantum chemical calculations, the Mo Kα HERFD spectra of the Mo site in nitrogenase and other biomimetic $MoFe_3S_4$ clusters are most congruent with a local oxidation state of Mo(III), exhibiting an atypical non-Hund's (↑ ↓ ↓) spin configuration of the d3 center, as corroborated by Mo L-edge X-ray magnetic circular dichroism (XMCD) measurements.[76] The XMCD method can also be transferred to other transition metals to investigate spin states, e.g., XMCD can also be used to demonstrate the properties of superparamagnetic iron oxide nanoparticles suspended in liquids. The spectral shape and magnetic contrast obtained from this experiment allow for assessing the site distribution and magnetic state of metal ions in the spinel phase.[77]

HERFD-XAS also has valuable application in coordination chemistry, where the element-specific method can resolve beside atomic structures of transition metal complexes, their solvent coordination, and electronic structure.[78]

3.1.2 Valence-to-core X-ray Emission Spectroscopy (vtc-XES)

The valence-to-core X-ray Emission Spectroscopy (vtc-XES) provides sensitivity to ligand identity and coordination geometry by probing the recombination from the HOMO orbitals.[79] Valuable chemical information is contained within the occupied metal p-DOS near the Fermi level. Through orbital mixing, ligand electrons contribute to the metal p-DOS, rendering the spectra sensitive to the local environment of 3d transition metal elements. **Figure 3.5.a** shows that one can effectively identify different ligands, such as oxygen, sulfur, and selenium via vtc-XES. DFT calculations state that the $K\beta_2$ peak mainly relies on dipole transitions, while the $K\beta_5$ peak also reflects 3d=>1s transitions, which are possible due to p-d orbital mixing, shown in **Figure 3.5.b.**[80]

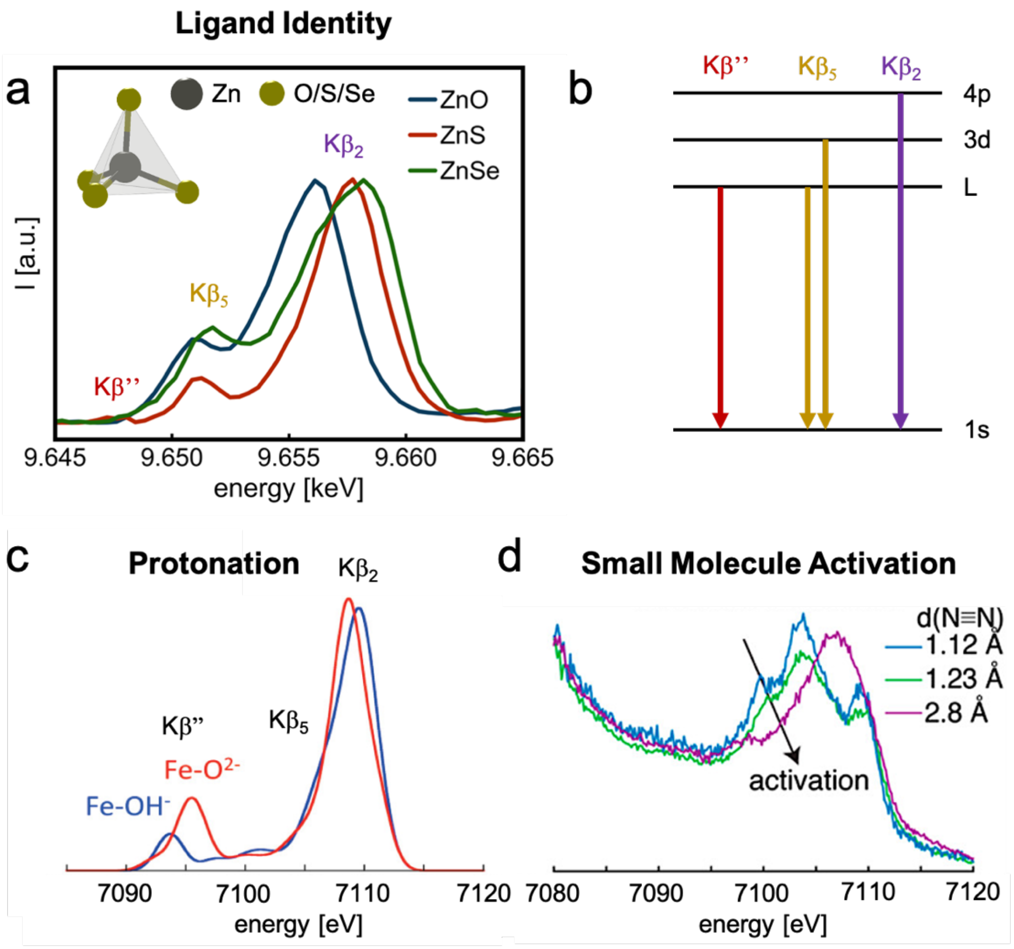

Figure 3.5: vtc-XES application examples. (a) Comparing experimental vtc-XES of ZnO (blue, Sigma Aldrich 544906), ZnS (red, Sigma Aldrich 244627), and ZnSe (green) nanoparticles[81] showcases the sensitivity of vtc-XES to the ligand identity. All spectra were normalized to the maximum intensity after baseline subtraction. (b) transitions, which induces the Kβ'', the $K\beta_5$ and $K\beta_2$ peaks in the Zn vtc-XES. (c) vtc-XES on Fe complexes with different electronic states of oxygen, highlighted the enhanced sensitivity of the Kβ" peaks on the oxidation states of ligands. (d) Example of small molecule binding to a Fe Complex and its change in bonding lengths. The figure is adapted with permission from Lee[82] and Cutsail III et.al.[64]

The ligand sensitivity of vtc-XES was essential in revealing the previously unidentified central light atom within the $[Fe_7S_9Mo\mathbf{X}]$ active-site cluster of nitrogenase, where it was conclusively demonstrated that X corresponds to a carbon atom from an interstitial carbide ligand.[83] Initial resolution protein crystallography efforts identified a light atom within this extensive cluster; however, its precise identity remained unresolved until a structure with 1.0 Å atomic resolution was achieved.[84] Furthermore, the capacity of vtc-XES to detect the presence of carbide within the nitrogenase M-clusters has also been leveraged to gain insights into the point of carbide insertion during the biosynthetic pathway,[85] in addition to confirming the presence of carbide in the active site of vanadium-dependent nitrogenases.[86] Additionally, it was also proven that vtc-XES could detect and characterize hybrid ligand systems by identifying crossover signals, where different ligands are coordinated on the probed transition metal.[87]

The initial application of vtc-XES to a biological system involved the Mn vtc-XES of the manganese oxygen-evolving complex (OEC) in a photosystem.[88] The Mn vtc-XES results for the photosystem demonstrated a moderate Kβ″ emission intensity, which, in comparison to various biomimetic manganese–oxygen complexes, was most effectively interpreted through the presence of multiple Mn–(μ-O)2–Mn motifs within the cluster. This vtc-XES investigation provided the first direct spectroscopic evidence for the existence of bridging oxo ligands. Although the study relied significantly on synthetic models for comparative analysis and the understanding of the biologically active site, advancements in quantum chemical methodologies now facilitate relatively accurate predictions of vtc-XES spectra.[89] More recently, Calcium vtc-XES has been employed to investigate protonation events in Mn_3CaO_4-based molecular mimics of the OEC, indicating its potential as a valuable tool for elucidating mechanistic insights into biological water-splitting processes.[90] However, it is noteworthy that preliminary published studies on Mn vtc-XES of different S-states within the catalytic cycle of the OEC suggest that the low count rates, combined with rapid sample degradation, render such experiments particularly challenging.[18]

Similar to the vtc-XES of other transition metals, [91] the vtc-XES on Fe can reliably discriminate among the chemical identity[92] and ionization state of ligands, as shown in **Figure 3.5.c.**[82] In both compared spectra, the iron center has a Fe-O bonding, while the main difference is the ionization state of the ligand. The biggest changes, based on a protonation of the ligand, are observable in the Kβ” peak. Recently, it has been shown that the resolution of Fe vtc-XES can be further increased by using a resonant excitation on the 1s => 3d transition (at the energy position of the pre-edge). This technique, also called resonant X-ray emission spectroscopy (RXES), results in vtc-RXES spectra, to which only states of maximum multiplicity can contribute.[93]

The capability of vtc-XES to investigate predominantly ligand molecular orbitals (MOs) has enabled the experimental examination of small molecule interactions with transition metal centers, specifically allowing for quantifying small molecule bond activation (**Figure 3.5.d**). vtc-XES has successfully identified the bonds of both N_2 and O_2^{2-} bond with iron[94] and copper[95] complexes, respectively. The distinct features observed in the vtc-XES spectra facilitate not only the detection of diatomic bonds but also the determination of their bond lengths. Additionally, related studies involving nitrosyl-coordinated iron[96] and nickel[97] complexes have illustrated vtc-XES capacity to discern coordination geometries, including the Ni–N–O bond angles, while also reporting the relative oxidation states of these ligands. These foundational studies establish a basis for future applications e.g., in catalysis research, where *operando* vtc-XES methodologies can be utilized to monitor reactions and investigate the bonding and transformation of small molecule reactants. In this context, *operando* vtc-XES studies of copper zeolites in the ammonia-assisted reduction of nitrogen oxides[98, 99] have contributed to a deeper understanding of the structural transformations of the Cu active site during the catalytic process.

Moreover, in pump–probe studies exploring transient intermediates, X-ray free electron lasers (XFELs) offer significant advantages. XFELs provide fluxes over 10^4 times greater per X-ray pulse compared to single pulses in high-repetition-rate synchrotron-based setups and feature ultrashort femtosecond pulse durations, unlike the tens of picoseconds achievable with the fastest synchrotron sources.[100] The exceptionally brief pulse lengths of XFELs enable the examination of rapid electronic and catalytic processes. This is particularly advantageous for high-valent catalytic intermediates, where the reduced pulse durations offer the potential to prevent X-ray-induced damage.

The ability to interpret vtc-XES spectra by considering only one-electron transitions within the framework of ground-state DFT significantly simplifies deriving insights into the electronic structure from the data. The following chapter elaborates on modeling experimental data with DFT calculations.

3.1.3 DFT calculations

A well-established way to identify chemical structures by HERFD-XAS and vtc-XES analysis, is to compare the experimental spectra with simulated electronic structure by density functional theory (DFT) calculations. DFT calculations are an extremely powerful simulation approach where the electronic properties of e.g. molecular complexes, nanostructures, or clusters can be simulated considering all electrons in the system of interest.

DFT calculations are based on key theoretical concepts from quantum chemistry. At the core are the Hohenberg-Kohn theorems, which establish that the ground state energy of a many-electron system is uniquely determined by its electron density.[101] This allows all properties of the system to be derived from that density. The Kohn-Sham approach further simplifies this by modeling a system of non-interacting electrons moving in an effective potential.[102] This potential includes contributions from external fields and complex electron-electron interactions through an exchange-correlation term.[103]

A critical component of DFT is the exchange-correlation functional,[104] which accounts for the intricate many-body interactions not captured by classical methods. Practical approximations like the Local Density Approximation (LDA),[105] Generalized Gradient Approximation (GGA),[106] or hybrid functionals such as B3LYP are used to compute it.[107] Often, DFT calculations involve solving the Kohn-Sham equations iteratively through a self-consistent field (SCF) procedure.[108] Starting from an initial guess, the electron density is iteratively updated until convergence is achieved, providing the ground state energy and density.

Many programs are available that use DFT to calculate electronic structures or perform structural optimization. In this thesis, DFT was used to correlate experimental spectroscopy data using the ORCA package.[109] Therefore, this section will mainly focus on ORCA.

To model vtc-XES spectra, the simulated spectra should be calculated using DFT because it accurately describes the ground-state electronic structure necessary for occupied orbital transitions, while XAS should be calculated using TDDFT because it effectively handles excitations to unoccupied states and dynamic responses.

In the following **Table 3.1.**, two ORCA input parameters for DFT calculations of vtc-XES spectra (left) and TDDFT calculations of XAS spectra (right). In the following section, the commands are explained one by one.

Table 3.1: Structure of ORCA input files for DFT (left) and TDDFT calculations (right).

spectra to simulate	vtc-XES	XAS
functional, basis-set, basic approximations and convergence criteria	!RKS B3LYP TightOpt TightSCF ZORA-def2-TZVP ZORA !FREQ	!RKS B3LYP TightSCF ZORA-def2-TZVP D3BJ RIJCOSX ZORA
output options (optional)	!Largeprint	!Largeprint
computing resources, parallel processing and memory (optional)	!PAL8 %maxcore 4000	!PAL8 %maxcore 4000
reading orbital configuration of ground-state DFT (optional)	-	!MOREAD %moinp "vtc-XES.gbw"
Type of simulation and parameters	%xes CoreOrb 0 OrbOp 0 end	%tddft orbwin[0]= 0,0,-1,-1 doquad true nroots 300 maxdim 50 end
Input structure, charge, multiplicity	*xyz [charge] [multiplicity] [atomic coordinates] end	*xyz [charge] [multiplicity] [atomic coordinates] end

The first command, '!RKS', sets a restricted Kohn-Sham (RKS) approximation for the calculations, assuming that electron pairs exhibit the same spin quantum number, which decreases the complexity of the calculations. The second command sets used functional in the calculations, here the B3LYP functional, which is a hybride functional combining Hartree-Fock exchange with DFT correlations. For coordination chemistry, the B3LYP functional has been reported as a reliable choice.[107]

In the first step of all quantum mechanical (QM) calculations, the input molecule needs to be geometrically optimized and relaxed. Geometry optimization is efficiently conducted using a set of program-generated redundant internal coordinates, which users can modify as needed. An arbitrary number of constraints can be imposed on the positions of individual atoms, bonds, angles, or dihedrals. If required, the program can optimize, excluding the positions of hydrogen atoms, or reverse all constraints. It is not necessary for the initial geometries to fulfill the constraints. The program will automatically reassign the coordinates if the set of redundant internal coordinates becomes invalid, such as when an angle nears linearity. ORCA provides various levels of accuracy of the relaxation, which can be selected with the convergence criteria in the calculations. For the simulations of the electronic structure, it is suggested to apply strict convergence criteria. The convergence criteria for the relaxation (Opt) as well as for the SCF, are set to 'Tight', which sets the tolerances to: Tol(E) = 1e^{-6}, Tol(RMSG) = 3e^{-5}, Tol(MaxG) = 1e^{-4}, Tol(RMSD) = 6e^{-4}, Tol(MaxD) = 1e^{-3}.[110]

Since the structure was optimized in DFT calculations (left), it can be reused in TDDFT calculations (right) without requiring a new optimization.

The zeroth-order regular approximation (ZORA), includes relativistic effects in the calculations, which is especially required for heavy atoms. Using a def2-TZVP basis set allows for a compromise between computational cost and accuracy. The triple-zeta quality (TZVP), combined with polarization functions (def2), provides a good balance for many chemical systems.[111]

D3BJ is an advanced dispersion correction method that incorporates a damping function to improve the modeling of weak intermolecular forces in DFT calculations, like Van-der-Waals interactions. This correction enhances the reliability of modeling solvent coordination on the metal complex.[112]

For functionals without Hartree-Fock (HF) exchange, like the used B3LYP functional, the resolution-of-the-identity (RI) approximation significantly accelerates the calculation of the Coulomb term (RI-J).[113] Exchange-correlation terms are handled through numerical integration using standard techniques. The nonlocal HF exchange term can be efficiently approximated using an asymptotically linear scaling Chain Of Spheres (COSX) algorithm, similar to pseudospectral techniques, and combined with RI-J to achieve the popular RIJCOSX approximation.[114] The RIJCOSX approximation results in substantial speed improvements without sacrificing accuracy.[115]

The '!FREQ' command instructs ORCA to compute the vibrational frequencies of the optimized molecular structure. This process involves calculating the Hessian matrix, which includes the second derivatives of the energy concerning nuclear displacements. The eigenvalues of this matrix correspond to the vibrational frequencies of the molecular system.

In the %xes mode in ORCA, the ‘CoreOrb 0’ and ‘OrbOp 0’ settings dictate how core orbitals are managed (not included) and indicate that orbital occupations should remain fixed during the calculation, respectively. These configurations help to streamline calculations while focusing on the electronic transitions relevant to X-ray emission processes.

In the %tddft mode, the orbwin[0] parameter specifies the orbital window for selecting the orbitals utilized in the calculation of excited states. It delineates the range of occupied and virtual orbitals to consider when calculating the excitation energies. The nroots parameter indicates the number of excited states (roots) to compute in the TDDFT calculation. By setting ‘nroots’ to ‘300’, you are instructing ORCA to search for up to 300 excited states. This setting is particularly useful when seeking a detailed spectral overview or when addressing large systems where many excited states may be accessible. The maxdim parameter determines the maximum dimension of the block in the diagonals of the Hamiltonian matrix during the calculation.

In conclusion, X-ray absorption spectra can be effectively calculated using TDDFT methods using the described tools in the ORCA program. Conversely, X-ray emission spectra can be accurately predicted using a simpler one-electron approach. Combining vtc-XES and HERFD-XAS analysis with the stationery and TDDFT methods enables researchers to resolve precisely the identity of Zn^{2+} complexes, as shown in **Figure 3.6.**

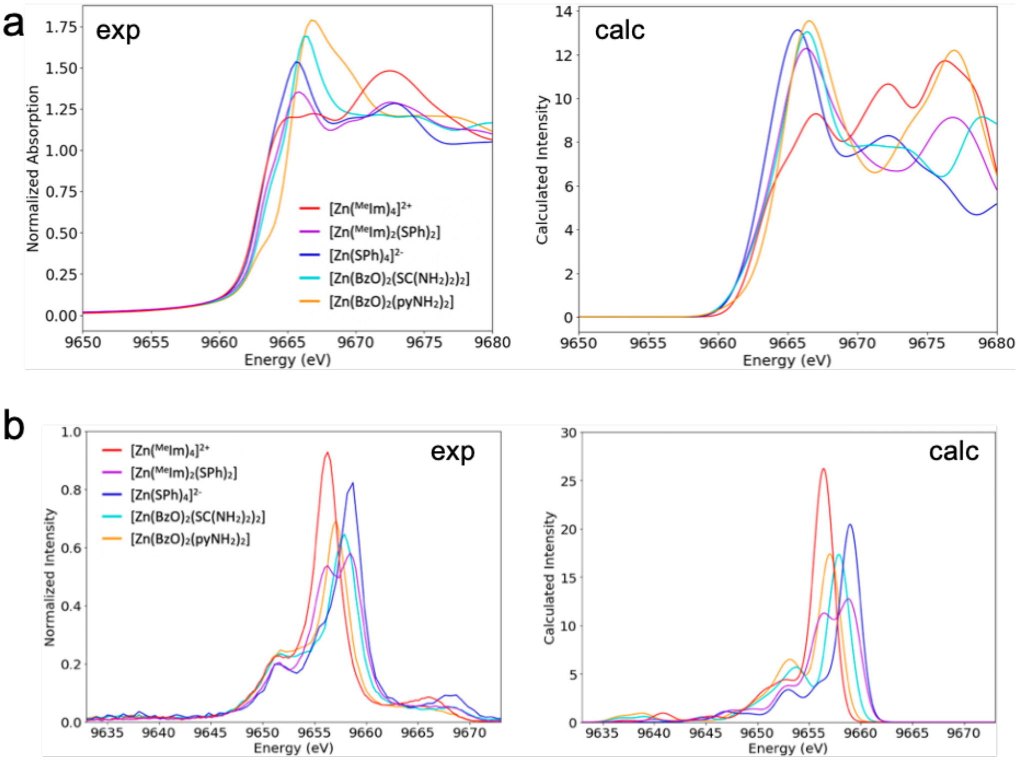

Figure 3.6: Confirming the identity of Zn^{2+} complexes with ORCA calculations. Experimental (left) and simulated (right) HERFD-XAS (a) and vtc-XES data (b) of different biologically relevant Zn^{2+} complexes showcase the capability of reproducing experimental spectra with ORCA calculations. The Figure is adapted within the CC-BY license from *Stepanic et al.*[80]

The **Figure 3.6.** also visualize the limitations of simulations. While the trends of shifts in energy position and intensity of distinct features in HERFD-XAS and vtc-XES can be reproduced by ORCA calculations, the absolute energies often mismatch experimental data and need to be corrected manually. The uncertainty at the absolute energy scale is often in the range between 10-30 eV, which is <1%. Furthermore, the relative shifts in E_0 position are also not always reproduced by the calculations. Additionally, the TDDFT for the HERFD-XAS analysis often fails to reproduce post-edge features, as indicated in **Figure 3.6.a**.

3.2 X-ray Scattering

An X-ray wave propagating through a medium creates an alternating electric field (E), which induces oscillations in the electron density. In response, these accelerated electrons generate an electromagnetic wave that radiates isotropically in directions perpendicular to the axis of electron oscillation, effectively scattering the incident radiation.

For unbound or weakly bound electrons, the oscillatory motion of these electrons occurs at the same frequency as that of the incoming X-rays. This phenomenon is classified as elastic scattering and is referred to as Thomson scattering. As a consequence of elastic scattering, the direction of the incident wavevector is altered, while its magnitude remains unchanged.

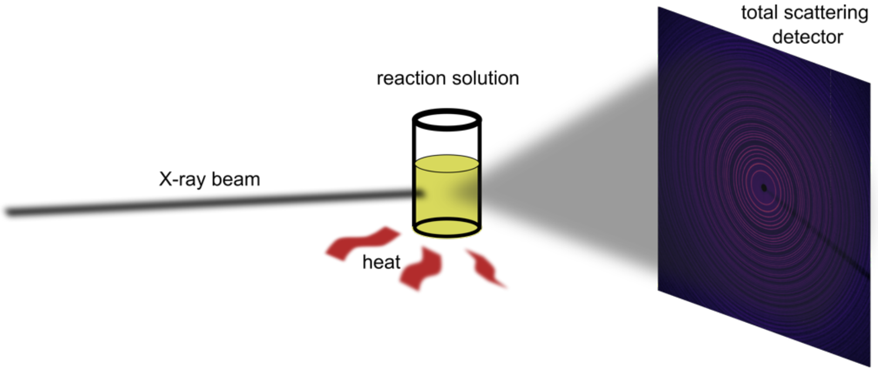

Figure 3.7: Experimental setup of scattering experiments in transmission geometry. Total scattering experiments are conducted in transmission geometry, where the reaction solution can be heated up during the experiment to track changes in the TS data *in situ*.

Figure 3.7. provides a schematic representation of an X-ray scattering measurement conducted in transmission geometry, utilizing an area detector. Because both the X-ray source and the detector are located at a certain distance from the scattering point, the far-field approximation is applicable, allowing the incoming and scattered X-rays to be treated as plane waves. The difference between the incident wavevector $\boldsymbol{k}$ and the scattered wavevector $\boldsymbol{k'}$ defines the wavevector transfer $\boldsymbol{q} = \boldsymbol{k} - \boldsymbol{k'}$, and the magnitude of q is related to the scattering angle as follows:

$$|\boldsymbol{q}| = 2k\, sin(\theta) = \frac{4\pi}{\lambda} sin(\theta) \tag{3.3}$$

In this case, we employ the kinematic approximation and omit the consideration of multiple scattering events. This assumption is justified for scattering experiments performed on materials characterized by short-range order or powders, as such samples generally demonstrate small scattering cross-sections and restricted coherent lengths.

The scattering amplitude $A(\boldsymbol{q})$ produced by an electron cloud is derived from the integration of the electron density $\rho(\boldsymbol{r})$:

$$A(\boldsymbol{q}) = -r_0 \int \rho\,(\boldsymbol{r}) e^{i\boldsymbol{q}*\boldsymbol{r}} dv_r \tag{3.4}$$

In this context, r_0 represents the Thomson scattering length, while v_r denotes the total volume of the scattering medium. The term $e^{i\boldsymbol{q}\cdot\boldsymbol{r}}$ incorporates the phase shift associated with wavevectors scattered at a distance **r** with a wavevector transfer $\boldsymbol{q}$.
In an X-ray scattering experiment, the quantity that is experimentally measurable is the scattering intensity $I\,(\boldsymbol{q})$, which corresponds to the square of the amplitude function:

$$I(\boldsymbol{q}) = \frac{|A(\boldsymbol{q})|^2}{r_0^2} = \int \rho\,(\boldsymbol{r}) \rho(\boldsymbol{r}') e^{i\boldsymbol{q}*(\boldsymbol{r}\prime-\boldsymbol{r})} dv_r dv_{r\prime} \tag{3.5}$$

Here, $I\,(\boldsymbol{q})$ is conventionally expressed in units of r_0. According to equation (3.4), the scattering intensity corresponds to the Fourier transform of the autocorrelation function of the electron density. Furthermore, the total electron density of the scattering medium can be represented as the sum of the electron densities surrounding individual atoms, utilizing the atomic form factor $f^0\,(\boldsymbol{q})$.

$$f^0(\boldsymbol{q}) = \int_{atom} \rho(\boldsymbol{r}) e^{i\boldsymbol{q}*\boldsymbol{r}} dv_r \tag{3.6}$$

In the case of forward scattering, where $\boldsymbol{q} = |\boldsymbol{q}| = 0$, the atomic form factor $f^0\,(\boldsymbol{q})$ corresponds to the atomic number Z, while its value tends toward 0 as $\boldsymbol{q}$ approaches 0. The precise value of the atomic form factor as a function of $\boldsymbol{q}$ is contingent upon the geometry of the atomic orbitals and is cataloged for each chemical element.

Equation (3.5) can be reformulated by substituting the integral with a summation over all pairs of atoms:

$$I(\boldsymbol{q}) = \sum_i \sum_j f_i^0(\boldsymbol{q}) f_j^{0*}(\boldsymbol{q}) e^{i\boldsymbol{q}*(\boldsymbol{r}_i-\boldsymbol{r}_j)} \tag{3.7}$$

In X-ray scattering experiments involving liquids, nanostructured dispersions, or powders, the X-rays interact with a randomly distributed assembly of atomic groups. Consequently, only the modulus of the wavevector transfer $\boldsymbol{q}$ is effectively sampled during the measurement, while the direction of $\boldsymbol{q}$ is isotropic. Equation (3.7) can therefore be reformulated by averaging the phase factor $e^{i\boldsymbol{q}\cdot\boldsymbol{r}}$ over all orientations, resulting in:

$$I(\boldsymbol{q}) = \sum_i \sum_j f_i^0(q) f_j^{0*}(q) \frac{\sin(q\, r_{ij})}{q\, r_{ij}} \tag{3.8}$$

This Equation (3.8.) is also well known as Debye Scattering Equation (DSE).

The experimental scattering pattern is sensitive to the atomic structure (high q) by analyzing the PDF, to the atomic lattice (around 1.5 – 10 Å^{-1}) by focusing on the XRD peaks, and to the shape, morphology and assembly of nanomaterials (>1.5Å) in the SAXS region. The regions are highlighted in the following **Figure 3.8.** and discussed individually in the following sections.

In chapter 4, an two-detector setup was used to simultaneously collect SAXS and WAXS data *in situ*. This setup was already reported in literature.[116]

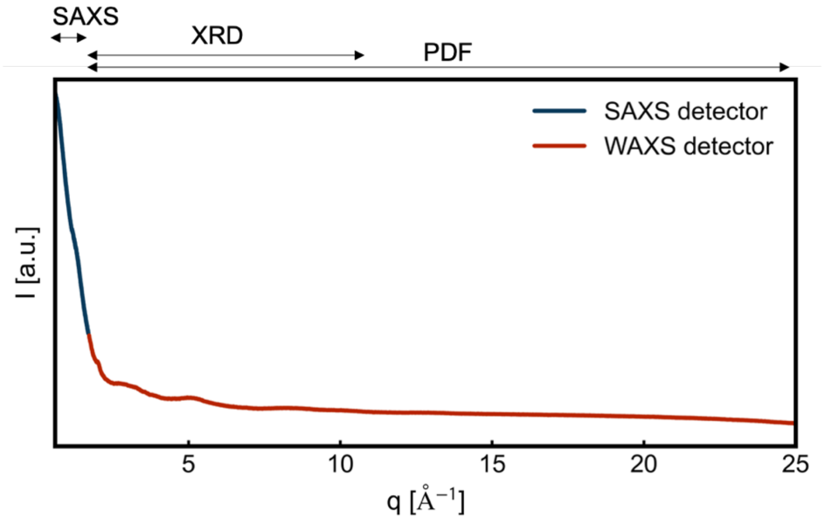

Figure 3.8: Combined SAXS/WAXS acquisition. Total scattering signal can be measured with a SAXS and a WAXS detector simultaneously. The covered range of q can be used for SAXS (>1.5Å), XRD (1 -10Å) and PDF analysis.

3.2.1 PXRD

When X-rays are interacting with a periodic arrangement of atoms, like a crystal, constructive interference of X-rays, scattered by the periodic lattice, result in high intensity peaks in the diffraction pattern. Since those reflexes are based on the diffraction of X-rays in a lattice, the method called X-ray diffraction (XRD). XRD is a common method to determine the atomic structure of crystalline materials by visualizing the lattice spacings in the reciprocal space. For this, we define a crystal lattice as a periodic arrangement of atoms with translational symmetry with a set of lattice vectors ***Rn***.

$$\boldsymbol{Rn} = n_1\boldsymbol{a_1} + n_2\boldsymbol{a_2} + n_3\boldsymbol{a_3} \tag{3.9}$$

Rn denotes each point within the lattice. Here, **a1**, **a2**, and **a3** represent the lattice vectors, while n1, n2, and n3 are integers. The vectors **a1**, **a2**, and **a3** define the dimensions of the unit cell, which serves as the repeating unit of the lattice. Utilizing a set of lattice vectors to characterize a crystal constitutes a powerful approach, as knowledge of the position r_j of each of the j atoms within the unit cell enables the use of vectors of the form $r_j + R_n$ to describe all atomic positions throughout the crystal. Consequently, the scattering amplitude from a crystal can be expressed as:

$$A^{crystal}(\boldsymbol{q}) = -r_0 \sum_{\boldsymbol{r_j}+\boldsymbol{R_n}} f_j(q) e^{i\boldsymbol{q}*(\boldsymbol{r_j}+\boldsymbol{R_n})} = -r_0 \underbrace{\sum_j f_j e^{i\boldsymbol{q}*\boldsymbol{r_j}}}_{A^{unit\,cell}(\boldsymbol{q})} \underbrace{\sum_n e^{i\boldsymbol{q}*\boldsymbol{R_n}}}_{A^{lattice}(\boldsymbol{q})} \tag{3.10}$$

Given that the dimensions of a crystal are significantly larger than those of the unit cell, the summation in the second term of Equation 3.10 encompasses a considerable number of unit cells. Consequently, the summation of terms $e^{i\boldsymbol{q}\cdot\boldsymbol{Rn}}$ will typically average to zero, unless the scattered waves from the various lattice points are in phase. In such instances, they interfere constructively, producing bright intensities in the diffraction pattern. The condition for constructive interference is mathematically represented as:

$$\boldsymbol{q} * \boldsymbol{R_n} = 2\pi * n_{integer} \tag{3.11}$$

To solve the Equation 3.11, one has to introduced the reciprocal lattice **G**, which is similar to the direct lattice (Equation 3.9) defined by reciprocal vectors $\boldsymbol{a}_i^*$:

$$\boldsymbol{G} = h\boldsymbol{a}_1^* + k\boldsymbol{a}_2^* + l\boldsymbol{a}_3^* \quad with\, \boldsymbol{a}_i^* = \frac{2\delta_{ij}}{\boldsymbol{a}_j} \tag{3.12}$$

Where *h,k,l,* are defined as Miller indices and δ_{ij} is the Kronecker delta. We can combine Equation 3.11 with 3.12 and result:

$$\boldsymbol{G} * \boldsymbol{R_n} = 2\pi(hn_1 + kn_2 + ln_3) \tag{3.12}$$

We thus conclude that the scattering amplitude from a crystal will be non-vanishing only for scattering vectors $\boldsymbol{q}$ that align with reciprocal lattice vectors. This phenomenon is referred to as the Laue condition. An alternative expression of the Laue condition is given by the well-established Bragg's law, which articulates the conditions for constructive interference for a family of planes denoted as *(h k l)*, characterized by an interplanar distance of d_{hkl}, as follows:

$$n\lambda = 2d_{hkl}sin(\theta) \tag{3.12}$$

with θ as the angle between the incident X-rays and the lattice planes, λ as the wavelength of radiation and n as an integer number.

The XRD data can be utilized to resolve the composition and atomic arrangement of a crystal, as well as to reveal additional structural characteristics at the atomic level, including the size and anisotropy of crystallites, strain, and atomic vibrations. In the absence of a single crystal, comparable information can be obtained by measuring a large number of randomly oriented crystallites in a powder X-ray diffraction (PXRD) experiment. Quantitative analysis of the PXRD data is typically conducted in reciprocal space using the widely employed Rietveld refinement method, which was also applied in **Chapter 4** and **Chapter 6**.

In case the scattering atoms are non-periodically ordered, it is not possible to extract structural information of a PXRD analysis. In this case, the use of total scattering to obtain an atomic-pair distribution function is a favorable option, as explained in the following chapter.

3.2.2 PDF

To extract structural information from diffuse scattering, one need to amplify the scattering intensity at high ***q*** values. Although the high-q region of the scattering pattern is generally neglected in conventional Bragg diffraction analyses, it becomes crucial for structural analysis in real space via the atomic pair distribution function. For this procedure, the *S(**q**)* and *F(**q**)* needs to be introduced.

The expression for the normalized *S(**q**)* is achieved by dividing the scattering intensity by the number of scatterers and the square of the averaged atomic scattering amplitude:

$$S(\boldsymbol{q}) \;=\; \frac{I(q)}{N\langle f(q)\rangle^2} \;=\; 1 \;+\; \frac{1}{N\langle f(q)\rangle^2}\sum_{i\neq j} f_i^0(q) f_j^{0*}(q)\frac{sin(q\, r_{ij})}{q\;\, r_{ij}} \tag{3.13}$$

If $q \to 0$, the *S(**q**)* approaches unity. Now the reduced total scattering structure function *F(**q**)* can be obtained by reformulating *S(**q**)*, as follows:

$$F(\boldsymbol{q}) \;=\; q(S(\boldsymbol{q})-1) \;=\; \frac{1}{N\langle f(q)\rangle^2}\sum_{i\neq j} f_i^0(q) f_j^{0*}(q)\frac{sin(q\, r_{ij})}{q\;\, r_{ij}} \tag{3.14}$$

As the atomic form factor approaches zero at elevated values of ***q***, the multiplication of *S(**q**)* by ***q*** enhances the influence of high-angle scattering data in the computation of *F(**q**)*. To understand the fundamentals of the PDF, the radial distribution function *R(r)*, which is closely related to the PDF, are introduced.

$$R(r) \;=\; 4\pi r^2 \rho(r) \tag{3.15}$$

Here, $4\pi r^2$ reflects the dimensions of the spherical shell at a distance *r*, while $\rho \;= {}^{N}\!/_{V}$ R(r) is the atomic density. Thus quantifies the number of atoms located at a specified distance *r* from the origin. Alternatively, *R(r)* can be represented as the histogram of scattering amplitudes corresponding to all atom-pair distances within the collection, averaged over the mean scattering amplitude of the constituent atoms:

$$R(r) = \frac{1}{N}\sum_{i}\sum_{j\neq i}\frac{f_i(q)f_i^*(q)}{\langle f(q)\rangle^2}\delta(r-r_{ij}) \tag{3.16}$$

Where δ are Dirac functions.

The relation between the radial distribution function and the PDF can be expressed by the following term:

$$G(r) = \frac{R(r)}{r} - 4\pi r\rho_0\gamma_0(r) \tag{3.17}$$

Experimentally, the *G(r)* is obtained by a fast Fourier transformation (FFT) of the *F(q)*, within the experimental achievable range of $\boldsymbol{q}$:

$$G(r) = \frac{2}{\pi}\int_{qmin}^{qmax} F(q)sin(qr)dq \tag{3.17}$$

The experiment is called X-ray total scattering (TS) since both the diffuse scattering intensity at high-q and the X-ray diffraction peaks are simultaneously recorded. In the PDF analysis, the G(r) can be obtained using a simplified methodology that employs an *ad hoc* correction algorithm. In this study, we favor this method, which is incorporated into the software package PDFGetX3.[117] By executing the Fourier transformation over a restricted range of $\boldsymbol{q}$, certain artifacts arise in the experimental *G(r)*, resulting from the convolution of the ideal *G(r)* with a step function that begins at *qmax*. These artifacts manifest as terminating ripples that oscillate with a period of approximately *2π/qmax*. Furthermore, the truncation of the scattering signal at low angles contributes to the presence of the second term in Equation 3.17, which induces a negative slope in the baseline at low-r. The derivation of this effect is presented in literature.[118]

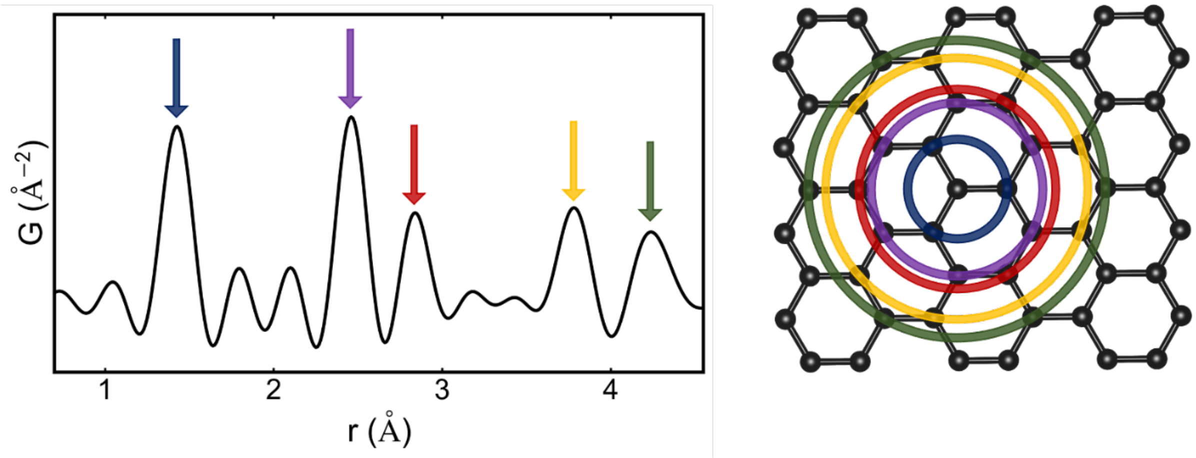

Figure 3.9: Principle of PDF analysis. Simulated PDF pattern of a graphene layer (left) with the corresponding coordination spheres (right). Peaks in the PDF pattern can be interpreted as histogram of interatomic distances in the material of interest.

The Pair Distribution Function (PDF) intuitively represents the scaled probability of locating two atoms at a distance r within a material. This interpretation is schematically depicted in **Figure 3.9.** Given its capacity to examine the local atomic environment, PDF analysis is particularly advantageous for investigating the atomic structure of materials that exhibit short-range order or amorphous characteristics.[119]

3.2.3 SAXS

While the medium and high $\boldsymbol{q}$ range can give rise to the atomic structure in crystalline and amorphous samples, the low $\boldsymbol{q}$ region is sensitive to the size, morphology and assembly of nanomaterials in solution. To understand the scattering behavior of a single particle, we need to introduce the single-particle form factor:

$$F(\boldsymbol{q}) = \frac{1}{V_p} \int_{V_p} e^{iqr} dV_p \tag{3.18}$$

Using the single-particle form Factor, the intensity of individual particles can be modeled.

$$I_{particle}^{SAXS}(\boldsymbol{q}) = \Delta\rho^2 V_p^2 |F(\boldsymbol{q})|^2 \tag{3.19}$$

Where $\Delta\rho^2$ reflects the scattering contrast between the particle and the background and V_p the volume of the particle. For simple shapes like spheres, rods and disks, the $|F(\boldsymbol{q})|^2$ is describable with analytical means, while provide direct access to the particle size, shape, and polydispersity from SAXS intensities by fitting the data with the corresponding form factor. More complex geometries necessitate numerical computations of the form factor. SAXS is frequently employed to investigate the *in situ* formation of nanoparticles,[120] and it is also capable of monitoring the development of mesocrystals and unoriented assemblies.[121]

3.3 Following chemical reactions with X-ray-spectroscopy

In Chapter 2, it has been explained that the increasing complexity in the synthesis of nanomaterials require advanced methods for *in situ* probing of reaction pathways. With the high brilliance of modern synchrotron sources, HERFD-XAS has become a powerful technique for this purpose. The development of specialized beamlines for photon-in/photon-out spectroscopy enables the acquisition of high-quality data from dilute reaction mixtures with high temporal resolution. Moreover, XAS does not depend on the sample's aggregation state and can analyze dissolved precursors, amorphous intermediates, and crystalline nanoparticles within a reaction mixture. Utilizing the absorption spectrum as a distinctive signature for a specific chemical compound is a common technique for tracking chemical reactions and chemical reaction during catalysis. A time-resolved series of spectra allows for the identification of which compounds are present at various stages of synthesis,[122] or during electrochemical cycles.[123]

In electrocatalysis, HERFD-XAS were used in the past decade for identifying active sides, degradation and oxidation of the catalyst during the reaction. As an example, the anodic oxidation of Pt islands on Rhodium and gold substrates during oxygen reduction reactions were influenced by the type of substrate used. The gold substrate induce stronger degradation of the Pt islands compared to the Rhodium.[124] Also the chemisorption of small molecules like hydrogen, oxygen or OH^- during the electrochemical oxidation of Pt nanoparticles were visualized by *in situ* HERFD-XAS studies on the Pt L3 Edge.[125]

Furthermore, the oxidation of Cu during the electroreduction of CO_2 was investigated by HERFD-XAS analysis[126] by highlighting the importance of the geometry and morphology of the Cu electrocatalyst. A Cu monolayer deposited on an Au substrate is more stable against oxide formation and undergoes a direct phase oxidation from Cu to CuO without an intermediate Cu_2O.[127] The surface morphology during the CO2 electroreduction to ethylene and muli carbon alcohols can also induced an electrolyte-driven nano structuring of the Cu catalyst, were *in situ* HERFD-XAS revealed a high selectivity for C^{2+} of these nanostructured surfaces.[128]

HERFD-XAS were also used to identify the chemical state of Co oxide during oxygen evolution reactions by *in situ* analysis of the pre-edge feature, revealing an increase of the oxidation state of Co by applying an potential.[129] Also the active sites in Co-Fe oxides were resolved by element specific HERFD-XAS analysis, revealing that that oxygen atoms directly interacted with 3d orbitals of Co ions rather than that of Fe ions.[130]

Besides its application in electrocatalysis, HERFD-XAS analysis were also used to describe the mechanisms in the synthesis of nanomaterials. In example, HERFD-XAS were used to characterize the oxidation of Ceria nanocubes during thermal treatment.[131]

In recent studies, the strength of HERFD-XAS to track chemical reactions *in situ* were combined with TS methods, which resolve the nucleation and growth process, to gain a comprehensive analysis of different nanoparticle synthesis routes.[132-134]

This combination revealed that $Co(acac)_3$ reduces to square-planar $Co(acac)_2$ when coordinated with two solvent molecules upon dissolving $Co(acac)_3$ in benzyl alcohol, while the TS tracked the crystallization of CoO nanoparticles and their assembly into superstructures.[132]

Combined TS and XAS were also used to reveal that the oxidation of Co^{2+} to $Co^{3+/2+}$ and the reduction of Co^{2+} to Co^0 occur simultaneously, leading to the formation of Co and Co_3O_4 nanoparticles. This is followed by the rapid formation of Co_3O_4 nanoparticles and their subsequent solid-state reduction to CoO. Meanwhile, metallic Co nanoparticles start to grow.[133]

In the synthesis of Cu_3PdN nanoparticles, combined HERFD-XAS and TS analysis reveal that the $Cu(OCH_3)^2$ and $Pd(acac)_2$ precursors dissolve in benzylamine form $[Cu_2(BnNH_2)_4(OCH_3)_2]^{2+}$ and $[Pd(BnNH_2)_4]^+$ complexes, which react to Cu_3PdN nanoparticles at a reaction temperature of 140°C.[134]

4 Utilizing high X-ray energy photon-in photon-out spectroscopies and X-ray scattering to experimentally assess the emergence of electronic- and atomic structure of ZnS nanorods

The content of this chapter was published in the Journal of American Chemical Society (JACS) 146 (49), 33475-33484 (2024) by Lars Klemeyer, Tjark L. R. Gröne, Cecilia Zito, Olga Vasylieva, Melike Gumus Akcaalan, Sani Y. Harouna-Mayer, Francesco Caddeo, Torben Steenbock, Sarah-Alexandra Hussak, Jagadesh Kopula Kesavan, Ann-Christin Dippel, Xiao Sun, Andrea Köppen, Viktoriia A. Saveleva, Surender Kumar, Gabriel Bester, Pieter Glatzel, and Dorota Koziej.

My contribution to this work compromises the synthesis of ZnS nanostructures, the measurement and analysis of HERFD-XAS and vtc-XES data, the DFT calculations, the analysis of PXRD data, the UV-Vis measurements and analysis, and the STEM images.

4.1 Abstract

The key to control the fabrication process of transition metal sulfide nanocrystals is to understand the reaction mechanism, especially the coordination of ligands and solvents during their synthesis. We utilize *in situ* high-energy resolution fluorescence detected X-ray absorption spectroscopy (HERFD-XAS) as well as *in situ* valence-to-core X-ray emission spectroscopy (vtc-XES) combined with density functional theory (DFT) calculations to identify the formation of a tetrahedral $[Zn(OA)_4]^{2+}$ and an octahedral $[Zn(OA)_6]^{2+}$ complex, and the ligand exchange to a tetrahedral $[Zn(SOA)_4]^{2+}$ complex (OA = oleylamine, OAS = oleylthioamide), during the synthesis of ZnS nanorods in oleylamine. We observe *in situ* the transition of the electronic structure of $[Zn(SOA)_4]^{2+}$ with a HOMO/LUMO gap of 5.0 eV towards an electronic band gap of 4.3 eV and 3.8 eV for 1.9 nm large ZnS wurtzite nanospheres and 2 x 7 nm sphalerite nanorods, respectively. Thus, we demonstrate how *in situ* multimodal X-ray spectroscopy and scattering studies can not only resolve structure, size, and shape during the growth and synthesis of NPs in organic solvents and at high temperature but also give direct information about their electronic structure, which is not readily accessible through other techniques.

4.2 Introduction

Zinc sulfide (ZnS) plays an important role in a wide range of applications, such as optoelectronic devices and field emitters,[135] photodetectors,[136] photocatalysis,[137-139] and protective shell material in core-shell nanostructures.[140, 141] Particularly, anisotropic structures like nanorods or nanosheets are of great interest, due to charge carrier confinement in different dimensions.[142] ZnS exhibits two crystal structures, sphalerite or zinc blende (cubic) and wurtzite (hexagonal) phases.[143] The phase transition from sphalerite to wurtzite can be either induced by thermal annealing at temperatures above 1000 °C [144-146] or directly in the solvothermal synthesis of nanocrystals (NC) at temperatures around 150 °C.[147-151]

Among non-aqueous synthesis routes,[15, 25, 151-153] the combination of elemental sulfur and oleylamine is widely explored in the synthesis of transition metal sulfides,[15] particularly of ZnS,[25, 154] but the understanding of their reaction with the metal precursor is still under debate.[153] It has been reported that elemental sulfur and oleylamine form various sulfur species with the formation of H_2S,[15, 155] but so far it is not clear which sulfur species interacts with the metal precursor and actively takes part in the formation of transition metal sulfides. The interaction between zinc acetate ($Zn(Ac)_2$) and elemental sulfur in oleylamine has not been studied to date *in situ*.

Optical methods like visible light fluorescence and absorption, commonly used for studying the semiconducting quantum dots, can hardly be utilized to follow *in situ* changes of the electronic structure of Zn species in solution due to the large ZnS band gap that overlaps with the absorption of the organic ligands in the reaction solution.[156] X-ray absorption spectroscopy (XAS),[80, 157] particularly high-energy resolution fluorescence detected X-ray absorption spectroscopy (HERFD-XAS), is element-specific and offers sensitivity to the local environment around the absorbing atom.[158-160,161] Data acquisition for HERFD-XAS is challenging due to the need to balance data quality, time resolution, and X-ray radiation damage. Additionally, valence-to-core X-ray emission Spectroscopy (vtc-XES) enables to probe the valence orbitals and can provide detailed information e.g. about ligand bonds to a metal center by mapping the occupied molecular orbitals.[19, 92, 162] The vtc-XES signal at the Zn edge is over 100 times weaker than core-to-core XES transitions, necessitating extended data acquisition times.[132, 163, 164]

Combining HERFD-XAS with X-ray scattering provides a comprehensive overview of the reaction pathways across various length scales,[132, 165, 166] by revealing a wide range of structural, chemical, and electronic properties of materials.[64, 167-171] However, there are no combined *in situ* HERFD-XAS/vtc-XES studies on the nucleation and growth of nanoparticles at high temperatures in solution at relevant time scales.

In this work, we conduct *in situ* experiments at a fourth-generation synchrotron, which provides enhanced flux and thus enables faster acquisition of vtc-XES data. We present a methodology to elucidate the chemical pathways leading to the formation of ZnS NC in the oleylamine-sulfur system, together with the emergence of their electronic properties by complementary *in situ* HERFD-XAS, vtc-XES, PXRD, and SAXS. Thereby, we propose the formation of $[Zn(OA)_4]^{2+}$, $[Zn(OA)_6]^{2+}$ and $[Zn(SOA)_4]^{2+}$ complexes (OA = oleylamine, SOA = oleylthioamide) and track their reaction to ZnS NC in wurtzite phase (w-ZnS) and the transition to ZnS nanorods in sphalerite phase (s-ZnS).

4.3 Results and Discussion

The dissolution of $Zn(Ac)_2$ and elemental sulfur in oleylamine leads to the formation of a tetrahedral $[Zn(SOA)_4]^{2+}$ complex, in which Zn^{2+} is coordinated by four thioamide ligands. When heating this complex to 155 °C, ZnS nanoparticles in the wurtzite phase (w-ZnS) form as an intermediate, which partially converts to ZnS nanorods in the sphalerite phase (s-ZnS). The findings of this work are arranged in three sections. First, we present the characterization of mixing precursors at room temperature. Then, we provide *in situ* characterization of the electronic structures during the synthesis of ZnS. Finally, we monitor the *in situ* nucleation, phase transition, and growth of ZnS.

4.3.1 Chemical transformation of $Zn(Ac)_2$ and elemental sulfur in oleylamine

We first investigate the coordination of Zn^{2+} ions at room temperature after the dissolution of $Zn(Ac)_2$ in oleylamine, before and after the addition of elemental sulfur. To unveil the nature of the Zn complexes formed, we compare the HERFD-XAS and vtc-XES measurements with the theoretical spectra simulated by density functional theory (DFT) using the ORCA code, as shown in **Figure 4.1**. The spectrum of $Zn(Ac)_2$ dissolved in oleylamine (light blue) exhibits a 0.8 eV shift in the XAS E_0 position (9.665 keV) to lower energies and a 0.6 eV shift of the $K\beta_{2,5}$ peak (9.657 keV) to higher energies, compared to the $Zn(Ac)_2$ reference (black), while the intensity of the white line increased. The white line corresponds to the position of maximal intensity in the XAS, while the E_0 reflects the maximum in the first derivative. The energy shifts might suggest the replacement of the Zn-O coordination by Zn-N coordination while the increased white line intensity indicates a change in the coordination of the Zn atom, from tetrahedral to partly octahedral. By comparing the experimental and simulated spectra, we propose that the dissolution of $Zn(Ac)_2$ in oleylamine leads to the displacement of the acetate ligands by four and six oleylamine molecules, resulting in a mixture of a tetrahedral $[Zn(OA)_4]^{2+}$(60%) and an octahedral $[Zn(OA)_6]^{2+}$ (40%) complex, visualized in **Figure 4.1b.** The DFT calculations show that the mixture of tetrahedral and octahedral N-coordinated complexes matches best to the experimental data as shown in **Figure 4.1b**, **Figure 8.1.1a,** and **Figure 8.1.2.**

The addition of elemental sulfur (dark blue) leads to a 0.6 eV shift of the E_0 to lower energies, while the $K\beta_{2,5}$ peak shifts 0.6 eV to higher energies, compared to the mixture without sulfur, as shown in **Figure 4.1c.** Furthermore, the addition of sulfur also results in a decrease in white line intensity. The energy shifts result from a ligand exchange around Zn, where the Zn-N coordination is replaced by Zn-S. The decrease in white line intensity indicates that the coordination number of Zn decreased from a mixture of four and six to only four. The theoretical XAS and XES spectra obtained from DFT (blue dashed line) simulations reveal that four and six oleylamine chains of the initial $[Zn(OA)_4]^{2+}$ and $[Zn(OA)_6]^{2+}$ complexes are replaced by four of their corresponding thioamide derivatives, resulting in the $[Zn(SOA)_4]^{2+}$ complex shown in **Figure 4.1a.** The formation of other Zn-S coordination, like $[Zn(H_2S)_4]^{2+}$ is ruled out in **Figure 8.1.1b**. The calculations of $[Zn(OA)_4]^{2+}$, $[Zn(OA)_6]^{2+}$, and $[Zn(SOA)_4]^{2+}$ were compared with a simulation of a molecular unit of $Zn(Ac)_2$ in the **Figure 8.1.3**.[172] A detailed analysis of the mixing fractions between $[Zn(OA)_4]^{2+}$ and $[Zn(OA)_6]^{2+}$ is shown in **Figure 8.1.4**. The transitions in vtc-XES as well as the donor orbital for each ORCA calculation are shown in **Figure 8.1.5**.

The change from a partly octahedral to a tetrahedral coordination geometry might be related to the steric hindrance of sulfur atoms, which occupy more space compared to nitrogen. Additional information on the formation of the tetrahedral $[Zn(SOA)_4]^{2+}$ complex is reported in **Figure 8.1.6**. To match the absolute energy scale of the theoretical and experimental spectra, the calculated energy positions were corrected, as described in Chapter 4.7

Thus, our experiments demonstrate that oleylamine and sulfur react already at room temperature in the presence of Zn^{2+} ions, forming the thioamide derivative of oleylamine, which so far has been evidenced by NMR and SAXS only at elevated reaction temperatures.[15, 155] ^{13}C NMR spectroscopy shows evidence of the thioamide functional group only in mixtures of oleylamine and sulfur heated at temperatures above 170 °C (see **Figure 8.1.7-8** and Chapter 8.1.).

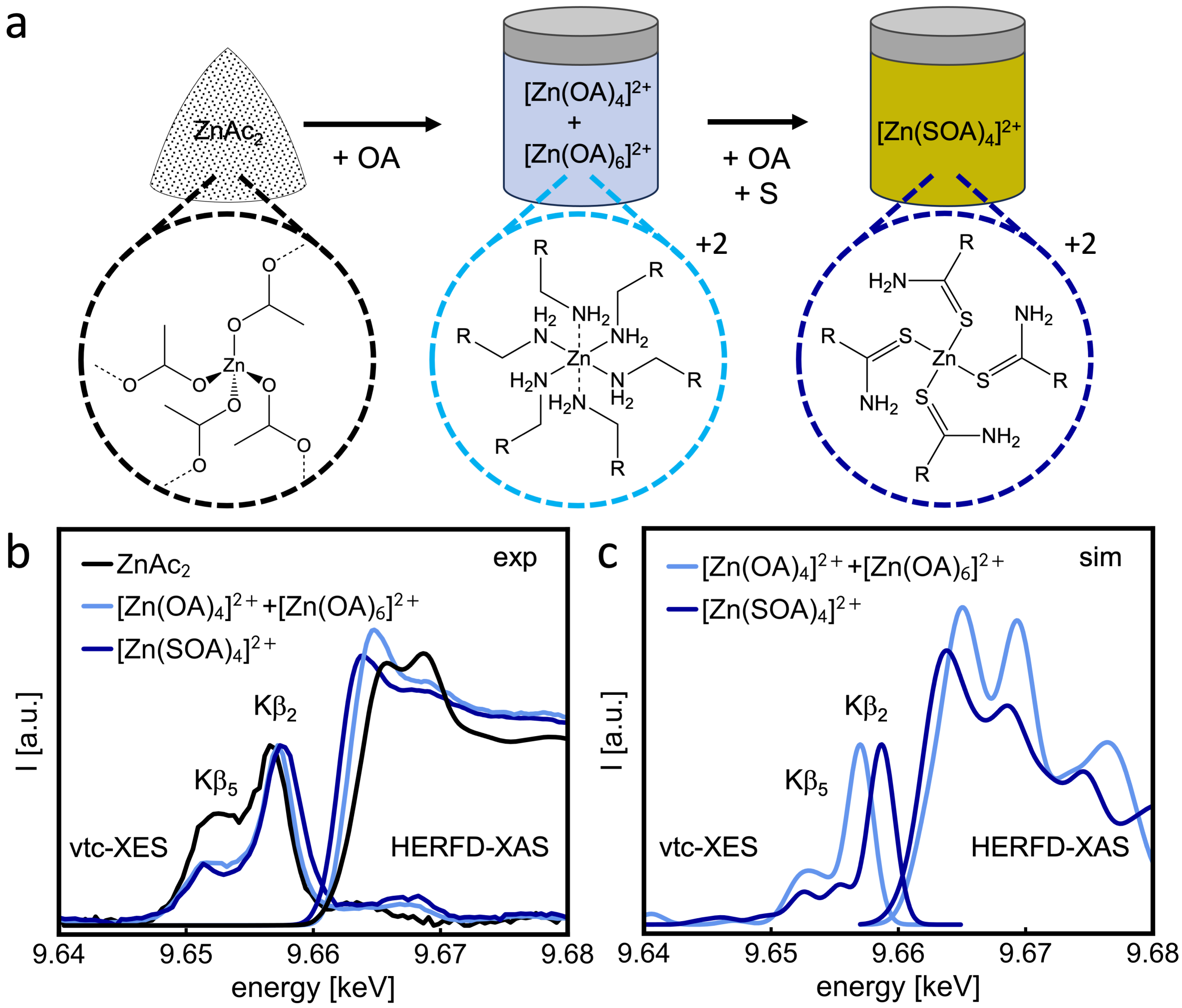

Figure 4.1: Identifying Zn coordination by vtc-XES and HERFD-XAS analysis. (a) Schematics of the reaction pathway from Zn(Ac)$_2$ precursor (black dashed circle) to a tetrahedral $[Zn(SOA)_4]^{2+}$ complex, (dark blue), which undergoes an intermediate step: a mixture of tetrahedral $[Zn(OA)_4]^{2+}$ (60%) and octahedral $[Zn(OA)_6]^{2+}$ (40%) complexes (light blue). The four and six oleylamine chains in the mixed complexes are replaced by four of their corresponding thioamide derivatives upon adding sulfur to the mixture. **(b)** Comparison of experimental HERFD-XAS and vtc-XES spectra of Zn(Ac)$_2$ (black line), Zn(Ac)$_2$ dissolved in oleylamine (light blue solid line) forming a mixture of $[Zn(OA)_4]^{2+}$ and $[Zn(OA)_6]^{2+}$, and Zn(Ac)$_2$ dissolved in oleylamine with sulfur (dark blue solid line), resulting in the $[Zn(SOA)_4]^{2+}$ complex. **(c)** Theoretical XAS and vtc-XES spectra obtained using DFT calculations of the proposed tetrahedral $[Zn(OA)_4]^{2+}$ mixed with octahedral $[Zn(OA)_6]^{2+}$ complexes at the ratio 60:40, and $[Zn(SOA)_4]^{2+}$ complex. Peaks in vtc-XES spectra above the Fermi level are described by multi-electron excitations in the literature.[173, 174] (R = $(CH_2)_7(HC{=}CH)(CH_2)_7(CH_3)$).

4.3.2 *In situ* HERFD-XAS and vtc-XES resolving the electronic structures during the synthesis

In **Figure 4.2a**, we present the *in situ* vtc-XES and HERFD-XAS datasets, which track the reaction of $[Zn(SOA)_4]^{2+}$ to s-ZnS NC. The HERFD-XAS data reveals a splitting of the white line during the formation of s-ZnS, as highlighted in the inset with peaks A and B. While the evolving shoulder (A) shifts to lower energy, which is typical for ZnS, the absorption maximum (B) shifts to higher energies.[160, 175] Notably, the intensity of the white line remains almost constant during the reaction which indicates a constant tetrahedral coordination of the Zn atoms through the reaction. The broadening of peaks B and C results in a non-global minima between the peaks which is untypical for s-ZnS and might suggest the co-formation of w-ZnS. To analyze the fraction of w-ZnS in the final product, multivariate curve resolution-alternating least squares (MCR-ALS) analysis, a multi-component analysis, was performed.[176, 177] Further information about the MCR-ALS method is available in Chapter 8.1., **Figure 8.1.9-10, Table 8.1.1-2**.

The MCR-ALS analysis allows us to track the time and temperature-dependent concentration profile of all components in the reaction, as shown in **Figure 4.2b**. In total, three different components are present during the reaction. In addition to the $[Zn(SOA)_4]^{2+}$ starting complex and the s-ZnS, w-ZnS ist identified as a by-product of the reaction. The recovered spectra of these components are shown in **Figure 4.2b top**, while their concentration profile is shown in **Figure 4.2b bottom**. At 40 °C (15 min), the $[Zn(SOA)_4]^{2+}$ complex begins to convert to w-ZnS. Upon reaching 110 °C (85 min), the transformation of the $[Zn(SOA)_4]^{2+}$ complex into w-ZnS is completed, marking the onset of the formation of s-ZnS. As the reaction temperature reaches 155 °C (130 min), the formation of s-ZnS persists, resulting in a final product composition of 60% w-ZnS and 40% s-ZnS.

Beyond the component analysis with MCR-ALS analysis, we combined *in situ* HERFD-XAS with *in situ* vtc-XES data to monitor the HOMO/LUMO gap during the reaction. For this, we calculated the energy difference between the resonant excitation in HERFD-XAS (1s => 4p - LUMO) and the highest energetic recombination in vtc-XES (3p => 1s - HOMO). The total energy scheme for photon-in (Ω) and photon-out (ω) spectroscopy with ground, intermediate, and final states at the Zn edge is shown in **Figure 4.2c**. The HOMO/LUMO gap was calculated by the difference between the global minima of the first derivative of the vtc-XES and the global maxima of the first derivative of the HERFD-XAS, as described in **Figure 4.2d.** More detailed information regarding the *in situ* HOMO/LUMO gap determination is available in SI.

We observe a decrease in the HOMO/LUMO gap (ΔE) as the reaction progresses and the transformation of the $[Zn(SOA)_4]^{2+}$ complex to the w-ZnS and s-ZnS takes place (**Figure 4.2e**). To calibrate the energy scale, we set the E at the end of the reaction to the band gap of s-ZnS (3.8 eV). We determine the HOMO/LUMO gap of the $[Zn(SOA)_4]^{2+}$ complex to be 5.0 eV. At 155 °C reaction temperature and a ramping rate of 1 °C/min, the HOMO/LUMO gap changes stepwise. First ΔE quickly drops by 0.7 eV from 5.0 eV to 4.3 eV, which reflects the band gap of w-ZnS during our synthesis. Therefore, we assume that the band structure has already evolved after 40 minutes. The band gap is comparably high for w-ZnS, which suggests a very small crystallite size due to quantum confinement effects.[178] To estimate the size of the w-ZnS we have performed atomic effective pseudopotential calculations and obtained, for an electronic gap of 4.3 eV, a diameter of around 2.1nm, as described in **Figure 8.1.11**.[179-186] After 100 minutes, the value reached 3.8 eV, which coincidences with the onset of s-ZnS formation shown in **Figure 2b**.

Moreover, the band gap ΔE estimation is consistent with the values determined by using *ex situ* UV-vis of unwashed aliquots (**Figure 4.2e, Figure 8.1.12, Table 8.1.3**). UV-Vis analysis struggles to discriminate between organic background and emerging w-ZnS, which explains the discrepancy, especially at the early reaction state.

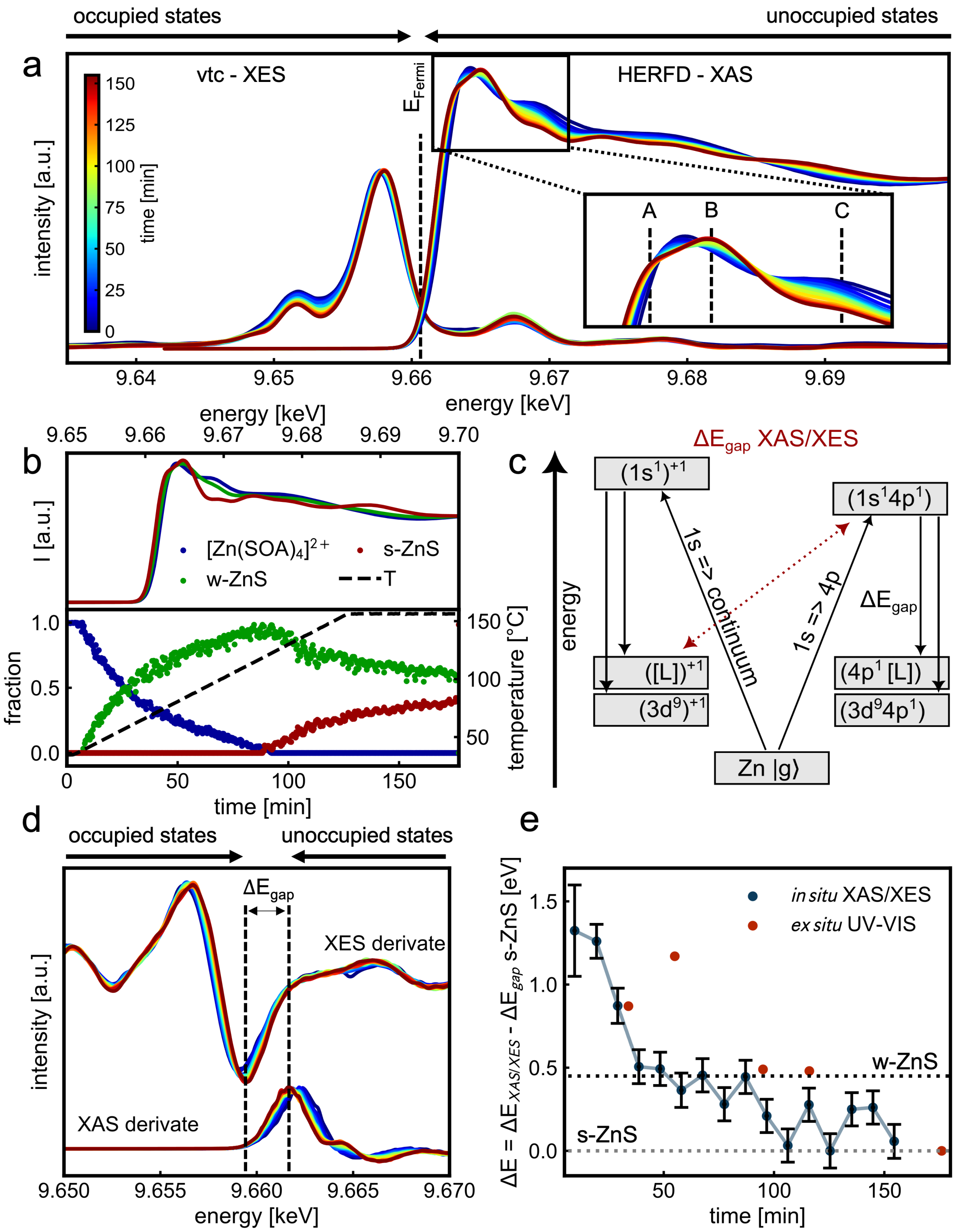

Figure 4.2: *In situ* X-ray spectroscopy of the synthesis of s-ZnS. (a) *In situ* Zn K-edge vtc-XES and HERFD-XAS spectra of the synthesis of s-ZnS where changes in the XAS are highlighted in the inlet. **(b)** MCR-ALS analysis of *in situ* HERFD-XAS data reveals individual contributions of three independent compounds, the [Zn(SOA)$_4$]$^{2+}$ complex, w-ZnS, and s-ZnS. **(c)** Schematic interstate transitions during non-resonant (left) and resonant (right) excitation result in a difference in the calculated band gap. **(d)** The difference between the minimum of the derivation of the XES signal and the maximum of the derivation of the XAS signal reflects

the HOMO/LUMO gap during the preparation of s-ZnS. **(e)** The HOMO/LUMO gap values determined by *in situ* XAS/XES during the reaction in solution are compared with the HOMO/LUMO optical gap values determined with *ex situ* UV-VIS analysis of unwashed aliquots (red).

4.3.3 Simultaneous *in situ* SAXS and PXRD resolving the atomic structures during the synthesis

To characterize the structural evolution of w-ZnS and s-ZnS, *in situ* small-angle X-ray scattering (SAXS) and powder X-ray diffraction (PXRD) was performed and compared with *ex situ* high-resolution transmission electron microscopy (HRTEM) images. The *in situ* SAXS data (**Figure 4.3a**) show an increased intensity at low q starting at approximately 70 minutes, indicating particle formation during the reaction. The particle size was calculated by applying a spherical fitting model to the experimental data, with the results shown in **Figure 4.3d**. The energy of >100 keV and the resulting high q-min of around 0.1 $Å^{-1}$ restricted the resolution to structures larger than 8 nm. However, the high background (lamellar, solvent) prevented us from deconvoluting the data into distinct spherical fits for w-ZnS and rod-like fits for s-ZnS. Further details about the SAXS fitting and background subtraction are available in **Figure 8.1.13-16**. Furthermore, the formation and dissolution of oleylamine lamellar structures were observed in the presence of zinc ions in solution, as depicted in **Figure 8.1.14**, aligning with findings from related studies on synthesis under similar reaction conditions.[155]

In situ PXRD data corroborate the previously described transformation of w-ZnS to s-ZnS during the reaction. This trend is evident by comparing the intensity ratios between the reflections of w(113) and s(220)/w(210), as depicted in **Figure 4.3a**. At around 110 minutes, the intensities of both reflections are equal. Thereafter, the intensity ratio shifts towards s(220)/w(210) until the reaction concludes. Additionally, PXRD data reveal a strong preferred growth direction along the s(111) axis. The formation of spherical w-ZnS as an intermediate in the formation of s-ZnS nanorods is already observed in comparable systems,[149] where the preferred growth direction is explained by an oriented attachment of w-ZnS.[148]

This preferred growth direction in s-ZnS is also evidenced by HRTEM analysis of aliquots taken throughout the reaction, as shown in **Figure 4.3b**. At 75 minutes, the formation of w-ZnS results in spherical NC with an estimated size of 1.9 ± 0.2 nm, which is in agreement with 2.1 nm obtained by HERFD-XAS/vtc-XES. Detailed size analysis and full images are provided in **Figure 8.1.17-19**.

While MCR-ALS analysis proposes that the formation of w-ZnS starts at 40 °C, SAXS and PXRD and HRTEM analysis confirm only the formation above 90 °C. This mismatch can be explained by the varying sensitivity of all methods. X-ray spectroscopy can detect already non-crystalline species and even molecular complexes, while SAXS and PXRD are highly sensitive to the crystal structure, size, and shape of ZnS NC.

The preferred growth direction, as well as the fractions of w-ZnS and s-ZnS, can be extracted from the PXRD data through sequential Rietveld refinement, as illustrated for the final PXRD pattern in **Figure 4.3c.** The Rietveld analysis fits a spherical model to the w-ZnS with a domain size of approximately 2 nm, while the s-ZnS demonstrates a preferred growth direction along s(111) and a domain 2 nm x 7 nm. Additional information on the sequential Rietveld refinement is given in SI. The fraction and domain sizes of s-ZnS and w-ZnS change throughout the reaction, as shown in **Figure 4.3d** and **Figure 8.1.20**. To compare the domain sizes calculated from the PXRD data with those obtained from the SAXS fit, the PXRD sizes were averaged, considering the varying phase fractions at different time points. The PXRD sizes are systematically underestimated compared to the SAXS sizes, as they reflect the domain size, whereas SAXS fitting represents the solvation size of nanoparticles in the solution. The ratio between s-ZnS and w-ZnS can be changed by increasing the reaction temperature to 170°C and the ramping rate to 10°C/min, as discussed in **Figure 8.1.21**.

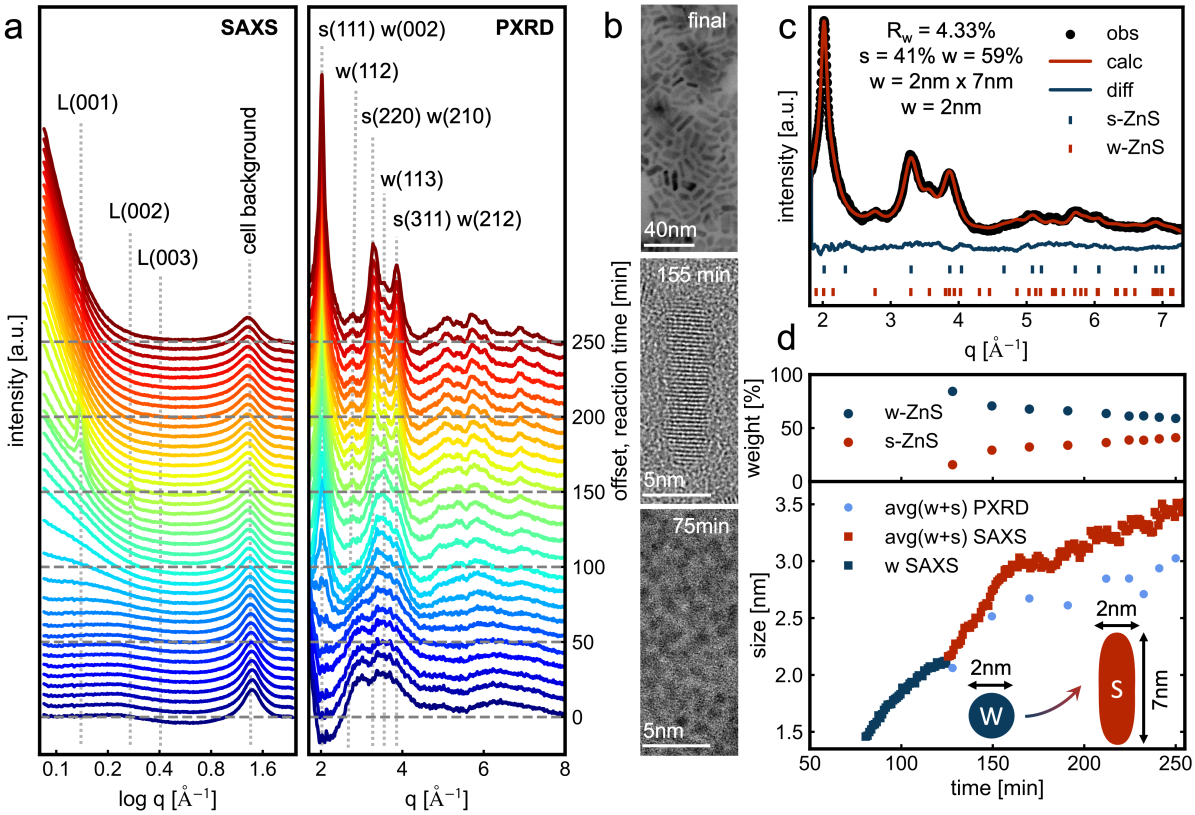

Figure 4.3: Simultaneous *in situ* SAXS and PXRD, as well as *ex situ* HRTEM analysis. (a left) *In situ* SAXS analysis shows an increasing intensity at low q, starting after approximately 70 minutes of reaction, indicating the formation of spherical nanoparticles. The oleylamine lamellae (L) and cell background (≈ 1.5 Å^{-1}) were indicated at the top. **(a right)** *In situ* PXRD analysis shows the formation of w-ZnS reflections after 70 minutes, with changes in the relative intensity of the w(210)/s(220) and w(113) peaks over time, revealing the formation of the s-ZnS phase during the reaction. The s(111) peak have comparable high intensity, thus implying a preferred growth direction in the s-ZnS along the s(111) facet. **(b)** HRTEM analysis of washed aliquots of the reaction reveals the formation of ZnS nanorods after 120 minutes, which explains the preferred growth direction along s(111), while at 75 minutes only spherical particles with 1.9 ± 0.2 nm are observed. **(c)** Rietveld analysis of the final product shows the presence of 41% s-ZnS and 59% w-ZnS. Moreover, the Rietveld analysis refines a spherical domain size of 2 nm in the w-ZnS and anisotropic domain sizes of 2 nm x 7 nm in the s-ZnS. The fraction of s-ZnS to w-ZnS evolves throughout the reaction, as shown in the top panel of **(d)**. The size calculated by fitting the SAXS data with a spherical model is compared with the average size obtained from the Rietveld analysis in the bottom panel of **(d)**. The smallest size we could resolve with Rietveld refinement of PXRD measurements of w-ZnS nanoparticles was 1.7 nm, while the smallest size we could fit within SAXS analysis was around 1.5 nm.

4.4 Conclusion

This work extends the application of Zn K-edge XAS and vtc-XES in inorganic and bioinorganic chemistry to investigate the emergence and growth of nanomaterials in solution at high temperatures. The integration of HERFD-XAS, $K\beta_{2,5}$ XES, and DFT theory allows for the identification of successive Zn-O, Zn-N, and Zn-S ligand exchanges.

Our findings reveal that even at room temperature, $Zn(Ac)_2$ undergoes a reaction with oleylamine to form a mixture of tetrahedral $[Zn(OA)_4]^{2+}$ and octahedral $[Zn(OA)_6]^{2+}$ complexes, which, upon sulfur addition, transforms into a tetrahedral $[Zn(SOA)_4]^{2+}$ complex. This rules out the formation of e.g. hydrogen sulfide Zn complexes, such as $[Zn(H_2S)_4]^{2+}$. By tracking the *in situ* heating of the $[Zn(SOA)_4]^{2+}$ complex above 155 °C, we observe the successive nucleation and growth of sphalerite and wurtzite ZnS nanostructures. Interestingly, we also monitor the evolution of the HOMO/LUMO gap from 5.0 to 4.3 and eventually to 3.8 eV, consistent with the $[Zn(SOA)_4]^{2+}$ complex and the 2.1 nm wurtzite and sphalerite structures, respectively.

The structural transformation of ZnS was further analyzed through simultaneous *in situ* SAXS and PXRD measurements. Our observations capture the formation of wurtzite spherical ZnS particles, progressing to the transformation into sphalerite ZnS rods oriented predominantly along the (111) axis. The shape, size, and band gap energy of the nanoparticles were validated through *ex-situ* HRTEM and UV-vis spectroscopy of powder samples.

In conclusion, this study provides a detailed insight into the coordination chemistry and structural changes during the synthesis of ZnS nanocrystals. The methodology showcases its potential to monitor the structural and electronic transitions during particle growth at elevated temperatures, particularly in scenarios where optical spectroscopy is not feasible. This approach holds promise for the study of other materials with high energy band gaps or in reaction environments where optical spectroscopy is limited, and elemental specificity is crucial for analysis in the future.

4.5 Acknowledgment

This research was supported by the European Research Council (LINCHPIN project, grant no. 818941), the Deutsche Forschungsgemeinschaft (DFG) through the Cluster of Excellence “Advanced Imaging of Matter” (EXC 2056, project ID 390715994) and the

Graduate School “Nanohybrid” (funding ID 408076438), and the Bundesministerium für Bildung und Forschung (BMBF) via the project 05K22GU7 (LUCENT II). Furthermore, we acknowledge DESY (Hamburg, Germany), a member of the Helmholtz Association, for the provision of experimental facilities. Parts of this research were carried out at PETRA III using beamlines P07 and P21.1 and P62 and at ESRF using beamline ID26 under proposals MA5353, MA5366 and HC-4929. [187-189]

4.6 Experimental Section

Chemicals:

Zinc (II) acetate ($Zn(Ac)_2$) (99.99%, anhydrous), sulfur (99.998% trace metal basis), and oleylamine (≥98% primary amine) were purchased from Sigma-Aldrich. All chemicals were used as received without further purification and stored, except for the sulfur, under an argon atmosphere.

Synthesis of ZnS:

The ZnS synthesis was performed in the *in situ* cell adopted from previous work[132, 133, 190], as described in **Figure 8.1.22**. Two individual solutions were prepared in oleylamine. First, 0.0489 g of $Zn(Ac)_2$ powder was dissolved in 1 mL of oleylamine. Then, 0.0128 g of sulfur was dissolved in 2 mL of oleylamine. Both solutions were stirred for one hour at room temperature under an argon atmosphere. The solutions were added into the microreactor in a volume ratio of 2:1 elemental sulfur:$Zn(Ac)_2$ solutions in a total volume of 66 µL and 174 µL for the scattering and spectroscopic experiments, respectively. The reactor was sealed under argon (99.9999%) and heated at a heating rate of 1 °C/min to 155 °C or at a heating rate of 10 °C/min to 170 °C. The *ex situ* samples for UV-Vis analysis were prepared under the same conditions in the *in situ* spectroscopy cell.

UV-Vis: UV-visible spectra were collected using the Cary 60 UV-VIS spectrometer (Agilent Technologies Inc., US) and a quartz cuvette. The samples were diluted with cyclohexane in the cuvette. The HOMO/LUMO gap and the band gap were calculated using the Tauc-Plot.[16]

NMR: Nuclear magnetic resonance (NMR) spectra were recorded on a Bruker Avance NEO 600 MHz NMR spectrometer using TopSpin 4.1.3 (BRUKER BIOSPIN GmbH, Rheinstetten, Germany) equipped with a 5 mm TCI Cryoprobe cooled with liquid nitrogen, operating at 600.25 MHz and 298.0 K. All chemical shifts were referenced to residual solvent peaks [$CDCl_3$: 7.26 ppm (^1H), 77.2 ppm (^{13}C); C_6D_6: 7.3 ppm (^1H), 128.0 ppm (^{13}C)]. One-dimensional (1D) ^1H and two-dimensional (2D) (^1H,^{13}C)-HSQC and 2D (^1H,^{13}C)-HMBC spectra were acquired using standard pulse sequences from the Bruker library. For the 1D ^{13}C(^1H)-NMR spectra (zgpg30) of the reaction mixture at room temperature, 1024 and 10240 scans (NS) were recorded.

Sample preparation for NMR analysis:

Sulfur in oleylamine: Under ambient conditions, sulfur powder (9.1 mmol) was introduced in a glass vial with further addition of oleylamine (45.5 mmol). The solution was stirred at room temperature until all sulfur was dissolved. The reaction mixture was heated to 170 °C by using an oil bath with stirring, and aliquots were taken at 60, 100, and 140 °C. When the solution reached 170 °C, the temperature was kept for 20 min, and the corresponding aliquot was taken. The mixture was further heated to 190 °C and was kept at 200 °C for 40 minutes before collection of the 200 °C aliquot.

$Zn(Ac)_2$ and S in oleylamine: Under ambient conditions, $Zn(Ac)_2$ (6.65 mmol) was introduced in a glass vial with further addition of oleylamine (45.5 mmol). The solution was stirred at room temperature for 30 min and sulfur (9.1 mmol) was added to the mixture as one portion followed by a further 50 min of stirring.

STEM and HRTEM analysis: STEM images were taken and probe-corrected with a Regulus 8220 (Hitachi High Technologies Corp., Japan) at an acceleration voltage of 30 kV and using the BFSTEM acquisition mode. HRTEM images were taken with a JEOL JEM-2200FS (JEOL Ltd., Japan) using an acceleration voltage of 200 kV.

Beamline setup and data acquisition:

The *in situ* HERFD-XAS and vtc-XES spectra were recorded at the ID26 beamline at the European Synchrotron Radiation Facility (ESRF), Grenoble, France. The HERFD-XAS were collected by measuring the intensity of the Zn K_a main line using a Si(642) crystal in Rowland Geometry while scanning the incident energy. The position of the X-ray beam was moved on the reaction cell to minimize radiation damage. XAS spectra were acquired every 16 s with an energy range from 9.64 to 9.8 keV and a stepsize of 0.2 eV. The vtc-XES spectra were recorded using four Ge(555) crystals in Rowland geometry over a total energy range from 9.63 to 9.71 keV. To decrease the acquisition time, the spectra region from 9.63 to 9.69 keV was measured with energy steps of 0.4 eV and an acquisition time of 532s (with motor movements), while the range from 9.69 to 9.71 keV was recorded in steps of 2 eV with a total acquisition time of 44 s. To exclude the occurrence of beam damage during the measurements, a beam damage study prior the experiments were performed, as described in **Figure 8.1.23**.

The X-ray total scattering and SAXS *in situ* data were collected in a SAXS/WAXS combined setup at the second experimental hutch (EH2) at beamline P07 of PETRA III at Deutsches Elektronen-Synchrotron (DESY), Hamburg, Germany.[116] The total scattering and SAXS data were collected every 0.5 s using two flat panel detectors (Varex XRD4343CT, Varex Imaging Corp., USA) with 2880 x 2880 pixels of 150 x 150 μm^2 size. During the experiments to synthesize W and S ZnS at 155 °C, the sample-to-detector distances (SDD) were 0.812 m for total scattering and 4.636 m for the SAXS data, determined from the calibration with LaB_6 calibrant, at an X-ray beam energy of 103.56 keV. For the synthesis at 170 °C with 10 °C/min heating rate, the SDD was determined as 0.765 m for total scattering data collection, obtained from calibration with LaB_6, and 4.613 m for the SAXS, from CeO_2 calibrant, at an X-ray beam energy of 103.60 keV.

The *ex situ* total scattering data were taken at Beamline P21.1 at PETRA III, DESY.[S2] The total scattering data were recorded with a Varex flat panel detector model XRD4343CT at an SDD of 0.377 m. Samples were enclosed in a quartz capillary, and the calibration was carried out by measuring the LaB_6 calibrant at an X-ray beam energy of 101.60 keV.

The *ex situ* SAXS data shown in **Figure 8.1.15** are collected at Beamline P62 at PETRA III, DESY.[191] The energy was set to 12 keV using a Si(111) monochromator. The beam size was 0.5x0.5 mm^2. The samples were mounted vertically in a multi-capillary holder. The sample-to-detector distances were calibrated to be 2.849 m using AgBH. The SAXS signals were collected by Eiger2 9M detector.

Data processing:

The HERFD-XAS and the vtc-XES data were processed using a self-written Python code. The vtc-XES data were normalized by the maximum intensity, since an area normalization led to unphysical intensity fluctuations in the *in situ* data set, as described in **Figure 8.1.24**. FEFF calculations of vtc-XES of w-ZnS and s-ZnS are shown **Figure 8.1.25**.[192, 193] The determination of the XAS edge position and normalization of the edge jump were performed by using the LARCH-XAFS module.[194] The spectroscopic data were treated with a Savitzky-Golay filter and further processed with the NumPy and SciPy package.[195, 196] The processed data are compared with raw data in **Figure 8.1.26**. The simulations of the XAS spectra were carried out using the ORCA 5.0.4 code[197], where the initial zinc complexes for DFT optimization were built using Avogadro: an open-source molecular builder and visualization tool. Version 1.2.0. [198] The Orca input files were adapted from *Stepanic et.al.*[80]

Azimuthal integration of the 2D detector patterns for PXRD and SAXS data was performed with the Python module pyFAI after masking out beam stop shadows, glitches, pixel defects, and noisy pixels.[199] For the background subtraction, *in situ* total scattering data of sulfur dissolved in oleylamine and pure oleylamine were collected under the same reaction conditions of the ZnS syntheses at 155 and 170°C, respectively. The background was subtracted from the original data set. The data were averaged over 60 frames, corresponding to 30 s time resolution. The Rietveld refinement was performed with GSAS-II package[200], employing a two-phase refinement with ZnS sphalerite and wurtzite phases sharing one particle size parameter. The sphalerite phase (ICSD-230703) and wurtzite phase (ICSD-67453) were taken from the ICSD database. The refinement was carried out in a sequential way starting from the XRD at the end of the reaction and going backward to earlier reaction times, ensuring a better reliability of the fit.

The fitting of the SAXS data was carried out over the range of 0.08 to 1.8 Å^{-1}. An empty capillary background was measured at room temperature and subtracted from the original *in situ* SAXS data set. The SAXS data were averaged over 120 frames (1 min resolution) and 10 frames (5 s resolution) for the ZnS reactions at 155 °C and 170 °C, respectively. The fit was carried out in SASview 5.0.6 [201] with the DREAM algorithm.[202] As a fitting function, a plugin was used, which contained a power law, a sphere, a symmetric pseudo-Voigt profile and a fitting function for the lamellae. The lamellae were fitted with a triplet of asymmetric pseudo-Voigt profiles sharing the ratio of Gauss to Lorentz factor eta and the FWHM. The peak height ratio was kept constant, while q was allowed a relaxation of ± 5% of the multiple of the first peak. For the reaction temperature of 170 °C, an additional sphere model was used with a constant radius of 5.11 Å, and to match the background, the first peak of the lamellae was constrained to be a Lorentz profile only, while the second and third peak shared the ratio of Gauss to Lorentz factor eta.

To improve the grammar and wording in parts of the manuscript and supporting information, ChatGPT 4 omni was used for proofreading, following the guidelines for using AI in scientific publications.[203]

5 Spatially Resolved *In Situ* HERFD-XANES studies of ZnS Nanoparticle Synthesis at the Water-Toluene Interface

The content of this chapter was published at Chemrxic.org (*doi.org/10.26434/chemrxiv-2025-800wx*)[204], in 2025 *by Lars Klemeyer†, Francesco Caddeo†, Tjark L. R. Gröne, Sani Y. Harouna-Mayer, Brian Jessen, Cecilia A. Zito, Jagadesh Kopula Kesavan, Ann-Christin Dippel, Fernando Igoa Saldaña, Olivier Mathon, Pieter Glatzel, and Dorota Koziej*

† These authors contributed equally

My contribution to this work compromises the synthesis of ZnS nanostructures, the measurement and analysis of HERFD-XAS data, the DFT calculations, the analysis of PDF and PXRD data.

5.1 Abstract

A two-phase synthesis has been well established for achieving precise control of nanoparticle properties. However, studying and understanding chemical transformation in such a spatially heterogeneous system is challenging. In this work, we introduce a two-phase synthesis route for ZnS nanoparticles (ZnS NPs) at the water-toluene interface. By employing spatially resolved *in situ* high-energy resolution fluorescence-detected X-ray absorption spectroscopy (HERFD-XAS) combined with density functional theory (DFT) calculations, we track the diffusion of Zn^{2+} species at the interface, identify key reaction intermediates, and monitor the nucleation and growth of ZnS NPs within the toluene phase. We propose the formation of a $[Zn(H_2O)_6]^{2+}$ complex upon dissolving $Zn(Ac)_2$ in water and the diffusion of Zn^{2+} ions from water to toluene driven by the formation of an octahedral $[Zn(OA)_6]^{2+}$ complex (OA = oleylamine). Furthermore, by complementing HERFD-XAS with total X-ray scattering analysis, we show the formation of an intermediate tetrahedral $[Zn(SR)_4]^{2+}$ complex at 60 °C and its successive transformation to non-crystalline ZnS nuclei at 80 °C and crystalline ZnS NPs starting at 100 °C. Thus, we demonstrate how in situ X-ray spectroscopy can elucidate the coordination and diffusion of Zn^{2+} ions, and, in combination with X-ray scattering studies, identify the emergence of atomic and electronic structures during the two-phase synthesis of ZnS nanoparticles.

5.2 Introduction

The synthesis of colloidal nanocrystals at the interface between two non-miscible liquids has been the subject of intense investigation since the first report on thiol-functionalized Au nanoparticles synthesized at the water-toluene interface.[205] The method has since been adapted and extended to the preparation of a number of metallic nanoparticles,[206-208] alloys,[209] various metal-oxides,[210-213] and core-shell nanostructures.[214]

In a two-phase synthesis, molecular precursors are separated in the aqueous and organic phases, and nucleation and growth of nanocrystals are governed by diffusion processes occurring at the liquid-liquid interface.[215] Compared with one-phase approaches such as the hot-injection, the two-phase method offers precise morphological control and monodispersity using milder reaction conditions.[216] Crucially, the two-phase method enables the use of common water-soluble metal precursors (e.g., acetates, nitrates, sulfates, etc.,) while at the same time leveraging the benefits of organic-phase syntheses, such as employing capping agents to shape and stabilize the desired nanostructures into colloidally stable dispersions.[217] Although the two-phase approach has been widely applied to synthesize various metal oxides, its use in preparing metal sulfides remains limited to a few reports focusing only on Cu_2S,[218] CdS [219, 220] and core-shell CdS-CdSe.[221]

Zinc sulfide (ZnS) is a wide band gap semiconductor that has been intensively investigated as a promising candidate for a wide range of applications, including sensors,[222, 223] optoelectronics,[135, 224] photodetectors,[224] solar cells,[225] photocatalysis,[226, 227] and photo-electrochemistry.[228, 229] Colloidally stable ZnS nanostructures are commonly prepared via one-phase solvothermal[150, 154] or hot-injection routes[230] using high boiling point organic solvents such as oleylamine or 1-octadecene. These methods have several drawbacks, including the requirement for very high reaction temperatures, inert atmospheres, and metal precursors that are soluble in non-polar solvents (e.g. diethyl zinc), which are often difficult to synthesize and handle.

In this study, we propose a two-phase solvothermal method for preparing colloidally stable ZnS nanoparticles (ZnS NPs). The method involves the use of water-soluble zinc acetate ($Zn(Ac)_2$) as the metal precursor, while elemental sulfur and oleylamine are dissolved in the toluene phase. The reaction proceeds under mild conditions (100 - 155 °C) without requiring an inert atmosphere, yielding colloidally stable sphalerite ZnS NPs. We employ spatially resolved *in situ* high-energy-resolution fluorescence-detected X-ray absorption spectroscopy (HERFD-XAS) and *in situ* X-ray total scattering to monitor the synthesis. HERFD-XAS is an element-specific technique that provides detailed insights into the local atomic environment around the absorbing atom.[80, 157, 159-161] *In situ* total scattering, particularly atomic pair distribution function (PDF) analysis, reveals information about interatomic distances present in the materials and, hence, local order, crystal structure, and domain size, and interatomic distances.[17, 21, 231-233] By combining *in situ* HERFD-XAS with X-ray scattering,[132] we track diffusion processes at the water-toluene interface, identify molecular intermediates, and monitor the nucleation and growth of ZnS NPs, as shown in **Figure 5.1**. We find that Zn^{2+} ions diffuse from the water to the toluene phase, driven by the formation of a stable octahedral $[Zn(OA)_6]^{2+}$ complex (OA = oleylamine). We propose that a tetrahedral $[Zn(SR)_4]^{2+}$ complex forms during the reaction at 60

°C, which subsequently converts into ZnS nuclei at 80 °C, promoting the growth of crystalline sphalerite ZnS NPs starting at 100 °C.

5.3 Results and Discussion

We prepare colloidally stable ZnS NPs adopting a two-phase water-toluene method, where zinc acetate ($Zn(Ac)_2$) is dissolved in water and elemental sulfur and oleylamine are dissolved in toluene, acting as sulfur source and ligand, respectively. (see the Experimental section for the synthesis details). The average size of sphalerite ZnS can be tuned from 2.3 nm to 7.5 nm by the temperature between 100 and 150 °C and reaction time, as indicated in PXRD analysis, shown in **Figures 8.2.1a-d**.

To unravel the reaction steps leading to the formation of the ZnS NPs, including the diffusion of Zn species from the water to the toluene phase, we carry out HERFD-XANES employing a micro-focused beam in combination with a movable stage, which allows us to discriminate between both phases, with a spatial resolution limited by the beam size of 0.5 x 0.5 µm.[234] We carry out the reaction employing an *in situ* cell described in a previous work.[235]

The sphalerite ZnS NPs synthesized in the *in situ* cell at 155°C for 1h have a size distribution close to that obtained in a conventional autoclave in similar reaction conditions, as shown in **Figure 8.2.2-4**.

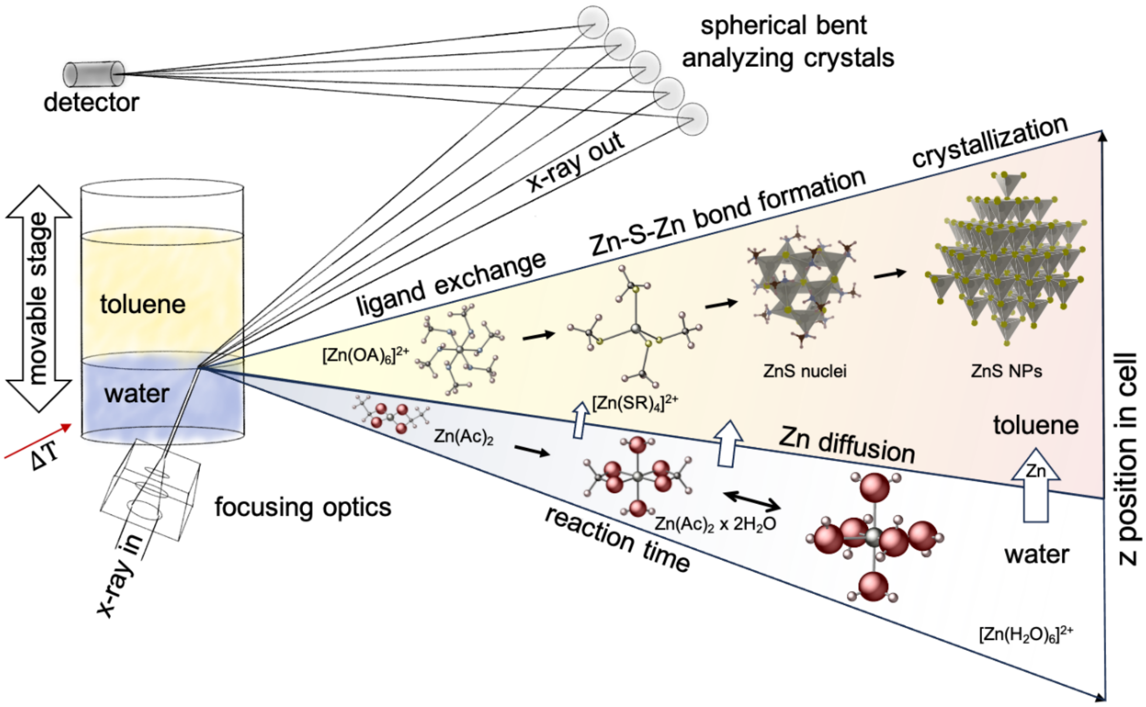

Figure 5.1: Schematic illustration of the *in situ* HERFD-XAS experiment to monitor the synthesis of ZnS NPs at the water-toluene interface and overview of the main findings. The spatial resolution provided by a movable stage and a micro-focused beam enables to probe separately the water and toluene phases. The $Zn(Ac)_2$ dissolved in water form a mixture of $[Zn(Ac)_2(H_2O)_2]$ and $[Zn(H_2O)_6]^{2+}$ complexes, where the Zn is octahedrally coordinated with six water molecules. During the reaction, the Zn^{2+} ions diffuse into the toluene phase and form an octahedral $[Zn(OA)_6]^{2+}$ complex. This complex converts at 60 °C to a tetrahedral $[Zn(SR)_4]^{2+}$ complex, which condensates at 80 °C to ZnS nuclei. The crystallization of sphalerite ZnS NPs starts at 100 °C.

We monitor the diffusion of Zn species at the water-toluene phase, collecting HERFD-XAS data using the micrometer-focused beam at room temperature, following the contact of the two phases. **Figure 5.2a** and **Figure 5.2b** show the XAS spectra collected at the water and toluene phases at room temperature, respectively. We detect the presence of Zn species in both the water and toluene phases immediately after contact at room temperature. Using ORCA DFT[236] calculations, we propose that, upon dissolution of the $Zn(Ac)_2$ used as a precursor, the Zn^{2+} ion forms the octahedral $[Zn(H_2O)_6]^{2+}$ complex with six water molecules, as shown in the inset in **Figure 5.2a**. The broadening of the white line in **Figure 5.2a** suggests that $Zn(Ac)_2$ and $[Zn(Ac)_2(H_2O)_2]$ are still present in the water phase and establish an equilibrium with the

$[Zn(H_2O)_6]^{2+}$ complex following reaction (1). The formation of a $[Zn(Ac)_2(H_2O)_2]$ complex during the dissolution of $Zn(Ac)_2$ in water is described in the literature.[237]

$$Zn(Ac)_2 \xrightarrow{+\,2H_2O} [Zn(Ac)_2(H_2O)_2] \rightleftharpoons [Zn(H_2O)_6]^{2+} + 2Ac^- \qquad \textbf{(1)}$$

The ORCA calculations points at the presence of a $[Zn(OA)_6]^{2+}$ (OA = oleylamine) complex in the toluene phase, as shown in **Figure 5.2b**, where Zn^{2+} ions are octahedrally coordinated by six oleylamine molecules. However, the ORCA calculation of $[Zn(OA)_6]^{2+}$ spectra shows discrepancies to the experimental spectra, which point to co-existence of tetrahedral $[Zn(OA)_4]^{2+}$ in the reaction solution.[235] Low contributions of other potential zinc-amino complexes cannot be excluded, however the main contribution stems from Zn^{2+} ions with octahedrally coordinated oleylamine. In general, the formation of the zinc-amino complexes, confirms the diffusion of Zn^{2+} ions through the water-toluene interface at room temperature.

To quantify the distribution of the Zn^{2+} species at room temperature, we collect HERFD-XAS spectra scanning across the water-toluene interface. We first observe a gradual energy shift of the E_0 by 1.3 eV towards lower energy, **Figure 5.2e**, as expected for a change in the local environment around the Zn atoms from a Zn-O to a Zn-N coordination.[235] The E_0 corresponds to the energy value where the first derivative of the XAS reaches its maximum, while the white line is the maximum intensity in the XAS spectra.[235, 238, 239]

Scanning the water-toluene interface while collecting the intensity of the $K_{\alpha 1}$ emission under illumination at 10 keV allows for the extraction of the concentration profile of the Zn species across the water-toluene interface, as shown **Figure 5.2c**. Moving from the water to the toluene phase, the Zn concentration decreases gradually when approaching the interface at the z position 0, shows a peak slightly above the interface on the toluene side, and then further decreases moving away from the interface. This agrees with a diffusion process across the water-toluene interface, likely driven by forming a stable $[Zn(OA)_6]^{2+}$ complex in toluene.

The collected HERFD-XAS data allow us to determine the fraction of $[Zn(H_2O)_6]^{2+}$ $[Zn(OA)_6]^{2+}$ complexes around the interface, **Figure 5.2d**, as recovered by Multivariate Curve Resolution-Alternating Least Squares (MCR-ALS) analysis of the spatially resolved HERFD-XAS data, shown in **Figure 5.2e**.[176, 177] More details about the MCR-ALS analysis are available in **Figure SI5-6** and **Table 8.2.1-2**. The analysis confirms that at room temperature, i.e., before the start of the reactions leading to the formation of the ZnS NPs, the Zn ions are distributed across the water-toluene interface through a diffusion process, with the formation of a

$[Zn(OA)_6]^{2+}$ complex in toluene occurring at the expenses of the $[Zn(H_2O)_6]^{2+}$ complex present in water. To exclude beam damage in the XAS measurements, extensive beam damage studies were performed in both phases, as shown in **Figure 8.2.7**.

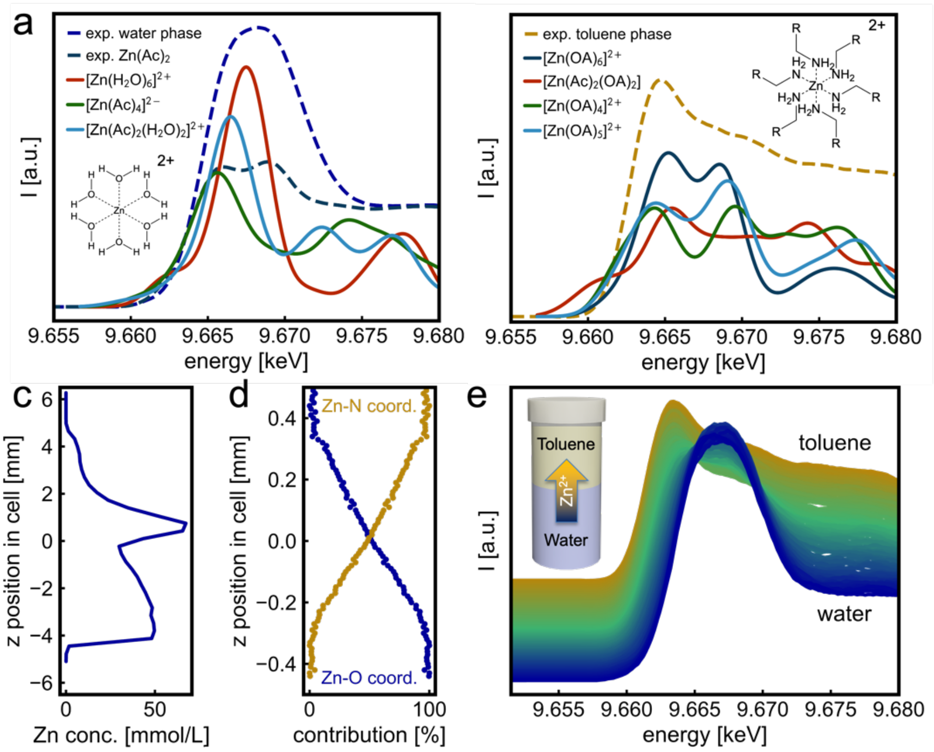

Figure 5.2: Diffusion of Zn2+ species at room temperature at the water-toluene interface monitored by HERFD-XAS. XAS spectra at the Zn K-edge in the water (a) and toluene (b) phases, compared with an experimental $Zn(Ac)_2$ reference and with the calculated XAS spectra by DFT calculations of $[Zn(H2O)_6]^{2+}$, $[Zn(Ac)_4]^{2-}$, $[Zn(Ac)_2(H2O)_2]^{2+}$ and $[Zn(OA)_6]^{2+}$, $[Zn(Ac)_2(OA)_2]$, $[Zn(OA)_4]^{2+}$ and $[Zn(OA)_5]^{2+}$, respectively. The comparison of experimental and theoretical spectra allowing the identification of a $[Zn(H_2O)_6]^{2+}$ and a $[Zn(OA)_6]^{2+}$ complexes in water and toluene, respectively. The concentration profile of Zn at the water-toluene interface (c) and the fraction profile of the $[Zn(H_2O)_6]^{2+}$ and $[Zn(OA)_6]^{2+}$ extracted by MCR-ALS analysis of the HERFD-XAS spectra (d). The HERFD-XAS spectra recorded at different positions z in the cell at RT, where 0 is the position of water-toluene interface. Inset shows a schematic drawing of Zn^{+2} diffusion at room temperature across the water-toluene interface (e). The data was acquired at the beamline ID24.

During the formation of ZnS NPs, one can observe color changes in the water and toluene phases as shown in **Figure 5.3a**. The Zn^{2+} concentration profiles before (blue curve) and after the reaction (red curve) show that a large fraction of Zn^{2+} is still dissolved at room temperature in the water phase. During the reaction, with increasing temperature, the Zn^{2+} diffuses from the water to the toluene phase up to around 80 °C, when the diffusion is complete. Therefore, we assume that the diffusion process does not limit the nucleation or the growth rate of ZnS NPs, which occurs at temperatures higher than 80 °C. The evolution of Zn^{2+} content in the toluene phase during the reaction is shown in **Figure 8.2.8**.

To monitor the reaction pathways leading to the formation of ZnS NPs in the toluene phase, we record *in situ* HERFD-XAS at different positions in the toluene phase. During the experiment, the reaction is performed with a slow heating rate of 1 °C/min, allowing to monitoring of the presence of reaction intermediates. The *in situ* HERFD-XAS data (**Figure 5.3b**) reveal an E_0 shift by around 1 eV to lower energies when the reaction temperature increases to 60 °C (first 40 minutes). This energy shift suggests a change in the coordination environment around Zn, where the amine ligand (Zn-N coordination) is likely substituted by thio-ligands (Zn-S), [80, 240, 241] as highlighted in the inset. Since the line shape of the HERFD-XAS at 60 °C differs from the one expected for ZnS, this might highlight the occurrence of one or more reaction intermediates.

We therefore perform MCR-ALS analysis of the HERFD-XAS dataset, as shown in **Figure 5.3c**. MCR-ALS can deconvolute the observed changes in the *in situ* HERFD-XAS data into four individual contributions. **Figure 5.3c** shows the XAS spectra of each contribution (top panel) extracted from the MCR-ALS analysis and their related concentration profiles during the reaction (bottom panel). The starting point of the reaction (blue line) is attributed to the $[Zn(OA)_6]^{2+}$ complex described in **Figure 5.2b**. The XAS spectra of the first intermediate (green line) show, in addition to the E_0 shift of around 1 eV that is characteristic of a Zn-S coordination, a slight decrease in white line intensity compared to the $[Zn(OA)_6]^{2+}$ complex, as highlited in the inset of **Figure 5.3b.** The decrease in white line intensity might indicate a change in coordination geometry, potentially from octahedral to tetrahedral.[80, 242] In **Figure 8.2.9,** we compare the XAS spectra of various tetrahedral and octahedral Zn-S complexes simulated by ORCA DFT with the XAS spectra of the intermediate extracted from the MCR-ALS analysis (green line). We find that the best-fitting simulated spectra correspond to a $[Zn(oleylthioamide)_4]^{2+}$ ($[Zn(SOA)_4]^{2+}$) complex. The simulated and experimental spectra match well in terms of white-line and intensity, with some discrepancies in the post-edge features originating from the second coordination sphere around Zn. In an earlier study, we performed DFT calculations of various tetrahedral Zn-S complexes, and we found that a tetrahedral $[Zn(SOA)_4]^{2+}$ complex forms also when zinc acetate is dissolved in oleylamine with the presence of elemental sulfur.[235] This complex likely occurs as an intermediate during our two-phase reaction in the toluene phase due to the presence of oleylamine and sulfur. However, due to the aforementioned discrepancies in the post-edge features of the XAS spectra, we assign this first intermediate to a generic tetrahedral $[Zn(SR)_4]^{2+}$ complex. The formation of molecular Zn-S complexes during the one-pot synthesis of ZnS NPs has already been proposed in the literature. [147, 148, 235, 243]

A detailed analysis of individual XAS features is required to identify the second intermediate recovered by MCR-ALS. Often, the formation of ZnS NPs in the sphalerite phase proceed via an intermediate in the wurtzite phase,[235] which only differs in the stacking arrangement of the ZnS tetrahedrons. We excluded the presence of wurtzite ZnS during the reaction by FEFF calculations, shown in **Figure 8.2.10a** and by PXRD analysis in **Figure 5.4e**.[160, 175, 244] Nevertheless, the in **Figure 5.3d** shown, less pronounced features in the post-edge region of the ZnS nuclei (yellow) suggest a lack of periodicity in its atomic structure compared to the ZnS NPs (red).[245] The experimental spectra of ZnS NPs were compared with a ZnS reference in **Figure 8.2.10b**.

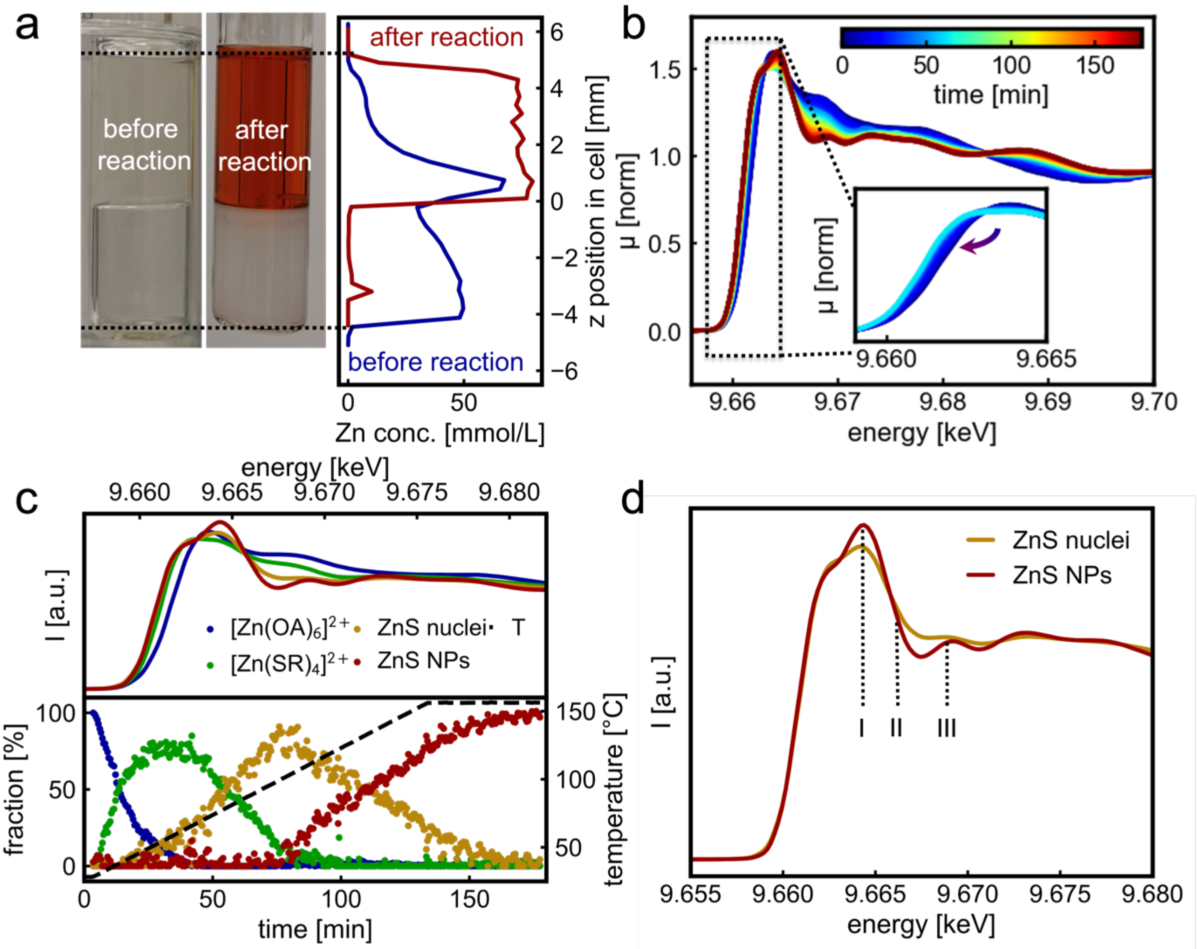

Figure 5.3: Diffusion of Zn complexes, ligand exchange, and nucleation of ZnS investigated by *in situ* HERFD-XAS and MCR-ALS analysis. Photographs of the reaction solutions (a) prior (left) and after the reaction (middle) and the corresponding Zn concentration profiles around the interface show the diffusion of Zn ions through the interface during the reaction (right). *In situ* HERFD-XAS data (b) reveal the transformation of [Zn(OA)$_6$]$^{2+}$ into ZnS NPs. In the beginning of the reaction, the position of the E$_0$ shifts from 9661.5 eV to 9660.5 eV, while the intensity of the white line is decreasing, indicating a transition from Zn-N to Zn-S bonding as highlighted in the inset. MCR-ALS analysis (c) deconvolutes the *in situ* HERFD-XAS data into four distinct components (top) and their related concentrations (bottom). Comparison of the XAS spectra (d) of the second intermediate (yellow) and the final product (red) obtained from MCR-ALS analysis. The spectra of the second intermediate exhibit similar features to s-ZnS, albeit less pronounced, indicating similar coordination structure but lack of long-range ordering in the second intermediate. The data was acquired at the beamline ID26.

To resolve the atomic structure of the second intermediate and monitor nucleation and growth of the ZnS NPs during synthesis, we perform *in situ* total scattering (TS) measured at the water-toluene interface and calculate the atomic-pair distribution function (PDF) to achieve a histogram of interatomic distances, as shown in **Figure 5.4a**. The dashed line highlights the emergence of the Zn-S interatomic distance, starting above 60 °C. This aligns with the presence of the $[Zn(SR)_4]^{2+}$ complex evidenced by MCR-ALS analysis of the *in situ* XAS data. In contrast to the XAS analysis, the TS data were collected with a 1 mm^2 beam size, with which we probed the water and toluene phases simultaneously.

However, if one isolates the PDF at times when the MCR-ALS analysis shows the maximum contributions, one can extract a PDF of the individual intermediates, as shown in **Figure 5.4b** and **Figure 5.4c**. At the beginning of the reaction, the PDF (blue) corresponds to a mixture of zinc complexes in both water and toluene, as shown by the presence of Zn-O and Zn-N interatomic distances. Furthermore, the $[Zn(H_2O)_6]^{2+}$ complex in the water phase might partly self-assemble into a molecular cluster as indicated by an increased extent of correlations and larger peak heights in the PDF, as discussed in **Figure 8.2.11** and observed for other transition-metal acetates in water.[246, 247] The decrease in the PDF peak amplitudes during the first 30 minutes, **Figure 5.4a**, can be attributed to the diffusion of Zn^{2+} to the toluene phase away from the interface, which lowers the Zn concentration in the water phase, and, consequently, in the beam path. After reaching 60 °C (40 minutes in to the reaction), the Zn-N peak disappears, substituted by an established Zn-S coordination, shown in **Figure 5.4b** (green line), characteristic of the $[Zn(SR)_4]^{2+}$ complex. At around 100 °C (80 minutes into the reaction), the PDF corresponding to the second intermediate, **Figure 5.4c** (yellow line), shows delocalized Zn-Zn interatomic distances at 3.3 Å, 3.7 Å, and 4.0 Å, besides the Zn-S interatomic distance at 2.4 Å, which do not correspond to the presence of wurtzite ZnS NPs. Additionally, the extent of the correlation in the PDF of the second intermediate is limited to around 10 Å. Therefore, we propose that the second intermediate corresponds to small ZnS nuclei, whose atomic arrangements do not have long-range ordering. The presence of such ZnS nuclei as an intermediate has already been discussed in the literature for other ZnS synthesis routes.[153, 248]

After increasing the reaction temperature above 100 °C, the ZnS nuclei evolve into crystalline ZnS NPs, as evidenced by the appearance of a strong peak at 3.8 Å corresponding to the typical Zn-Zn distance in sphalerite, **Figure 5.4c**. The ZnS NPs show a continuously increasing extent of correlations, reflecting their growth. The corresponding refinement is shown in **Figure 5.4d**. The refined PDF of ZnS in the sphalerite phase is compared with the last experimental PDF of the *in situ* run in **Figure 8.2.12**. The domain size of the ZnS NPs grows up to 2.3 nm for a reaction time of 1 h. Details about the PDF fitting procedure are shown in **Figure 8.2.13**.

In situ powder X-ray diffraction analysis (**Figure 5.4e**) reveals the crystallization of ZnS NPs in the sphalerite phase starting at 100 °C and does not provide any evidence for the presence of an intermediate wurtzite ZnS phase, in line with the HERFD-XAS and PDF analysis. Consequently, we can rule out the formation of wurtzite ZnS NPs, which is instead observed in other ZnS syntheses. [147, 148, 235, 243] Additionally, the ZnS nuclei, which form during the reaction at around 80 °C, do not exhibit a long-range order, since a long-range order in the ZnS nuclei would result in visible contributions in the PXRD pattern. Therefore, we suggest that nanoparticle growth occurs above 100 C, where ZnS nuclei grow directly into crystalline ZnS sphalerite particles. The PXRD pattern of the resulting ZnS NPs is further analyzed by Rietveld refinement and confirms the domain size of around 2.3 nm, as shown in **Figure 5.4f**.

By integrating information on Zn coordination throughout the synthesis from *in situ* HERFD-XAS data analysis with interatomic distances and sizes obtained from *in situ* PDF analysis, along with insights into the crystallographic phase from *in situ* PXRD data, we propose a reaction mechanism for the two-phase synthesis of ZnS NPs, as illustrated in **Figure 5.4g**. The oleylamine ligands in the $[Zn(OA)_6]^{2+}$ complex in toluene are replaced by sulfur ligands at temperatures above 60 °C, forming a $[Zn(SR)_4]^{2+}$ complex. Reaching around 80 °C, the ZnS tetrahedrons undergo a Zn-S-Zn bond formation, arranging into a non-periodical structure and creating non-crystalline ZnS nuclei approximately 10 Å in size. The crystallization of ZnS NPs in the sphalerite phase starts at 100 °C, followed by continuous domain growth, reaching approximately 2.3 nm after 60 min at 155 °C.

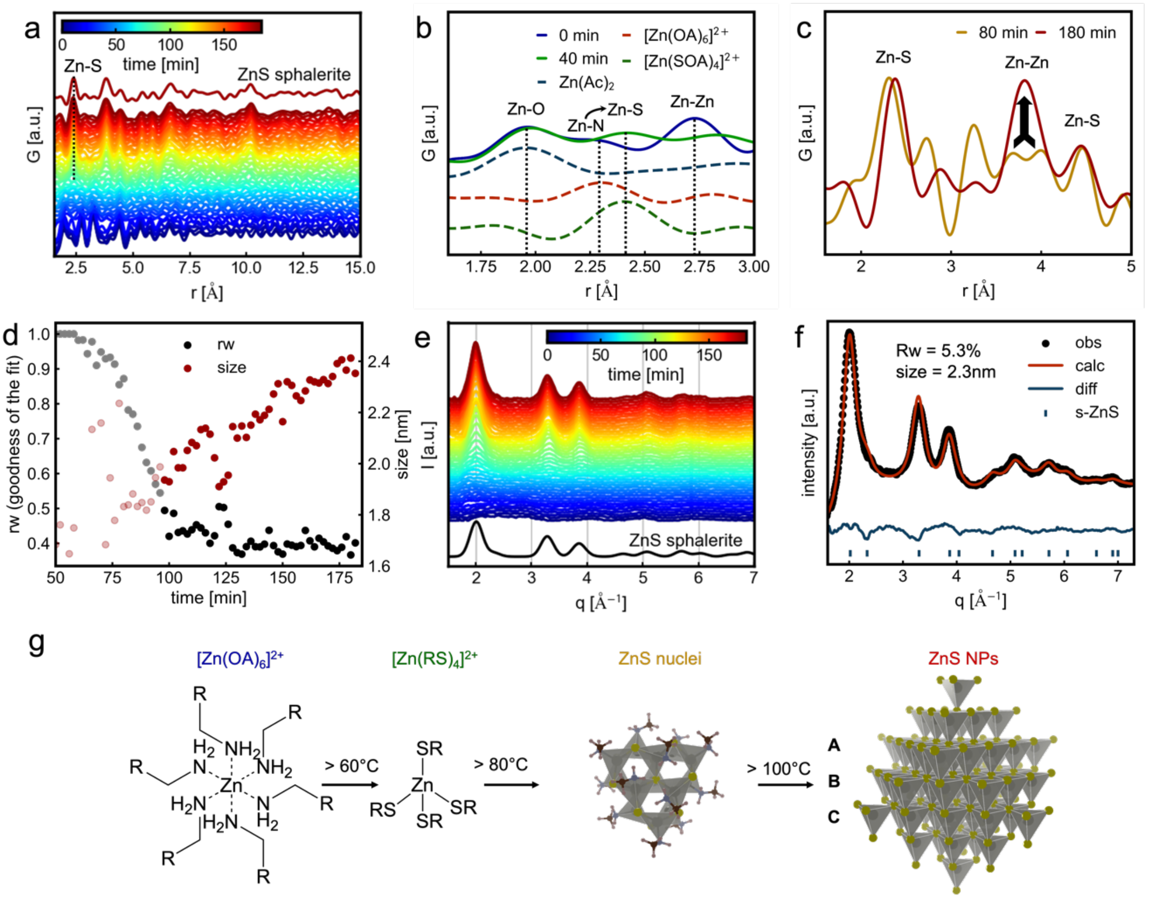

Figure 5.4: Ligand exchange, nucleation, crystallization, and growth investigated by *in situ* PDF and PXRD analysis. *In situ* PDF analysis (a) showing the emergence of Zn-S interatomic distances (dotted line) after 30 min reaction time. The comparison of the PDF (b) at the beginning of the reaction (solid blue) and after 40 min of reaction time (solid green), with simulated PDFs of $Zn(Ac)_2$ (dashed blue), $[Zn(OA)_6]^{2+}$ (dashed red), and $[Zn(SOA)_4]^{2+}$ (dashed green). The experimental PDFs are normalized to the Zn-O peak. The occurrence of the Zn-Zn peak at the starting point of the reaction is assigned to the condensation of $[Zn(H_2O)_6]^{2+}$ into polymorphs, as described in Figure SI10. After 40 min of the reaction, the peak corresponding to Zn-S atomic pairs is visible at around 2.4 Å. Comparison of PDF (c) at 80 min (100°C) and 180 min reaction time, reflecting the PDF of ZnS nuclei (yellow) and ZnS NPs (red). The peak at 3.8 Å, characteristic for Zn-Zn distances in ZnS NPs, is not present in ZnS nuclei, which confirms their non-crystalline nature. Both PDFs were normalized to the Zn-S peak height. The *in situ* PDF fitting (d) with ZnS in sphalerite phase. The fit becomes meaningful after a 100 min reaction time (120°C) when the rw value drops below 0.5, visualized by blurring the markers before 100 min reaction time. *In situ* PXRD analysis (e) shows the emergence of ZnS in the sphalerite phase (s-ZnS) during the reaction without any ZnS content

in the wurtzite phase. Rietveld refinement (f) of the final PXRD pattern confirms a domain size of around 2.3 nm in the ZnS NPs. The proposed reaction mechanism is illustrated (g).

5.4 Conclusion

In this work, we present a synthetic route yielding sphalerite ZnS NPs at the water-toluene interface. We provide spatially resolved insights into the coordination chemistry and the structural changes occurring during the synthesis of ZnS NPs in a two-phase system. The *in situ* HERFD-XANES showed that Zn^{2+} species diffuse from water to toluene through an equilibrium involving $[Zn(H_2O)_6]^{2+}$ and $[Zn(OA)_6]^{2+}$ complexes forming in water and in toluene, respectively. The *in situ* studies reveal at 60 °C a ligand exchange process where the octahedral $[Zn(OA)_6]^{2+}$ complex evolves into a tetrahedral $[Zn(SR)_4]^{2+}$ complex. Above 80 °C, this complex subsequently condenses to form Zn–S–Zn bonds, leading to ZnS nuclei, which then grow into crystalline sphalerite ZnS NPs above 100 °C. The studies are complemented by *in situ* X-ray scattering measurements, which further confirm the transformation of non-crystalline ZnS nuclei directly to ZnS in the sphalerite phase.

In conclusion, this work highlights the potential of spatially resolved HERFD-XANES as a tool for monitoring chemical reactions in nonhomogeneous two-phase reactions that are inaccessible by other methodologies. The insights gained through this approach not only enhance our understanding of two-phase ZnS synthesis but also open new opportunities for exploring the synthesis of a wider range of nanostructures or quantum dots.

5.5 Acknowledgment

This research was supported by the European Research Council (LINCHPIN project, grant no. 818941), the Deutsche Forschungsgemeinschaft (DFG) through the Cluster of Excellence “Advanced Imaging of Matter” (EXC 2056, project ID 390715994) and the Graduate School “Nanohybrid” (funding ID 408076438), and the Bundesministerium für Bildung und Forschung (BMBF) via the project 05K22GU7 (LUCENT II). Furthermore, we acknowledge DESY (Hamburg, Germany), a member of the Helmholtz Association, for the provision of experimental facilities. Parts of this research were carried out at PETRA III using beamline P21.1 and at ESRF using beamline ID24 and ID26 under proposals MA5353, MA5366.[188, 189] We would like to acknowledge Andrea Köppen for providing HRTEM images and Dr. Viktoriia Saveleva, Philipp Glaevecke for their assistance at the beamlines ID26 (ESRF) and P21.1. (DESY), respectively.

5.6 Experimental Section

Chemicals:

Zinc (II) acetate ($Zn(Ac)_2$) (99.99%, anhydrous), sulfur (99.998% trace metal basis), toluene (anhydrous, 99.8%), and oleylamine (≥98% primary amine) were procured from Sigma-Aldrich. All chemicals were utilized in their as-received state without undergoing additional purification.

ZnS synthesis:

For the preparation of ZnS precursor solutions, 0.184 g of $Zn(Ac)_2$ (1 mmol) was dissolved in 15 mL of Milli-Q water. The resulting solution was subjected to filtration using 200 nm screw-on syringe filters. Simultaneously, 1.5 mL of oleylamine (~98%) and 0.096 g (3 mmol) of elemental sulfur were dissolved in 15 mL of anhydrous toluene. For the *in situ* studies, 50 microliters of the aqueous solution and 100 microliters of the toluene solution were sequentially introduced into the reaction cell, and the reaction was performed with a heating rate of 1 °C/min up to 155 °C for 1 h. A control reaction was also carried out in a standard 45 mL stainless-steel autoclave, with a temperature range of 100 – 150 °C and reaction times from 1 to 24 h.

Beamline setup and data acquisition:

The HERFD-XANES were acquired at the ID26 and ID24 beamlines at the European Synchrotron Radiation Facility (ESRF) in Grenoble, France. On both beamlines, the Si(111) reflection of a double crystal monochromator was chosen for selecting the incoming energy. The HERFD-XANES data were obtained by measuring the intensity of the Zn Kα main line utilizing Si(642) crystals in Rowland Geometry within a Johann-type X-ray emission spectrometer.[68] The crystal bending radius was 1m on ID26 and 0.5m on ID24. This measurement involved continuous scanning of the monochromator together with the undulator gap. The scans across the interface shown in Figure 2 were performed at ID24, with a focused beam size of 0.5 μm x 0.5 μm. The *in situ* data shown in Figure 3 were collected at ID26 with a beam size of 0.2 mm x 0.4 mm. To minimize radiation damage, the position of the X-ray beam center was varied among different points on the reaction cell. XANES spectra were recorded at intervals of 16 seconds, with the energy range set from 9.64 to 9.8 keV and an energy step of 0.2 eV.

The *in situ* X-ray total scattering data were obtained at the P21 beamline of PETRA III, situated at the Deutsches Elektronen-Synchrotron (DESY) in Hamburg, Germany. The total scattering measurements were performed at intervals of 0.5 s using a flat panel detector (PerkinElmer XRD1621, Varex Imaging Corp.) featuring 2048x2048 pixels with a size of 200 x 200 μm^2. Throughout the experiments involving the synthesis of ZnS NPs at 155 °C, the sample-to-detector distances (SDD) for total scattering data were set at 0.39 m. The SSD for the XRD data was set to 1.54 m. These distances were determined through calibration with a LaB6 calibrant, and the X-ray beam energy employed for the measurements was 101.8 keV.

Data processing:

The HERFD-XAS were processed through a custom Python code built upon previously published packages. Edge position determination and edge jump normalization were executed using the LARCH-XAFS module.[194] Spectroscopic data underwent treatment with a Savitzky-Golay filter and further processing utilizing the NumPy[195] and SciPy[196] packages. XANES spectra simulations were carried out using the ORCA 5.0.4. code,[197] where the initial complex before relaxation was built with Avogadro 1.2.0., an open-source molecular builder and visualization tool.[198] XANES spectra simulations in SI were conducted using the FEFF09 code[193]. ORCA and feff parameters were listed in SI.

Azimuthal and radial integration of the 2D detector patterns for PDF and XRD data was done using the Python module pyFAI[199], excluding beam stop shadows, glitches, defective, and noisy pixels. Background data collection under identical reaction conditions of the ZnS syntheses at 155 °C. The background data were subtracted from the sample data set using a fitted scaling factor constrained to a maximum value between 0.95 and 1.1. Data averaging over 120 frames, corresponding to a 1-minute time resolution, was performed. PDFs (G(r)) were calculated in the r-range (lowest to highest r extracted from the Fourier transformation) of 0 - 30 Å^{-1} in steps of 0.01 Å^{-1} using the software PDFgetX3.[117] The PDFs were obtained with a Qmaxinst (highest Q usable under given experiment conditions) of 25 Å^{-1} over a Q-range (upper to lower cut-off) of 0.1-14.8 Å^{-1} and an r-poly of 1.1. The latter corresponds to the range of polynomial fitting in ad-hoc correction (here, a five-degree polynomial correction, n=rpolyQmaxinst/π). The PDF fittings were done utilizing Diffpy-CMI, employing a single-phase refinement with ZnS sphalerite. The sphalerite phase (mp-10695) was extracted from the materials project database,[249] and the refinement was conducted sequentially, starting from the PDF at the end of the reaction and proceeding backward to earlier reaction times to ensure improved fit reliability. The Rietveld refinement was performed with GSAS-II package.[200] The sphalerite phase (ICSD-230703) were used from the ICSD database. The refinement was carried out in a sequential way, starting from the XRD at the end of the reaction and going backward to earlier reaction times, ensuring a better reliability of the fit.

The wording and readability of the manuscript were improved by ChatGPT 4.0, following the guidelines of ACS journals. [203]

6 Further perspectives: *in situ* formation of Fe_3S_4 nanostructures

My contribution to this work compromises the synthesis of Fe_xS_y *nanostructures in toluene, the measurement and analysis of vtc-XES, HERFD-XAS and RIXS data, the DFT calculations, the analysis of PDF and PXRD data.*

The synthesis of Fe_3S_4 *in benzyl alcohol were developed and established by Dr. Cecilia A. Zito, Brian Jessen and Dr. Francesco Caddeo.*

A first characterization of this synthesis was already presented and discussed in the master thesis of Brian Jessen.

The discussed diffraction data were acquired by Dr. Cecilia Zito, Sani Y. Harouna-Mayer, Dr. Chia-Shuo Hsu, Tjark L. R. Gröne and Jagadesh Kopula Kesavan at P21.1. The discussed spectroscopic data were acquired with Sarah A. Hussak, Lian Belgardt, Dr. Cecilia Zito, Tjark L.R. Gröne and Dr. Chia-Shu Hsu.

6.1 Introduction

Iron sulfides (Fe_xS_y) are an earth-abundant class of materials since they are an essential part of the global biochemical sulfur cycle.[250] Besides their high chemical stability and interesting magnetic properties[251], especially the tetragonal mackinawite (FeS) and the cubic spinel structure greigite (Fe_3S_4) phases are well known for their performance in electrochemistry, where they find applications in sodium-ion batteries,[252, 253] in the hydrogen evolution reaction[254, 255] or in the reduction of CO_2.[256] All potential applications of iron sulfides are based on their unique orbital composition and electronical properties.[257] The presence of delocalized charge carriers in Fe_3S_4 can be attributed to electron hopping between ferrous (d6) and ferric (d5) Fe on octahedral sites, leading to a semimetallic nature with a band gap of around 0.8 eV.[258, 259] This narrow energy band gap compared to Fe oxides, e.g., enhances electrical transport properties.[252]

The synthesis of iron sulfides is well described in the literature.[260] Tetragonal FeS has the lowest reaction temperature among the various phases. When the reaction conditions permit the incorporation of excess sulfur, the nucleation of FeS initiates a transformational pathway that progresses through greigite (Fe_3S_4) and finally leads to pyrite (FeS_2). The transition to a hexagonal close-packed (hcp) lattice is kinetically hindered,[261] even though the hcp phases exhibit intermediate enthalpies.[260] However, the phase transition through an intermediate FeS structure during the synthesis of Fe_3S_4 nanomaterials has already been proposed,[260] but to date, obtaining the desired phase follows mostly a try-and-error approach. An *in situ* investigation of the emergence of atomic electronic structures in iron sulfide synthesis could propose a reaction mechanism, allow the identification of intermediate structures, and help to understand the phase transitions during the solvothermal synthesis, but it has not been reported to date.

In this chapter, we presented a preliminary analysis of a multi-model approach to link the emergence of the electronic structure with the atomic structure by establishing *in situ* vtc-XES on the Fe K-Edge during the solvothermal synthesis of Fe_3S_4 nanocrystals. The *in situ* vtc-XES analysis provided detailed insights into the donor orbitals of the recombination, which directly correlates to the changes in iron coordination throughout the reaction. Thereby, we prove the reduction and solvent coordination of $Fe(acac)_3$ precursor forming a $[Fe(acac)_2(BA)_2]$ complex. We combine the results with *in situ* HERFD-XAS and PXRD analysis to identify the structure and morphology of FeS nanosheets as an intermediate and follow the phase transformation to isotropic Fe_3S_4 nanocrystals.

6.2 Result and Discussion

6.2.1 The crystallization of FeS nanosheets and the phase transition to Fe_3S_4 nanocrystals

To monitor the structural evolution of Fe_3S_4 nanocrystals, we conducted *in situ* PXRD analysis during the synthesis at 180 °C with combined sequential Rietveld refinement. We observe the formation of tetragonal FeS (*P4/nmm*) nanosheets as an intermediate step prior to the phase transition to the cubic spinel structure of Fe_3S_4 (*Fd3m*), as schematically illustrated in **Figure 6.1.a.** In the early stages of the reaction, only a peak below 2 $Å^{-1}$ related to the residual background is observable, indicating the absence of crystalline species in the solution, as shown in **Figure 6.1.b.** The first reflection at around 3.4 $Å^{-1}$ appears when the temperature reaches about 120 °C, followed by the emergence of reflections at approximately 2.4, 2.8, and 4.8 $Å^{-1}$, corresponding to the initial formation of FeS nanosheets. Upon reaching the final reaction temperature of 180 °C, the characteristic peaks of Fe_3S_4 nanocrystals becomes evident. The intensity of the reflections related to Fe_3S_4 increases alongside a correlated decrease in the intensity of the reflections related to FeS. Fe_3S_4 becomes the predominant crystalline phase as the reaction progresses, persisting until the end after 75 minutes.

We perform the sequential Rietveld refinement on the *in situ* PXRD data to monitor the contributions of the two Fe_xS_y phases and crystal size throughout the reaction, as shown in **Figure 6.1.c**. After 15 min reaction time, the PXRD pattern can be refined by a mixture of around 75% anisotropic FeS domains and 25 % isotropic Fe_3S_4, as plotted in **Figure 6.1.d**. The FeS contribution is refined using an uniaxial model, with (001) as a unique axis, resulting in a disk-like structure with a thickness of around 3 nm and a diameter of around 50 nm. Therefore, the FeS tetrahedrons are oriented along the (001) lattice plane, forming a layered structure, as shown in **Figure 6.1.a**. The Fe_3S_4 contributions are fitted with a spherical domain, which grows from 15 nm after 15 min to 22 nm after 75 min. After 60 min, the FeS contribution converges to zero, indicating a single crystalline phase at the end of the reaction. An overview of the Rietveld analysis is provided in **Figure 8.3.2.1.-3.** and in **Table 8.3.2.1.**

Although the final Fe_3S_4 phase is fitted very well with an isotropic domain, SEM images reveal a platelet-like nanoparticle assembly at the end of the reaction, as shown in **Figure 6.1.f**. Additional SEM images are available in **Figure 8.3.2.4.-6.**, comparing the morphology of the final product at different reaction temperatures**.** To understand the transformation from the FeS layered structure to the Fe_3S_4 platelet-like morphology, *in situ* imaging techniques like ptychography or *in situ* morphology analysis like *in situ* SAXS can gain insights into the assembly and morphology during the synthesis, which is beyond the scope of this thesis.

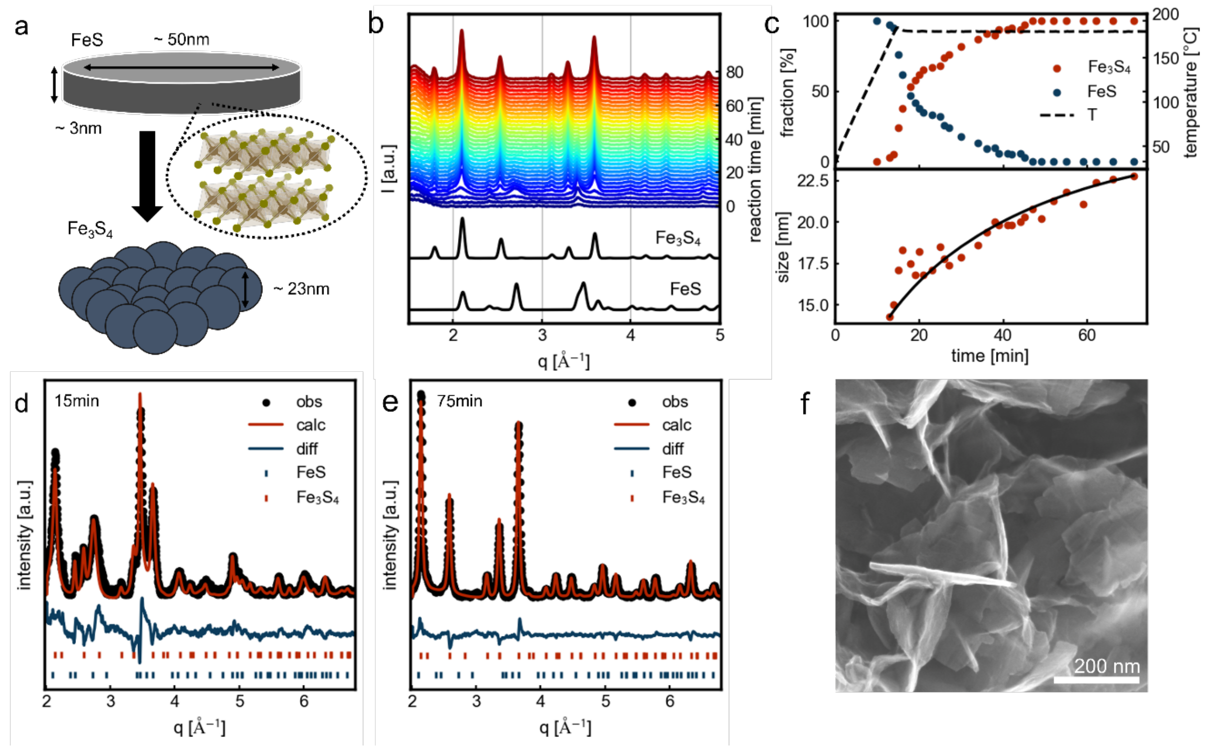

Figure 6.1: *In situ* PXRD analysis of Fe_3S_4 synthesis at 180°C. (a) Illustration of the phase transformation from FeS nanosheets to Fe_3S_4 nanocrystals. **(b)** *In* situ time-resolved PXRD patterns for the synthesis of Fe_3S_4 nanocrystals at 180 °C, compared with the standard patterns for greigite Fe_3S_4 (*Fd-3m*) and mackinawite FeS (*P4/nmm*) phases. **(c)** Sequential Rietveld refinement quantifies the fraction between FeS and Fe_3S_4 (top) and the growth of Fe_3S_4 nanocrystals (bottom). **(d)** Rietveld refinement of the phase mixture after 15 min reaction time at 180 °C shows a strong contribution of FeS. The dimensions refined in the uniaxial model with (001) as a unique axis suggest a layered structure of FeS. **(e)** The only crystalline phase at the end of the reaction is Fe_3S_4, as shown in the Rietveld refinement after 75 min reaction time. **(f)** SEM image of the reaction product shows a platelet-like assembly of Fe_3S_4 nanocrystals.

As depicted in **Figure 6.2,** lowering the synthesis temperature to 160 °C or 140 °C slows the transformation of FeS into Fe_3S_4. Even after 180 min of reaction time, both crystalline phases are mixed, with FeS being the main phase at the end of the reaction at 140 °C, as shown in **Figure 6.2.**

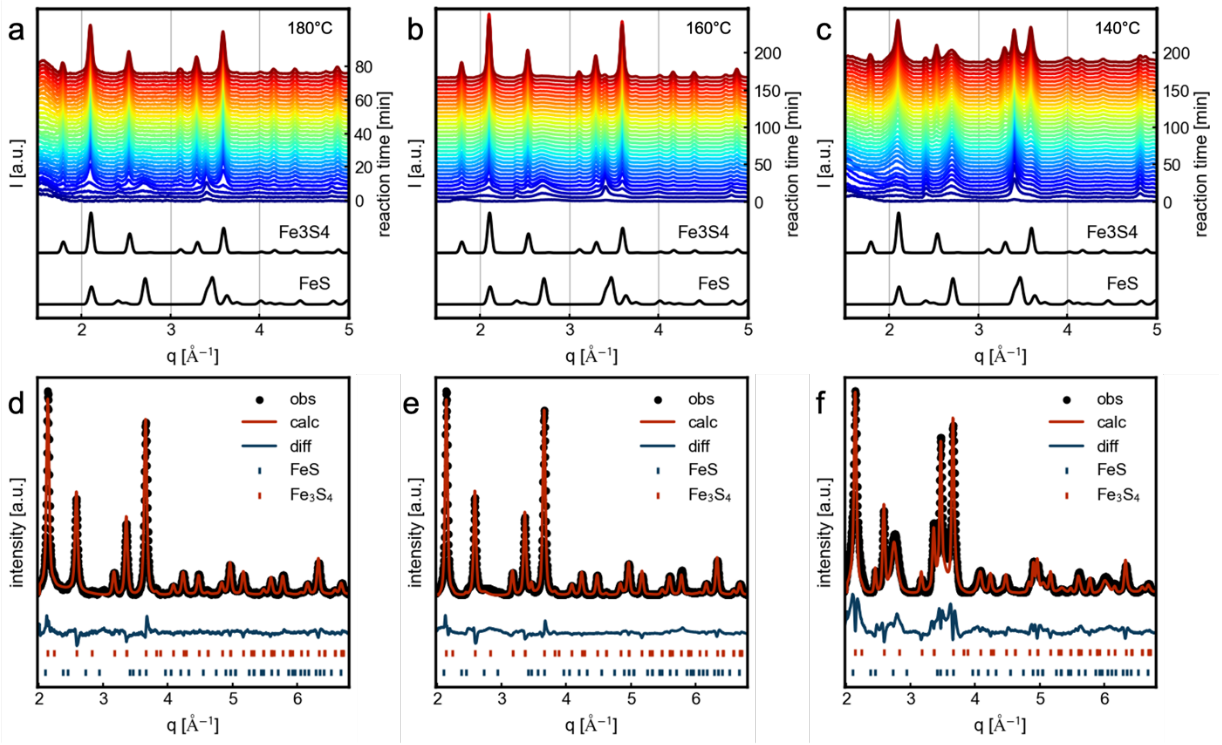

Figure 6.2: ***in situ* PXRD analysis of Fe_3S_4 synthesis at different reaction temperatures.** **(a)** *In situ* time-resolved PXRD patterns for the synthesis of Fe_3S_4 at 180 °C with 10°C/min heating rate, compared with reactions at reaction temperatures of 160 °C **(b)** and 140 °C **(c)** with 1°C/min heating rate. Rietveld refinements of the final products reveal an estimated ratio between FeS and Fe_3S_4 of 0% FeS and 100% Fe_3S_4 at 180°C **(d)**, 7% FeS and 93% Fe_3S_4 at 160 °C **(e)** and 61% FeS and 39% Fe_3S_4 at 140 °C **(f)** reaction temperatures.

6.2.2 The chemistry of Fe_3S_4 nanocrystal formation

The PXRD shows the formation of phase-pure spinel Fe_3S_4 nanocrystals and confirms tetragonal FeS as the crystalline intermediate. However, it fails to provide information at the molecular level before the crystallization of the nanoparticles. Hence, we conduct *in situ* HERFD-XAS and vtc-XES measurements at the Fe K-edge while synthesizing Fe_3S_4 nanocrystals to track chemical changes surrounding the Fe atoms. The reaction is performed at a heating rate of 1 °C/min rather than 10 °C/min to account for the slower acquisition time of *in situ* HERFD-XAS and vtc-XES compared to PXRD. This allows to obtain detailed information about the reaction mechanism and determination of emerging Fe compounds during heating to the reaction temperature of 180 °C.

The *in situ* HERFD-XAS data is shown in **Figure 6.3.a.** Upon heating, the absorption edge shifts to lower energies, indicating the reduction of Fe^{3+} in the precursor and a possible change in the coordinating atoms. These changes are accompanied by the pre-edge features shift to lower energies and increasing in intensity, as highlighted in **Figure 6.3.b. (I)**. After reaching 180 °C, the pre-edge reaches its highest intensity, then gradually shifts to higher energy with a decrease in intensity as the reaction progresses **(II)**. Since the pre-edge corresponds to the forbidden 1s→3d transition, high pre-edge intensities are associated with a high hybridization degree of the unoccupied 3d and 4p orbitals due to deviations from perfectly centrosymmetric coordination.

To understand the coordination geometry, RIXS analysis of the reaction solution was conducted before and after the reaction, as shown in **Figure 6.3.c-f.** Prior to the reaction, the spectral shape of the reaction solution corresponds to $Fe(acac)_3$ where the pre-edge is divided into T_{2G} and E_G contributions, as indicated by the arrows in **Figure 6.3.c.** By fitting a line scan, represented by the white dotted line, with two pseudo Voigt functions, the position of the T_{2G} and E_G contribution were determined to 7112.81 eV and 7114.41 eV, respectively. These values match well with the energy position of pre-edge peaks of Fe(acac)3, which are reported with 7112.79 eV and 7114.31 eV, respectively.[262] The fit and the deconvolution into T_{2G} and E_G contributions are shown in **Figure 6.3.d.** This splitting is due to crystal-field splitting in the octahedral coordination of Fe^{3+}, as already reported for $Fe(acac)_3$.[70] While the T_{2G} describes the transition into three d-orbitals oriented between the axes (d_{xy}, d_{xz}, d_{yz}), the E_G describes the transition into the two d-orbitals oriented along the axis ($d_{x^2-y^2}$, d_{z^2}). For an Fe2+ state of iron, the crystal field splitting is much weaker, and the pre-edge are mainly based on T_1 and T_2 d-Orbitals.[262]

However, the pre-edge feature in RIXS analysis of the final reaction product, shown in **Figure 6.3.e.**, reveals a splitting into T_{2G} and E_G contributions based on the remainder in octahedral coordination in Fe_3S_4. Since the RIXS analysis was performed on the reaction solution, it may include unreacted contributions of other components, which could influence the shape of the pre-edge. Therefore, the peak positions and relative intensities of each contribution to the pre-edge in the reaction product were discussed later with the result of the MCR-ALS analysis.

Table 6.1: Pre-edge analysis of the reaction solution before and after the reaction to Fe_3S_4.

	Ox. state	Centroid	Peak 1	Peak 2
Before reaction	Fe^{3+}	7113.24	7112.81	7114.41
After reaction	Fe^{3+}/Fe^{2+}	7112.27	7111.9	7112.93

The presence of an intermediate during this reaction are suggested by an rise in intensity of the pre-edge during the reaction when reaching the final reaction temperature, as shown in **Figure 6.3.b**., corresponds to the crystalline intermediate FeS, also identified by PXRD, where Fe is solely tetrahedrally coordinated. The tetrahedral coordination in FeS leads to the absence of Eg contributions to the pre-edge, as discussed later in **Figure 6.5.c.**

To perform a RIXS analysis of FeS, a synthesis of Fe_xS_y was performed, heating $Fe(acac)_3$ with oleylamine and elemental sulfur dissolved in toluene to 100°C. This synthesis is discussed in **Chapter 8.3.1.**

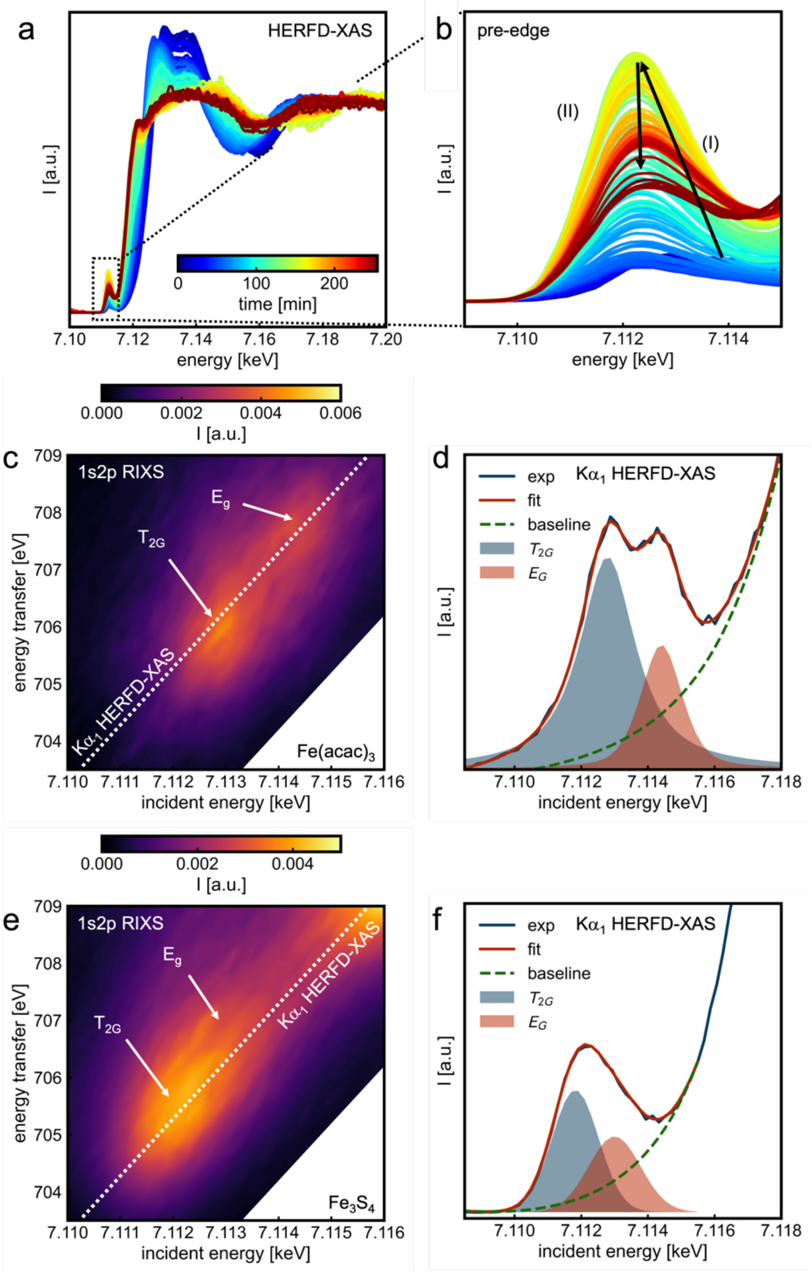

Figure 6.3: *In situ* HERFD-XAS analysis of the Fe_3S_4 synthesis at 180°C and RIXS analysis of the reaction solutions. (a) *In situ* HERFD-XAS data during the synthesis of Fe_3S_4. **(b)** Pre-edge analysis indicates the change in coordination geometry from octahedral to tetrahedral (I) and from tetrahedral to partly octahedral (II). RIXS analysis of the reaction solution before **(c)** and after the reaction **(e)** showed a crystal-field splitting of *d*-orbitals into T_{2G} and E_G in the octahedral coordination of $Fe(acac)_3$ and Fe_3S_4, respectively. Fitting the $K\alpha_1$ HERFD-XAS cuts (dashed, white lines) of $Fe(acac)_3$ **(d)** and Fe_3S_4 **(f)** show the T_{2G} and E_G orbital contributions.

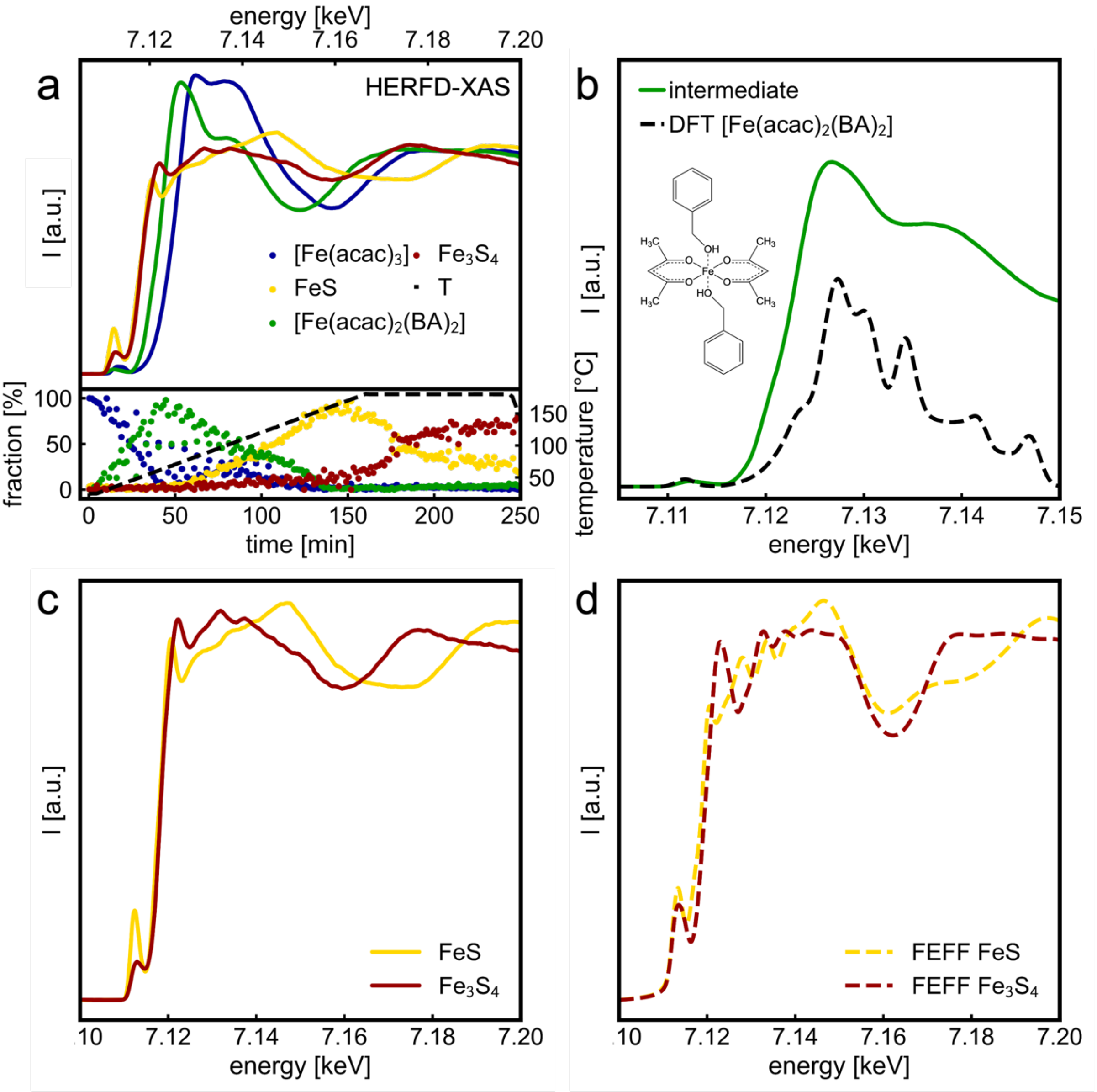

Figure 6.4: MCR-ALS Component analysis of *in situ* HERFD-XAS data of the Fe_3S_4 synthesis at 180°C. MCR-ALS component analysis of the HERFD-XAS data (a) recovers four components with their related concentration profile during the reaction. (b) The spectra of the first intermediate (green line) are in good agreement with a TD-DFT calculated spectra of a[$Fe(acac)_2(BA)_2$] complex (black, dashed line). The [$Fe(acac)_2(BA)_2$] complex is shown as an inset. The recovered spectra of the second intermediate (yellow line) and the final product (red line) (c) agree with the calculated spectra (d) of FeS (yellow, dashed line) and Fe_3S_4 (red, dashed line) by FEFF.

To characterize individual contributions in the *in situ* HERFD-XAS data, we performed MCR-ALS as a component analysis, shown in **Figure 6.4.** MCR-ALS analysis allows us to identify four independent components in our reaction, their recovered spectra and their relative concentration over reaction time. Details about the MCR-ALS analysis are shown in **Figure 8.3.2.7.** and in **Table 8.3.2.2.**

The starting component, the blue trace in **Figure 6.4.a**, matches the reference spectrum of $Fe(acac)_3$ as a pellet with an edge position at 7127 eV. This indicates that no significant changes occur to the precursor when dissolved with thioacetamide in benzyl alcohol, as shown in **Figure 8.3.2.8.**

In the first recovered intermediate in the reaction (shown in green), the edge position at 7123.2 eV indicates the presence of Fe^{2+}. However, the edge position is not at low energies as in the last two compounds, which are likely the Fe_xS_y phases identified by *in situ* PXRD. This observation suggests the coordination around Fe does not contain sulfur in the first coordination sphere. To uncover the nature of this component, we simulate theoretical XANES spectra using ORCA DFT. The experimental HERFD-XAS of this intermediate are compared to the calculated spectra in **Figure 6.4.b.** TD-DFT calculations on different possible Fe^{2+} and Fe^{3+} complexes were performed and compared with the experimental data, shown in **Figure 8.3.2.9.-11.** The observed spectral shape of the HERFD-XAS can be exclusively reproduced by a $[Fe(acac)_2(BA)_2]$ complex. Therefore, we propose that the solvent BA also works as a reducing agent at slightly elevated temperatures by replacing one acetylacetonate group with two BA, forming an intermediate $[Fe(acac)_2(BA)_2]$ complex.

In a similar system in benzyl alcohol, we previously identified an octahedrally coordinated $Co(acac)_2$ with two solvent molecules as an intermediate species.[9] The spectral features of the second compound of our reaction agreed well with the theoretical spectra of $Fe(acac)_2$ coordinated with benzyl alcohol.

At the end of the reaction, PXRD pointed out the existence of Fe_3S_4 nanocrystals. Therefore, we can assign the last recovered component as Fe_3S_4. The third and fourth compounds have similar spectral features, with E_0 of 7117.8 eV for FeS and 7118.8 eV for Fe_3S_4. Both recovered spectra in **Figure 6.4.c.** can be reproduced by FEFF calculations, as shown in **Figure 6.4.d.** Details about the FEFF calculation are shown in **Table 8.3.2.3.**

To verify the coordination in each recovered intermediate, the pre-edges of each intermediate were fitted with two pseudo Voigt functions to deconvolute the pre-edge into individual contributions, as shown in **Figure 6.5.**

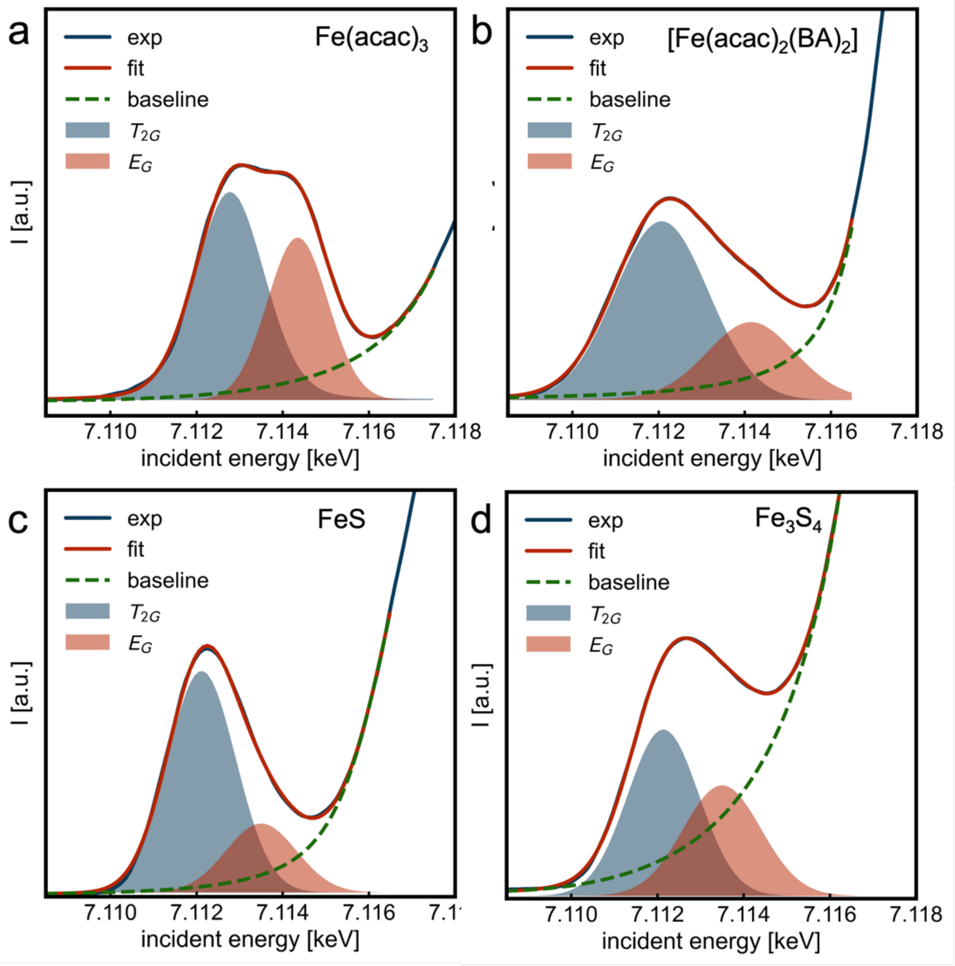

Figure 6.5: Pre-edge analysis of recovered compounds by MCR-ALS. Pre-Edge of $Fe(acac)_3$ (a) $[Fe(acac)_2(BA)_2]$ (b), FeS (c) and Fe_3S_4 (d) fitted with pseudo Voigt-functions which simulate the orbital contributions of *d*-Orbitals (blue/red) to the pre-edges. The pseudo Voigt functions, added to a baseline (dashed green), are shown as 'fit' (red line).

Table 6.2: Pre-edge analysis of MCR-ALS recovered compounds.

	Oxidation state	Coordination number	Centroid	Peak 1	Peak 2	ΔE
$Fe(acac)_3$	Fe^{3+}	6	7113.38	7112.78	7114.34	1.6 eV
$Fe(acac)_2BA_2$	Fe^{2+}	6	7112.70	7112.07	7114.14	2.1 eV
FeS	Fe^{2+}	4	7112.45	7112.11	7113.50	1.4 eV
Fe_3S_4	Fe^{3+}/Fe^{2+}	6/4	7112.98	7112.30	7114.00	1.7 eV

In general, the position of the pre-edge feature (centroid position) gives rise to the oxidation state of iron, while the energy difference between individual peak contributions directly correlates to the crystal field splitting. A large energy difference implies a strong crystal field splitting, which suggests octahedral coordination, while a smaller energy difference implies weaker crystal field splitting, for example, in tetrahedral geometry. The intensity of the pre-edge contribution directly correlates with the density of d-Orbitals at the desired energy. As described above in the RIXS analysis, the peak positions of $Fe(acac)_3$ are in good agreement with the literature. The centroid peak of the first intermediate, $[Fe(acac)_2(BA)_2]$, is shifted to lower energies by 0.68 eV compared to $Fe(acac)_3$, which suggests a change in oxidation state from Fe^{3+} to Fe^{2+}. The energy difference between the two main contributions of the pre-edge is 2.1 eV, which is quite significant, indicating strong crystal field splitting and an octahedral coordination of Fe^{2+}. The energy differences for other octahedral Fe^{2+} complexes, such as $FeCl_2$,[263] FeF_2,[264] $Fe(imidazole)_6$,[265, 266] or $Fe(H_2O)_6$,[267, 268] are reported[262] to be in the range of 2.1 eV to 2.4 eV, supporting the proposed formation of the $[Fe(acac)_2(BA)_2]$ complex. In the pre-edge analysis of the FeS, the centroid shifts further to lower energies by 0.25 eV, indicating a ligand exchange from Fe-O to Fe-S coordination, where the oxidation state remains Fe^{2+}. The decrease in energy difference between the two contributions to the pre-edge to 1.4 eV suggests a less pronounced decrease in coordination number from 6 to 4. The Fe_3S_4 centroid shifts back to higher energies by 0.53 eV, and the energy difference between the two pre-edge contributions increases. This suggests a partial rise in oxidation state from Fe^{2+} to a mixture of Fe^{2+} and Fe^{3+}, as well as a partial increase in coordination number from 4 to a mix between 4 and 6. This evidence that the mackinawite FeS and greigite Fe_3S_4 components, as discussed before, present different degrees of tetrahedral geometry, i.e., full *versus* one-third.

Vtc-XES analysis can provide valuable insights into the ligand identity and coordination of absorbing Fe atoms. However, due to the long acquisition times of vtc-XES, no *in situ* vtc-XES studies on Fe K-edge are reported in the literature. **Figure 6.6.a** shows the *in situ* vtc-XES analysis during the synthesis of Fe_3S_4 nanocrystals**.**

At the beginning of the reaction, the vtc-XES shows the characteristic line shape of $Fe(acac)_3$, as already described in the literature.[82] The $K\beta_2$ peak at around 7107 eV exhibits a shoulder at around 7112 eV, while the weak $K\beta_5$ at around 7102 eV induces a broad behavior of the vtc-XES spectra. The Kβ” peaks are extremely weak in intensity and are therefore not observable in the experimental vtc-XES spectra of $Fe(acac)_3$.[82] Notably, in the first 50 min of the reaction, the Kβ2 shoulder intensity decreases, while the Kβ5 and Kβ” peaks become more pronounced, as shown in **Figure 6.6.b.** The overall line shape remains quite similar since the position of the Kβ2 peak does not change in this early reaction stage. Hence, we assume that the first coordination sphere remains an octahedral coordination of Fe-O.

DFT calculations on different possible Fe^{2+} and Fe^{3+} complexes were performed and compared with the experimental data, shown in **Figure 8.3.2.9.-11.** The observed emerging transitions can be exclusively reproduced by a $[Fe(acac)_2(BA)_2]$ complex, as shown in **Figure 6.6.b.** DFT calculations can also give rise to the donor orbitals of the transitions, which allowed us to assign individual peaks in the vtc-XES to functional groups in the $[Fe(acac)_2(BA)_2]$ complex, visualized in **Figure 6.6.c.**

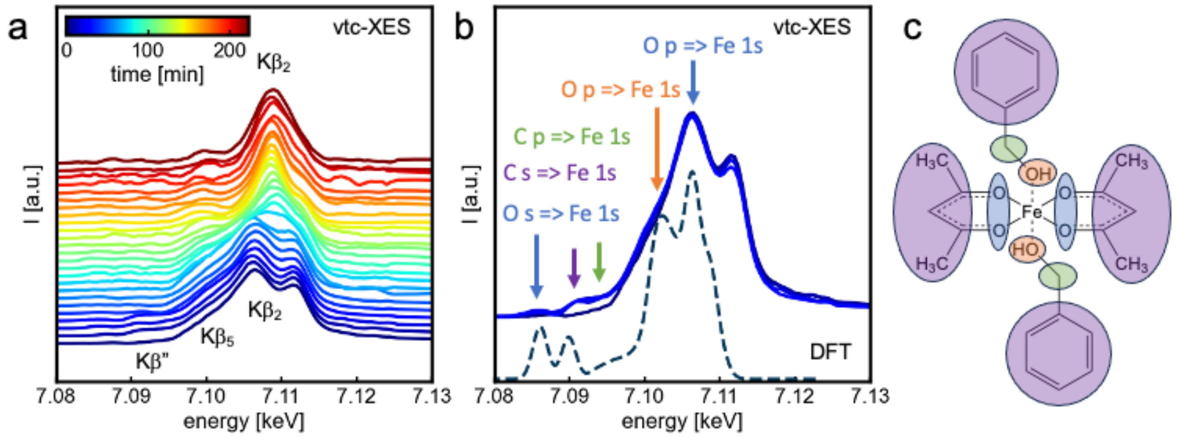

Figure 6.6: *in situ* vtc-XES analysis of the Fe_3S_4 synthesis at 180 °C. (a) waterfall plot of *in situ* time-resolved vtc-XES spectra during the synthesis of Fe_3S_4 at 180 °C. Focusing on the first 4 scans of the *in situ* dataset **(b)**, one could observe the occurrence of additional Kβ” peaks, as well as an increased intensity of the Kβ5 peak, which can be attributed to the formation of an octahedral $[Fe(acac)_2(BA)_2]$ complex (dashed line), as visualized in **(c)**. The unlabeled peak at 7.112 eV belong to $Fe(acac)_3$.

Throughout the reaction, the Kβ2 splitting disappears while the Kβ2 shifts from 7107 eV to 7109 eV, which indicates a ligand exchange from Fe-O to Fe-S coordination. At around 145 min reaction time, the experimental vtc-XES can be reproduced well by FEFF calculations of FeS, as shown in **Figure 6.7**. By the end of the reaction, the emergence of a Kβ” peak at 7092 eV became noticeable, induced by the presence of octahedral coordination in Fe_3S_4, which can be reproduced by FEFF calculations for the transition of FeS to Fe_3S_4, as shown in **Figure 6.7**. As noticeable, there is a discrepancy between the absolute energy positions of the individual peaks between experimental data (**Figure 6.7.a**) and FEFF calculations (**Figure 6.7.b**). The difficulties of reproducing experimental vtc-XES data by FEFF calculations are systematically described, also with the example of FeS, in the literature.[192]

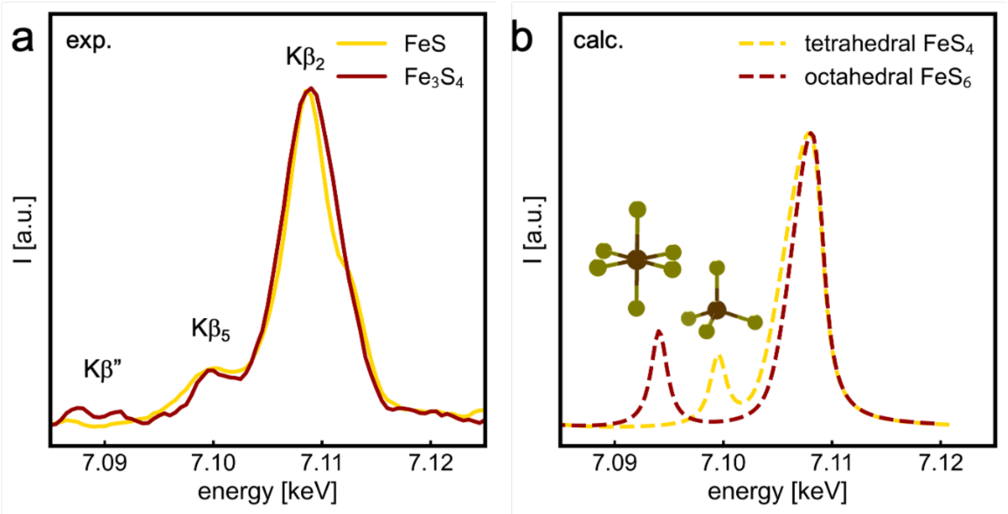

Figure 6.7: vtc-XES analysis of FeS and Fe_3S_4. (a) Experimental vtc-XES of FeS (145 min reaction time) and Fe_3S_4 (end of the reaction) show differences in the Kβ" intensity, related to the presence of octahedral-coordinated Fe in Fe_3S_4. **(b)** FEFF calculations of tetrahedral-coordinated FeS and octahedral-coordinated FeS in Fe_3S_4, predict the emergence of a Kβ" peak in Fe_3S_4.

Overall, combining *in situ* HERFD-XAS and vtc-XES analysis resolves the chemical reactions during the synthesis of Fe_3S_4 nanocrystals and proposes a reaction mechanism that undergoes the formation of a $[Fe(acac)_2(BA)_2]$ complex and FeS as intermediate structures.

6.3 Conclusion

This chapter presented a synthetic route yielding phase pure Fe_3S_4 nanocrystals. We demonstrated the complementary use of *in situ* HERFD-XAS, vtc-XES, and *in situ* PXRD to characterize the formation of reaction intermediates and propose a reaction mechanism. We showed that at the beginning of the reaction, $Fe(acac)_3$ is partly reduced and coordinated by BA, forming a $[Fe(acac)_2(BA)_2]$ complex, identified by combined HERFD-XAS analysis and DFT calculations and confirmed by electronic transitions from molecular orbitals of BA to Fe 1s, recorded by *in situ* vtc-XES. The formation of Fe_3S_4 undergoes another intermediate state, the crystalline FeS phase, which could be refined with disk-like domains with 3 nm thickness and around 50 nm diameter. The FeS nanosheets convert at the reaction temperature of 180 °C to Fe_3S_4 nanocrystals, as observed by *in situ* HERFD-XAS and PXRD analysis.

In conclusion, this study provides detailed insight into the coordination chemistry and structural changes occurring during the synthesis of Fe_3S_4. In particular, the *in situ* vtc-XES analysis showcases its potential to monitor structural and electronic transitions before particle formation at elevated temperatures.

6.4 Experimental Section

Materials:

Iron acetylacetonate(III) (≥99.9% trace metals basis), and benzyl alcohol (≥ 99.0%) were purchased from Sigma-Aldrich and thioacetamide (98%) was obtained from Thermo Scientific. The chemicals were used as received without further purification.

Synthesis of the Fe_3S_4 nanocrystals:

The Fe_3S_4 nanocrystals were synthesized *via* a solvothermal approach. In separate containers, a 0.2 mol/L solution of $Fe(acac)_3$ in benzyl alcohol and a 0.6 mol/L solution of thioacetamide in benzyl alcohol were prepared. Both solutions were homogeneously mixed, and an aliquot of 200 µL was transferred to a PEEK reaction container, which was sealed and heated using our self-build *in situ* cell.[9] The solutions were heated at 180 °C under constant magnetic stirring for 60 min at a heating ramp of 10 °C/min. For comparison purposes, the reaction was also carried out at 140 °C and 160 °C.

S(T)EM images:

The scanning electron microscopy (SEM) and scanning transmission electron microscopy (STEM) images were acquired using a Regulus 8220 microscope (Hitachi High Technologies Corp., Japan) at an acceleration voltage of 30 kV.

HERFD-XANES and vtc-XES data acquisition:

The *in situ* HERFD-XAS and vtc-XES spectra were recorded at the ID26 beamline at the European Synchrotron Radiation Facility (ESRF), Grenoble, France. The HERFD-XAS were collected by measuring the intensity of the Fe K_a main line using a Ge(440) crystal in Rowland Geometry while scanning the incident energy. The position of the X-ray beam was moved on the reaction cell to minimize radiation damage. XAS spectra were acquired for 35 s with an energy range from 7.10 to 7.22 keV and a stepsize of 0.1 eV. The vtc-XES spectra were recorded using four Ge(620) crystals in Rowland geometry over a total energy range from 7.065 to 7.135 keV. To decrease the acquisition time, the spectra region from 7.082 to 7.125 keV was measured with energy steps of 0.5 eV and an acquisition time of 3 s per point, while the range from 7.065 to 7.08 keV was measured with 7 datapoints, and the range of 7.1255 to 7.135 keV was measured with 4 datapoints, both with 1s acquisition time per point. In total, the total acquisition time for one vtc-XES was 490 s including motor movements.

Vtc-XES and HERFD-XANES processing:

The HERFD-XAS and the vtc-XES data were processed using a self-written Python code. The vtc-XES data were normalized by the maximum intensity. The determination of the XAS edge position and normalization of the edge jump were performed by using the LARCH-XAFS module.[194] The spectroscopic data were treated with a Savitzky-Golay filter and further processed with the NumPy and SciPy package.[195, 196] The simulations of the XAS spectra were carried out using the FEFF09[192, 193] and ORCA 5.0.4 code.[197] The initial iron complexes for DFT optimization were built using Avogadro: an open-source molecular builder and visualization tool. Version 1.2.0. [198]

PXRD data acquisition:

PXRD measurements were carried out at beamline P21.1 of PETRA III at Deutsches Elektronen-Synchrotron (DESY), Hamburg, Germany. Diffraction patterns were collected every second at an incident X-ray energy of 101.84 keV (λ of 0.12183 Å) employing a flat panel detector XRD1621 (Perkin Elmer Inc., USA) with a pixel size of 200 × 200 μm^2 and a sample-to-detector distance (SDD) of 1.54 m. The SDD value was obtained from the calibration from the measurement of the LaB_6 powder filled in the glass reaction container of the *in situ* cell.

PXRD processing:

The 2D diffraction patterns were integrated using pyFAI, which was used for obtaining instrumental parameters, masking unwanted elements such as dead pixels, shadows from the beam stop, etc. For the background subtraction, only thioacetamide dissolved in benzyl alcohol was measured under the same conditions of the synthesis, i.e., at 180 °C at a heating rate of 10 °C/min. The data were averaged over 60 frames, yielding a time resolution of 60 s. The resulting PXRD patterns were sequentially refined using GSAS-II package,[10] starting from the PXRD pattern at the end of the reaction and moving back to earlier reaction times. The refinements were performed using the crystallographic data of cubic spinel Fe_3S_4 (*Fd-3m* (227) space group) from the Inorganic Crystal Structure Database (ICSD)-42535, and tetragonal FeS (*P4/nmm* (129) space group) ICSD-81087.

7 Conclusion and Outlook

This thesis expands the application of Zn and Fe K-edge HERFD-XAS and vtc-XES in inorganic and bioinorganic chemistry to investigate the emergence and growth of nanomaterials in solution at elevated temperatures. Complemented by total scattering methods, these techniques resolve the electronic and atomic structure formation during the synthesis of ZnS nanoparticles and nanorods, FeS nanosheets, and Fe_3S_4 nanocrystals, enabling us to puzzle the reaction mechanisms involved in these syntheses.

The integration of HERFD-XAS, vtc-XES, and DFT calculations enables the identification of successive Zn-O, Zn-N, and Zn-S ligand exchanges (Chapter 4.3.1). Our findings indicate that even at room temperature, $Zn(Ac)_2$ reacts with oleylamine to form a mixture of tetrahedral $[Zn(OA)_4]^{2+}$ and octahedral $[Zn(OA)_6]^{2+}$ complexes, which, upon the addition of sulfur, transforms into a tetrahedral $[Zn(SOA)_4]^{2+}$ complex. This eliminates the possibility of hydrogen sulfide Zn complexes forming, such as $[Zn(H_2S)_4]^{2+}$. By monitoring the *in situ* heating of the $[Zn(SOA)_4]^{2+}$ complex above 155 °C, we observe the successive nucleation and growth of sphalerite and wurtzite ZnS nanostructures. Notably, we also track the evolution of the HOMO/LUMO gap from 5.0 to 4.3 and eventually to 3.8 eV, consistent with the $[Zn(SOA)_4]^{2+}$ complex and the 2.1 nm wurtzite and sphalerite structures, respectively (Chapter 4.3.2). The structural transformation of ZnS was further examined through simultaneous *in situ* SAXS and PXRD measurements. Our observations capture the formation of wurtzite spherical ZnS particles, progressing to the transformation into sphalerite ZnS rods primarily oriented along the (111) axis (Chapter 4.3.3). The shape, size, and band gap energy of the nanoparticles were validated through ex-situ HRTEM and UV-vis spectroscopy of powder samples.

Furthermore, this thesis presented a two-phase synthetic route yielding sphalerite ZnS NPs at the water-toluene interphase. We showed that Zn^{2+} species diffuse from the water to the toluene phase through an equilibrium involving a $[Zn(H_2O)_6]^{2+}$ and a $[Zn(OA)_6]^{2+}$ complexes forming in water and in toluene, respectively. The *in situ* studies reveal a ligand exchange process where the octahedral $[Zn(OA)_6]^{2+}$ complex evolves into a tetrahedral $[Zn(RS)_4]^{2+}$ complex at 60°C. This complex subsequently condenses to form Zn–S–Zn bonds, leading to ZnS nuclei above 80°C, which then grow into crystalline sphalerite ZnS NPs above 100°C. In conclusion, this study provides detailed insight into the coordination chemistry and the structural changes occurring during the synthesis of ZnS NP in a two-phase system (Chapter 5.3).

This thesis demonstrated the versatility of *in situ* vtc-XES and HERFD-XAS studies by preliminary analysis a synthetic route yielding phase pure Fe_3S_4 nanocrystals (Chapter 6). We showed that at the beginning of the reaction, $Fe(acac)_3$ is partly reduced and coordinated by BA, forming a $[Fe(acac)_2(BA)_2]$ complex, identified by combined HERFD-XAS analysis and DFT calculations and confirmed by electronic transitions from molecular orbitals of BA to Fe 1s, recorded by *in situ* vtc-XES. The formation of Fe_3S_4 undergoes another intermediate state, the crystalline FeS phase, which could be refined by simulating disk-like domains with 3nm thickness and around 50 nm diameter. The FeS nanosheets convert at the reaction temperature of 180°C to Fe_3S_4 nanocrystals, as observed by *in situ* HERFD-XAS and PXRD analysis. To characterize the change in morphology, the presented data can be complemented in future by *in situ* SAXS or ptychography analysis, to understand the formation of the FeS sheets and there transformation into Fe_3S_4 platelet like structure.

In conclusion, this thesis provides a detailed insight into the coordination chemistry and structural changes during the synthesis of ZnS and Fe_xS_y nanomaterials. In particular, the *in situ* vtc-XES and HERFD-XAS analysis showcase its potential to monitor structural and electronic transitions before and during particle nucleation and growth at elevated temperatures without interfering with electronic transitions of organic compounds. This approach holds promise for studying other materials with high energy and small band gaps or in reaction environments where optical spectroscopy is limited and elemental specificity is crucial for analysis in the future. Complemented analysis by means of *in situ* PXRD, PDF, and SAXS enables scientists to correlate the orbital composition of materials with their atomic structure, providing essential information for designing nanomaterials in the future.

8 Appendix

8.1 Supporting Information: Utilizing high X-ray energy photon-in photon-out spectroscopies and X-ray scattering to experimentally assess the emergence of electronic- and atomic structure of ZnS nanorods

DFT calculations of vtc-XES and XAS spectra:

The energy positions of the $K\beta_{2,5}$ and white line, as well as the white line intensity in the simulations slightly differ from the experimental data, showing a stronger change than one could observe in the experimental data when comparing the $[Zn(OA)_6]^{2+}$ and $[Zn(SOA)_4]^{2+}$ complexes. This might be caused by inaccuracies in the DFT calculations of those charged complexes. All calculated spectra are redshifted by 18.2 eV for XAS and 14.8 eV for vtc-XES to correct the mismatch between calculations and experimental data.

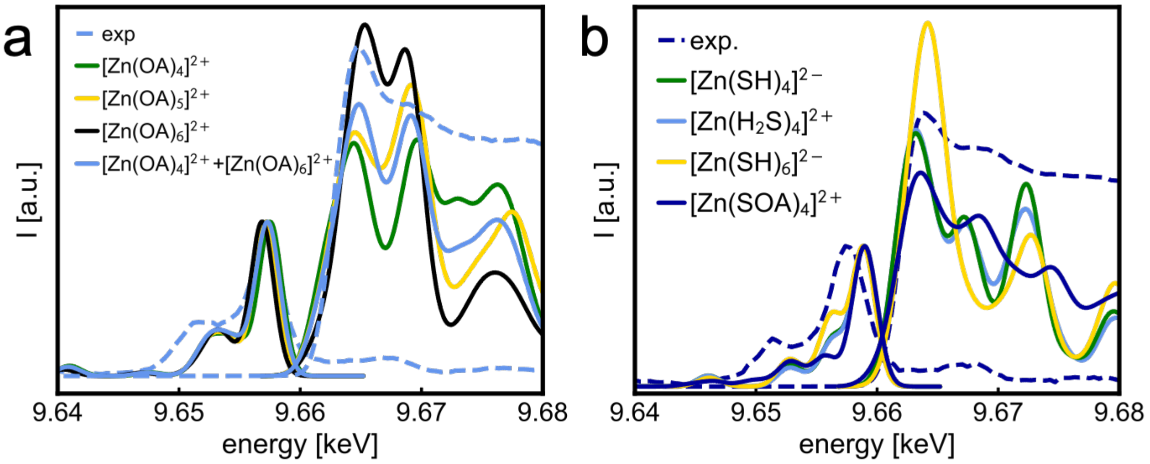

Figure 8.1.1: DFT calculations of different Zn species. Additional calculations of other coordination numbers and chemical environments for **(a)** $[Zn(OA)_4]^{2+}$, $Zn(OA)_5]^{2+}$ and $[Zn(OA)_6]^{2+}$ compared with the mixed tetrahedral $[Zn(OA)_4]^{2+}$ (60%) and octahedral $[Zn(OA)_6]^{2+}$ (40%) complexes and **(b)** $[Zn(SH)_4]^{2-}$, $[Zn(H_2S)_4]^{2+}$, $[Zn(SH)_6]^{2-}$ and $[Zn(SOA)_4]^{2+}$**.** Some complexes such as $[Zn(SOA)_5]^{2+}$, as well as a $[Zn(SOA)_6]^{2+}$ complex, are not compared in this Figure since the molecules explode during geometrical optimization which indicates the instability of those complexes.

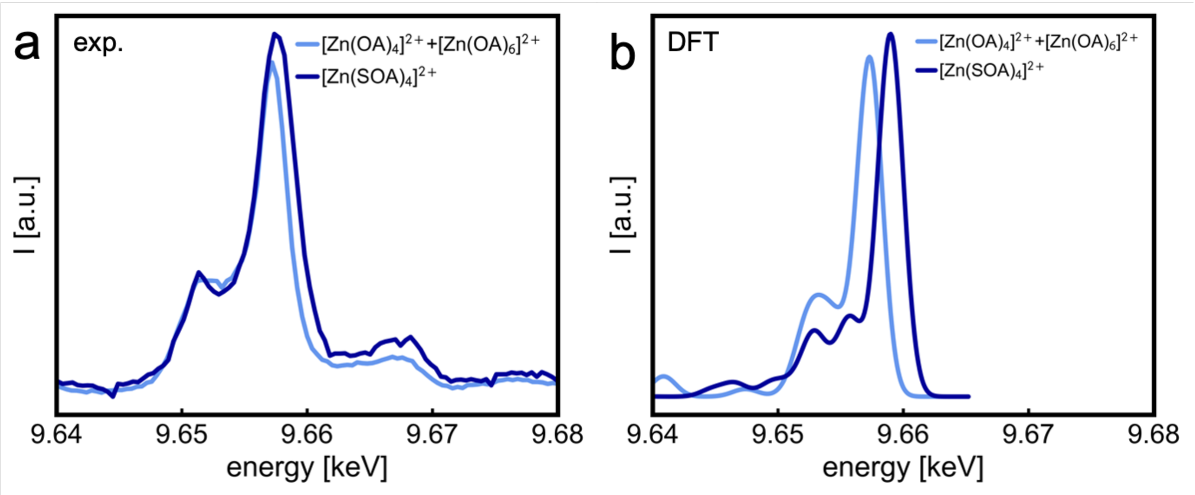

Figure 8.1.2: vtc-XES analysis using area normalization. Comparing experimental vtc-XES (**a**) with calculated (**b**) spectra of $[Zn(OA)_4]^{2+}$ and $[Zn(OA)_6]^{2+}$ 60:40 ratio (light blue) and $[Zn(SOA)_4]^{2+}$ (dark blue) complexes, experimental data were normalized by the area. Calculated data were not normalized. The expected trends in intensity and energy position were reproduced in the simulations.

However, this normalization procedure does not work at all for the vtc-XES *in situ* dataset, since short acquisition times decrease the S/N ratio and complicated the baseline fitting, resulting glitches have a higher impact on the total area. Therefore, the intensity of the vtc-XES shows an unphysical intensity difference between individual scans, as shown in **Figure 8.1.24**.

In **Figure 8.1.3**, we show ORCA calculations of a molecular unit of $Zn(Ac)_2$, cut out of a $Zn(Ac)_2$ crystal with the monoclinic phase. The energy positions of the whiteline in the HERFD-XAS and the $K\beta_2$ peak are corroborated. Furthermore, the relative intensity between the $K\beta_5$ and $K\beta_2$ peaks aligns with the experimental data. However, the $K\beta_5$ peak exhibits multiple contributions, where the transition at lower energy (primarily based on dipole transitions from O p => Zn 1s, as shown in **Figure 8.1.5**) is underrepresented in the experimental data. This contributes to the broad nature of the $K\beta_5$ peak, as noted in the first revision comment. A possible reason for overestimating this transition is that, in reality, the oxygen in the third coordination sphere of Zn^{2+} is bonded to another Zn^{2+} ion, which is not accounted for in this ORCA calculation. The lineshape of the edge and post-edge features in the simulated HERFD-XAS spectra does not match the experimental data, which is anticipated when comparing a molecular unit with a macroscopic crystal.

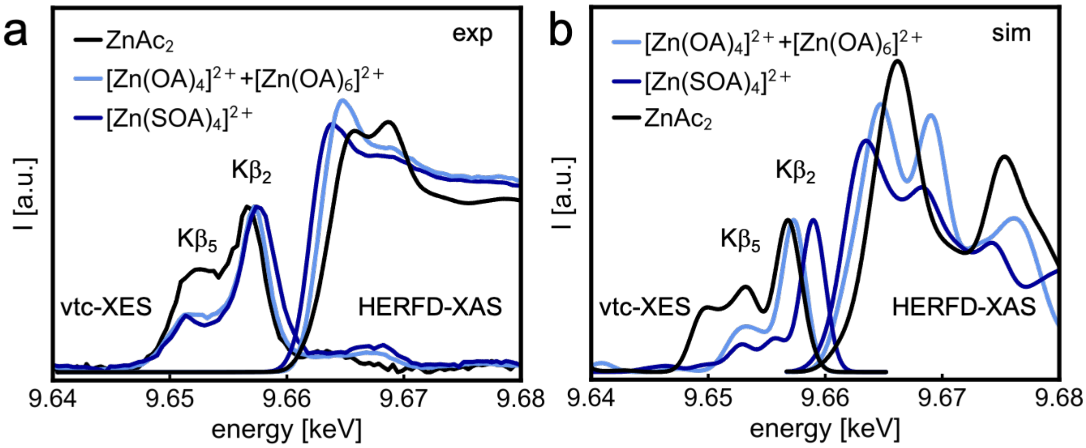

Figure 8.1.3: Experimental (**a**), and simulated (**b**) vtc-XES and HERFD-XAS data of $Zn(Ac)_2$ (black), the $[Zn(OA)_4]^{2+}$ + $[Zn(OA)_6]^{2+}$ (light blue), and $[Zn(OAS)_4]^{2+}$ (dark blue) complexes. The energy shifts of the Kβ2, as well as the relative intensity between the Kβ2 and Kβ5 peaks, are also present in the ORCA calculations. The ORCA calculations reproduce the shift in the whiteline from $Zn(Ac)_2$ to $[Zn(OA)_4]^{2+}$ + $[Zn(OA)_6]^{2+}$, and to $[Zn(OAS)_4]^{2+}$.

To match the simulation with the experimental data, we compared intensities and energy positions of the vtc-XES and HERFD-XAS by different mixing fractions between $[Zn(OA)_4]^{2+}$ and $[Zn(OA)_6]^{2+}$. Those behaviors can be exclusively reproduced by the fractions used 60% $[Zn(OA)_4]^{2+}$ and 40% $[Zn(OA)_6]^{2+}$, which are shown in **Figure 8.1.4**.

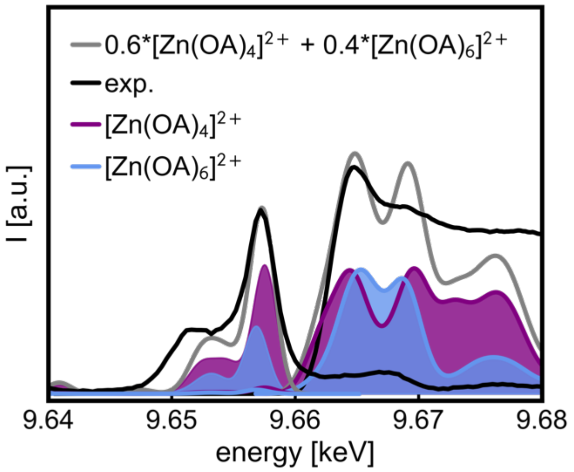

Figure 8.1.4: Comparing experimental data of $Zn(Ac)_2$ in oleylamine with simulated vtc-XES and HERFD-XAS data of a linear combination of 60% $[Zn(OA)_4]^{2+}$ and 40% $[Zn(OA)_6]^{2+}$ (gray), with the individual of contribution of $[Zn(OA)_4]^{2+}$ (purple) and $[Zn(OA)_6]^{2+}$ (blue) to the mixture. The intensity of the vtc-XES and HERFD-XAS simulations were calibrated by comparing simulations of $[Zn(SOA)_4]^{2+}$ with experimental data. The energy position and the

intensity of the Kβ_2 peak, as well as the energy position of HERFD-XAS peaks, can be exclusively reproduced by the used fractions of 60% $[Zn(OA)_4]^{2+}$ and 40% $[Zn(OA)_6]^{2+}$.

To evaluate differences between simulated and experimental data, the transitions reflected in the simulated vtc-XES spectra were analyzed in the following **Figure 8.1.5**. Additionally, we visualized the corresponding donor orbitals of the transitions with the strongest contributions.

As shown in **Figure 8.1.5**, by comparing the Kβ_5 spectra of $[Zn(SOA)_4]^{2+}$ with those of $[Zn(OA)_4]^{2+}$ and $[Zn(OA)_6]^{2+}$, it becomes apparent that the transition from C p => Zn 1s is not well-represented in the $[Zn(OA)_4]^{2+}$ and $[Zn(OA)_6]^{2+}$ spectra. This might result from the approximation of using a calculated methylamine group instead of the actual oleylamine ligand. The different lengths of the carbon chain might lead to varied donating behaviors of the C p-orbitals. Therefore, the simulated Kβ_2 peaks in $[Zn(OA)_4]^{2+}$ and $[Zn(OA)_6]^{2+}$ appear to be narrower than those in the experimental data

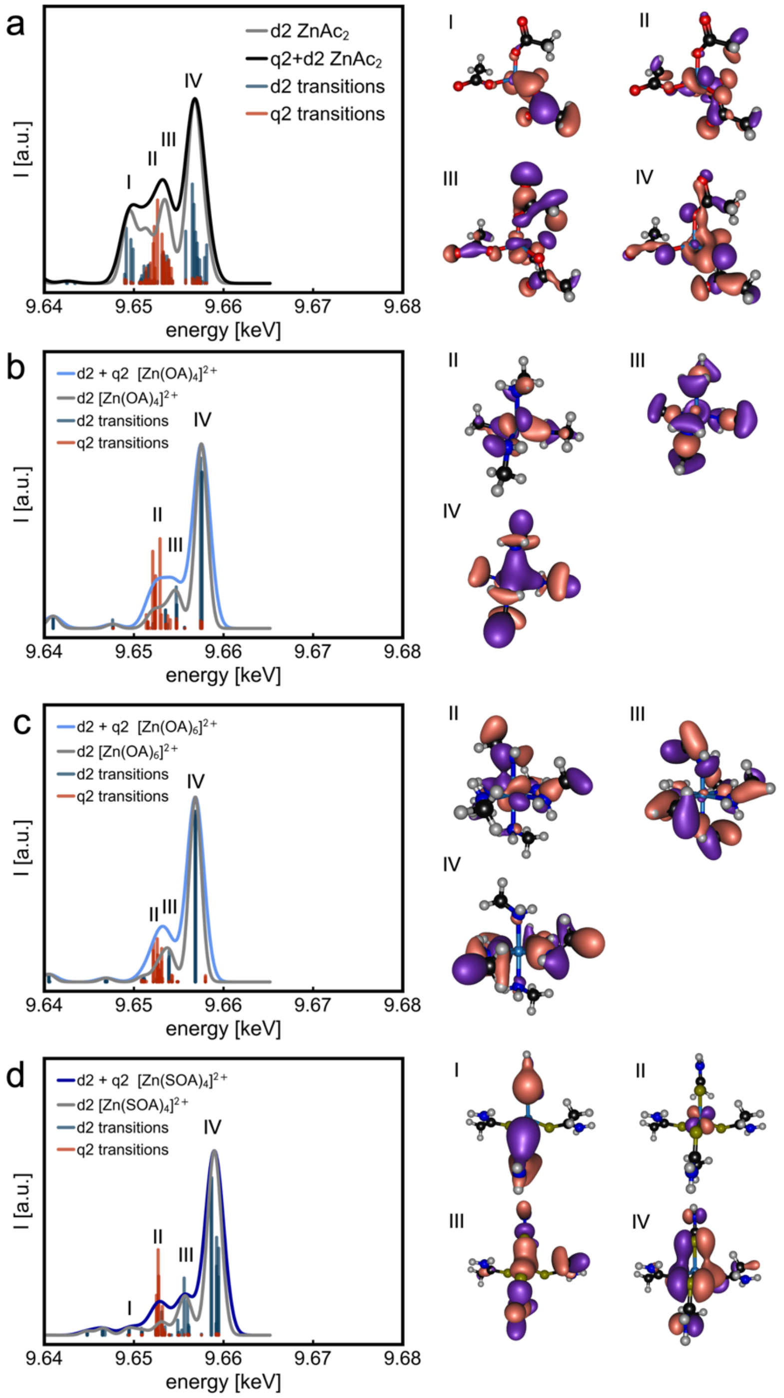

peak	transition	donor orbitals
I	O p => Zn 1s	O px py pz (MO38)
II	Zn d => Zn 1s	Zn dz^2 dx^2y^2 (MO57)
III	O p => Zn 1s	Zn 6px 6py 6pz O px py pz (MO58)
IV	Zn 6p => Zn 1s	Zn 6px 6py 6pz O px py pz (MO67)

peak	transition	donor orbitals
II	Zn d => Zn 1s	Zn dz^2 dxy N px py pz (MO31)
III	N p => Zn 1s	Zn dz^2 dxy N px py pz (MO39)
IV	Zn 6p => Zn 1s	Zn dz^2 dxy 6px 6py 6pz (MO47)

peak	transition	donor orbitals
II	Zn d => Zn 1s	Zn dyz dxy dx^2y^2 N px pz (MO42)
III	N p => Zn 1s	N px py pz (MO52)
IV	Zn 6p => Zn 1s	Zn 6py 6pz N py (MO65)

peak	transition	donor orbitals
I	C p => Zn 1s	C px (MO52)
II	Zn d => Zn 1s	Zn dx^2y^2 (MO66)
III	S p => Zn 1s	S px py (MO75)
IV	Zn 6p => Zn 1s	Zn 6py S py pz (MO88)

Figure 8.1.5: (left) Calculated spectra and the dipole and quadrupole contributions for (**a**) $Zn(Ac)_2$, (**b**) $[Zn(OA)_4]^{2+}$, (**c**) $[Zn(OA)_6]^{2+}$, and (**d**) $[Zn(SOA)_4]^{2+}$. The most intense contributions to the vtc-XES spectra are visualized (middle). The transitions responsible for the marked peaks in the vtc-XES spectra are listed in a table (right), along with the donor orbitals of the most intense transitions. A detailed list of all transitions, their intensities, and all corresponding donor orbitals is available in the .out files in the repository, as described earlier and in the chapter.

All the structural optimization, as well as the calculations of the vtc-XES (left) and TD-DFT for XAS calculations (right), were performed with the following example ORCA .inp parameters, adapted from *Stepanic et. all*:[80]

```
!RKS B3LYP TightOpt TightSCF ZORA-def2-TZVP
ZORA
!FREQ Largeprint Printbasis
%maxcore 4000
%xes
CoreOrb 0
OrbOp 0
end
* xyz 2 1
…
```

```
!RKS B3LYP TightSCF ZORA-def2-TZVP D3BJ
RIJCOSX ZORA
!Normalprint MOREAD
%maxcore 4000
%moinp "name.gbw"
%tddft
orbwin[0]= 0,0,-1,-1 doquad true
nroots 300
maxdim 50
end

* xyz 2 1
…
```

A detailed description of the used functionals and parameters can be found in the ORCA input library.[269]

To export the spectra, the resulting output files are processed with orca_mapspc.

XES: orca_mapspc name.out xesq -eV -x09000 -x110000 -n10001 -w2.25

XAS: orca_mapspc name.out absq -eV -x09000 -x110000 -n10001 -kw0.03

The spectra of vtc-XES without quadrupole transitions, shown in Figure SI2, were obtained by: orca_mapspc name.out xes -eV -x09000 -x110000 -n10001 -w2.25

The .inp Files, the optimized .xyz files of all shown complexes, and the experimental raw data are available under the following DOI: 10.25592/uhhfdm.14737

Coordination of thioamide ligands in Zn[SOA] complexes:

DFT calculations were conducted to identify the coordination of thioamide ligands in the experiment from the two possible coordinations depicted in **Figure 8.1.6**.

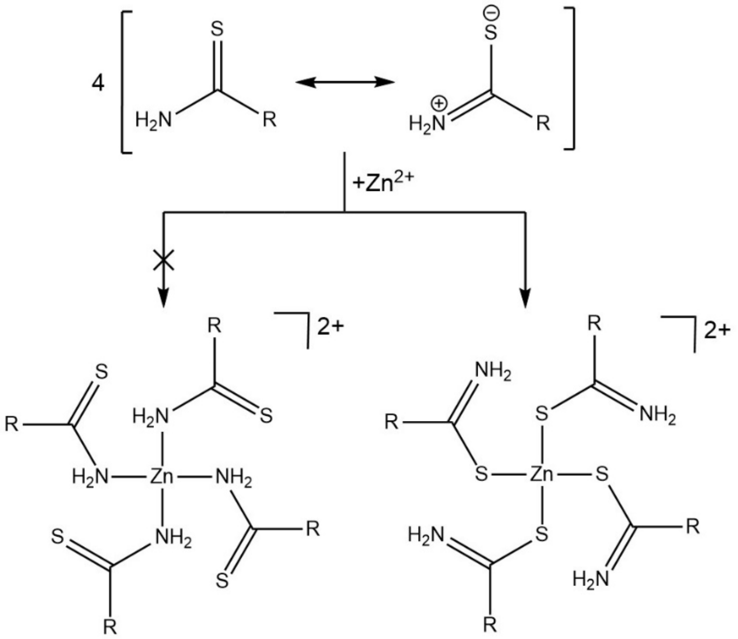

Figure 8.1.6: Illustration of Zn^{2+} coordination in the $[Zn(SOA)_4]^{2+}$ complex. DFT structural optimization reveals that the thioamide group favors the coordination via the sulfur atom.

Thioamides show two resonance structures, one neutral form and one charge-separated form with a negative charge being located on the sulfur atom. The former resonance structure favours the coordination of the thioamide groups via the nitrogen to the Zn(II) cations, while the latter resonance structure favours the coordination via sulfur. In order to see which coordination is preferred, we carried out structure optimizations for both complexes depicted in **Figure 8.1.6.** The optimization of the left and the right structures obtained the sulfur-coordinated complex regardless of the initial structure, which supports that the sulfur-coordinated complex is formed in the experiment, once the oleylamine and sulfur form a thioamide group.

NMR-analysis:

As shown in literature[15], the formation of thioamide in sulfur-amine reaction mixtures is detectable with ^{13}C NMR spectroscopy of reaction mixture aliquots. Analogously to their approach, aliquots from a reaction mixture of sulfur and oleylamine were taken at different temperatures and analyzed by ^{1}H and ^{13}C NMR spectroscopy. The ^{13}C(^{1}H)-NMR spectra are shown in **Figure 8.1.7.**

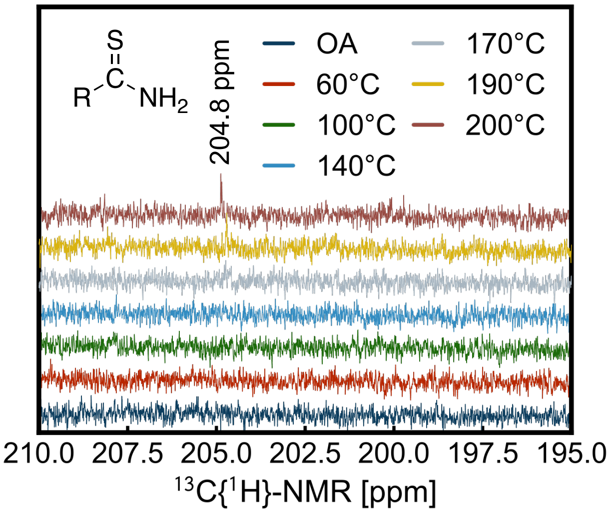

Figure 8.1.7: ***ex situ*** **NMR analysis of aliquots.** ^{13}C(^{1}H)-NMR spectra of aliquots taken from a mixture of sulfur (9.1 mmol) in oleylamine (45.5 mmol) indicating the formation of thioamide at temperatures above 170 °C. Spectra of aliquots collected at and below 170 °C and the spectrum of oleylamine in the absence of sulfur do not exhibit a signal corresponding to the thioamide group.

^{13}C(^{1}H)-NMR spectra of pure oleylamine and reaction mixtures collected at the temperature range of 60-170 °C do not exhibit signals in the downfield from 195—210 ppm. On the other hand, aliquots collected from mixtures heated to 190 °C and 200 °C exhibit a weak signal at 204.8 ppm. Such a peak is an indication of the thioamide formation, since the carbon nucleus of a thioamide functional group is expected to occur in the downfield of around 204 ppm.[15]

The aliquot collected from the reaction mixture of $Zn(Ac)_2$, sulfur and oleylamine at room temperature was measured with an increased number of scans (NS=10240) to improve the signal-to-noise ratio, which increases as the square root of the number of scans. Despite an increased number of scans, the $^{13}C(^{1}H)$-NMR spectrum (**Figure 8.1.8**) does not exhibit a signal in the range of 200—210 ppm, which could correspond to a thioamide.

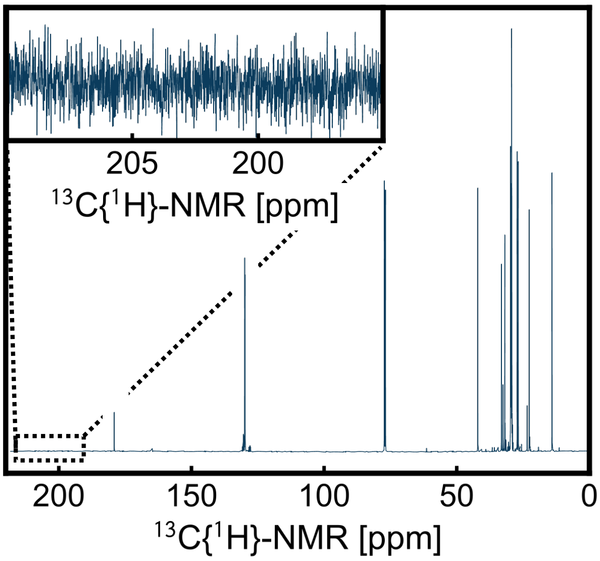

Figure 8.1.8: *ex situ* NMR analysis at room temperature. $^{13}C(^{1}H)$-NMR spectrum acquired with 10240 scans of the reaction mixture $Zn(Ac)_2$ (6.65 mmol), S (9.1 mmol) and oleylamine (45.4 mmol) at room temperature. The spectrum does not exhibit a peak above 200 ppm which could indicate the formation of a thioamide functional group.

MCR-ALS analysis:

The multivariate curve resolution-alternating least squares (MCR-ALS) method employs a constrained alternating least squares (ALS) algorithm to solve the bilinear model. The bilinear equation is expressed as follows:

$$\mathbf{D} = \mathbf{C}\mathbf{S}^{\mathbf{T}} + \mathbf{E} \quad (1)$$

where **D** represents the raw data set, **C** denotes the concentration profiles for each recovered compound, $\mathbf{S}^{\mathbf{T}}$ stands for the related pure spectra, and **E** is the matrix of residuals not accounted for by the model. The ALS algorithm operates on the principle of alternately fixing one set of variables while solving for the other. Specifically, the process begins by initializing $\mathbf{S}^{\mathbf{T}}$ and solving a linear algebra problem for **C** while keeping $\mathbf{S}^{\mathbf{T}}$ constant. Subsequently, **C** is held constant, and the system is solved for $\mathbf{S}^{\mathbf{T}}$. This cycle is repeated until convergence is achieved. Convergence is defined by the condition that, in two consecutive iterative cycles, the relative differences in the standard deviation of residuals between experimental and ALS-calculated data values are less than a pre-determined threshold. Quality assessments of a converged fit are derived from the unexplained residuals **E**, representing the disparity between the experimental data and the bilinear model, with the **lack of fit (%)** expressed as:

$$\textbf{lack of fit (\%)} = 100\sqrt{\frac{\sum_{i,j} e_{ij}^2}{\sum_{i,j} d_{ij}^2}} \quad (2)$$

where **d** denotes an element of the data matrix, and e corresponds to the respective element in the residuals matrix **E**. Furthermore, the variance $\mathbf{R}^2$ explained in the model can be estimated using:

$$\mathbf{R}^2 = \frac{\sum_{i,j} d_{ij}^2 - \sum_{i,j} e_{ij}^2}{\sum_{i,j} d_{ij}^2} \quad (3)$$

The standard deviation of the residuals $\boldsymbol{\sigma}$ is given by:

$$\sigma = \sqrt{\frac{\sum_{i,j} e_{ij}^2}{nm}} \tag{4}$$

Here, n and m denote the dimensions of the raw data matrix **D**.

Furthermore, the ALS algorithm can adhere to physically or chemically meaningful constraints, such as non-negativity or unimodality for concentration and spectra profiles, as well as closure.[176]

To conduct the MCR-ALS analysis, the XAS data were organized into a matrix, where each row corresponds to an absorption spectrum recorded *in situ*. The number of rows equals the quantity of acquired spectra, and the number of columns corresponds to the number of data points in each spectrum. Prior to implementing the ALS optimization, the determination of the number of components and initial spectra was undertaken. The selection of the number of components was based on the outcomes of Singular Value Decomposition (SVD). The computed eigenvalues from the data provide insights into the extent of variance each factor or component can elucidate. The factor associated with the highest eigenvalue exhibits the greatest variance, while the one with the second highest eigenvalue follows, and so forth. Eigenvalues below a certain threshold are indicative of noise in the data. The determined Eigenvalues in both shown datasets are plotted as Scree plot in **Figure 8.1.9** and are listed in **Table 8.1.2**.

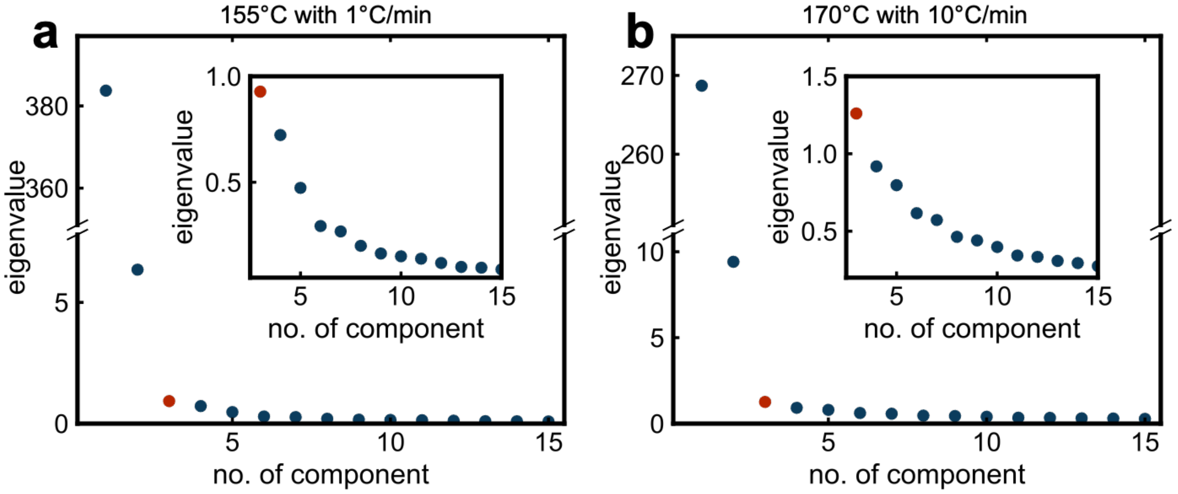

Figure 8.1.9: Eigenvalues of MCR-ALS analysis. Scree plot of eigenvalues of the ZnS reaction with reaction temperature of **(a)** 155 °C with heating rate of 1 °C/min and of **(b)** 170 °C with a heating rate of 10 °C/min. The alignment of eigenvalues of four or more components that belong to noise. The red dot marks the last used component.

Table 8.1.1: Eigenvalues determined by SVD of the MCR-ALS analysis.

Number of components	**Eigenvalues of synthesis at 155 °C – 1°C/min (Fig. SI6a)**	**Eigenvalues of synthesis at 170 °C - 10°C/min (Fig. SI6b)**
1	383.717	268.701
2	6.351	9.415
3	0.928	1.260
4	0.723	0.918
5	0.474	0.797
6	0.294	0.616

Table 8.1.2: Fitting parameters of the MCR-ALS analysis.

	Synthesis at 155 °C – 1°C/min (Fig. 2b)	**Synthesis at 170 °C - 10°C/min (Fig. SI17)**
fitting error (%)	2.505	2.360
R^2	99.937	99.944
σ	0.023	0.022

Owing to the limited solubility of $Zn(Ac)_2$ in oleylamine, the initial 22 spectra at room temperature have been excluded from the data matrix D for the experiment conducted at a reaction temperature of 155 °C and a ramping rate of 1°C/min. This exclusion is necessary because fluctuations in Zn concentrations introduce non-physical features. To facilitate the recovery process during the MCR-ALS analysis of ZnS nanocluster formation, the spectrum of ZnS nanoparticles was appended as the final spectrum.

During the MCR-ALS analysis, two to four different components were checked, and the results were investigated in detail. To discriminate meaningful analysis, we followed this selection procedure:

1. Setting the convergence criteria: We set criteria for a meaningful MCR-ALS analysis, e.g., that the concentration of individual components cannot be negative, and show unimodal behavior. Also, the addition of all concentrations at each timestep of the reaction has to be 100%. Further, the XANES spectra cannot run negative.

   a. The MCR-ALS analysis with four components does not achieve convergence with these criteria and can be excluded.
2. Of every MCR-ALS analysis that achieved a convergence (here, for two and three components) the spectral profile was checked if unphysical features might appear. (e.g. pre-edges in Zn K-Edge)
   a. For two and three components, the resulting spectral profiles did not show any unphysical behavior
3. If multiple MCR-ALS analyses achieve convergence and show physically meaningful spectral profiles, the quality of reproducing the first spectra of the reaction with the first component can give rise to the total recovering quality.
   a. The two-component MCR-ALS shows a high fitting error and cannot explain all spectral changes. As shown in the following **Figure 8.1.10**, the starting point was recovered with two components in a crude way.

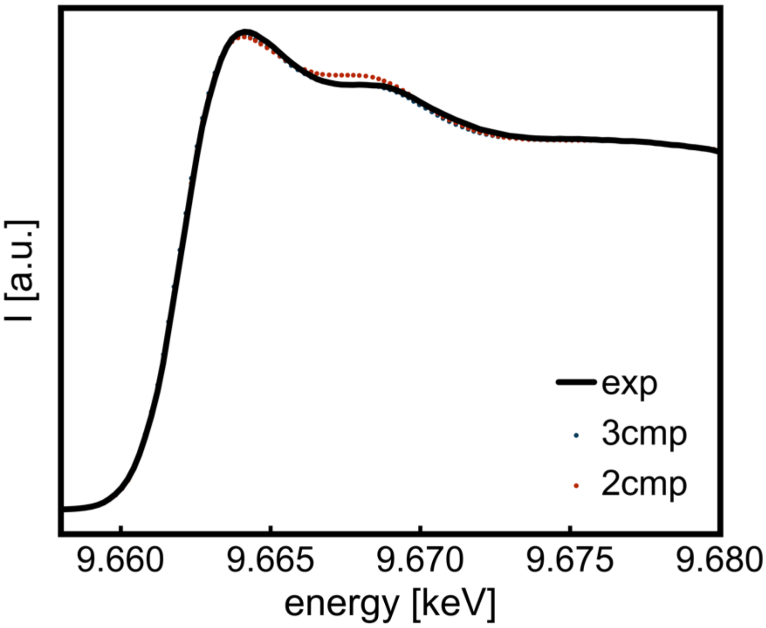

Figure 8.1.10. The first component of MCR-ALS analysis uses in total three components (blue) and two components (red). The experimental starting complex (black) was reproduced with low error by three-component analysis, while the two-component analysis crudely recovered the first experimental spectra.

Band gap analysis of HERFD-XAS/vtc-XES data:

The resonance energy is material-dependent and changes during the reaction, thus for the *in situ* studies in solution, we excite non-resonant at 9.7 keV and collect the vtc-XES spectra. We are comparing the ionized HOMO and the non-ionized LUMO to calculate the energy difference indicated in red in **Figure 4.2c**. Thus, the E_{gap} is systematically underestimated by about 1.5 eV. The difference between the minimum of the derivative of the XES data and the maximum of the derivative of the HERFD-XAS data reflects the HOMO/LUMO gap at every reaction time.

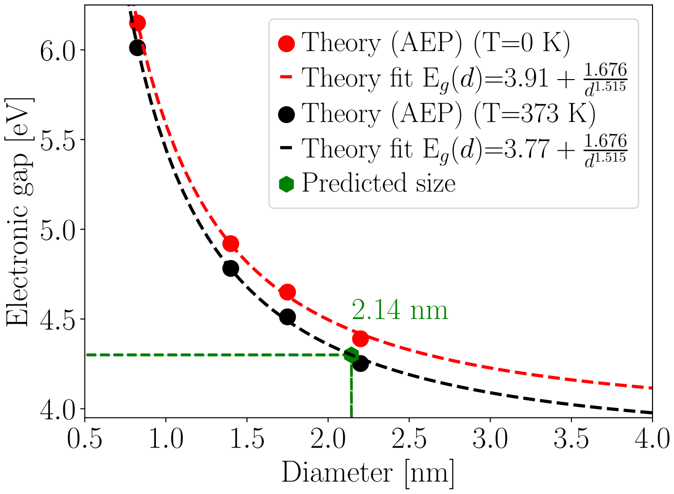

Figure 8.1.11: Electronic band gap of w-ZnS as a function of diameter. Electronic band gap of wurtzite ZnS quantum dots (QDs) as a function of diameter, calculated using atomic effective pseudopotentials (AEPs) (see text for details). The filled red (black) circles are the electronic gaps at T=0 K (372 K) and the red (black) solid line is a diameter-dependent fit. The green dot shows our measured electronic gap and the ensuing dot diameter.

We calculate the single-particle (SP) electron and hole eigenenergies and wavefunctions using atomic effective pseudopotentials (AEPs) including spin-orbit coupling effects.[180, 181] The AEPs are derived from density functional theory (DFT) calculations and subsequently corrected for the electronic band gap.[182] The quantum dots (QDs) are passivated with fractional charge non-spherical pseudo-hydrogen atoms.[183] This approach has often been used successfully in the past to calculate optical and electronic gaps.[182, 184, 185]

Since our SP calculations are performed at zero temperature, we include temperature effects *a posteriori* via an analytical expression for the temperature dependence of the experimental band gap presented in Literature:[186]

The parameters used in the equation are given as:

$$E(T) = E(0) - \frac{\alpha\Theta_\rho}{2}\left\{\frac{\rho}{2}\left(\left(\sqrt[4]{1+\frac{\pi^2}{6}\left(\frac{4T}{\rho}\right)^2+\left(\frac{4T}{\rho}\right)^4}\right)-1\right)+(1-\rho)\left[coth\left(\frac{\Theta_\rho}{2T}\right)-1\right]\right\}$$

E(0) = 3.91 eV

α = 0.548 meV/K

Θ_ρ = 350 K

ρ = 0.389

This approach leads to a 138 meV red shift of the band gap when going from zero to room temperature (373 K). This value has been subtracted from our calculated band gap. With this procedure, we obtain a QD diameter of 2.1 nm corresponding to our measured electronic gap of 4.3 eV, which is consistent with our dot size distribution.

UV-VIS analysis:

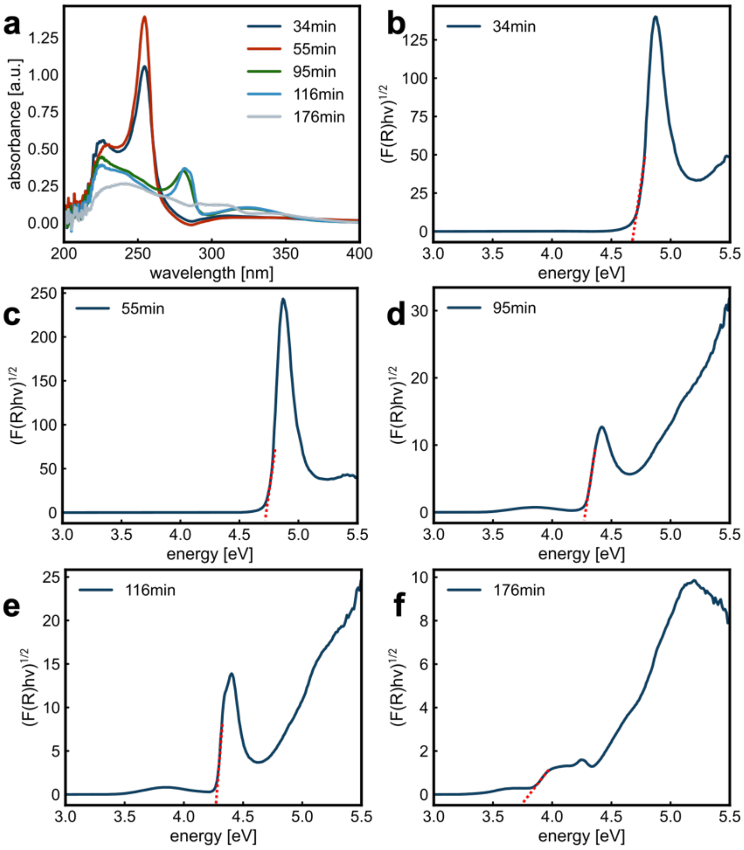

Figure 8.1.12: *ex situ* UV-VIS analysis. (a) UV-Vis spectra of the quenched reaction at various time steps. The reaction times of 34, 55, 95, 116, and 176 min correspond to the reaction temperatures of 75, 95, 135, 155 and 155 °C, respectively. **(b-f)** Tauc-Plot analysis from the UV-vis data, providing the values for the optical band gap, summarized in **Table 8.1.3** and shown in **Figure 4.2**. Since the synthesis of s-ZnS undergoes the co-preparation of w-ZnS as well as possible organic byproducts, one can observe multiple peaks in the range of 3.8 eV to 4.5 eV, especially at 116min and 176 min.

The linear fit has the general equation of y = ax+b. The values for the intercept and slope, and the calculated band gap for each reaction step, are summarized in **Table 8.1.3**.

Table 8.1.3: Values of fitting the Tauc-plots from UV-Vis data and the corresponding band gap.

	34 min - 75 °C	**55 min - 95 °C**	**95 min - 135 °C**	**116 min - 155 °C**	**176 min - 155 °C**
a	-1170.4 ± 123	-1841 ± 392	-413.18 ± 22.7	-638.38 ± 55	-24.84 ± 0.51
b	251.21 ± 26.2	392.49 ± 47.3	96.685 ± 5.27	149.51 ± 12.8	6.54 ± 0.13
ΔE	4.66 eV	4.69 eV	4.28 eV	4.27 eV	3.79 eV

SAXS background processing:

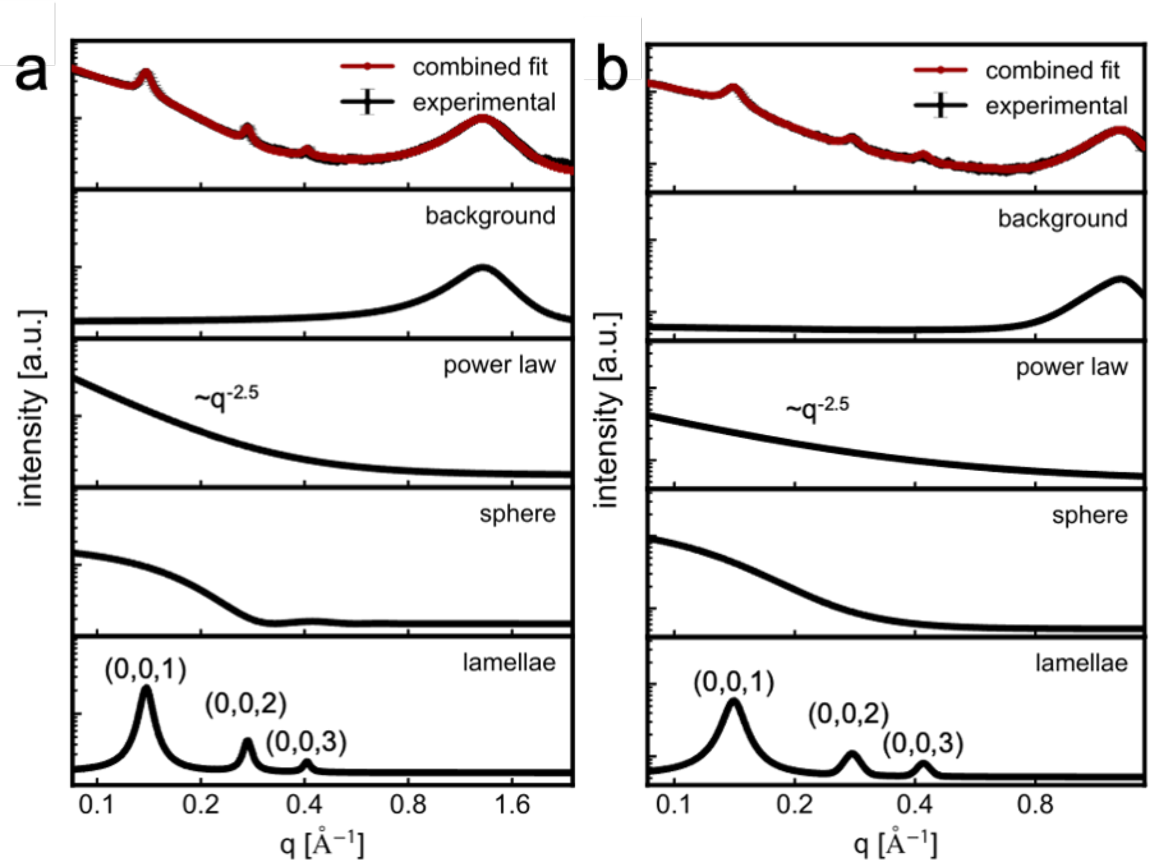

Figure 8.1.13: SAXS background subtraction in the synthesis at (a) 155°C with 1°C/min ramping rate and (b) 170°C and 10°C/min ramping rate. SAXS fitting of a representative scan (top), exhibiting the individual contributions (background, power law that is treated as part of the background, sphere to represent the NP and the lamellae formed by the solvent) The lamellae induce a sharp peak with 2-5 multiplets which is observed in the SAXS signal. This behavior is well known from lipid bilayers and has been reported for thio-derivatives of oleylamine, with a bilayer distance around 38 Å.[155] Nevertheless, the lamellae occur only during the synthesis of ZnS NC, as shown in **Figure 8.1.14**.

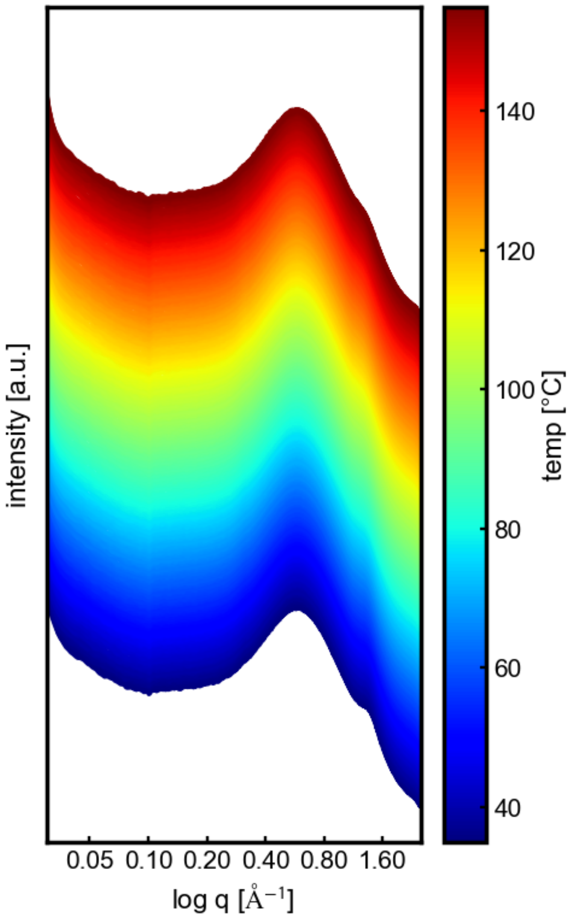

Figure 8.1.14: Control *in situ* SAXS data of oleylamine and sulfur solution heated to 155°C with 1°C/min ramping rate. Unlike in **Figure 4.3a** where Zn(ac)$_2$ is present in solution, the lamellas do not form.

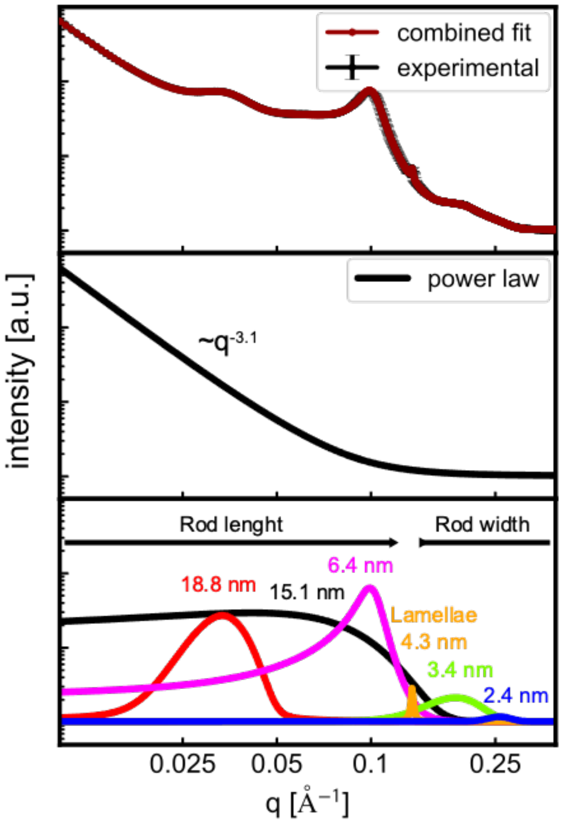

Figure 8.1.15: SAXS fit of the reaction mixture after cooling down. Measured with a lower q-min to visualize the limitations of the used *in situ* SAXS dataset. (top) deconvoluted into the power law (middle) and individual size distributions (bottom) of the ZnS NP. All larger sizes with contributions lower than 0.08 Å^{-1} are not accessible by *in situ* SAXS. The high energy is mandatory for achieving a high q_{max} in the SAXS/WAXS combined detector setup at P07.[116] The combined SAXS/WAXS signal is shown in **Figure 8.1.16**.

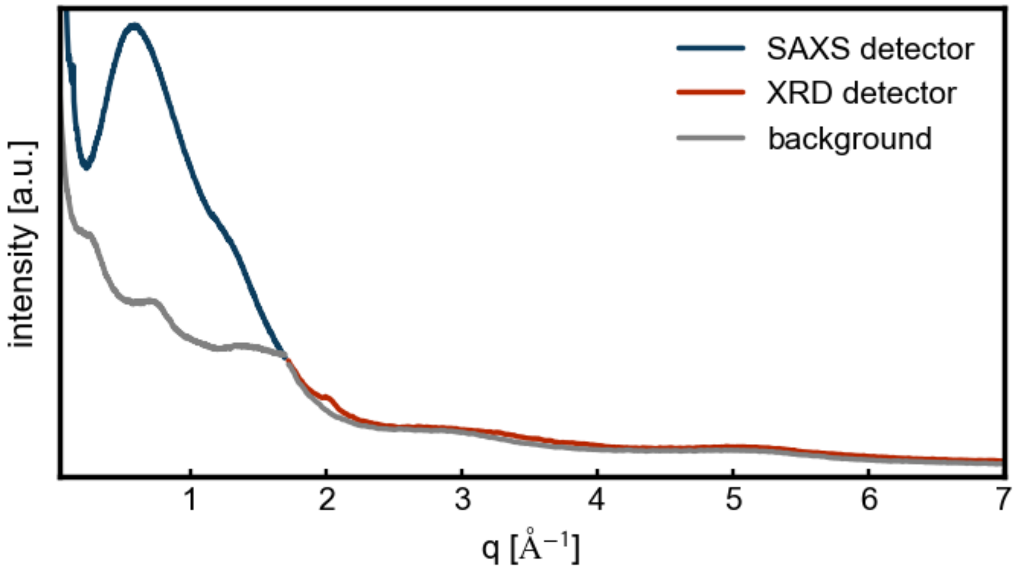

Figure 8.1.16: Simultaneous acquired SAXS and PXRD data. Simultaneous acquired SAXS (blue) and PXRD (red) data of the reaction solution after 250 min of the reaction, with the background of oleylamine and sulfur (gray) at 155°C.

Ex situ characterization of s-ZnS:

The size of the s-ZnS nanorods is described by STEM analysis as 3.1 ± 1.4 nm width and 10.8 ± 2.8 nm length, while the domain size, calculated by Rietveld analysis of PXRD data, reveals a domain size of 3nm x 6nm, as shown in **Figure 8.1.17**. Consequently, the nanorods mostly consist of multiple crystalline domains, attached along the s(111) axis.

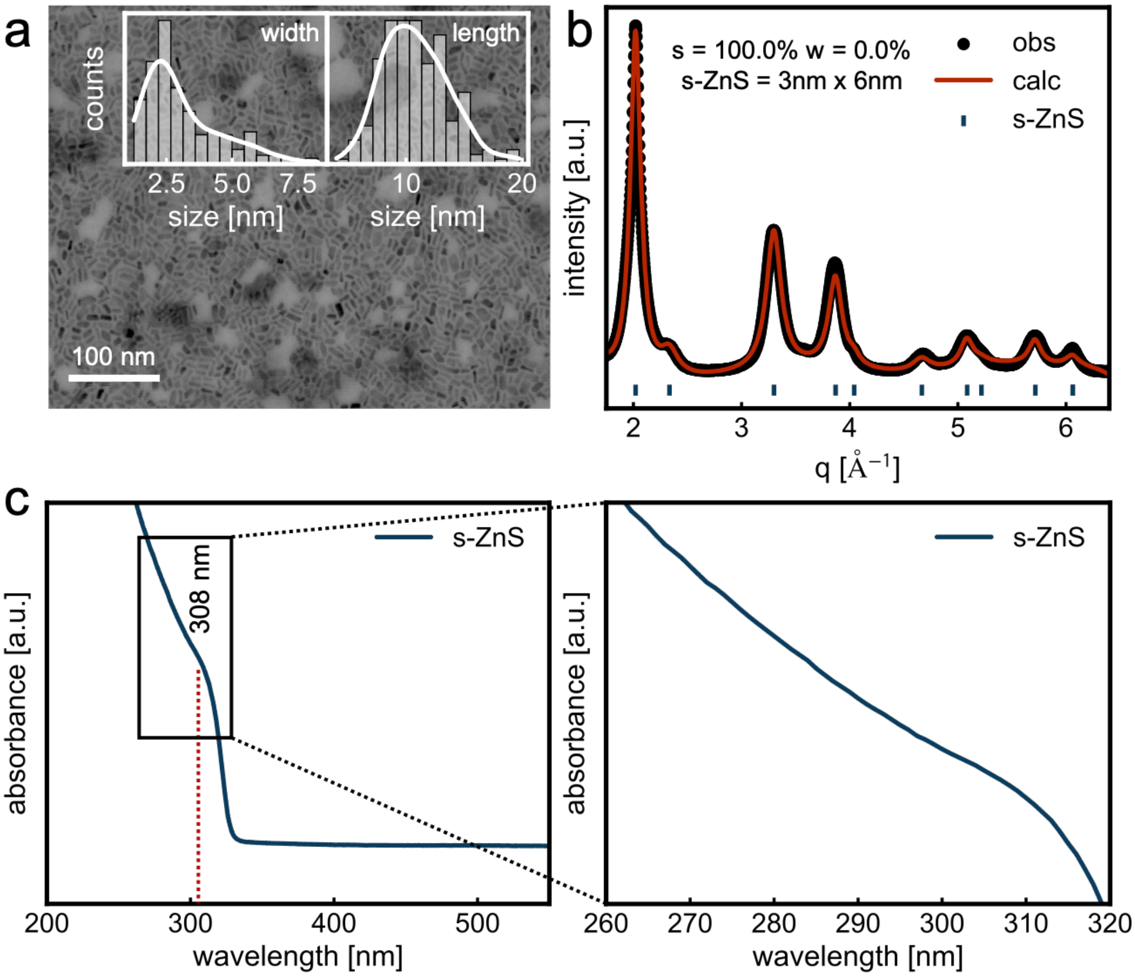

Figure 8.1.17: STEM image, Rietveld refinement and UV-Vis analysis of the final product after washing procedure. (a) STEM analysis shows nanorods with a size of 3.1 ± 1.4 nm width and 10.8 ± 2.8 nm length. In the inset, we present a size histogram based on the analysis of 207 particles. **(b)** Rietveld analysis of PXRD data of the final product conclude phase pure ZnS nanorods in sphalerite phase with domain sizes of 3nm x 6nm. **(c)** UV-VIS analysis shows a rod-like absorption behavior with a peak of s-ZnS at 308nm.[147]

Upon the initiation of sphalerite ZnS formation, rod-like structures in the sphalerite phase are observed, with dimensions approximately 2 nm in width and 7 nm in length. By the end of the reaction, the s-ZnS grows to a thickness of 3.1 ± 1.4 nm and a length of 10.8 ± 2.8 nm, as described in **Figure 8.1.17**. To enhance the image quality of the s-ZnS shown in **Figure 8.1.18 and Figure 4.3b (top, middle)**, the aliquots were washed before the deposition on a TEM grid.

HRTEM analysis of the s-ZnS:

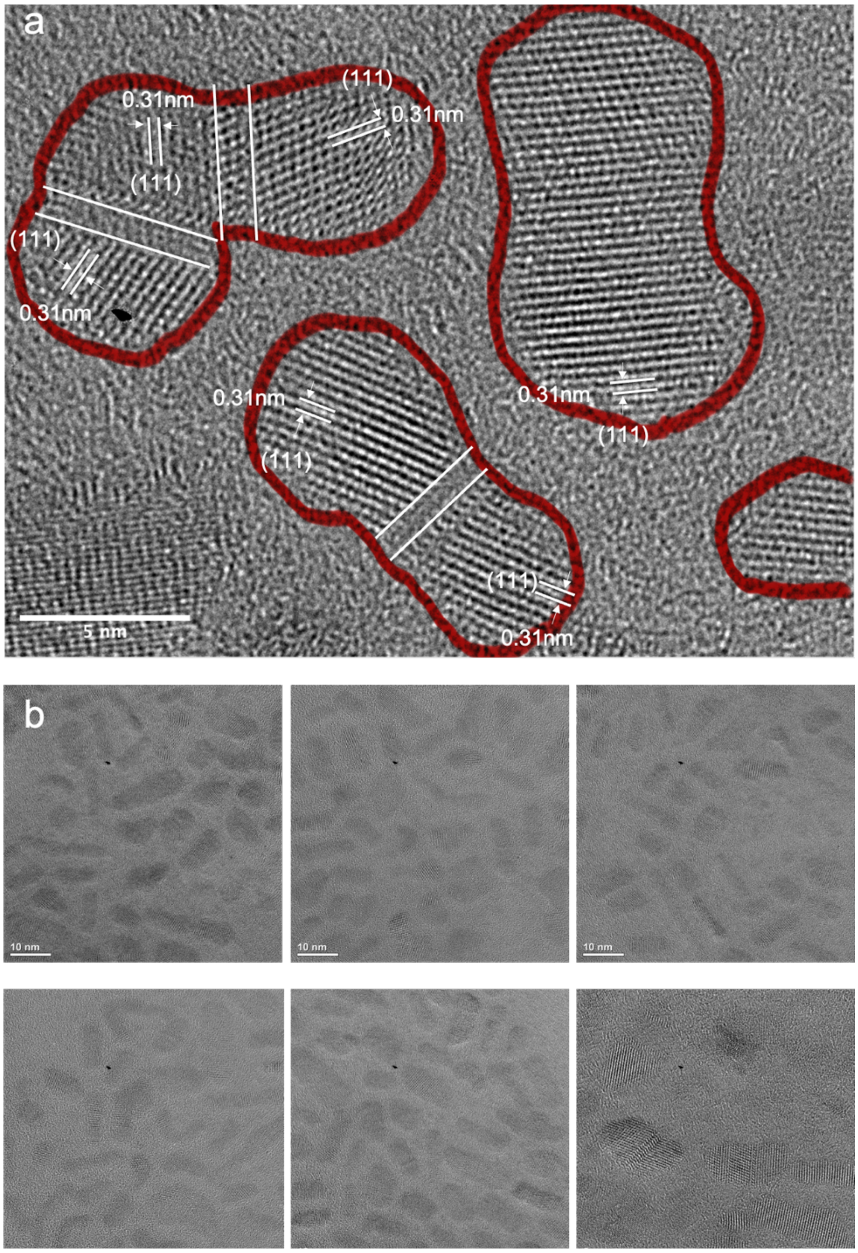

Figure 8.1.18: HRTEM analysis of the s-ZnS. HRTEM images of an aliquot at 155 min after eliminating the w-ZnS contribution by washing procedures. (a) The lattice fringes are indexed to the ZnS sphalerite phase. Contour lines highlighting the shape of the s-ZnS. (b) Overview of HRTEM pictures at different spots on the grid. The analysis reveals that the elongated structures seen in the HRTEM images are the s-ZnS. We assume that w-ZnS nanoparticles agglomerate/assemble before transforming into s-ZnS rods. The lattice fringes suggest an intergrowth process rather than dissolution-recrystallization.

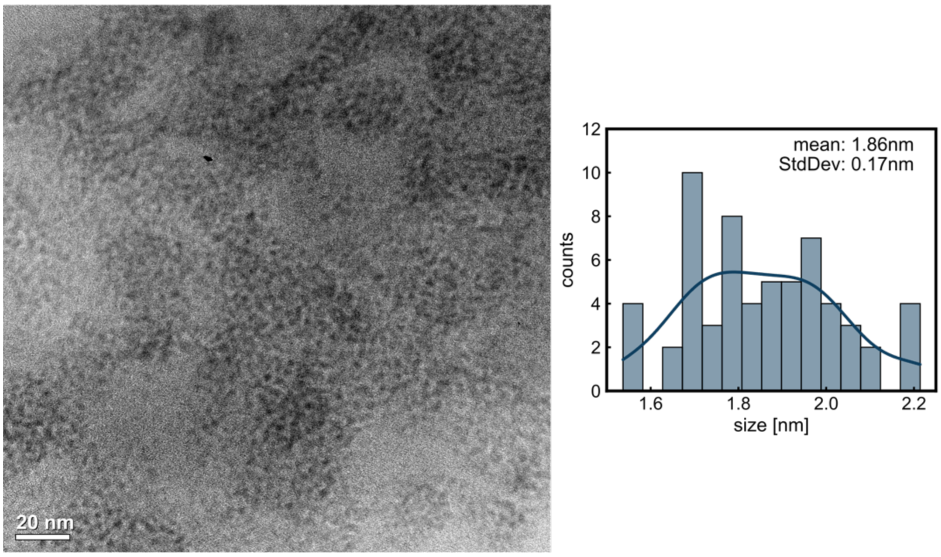

Figure 8.1.19: HRTEM analysis of the w-ZnS. HRTEM images of an unwashed aliquot at 75min reaction temperature, reveal 1.9 ± 0.2 nm large particles, which belong to w-ZnS.

Sequential Rietveld refinement:

Rietveld refinement utilizes the peak widths of reflections in the diffraction pattern to determine the crystallite sizes of simulated reference patterns through least-squares analysis. In this study, the diffraction pattern of the final reaction product could not be adequately described by a single ZnS phase. Consequently, we implemented a two-phase refinement, incorporating a linear combination of two simulated diffraction patterns corresponding to wurtzite ZnS (w-ZnS) and sphalerite ZnS (s-ZnS). We observed discrepancies in peak intensities compared to simulations, notably the (111) reflection of s-ZnS appeared narrower and exhibited higher intensity relative to other reflections in the pattern. To address this, we modeled anisotropy in s-ZnS along the (111) orientation. The least-squares fitting process optimized the proportions of w-ZnS and s-ZnS, as well as their respective crystallite sizes.

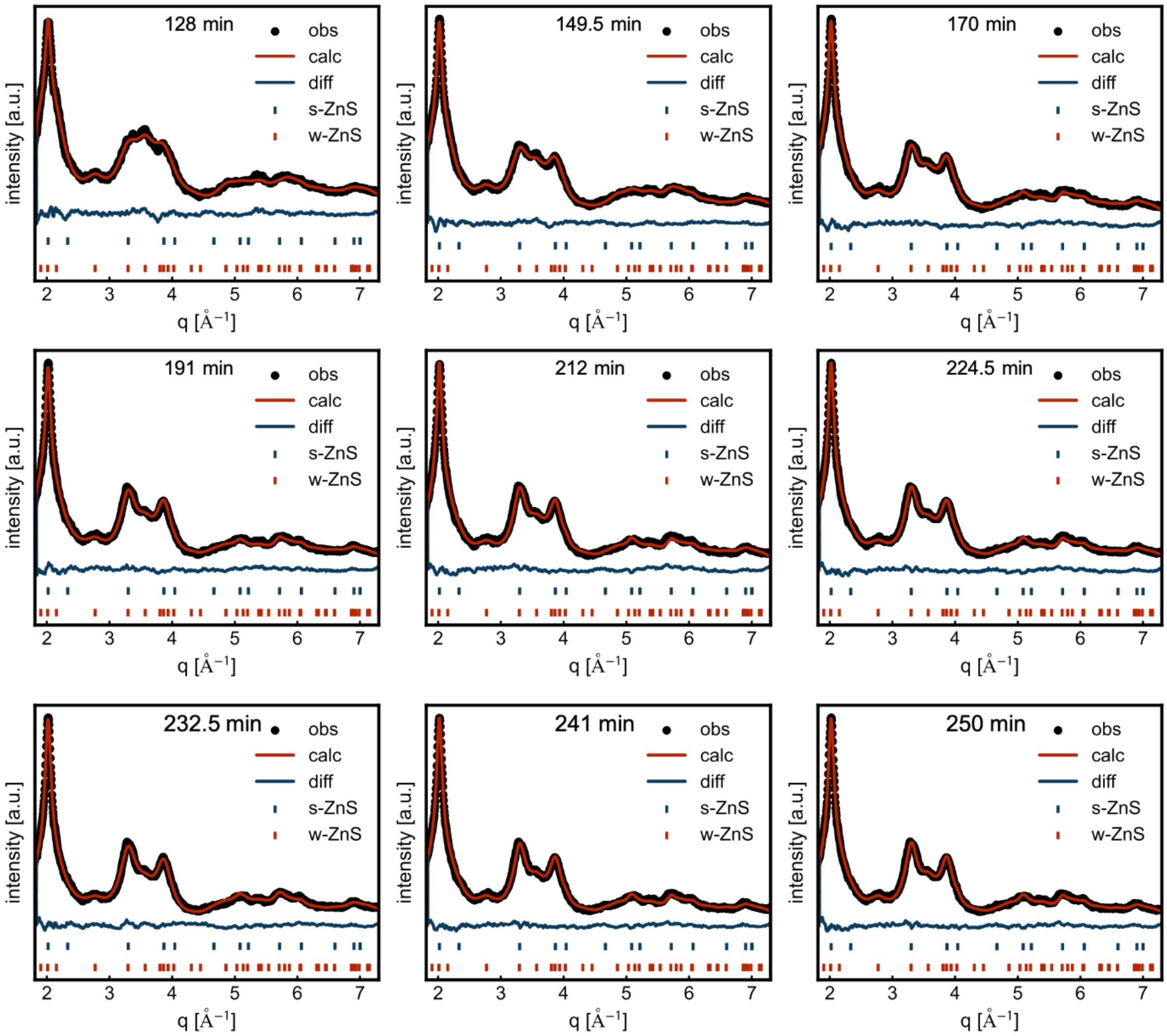

Figure 8.1.20: Sequential Rietveld refinement of PXRD. The data analysis assigns changes in the reflexes during the reaction to changes in domain sizes and fractions between s-ZnS and w-ZnS, as summarized in **Table 8.1.4**.

Table 8.1.4: Rietveld refinement results at different times of the reaction.

	Rw	**s-ZnS**	**w-ZnS**	**size s-ZnS**	**size w-ZnS**
128 min	4.55 %	15.7%	84.3 %	1 nm x 7 nm	1.7 nm
149.5 min	3.62 %	29.3%	70.7 %	1 nm x 7 nm	1.9 nm
170 min	4.77 %	32.3 %	67.7 %	2 nm x 7 nm	1.8 nm
191 min	4.04 %	33.9 %	66.1 %	1 nm x 7 nm	1.9 nm
212 min	5.69 %	36.4 %	63.6 %	2 nm x 7 nm	1.9 nm
224.5 min	4.35 %	38.8 %	61.2 %	2 nm x 7 nm	1.8 nm
232.5 min	5.53 %	38.6 %	61.4 %	1 nm x 7 nm	1.9 nm
241 min	4.46 %	39.9 %	60.1 %	2 nm x 7 nm	1.9 nm
250 min	4.33 %	41.0 %	59.0 %	2 nm x 7 nm	2.0 nm

In situ vtc-XES, HERFD-XAS, SAXS and PXRD characterization of the synthesis of s-ZnS at 170°C with a heating rate of 10°C/min:

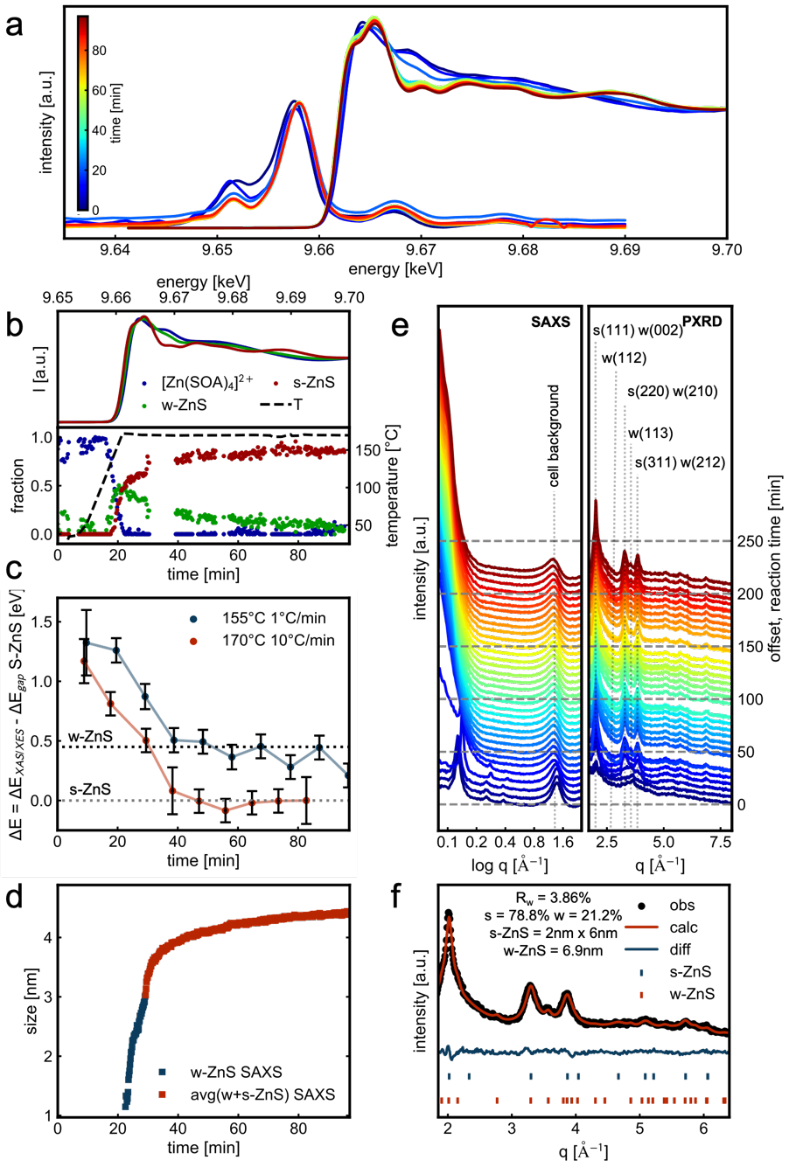

Figure 8.1.21: *In situ* X-ray spectroscopy, SAXS and PXRD analysis of synthesis at 170°C with 10°C/min heating rate.

(a) *in situ* vtc-XES and HERFD XAS, analyzed by MCR-ALS in **(b)**. The recovered spectra matched with the MCR-ALS of the in **Figure 4.3b**. The *in situ* band gap calculation in **(c)** suggests a faster formation of s-ZnS which is in good agreement with the MCR-ALS data. **(d)** The size was calculated by fitting the SAXS data with a spherical model. **(e left)** *In situ* SAXS analysis. The increasing intensity at low q, starting after approximately 20 minutes, indicates the formation of nanoparticles during the synthesis. **(e right)** *In situ* PXRD analysis shows the formation of crystalline reflections after 20 minutes, with changes in the relative intensity of the w(210)/s(220) and w(113) peaks over time, suggesting the formation of the sphalerite phase during the reaction. The s(111) peak appears to be comparably intense, implying a preferred orientation in the s along the (111) facet. **(f)** Rietveld analysis of the final product shows the presence of 79% s-ZnS and 21% w-ZnS.

***In situ* reaction cell:**

To run the reactions at the beamlines, adapted versions of reaction cells from previous work were used.[133, 190] **Figure 8.1.22a** presents the body of the *in situ* cell. For *in situ* HERFD-XAS and vtc-XES studies, a PEEK reaction container (diameter 2.5mm) surrounded by a flat, thin wall (0.2 mm) for X-ray entrance and exit was used to obtain enough signal from diluted solutions but with enough mechanical stability (see **Figure 8.1.22a**). For the combined X-ray scattering measurements, an adapted PEEK inlet works as a holder for a glass capillary, described in detail in the literature.[190] The glass capillaries have a 0.5 mm wall thickness and 2.5 mm inner diameter. A detailed view of the inlet used in the X-ray scattering experiments is shown in **Figure 8.1.22b**.

The total volume of 66 µL and 174 µL for the scattering and spectroscopic experiments, respectively. The main potential differences can occur in different heat capacities and therefore different heat ratios. To estimate the impact on the total heat consumption of the cell, we calculated the required energy to heat 66 µL and 174 µL of oleylamine (in the assumption that oleylamine has a comparable specific heat capacity to oleic acid of 2.4 $\frac{\mathrm{kJ}}{\mathrm{kg*K}}$) to 155°C to 16.1 J and 42.5 J respectively. Concerning the required energy of around 23 kJ to heat our heating cell to 155°C, the impact of the sample volume is below 0.2%. Therefore, we did not expect any impact of the sample volume on our reaction kinetics.

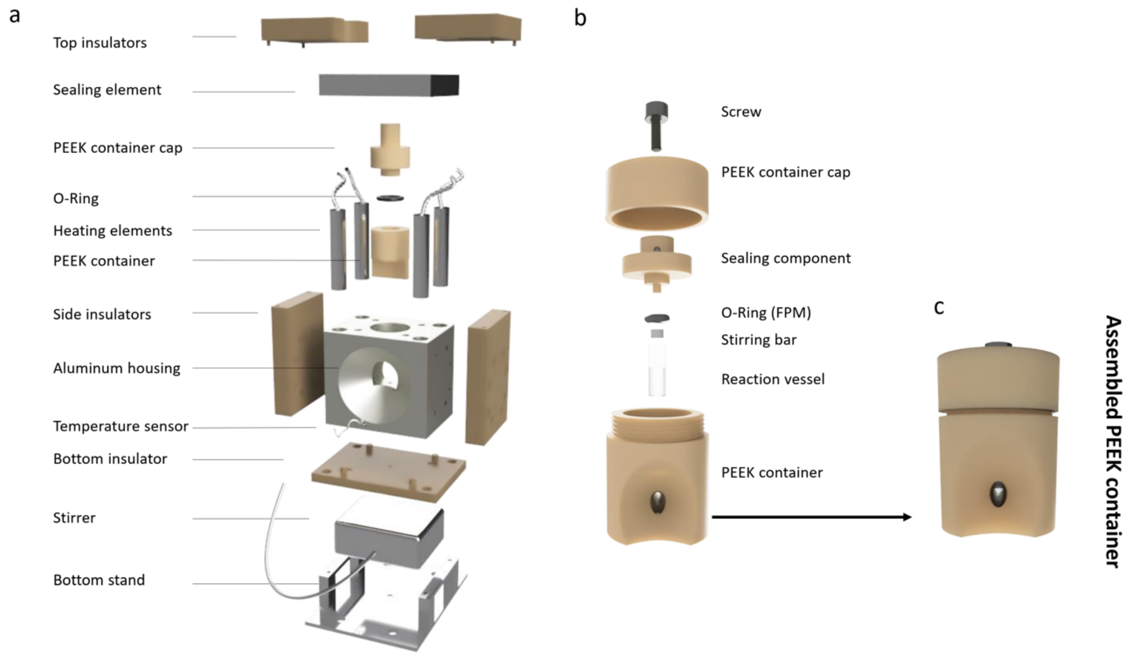

Figure 8.1.22: Schematic of the used reaction container. (a) Unassembled view of the reaction cell, used in X-ray spectroscopy experiments. **(b)** Adapted PEEK inlet with glass capillary as a reaction vessel, used in X-ray scattering experiments.

Beam damage study:

To exclude the occurrence of beam damage, we performed radiation damage studies before the measurement, collecting multiple XANES spectra at the same position on the pellet/cell and checking if any changes in the spectra due to the radiation can be observed.

$Zn(Ac)_2$ powder diluted in boron nitride and pressed to pellet.

We observed rapid radiation damage during XANES scans, as shown in **Figure 8.1.23a**. The occurrence of radiation damage led us to limit the acquisition time of an XANES to 6s, and average the XANES over 40 XANES spectra from different points on the pellet.

Zn solution: In the XANES spectra of $Zn(Ac)_2$ dissolved in oleylamine, we do not see any effect of radiation damage, as shown in the **Figure 8.1.23b**. We collected 20 XANES spectra on the same spot in the *in situ* cell, where every XANES scan took 10s. To mitigate the beam damage during the reaction: we moved the *in situ* cell between the scans to an exposed spot in the reaction container and stirred during the reaction.

vtc-XES studies: For each datapoint in the vtc-XES scan a fresh spot on the pellet was used with a collection time of 1s per spot. To perform a concentration correction on the vtc-XES dataset, we moved again to all measured spots and collected the intensity of the Kβ main. The intensity variations on the vtc-XES are based on inhomogeneities in the pellet, or thickness of the in-situ cell. The thickness inhomogeneity in the cell relates to the precision of the machining of the *PEEK* container.

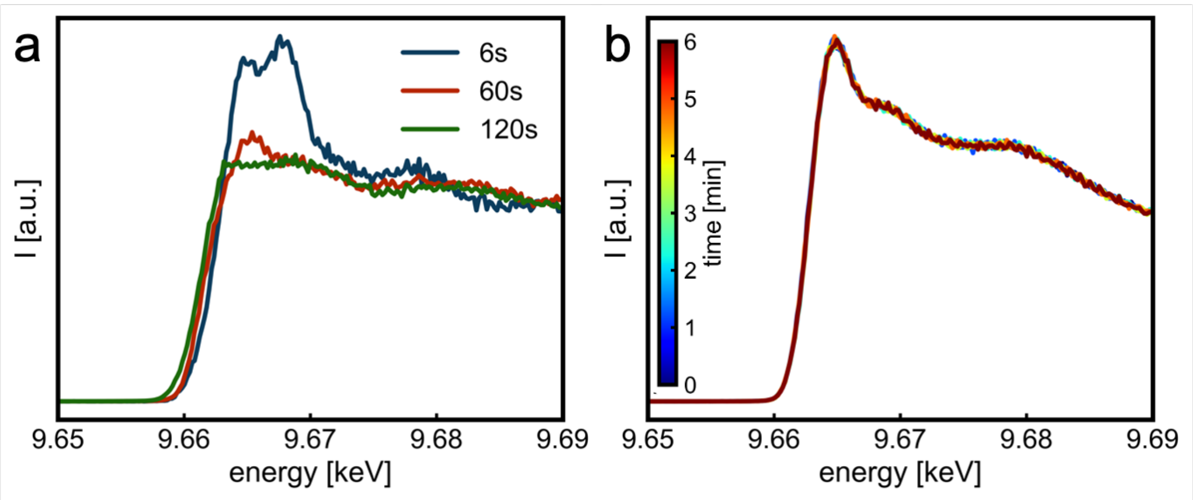

Figure 8.1.23. Radiation damage study on $Zn(Ac)_2$ pellet (a) and $Zn(Ac)_2$ dissolved in oleylamine (b). While pure $Zn(Ac)_2$ shows a fast occurrence of beam damage, the $Zn(Ac)_2$ dissolved in oleylamine seems unaffected by incident X-ray radiation.

Normalization of vtc-XES:

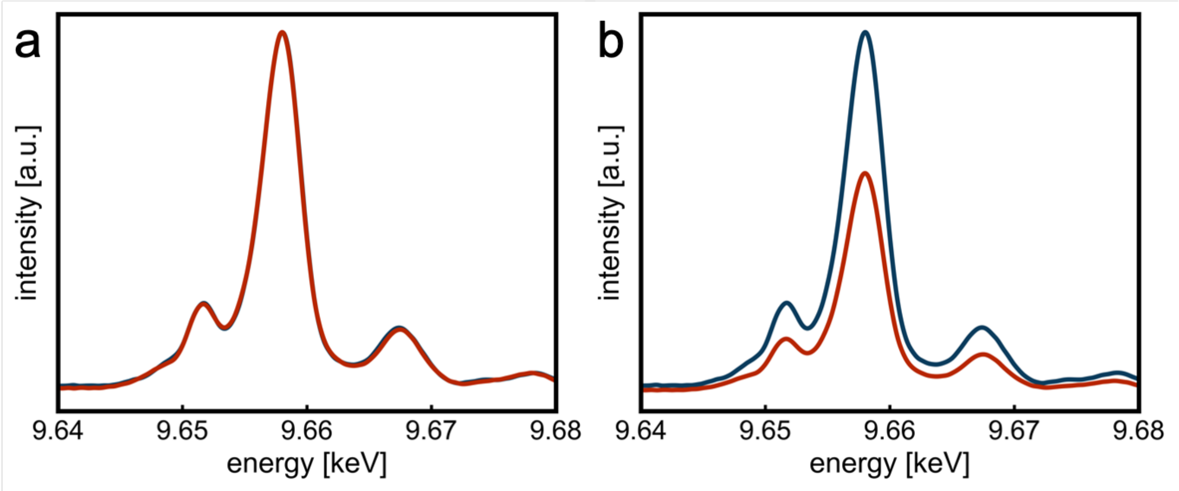

Figure 8.1.24: *In situ* vtc-XES after smoothing and interpolation (as explained in **Figure 8.1.22a**) with normalization by max intensity (a), show two almost identical scans at the end of the reaction, while an area normalization (b) would show an unphysical overall intensity difference.

In summary, the most elegant way to normalize the *in situ* data was a normalization of the intensity of the Kβ main line. But this would lead to a significant decrease in time resolution. Thus, we maintained normalization by maximum intensity rather than by area, which allows us to compare the relative intensities between the individual peaks and avoid unphysical misinterpretation of intensities due to glitches.

FEFF calculations of vtc-XES and data processing:

We perform FEFF calculations[193] of w-ZnS and s-ZnS to check if we would expect large changes between the vtc-XES spectra. The calculations reveal only small changes in maximum intensity as shown in the following **Figure 8.1.25**. In General, the limitation of FEFF to reproduce experimental spectra is limited, as described in the literature.[192]

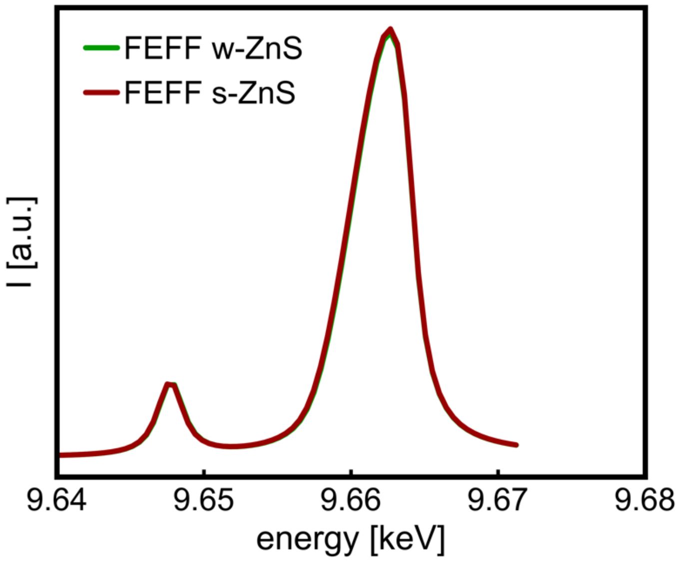

Figure 8.1.25. FEFF simulation of w-ZnS and s-ZnS reveals only small changes in maximum intensity.

The FEFF calculation were performed with the following parameters:

```
EDGE K
S02 1.0
CONTROL 1 1 1 1 1 1
PRINT 1 0 0 0 0 3
XES 4.0 0.005 0.0
EXCHANGE 0 0.0 0.0 -1
SCF 9 0 100 0.2 10
COREHOLE FSR
```

```
LDOS -20 30 0.5
MULTIPOLE 2 0
```

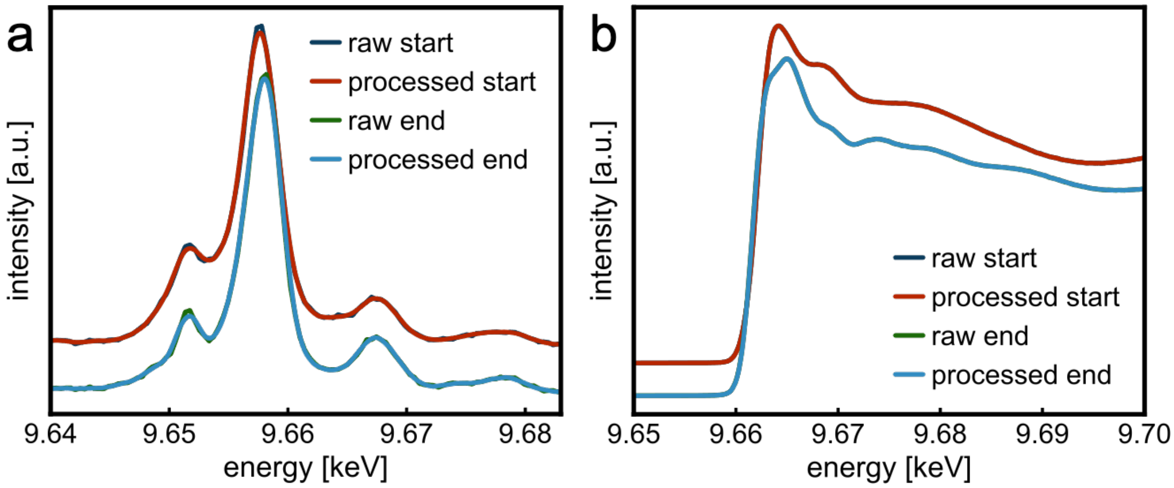

Figure 8.1.26: Data processing in HERFD-XAS and vtc-XES data. vtc-XES **(a)** and HERFD-XAS data **(b)** were interpolated and filtered as described in the experimental section. This data optimization was required to ensure a reliable determination of the energy position of the maximum in the derivation. To verify that the data were not significantly affected by the processing, the filtered and raw data at the beginning and the end of the *in situ* runs are combined and plotted with an offset.

8.2 Supporting Information: Chapter 5

TEM analysis of ZnS NPs produced in the autoclave:

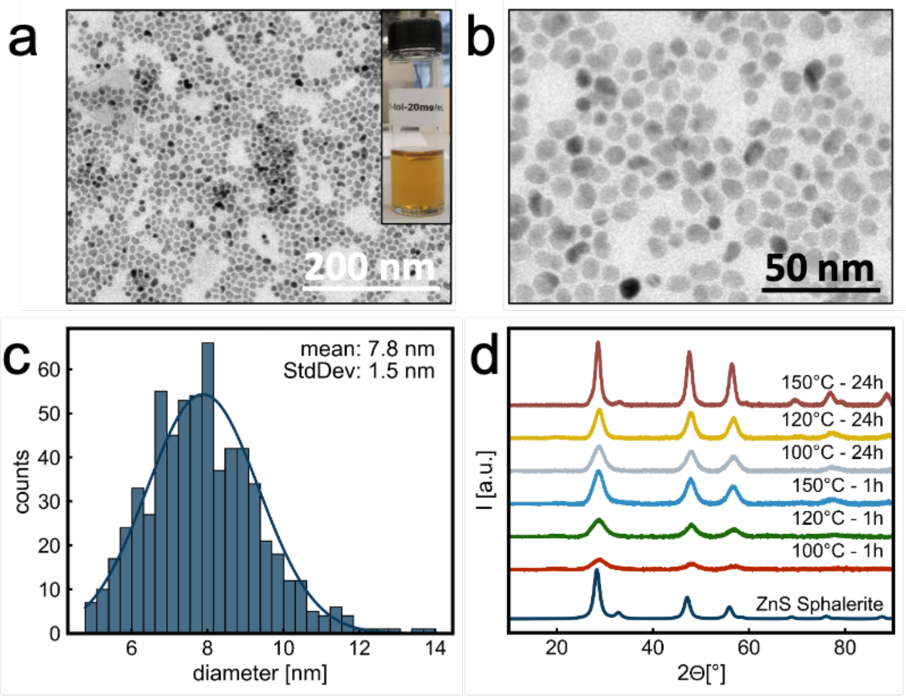

Figure 8.2.1: TEM images (**a,b**) and particle size distribution (**c**) of ZnS NPs produced in an autoclave at 150 °C for 24 hours ; XRD patterns (**d**) of ZnS NP produced in an autoclave with reaction temperatures between 100 and 150 °C and reaction time of 1 h and 24 h. .

TEM and HRTEM analysis of ZnS NPs produced in the *in situ* cell:

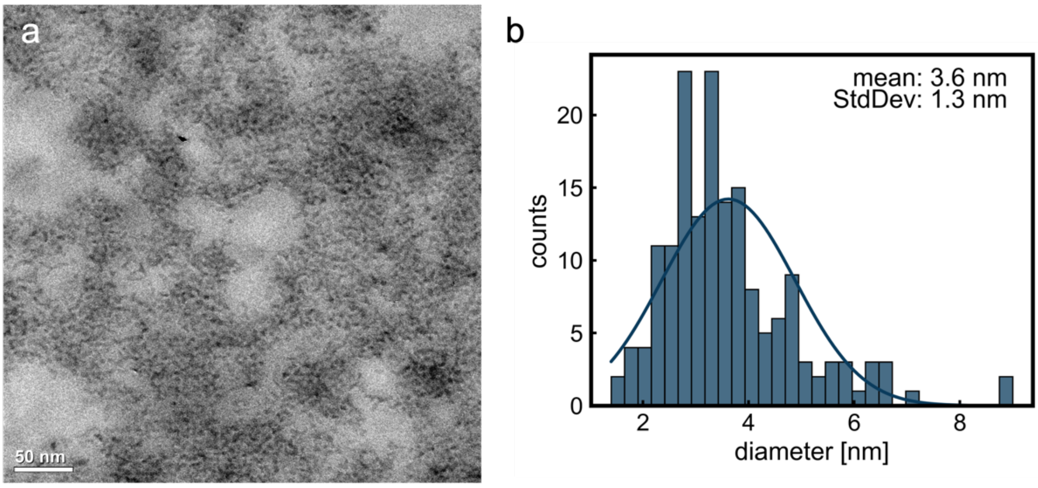

Figure 8.2.2: (a) TEM image and **(b)** the particle size distribution of ZnS NPs as a final product of the described *in situ* synthesis (155 °C for 60 min) reveals an average size of 3.6 nm with a standard deviation of 1.3 nm.

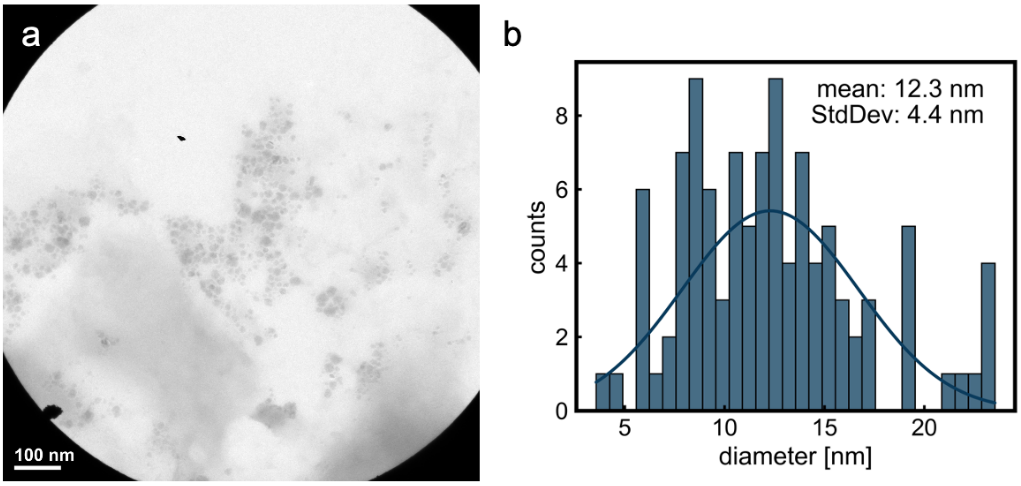

Figure 8.2.3: HRTEM **(a)** and size analysis **(b)** of ZnS NPs as a final product of the described *in situ* synthesis (155 °C for 60 min) reveals an average size of 12.3 nm with a standard deviation of 4.4 nm. Therefore, the final product contains small and larger particles. The size distribution depends on the position of the grid.

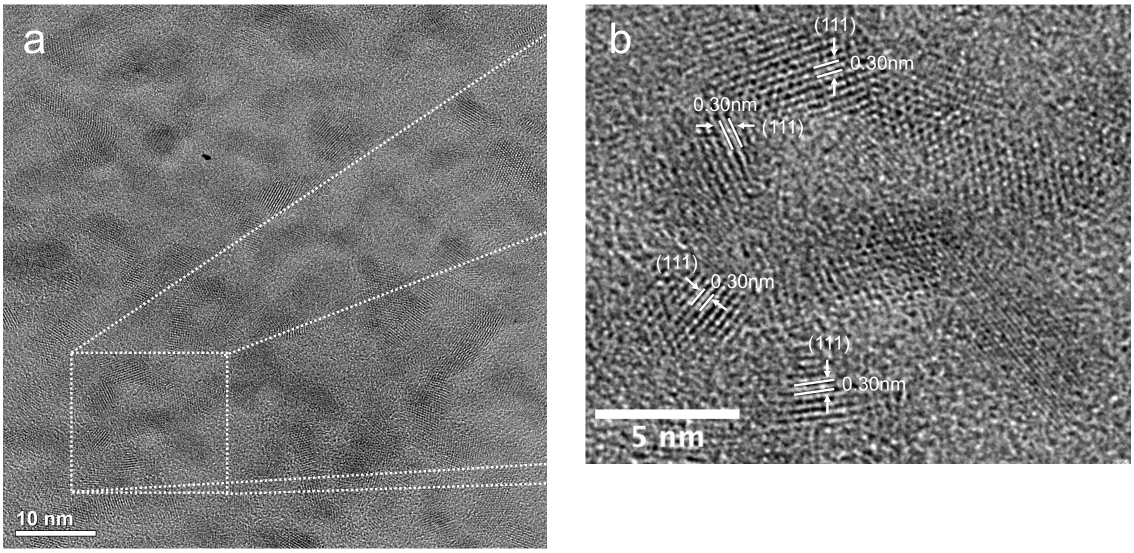

Figure 8.2.4: HR-TEM analysis of ZnS NPs as a final product of the described *in situ* synthesis (155 °C for 60 min) shows 3-4 nm large particles.

DFT calculations of Zn^{2+} complexes in water/toluene:

All the structural optimization (left) and TD-DFT for XANES calculations (right), were performed with the following example ORCA .inp parameters:

```
!RKS B3LYP TightOpt TightSCF ZORA-def2-TZVP
ZORA
!FREQ Largeprint Printbasis
%maxcore 4000
%xes
CoreOrb 0
OrbOp 0
end
* xyz 2 1
…
```

```
!RKS B3LYP TightSCF ZORA-def2-TZVP D3BJ
RIJCOSX ZORA
!Normalprint MOREAD
%maxcore 4000
%moinp "Zn6H20_XES.gbw"
%tddft
orbwin[0]= 0,0,-1,-1 doquad true
nroots 300
maxdim 50
end

* xyz 2 1
…
```

The resulting output files are processed with orca_mapspc to export the spectra:
XAS: orca_mapspc name.mpi8.out absq -eV -x09000 -x110000 -n10001 -kw0.03

The .inp Files, the optimized .xyz files of all shown complexes, and the experimental raw data are available here: 10.25592/uhhfdm.16646

To propose the coordination of Zn^{2+} ions in the water and toluene phases, DFT calculations using ORCA were performed on many possible coordinations, shown in **Figure 8.2.9**. The position and intensity of the white line were best reproduced with $[Zn(H_2O)_6]^{2+}$ in water and $[Zn(OA)_6]^{2+}$ in the toluene phase, respectively. All calculated spectra are redshifted by 18.3 eV to correct the mismatch between the calculations and experimental data.

MCR-ALS:

The MCR-ALS method use a constrained Alternating Least Squares (ALS) algorithm to solve a bilinear model. The bilinear equation is described as follows:

$$\mathbf{D} = \mathbf{C}\mathbf{S}^{\mathbf{T}} + \mathbf{E} \tag{1}$$

where **D** refers to the raw data set, **C** to the concentration profiles for each recovered compound, $\mathbf{S}^{\mathbf{T}}$ to the related pure spectra, and **E** to the matrix of residuals not accommodated by the model. The ALS algorithm operates based on the iterative principle of alternately fixing one set of variables while solving for the other. To elaborate, the process initiates by initializing $\mathbf{S}^{\mathbf{T}}$ and solving a linear algebra problem for **C** while maintaining $\mathbf{S}^{\mathbf{T}}$ as a constant. Subsequently, **C** is held steady, and the system is solved for $\mathbf{S}^{\mathbf{T}}$. This alternating cycle continues until convergence is attained. Convergence is defined by the criterion that, in two consecutive iterative cycles, the relative differences in the standard deviation of residuals between experimental and ALS-calculated data values fall below a predetermined threshold. The evaluation of the fit's quality, upon convergence, is based on the unexplained residuals **E**, signifying the disparity between the experimental data and the bilinear model. The **lack of fit (%)** is quantified as:

$$\textbf{lack of fit (\%)} = 100\sqrt{\frac{\sum_{i,j} e_{ij}^2}{\sum_{i,j} d_{ij}^2}} \tag{2}$$

Here, *d* represents an element within the data matrix, and *e* corresponds to the respective element in the residuals matrix **E**. Additionally, the model's explained variance $\mathbf{R}^2$ can be estimated using:

$$\mathbf{R}^2 = \frac{\sum_{i,j} d_{ij}^2 - \sum_{i,j} e_{ij}^2}{\sum_{i,j} d_{ij}^2} \tag{3}$$

The standard deviation of the residuals $\boldsymbol{\sigma}$ is given by:

$$\boldsymbol{\sigma} = \sqrt{\frac{\sum_{i,j} e_{ij}^2}{nm}} \quad (4)$$

In this context, n and m represent the dimensions of the raw data matrix, denoted as **D**. Additionally, the ALS algorithm can conform to physically or chemically meaningful constraints, such as enforcing non-negativity or unimodality for concentration and spectra profiles and closure.[176]

For the MCR-ALS analysis, the XANES data were structured into a matrix, where each row corresponds to an absorption spectrum recorded *in situ*. The number of rows is equivalent to the quantity of acquired spectra, and the number of columns corresponds to the number of data points in each spectrum. Before implementing the ALS optimization, the number of components and initial spectra was determined. The selection of the number of components was guided by the Singular Value Decomposition (SVD) outcomes. The computed eigenvalues from the data offer insights into the extent of variance each factor or component can elucidate. The factor associated with the highest eigenvalue represents the greatest variance, followed by the one with the second highest eigenvalue, and so forth. Eigenvalues below a certain threshold indicate noise in the data. The determined eigenvalues in both datasets are illustrated in the Scree plot in **Figure 8.2.5** and are listed in **Table 8.2.1**.

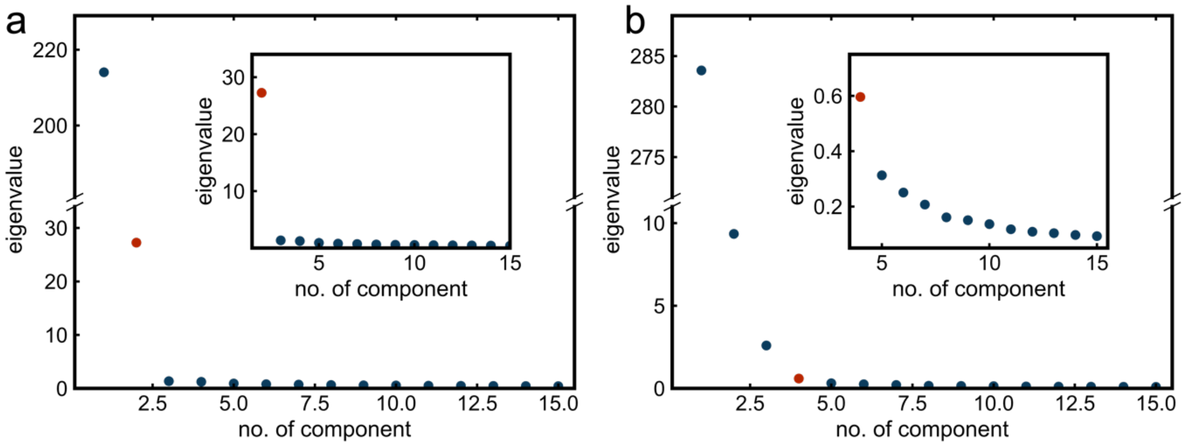

Figure 8.2.5: Scree plot of eigenvalues of **(a)** the scan across the water-toluene interface prior to the reaction and **(b)** the *in situ* preparation of ZnS NP. Linear-aligned eigenvalues correspond to noise. The number of used components is indicated in red.

Table 8.2.1: Eigenvalues determined by SVD of the MCR-ALS analysis.

Number of components	Eigenvalues of scanning across the water-toluene interface prior the reaction (Figure 2)	Eigenvalues of synthesis of ZnS NP (Figure 3)
1	214.056	283.575
2	27.255	9.347
3	1.352	2.595
4	1.234	0.596
5	0.919	0.312
6	0.783	0.250

Table 8.2.2: Fitting parameters of the MCR-ALS analysis.

	Fitting parameters of scanning across the water-toluene interface prior the reaction (Figure 2)	Fitting parameters of the synthesis of ZnS NP (Figure 3)
fitting error (%)	0.81	0.042
R^2	99.9934	100
σ	0.0095	0.00041

The eigenvalues of the in-situ HERFD-XAS dataset suggest four distinct components during the reaction to ZnS NPs. The spectral features of the starting point and the final product were also slightly better reproduced using four components instead of three, as indicated by the standard deviations in the following **Figure 8.2.6**.

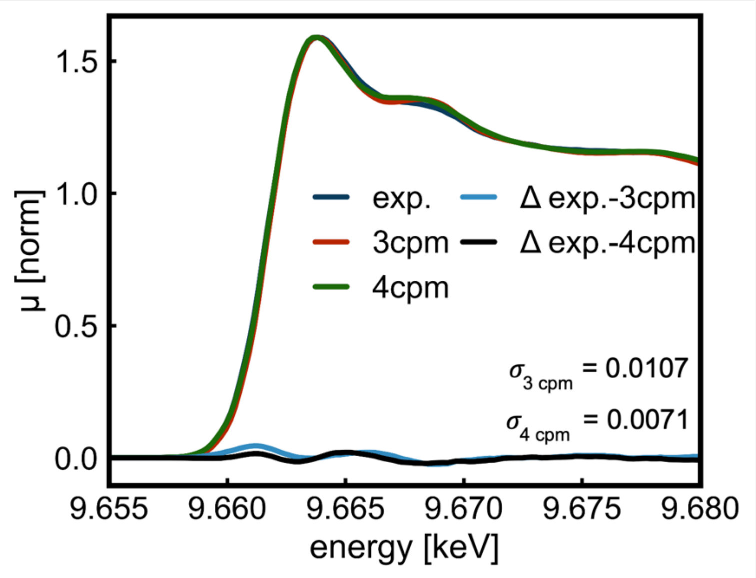

Figure 8.2.6: Experimental spectra (blue lines) of the starting point compared with the MCR-ALS recovered contributions of three component (red lines) and four component (green lines) MCR-ALS analysis. The standard deviation between four component spectra is lower compared to three component spectra.

Beam damage study in water and toluene phase:

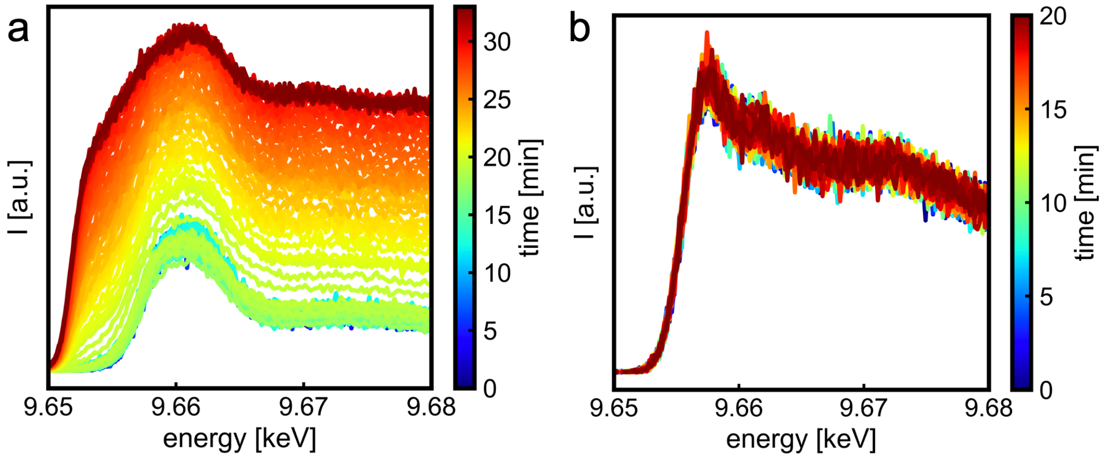

Figure 8.2.7: Beam damage study of the precursor solution in **(a)** the water and **(b)** the toluene phase. In the water phase **(a)**, a deposition of metallic Zn on the reaction container could be observed, starting after 10 minutes of illumination. This was indicated by a shift of E_0 towards lower energies combined with an overall increased intensity. In the toluene phase, no formation of metallic Zn can be observed. The acquisition time for each spectrum was 15 s. The datasets were collected at Beamline ID24.

***In situ* diffusion of Zn^{2+} through the water-toluene interface:**

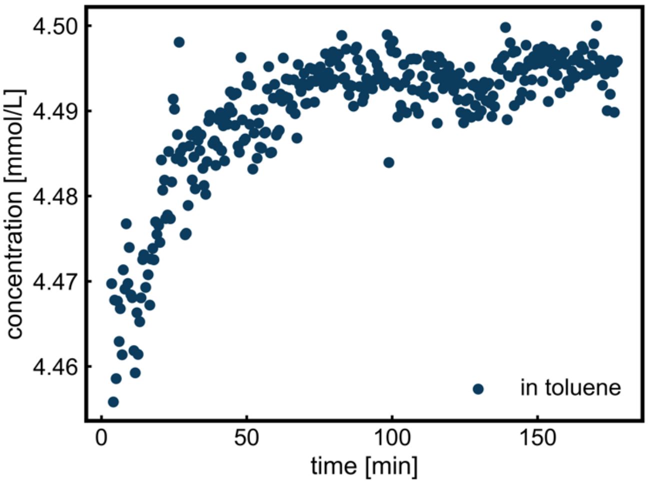

Figure 8.2.8: Concentration profile of Zn^{2+} ions in the toluene phase during the *in situ* reaction. The Zn^{2+} concentration in the toluene phase reached its equilibrium after around 60 min reaction time (80 °C).

DFT calculations of Zn^{2+} complexes in water/toluene:

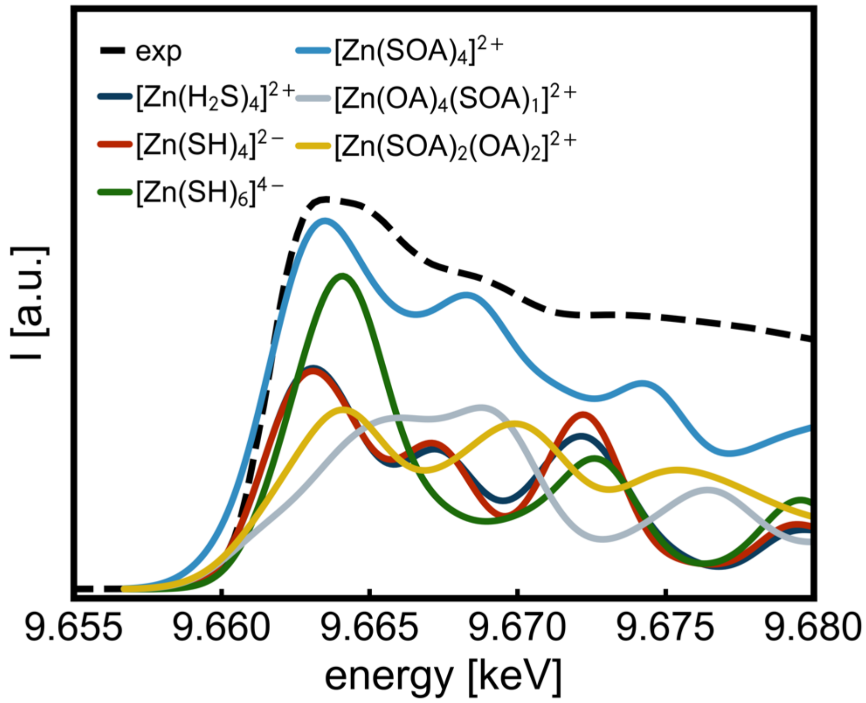

Figure 8.2.9: The first recovered intermediate (black, dashed) compared with DFT calculations of $[Zn(H_2S)_4]^{2+}$, $[Zn(SH)_4]^{2-}$, $[Zn(SH)_6]^{4+}$, $[Zn(SOA)_4]^{2+}$, $[Zn(OA)_4(SOA)_1]^{2+}$ and $[Zn(SOA)_2(OA)_2]^{2+}$. None of the calculations explain the broad behavior of the white line, while the best agreement is achieved by assuming a $[Zn(SOA)_4]^{2+}$ complex.

Due to the differences between experimental and simulated data, we propose the presence of a $[Zn(SR)_4]^{2+}$ as the first intermediate, where the identity of the R is still unknown.

FEFF calculations of ZnS nuclei and ZnS NPs:

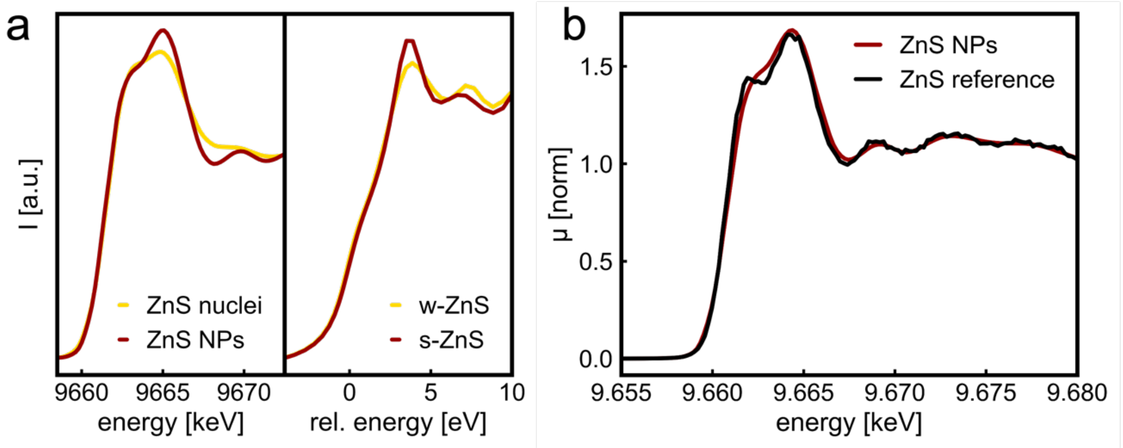

Figure 8.2.10: (a) Experimental spectra of ZnS nuclei (yellow line) and ZnS NPs (red line) recovered by MCR-ALS analysis (left) compared to simulated spectra of wurtzite (yellow line) and sphalerite (red line) phases by FEFF calculations (right). **(b)** Experimental spectra of ZnS NPs (red) compared with experimental spectra of a ZnS reference (black, Sigma Aldrich, Product 244627)**.**

The white line is split into a shoulder at lower energies, and the global maximum present in both spectra is characteristic of ZnS.[160, 175] While the shoulder in both cases is located at the characteristic energy for the tetrahedral coordination of Zn-S, the intensity of the maximum is higher for the sphalerite phase since this mainly reflects the higher periodicity of the Zn-S-Zn interatomic distances in the higher symmetric ABC-ABC stacking of the ZnS tetrahedrons in sphalerite, compared to the AB-AB stacking in the wurtzite phase.[244] However, the wurtzite phase has a higher intensity in the post-edge peaks compared to the sphalerite phase, as shown by the FEFF simulation, and this is not visible in the recovered spectra by MCR-ALS.

FEFF calculation parameters:

The FEFF calculations of w-ZnS and s-ZnS were performed with the following input parameters and the FEFF09 code.

```
EDGE K
S02 1.0
CONTROL 1 1 1 1 1 1
PRINT 1 0 0 0 0 3
EXCHANGE 0 0.0 0.0 -1
SCF 9 0 100 0.2 10
COREHOLE FSR
XANES 5.0 0.05 0.05
FMS 9 0
RSIGMA
LDOS -20 30 0.5
```

PDF analysis and the parameters of fit:

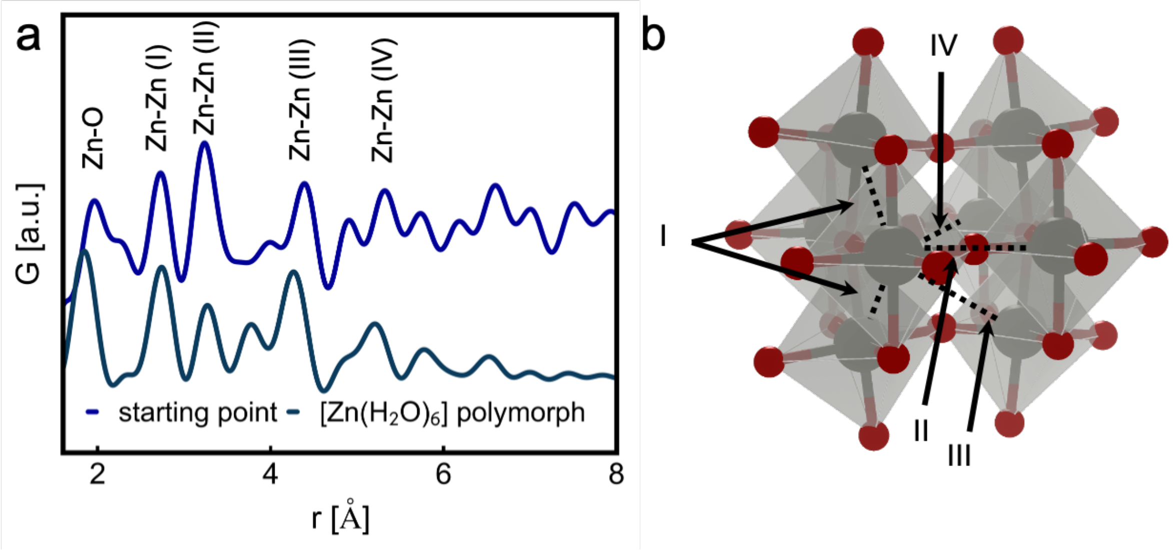

Figure 8.2.11: (a) experimental PDF of the starting point (top) compared with simulated PDF of a $[Zn(H_2O)_6]^{2+}$ **(b)** Visualization of a $[Zn(H_2O)_6]^{2+}$ polymorph, where the Zn atoms are shown in gray and the oxygen is shown in red. The dashed lines correspond to Zn-Zn interatomic distances. The Index of the Zn-Zn interatomic distances (I, II, III, IV) corresponds to maxima in the PDF data, shown in (a). The hydrogen atoms are not shown in the scheme.

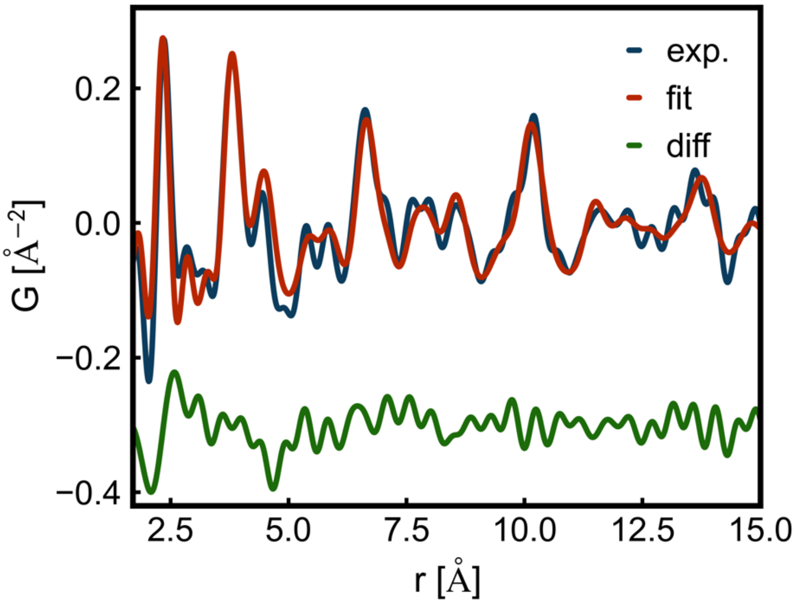

Figure 8.2.12: PDF refinement of the final product with ZnS sphalerite. The goodness of the fit (Rw) is 0.37, while the average crystallite size was refined to be 2.4 nm.

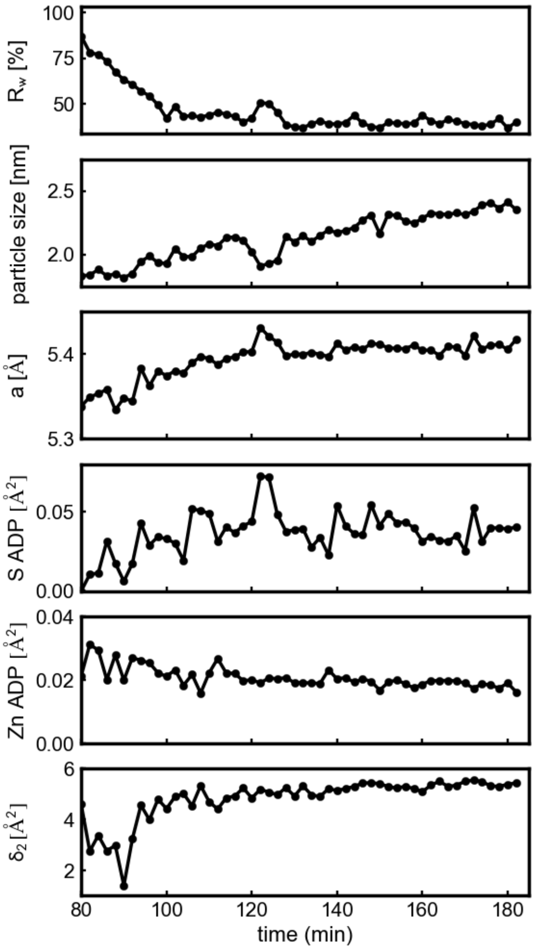

Figure 8.2.13: Fitting parameters of *in situ* PDF refinement during the synthesis of ZnS NP. The fit became reliable only after 100 min.

8.3 Supporting Information: Further perspectives: *in situ* formation of Fe_3S_4 nanostructures

8.3.1 Synthesis of Fe_xS_y in Toluene

To yield Fe_3S_4 nanostructures, $Fe(acac)_3$ was dissolved in toluene, along with elemental sulfur and oleylamine. This reaction mixture was heated to a temperature of 180°C at a rate of 5°C/min while in-situ HERFD-XAS data were collected. Above 100°C, the data quality deteriorated significantly, which may have two potential explanations: First, toluene forms bubbles upon reaching its boiling point of around 104°C in the autoclave, or the Fe_xS_y structures were in the size range of the beam spot and moved in and out of the beam during each scan. To eliminate these glitches, the reaction temperature was decreased to 100°C. RIXS analysis of the reaction solution prior (**Figure SI8.3.1.1.a, c**) and after the reaction (**Figure SI8.3.1.1.b, d**) demonstrates the formation of FeS by the end of the reaction, as indicated by pre-edge fitting in **Figure SI8.3.1.1.f**.

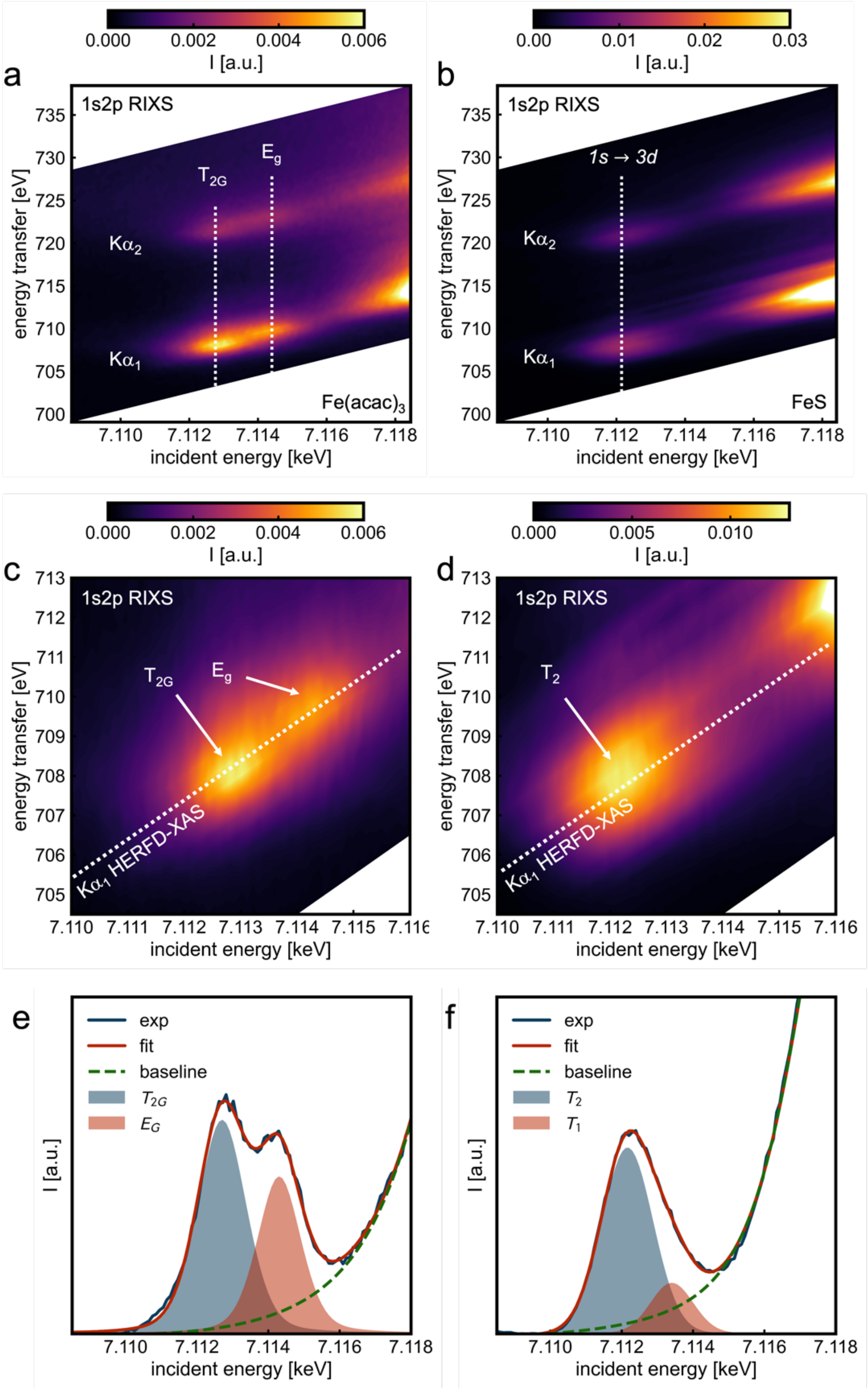

Figure SI8.3.1.1 RIXS analysis **(a-d)** and pre-edge fitting pseudo-voigt functions **(e,f)** of reaction solutions for the synthesis of Fe$_x$S$_y$ in toluene at 100°C, before (left) and after the reaction (right). The iron identity in the reaction solution before the reaction aligns with Fe(acac)$_3$, while after the reaction, FeS is mainly present.

In situ HERFD-XAS studies on the Fe_xS_y synthesis in toluene, underline the formation of FeS as final product of this reaction, undergoing the formation of a $[Fe(acac)_2(BA)_2]$ complex.

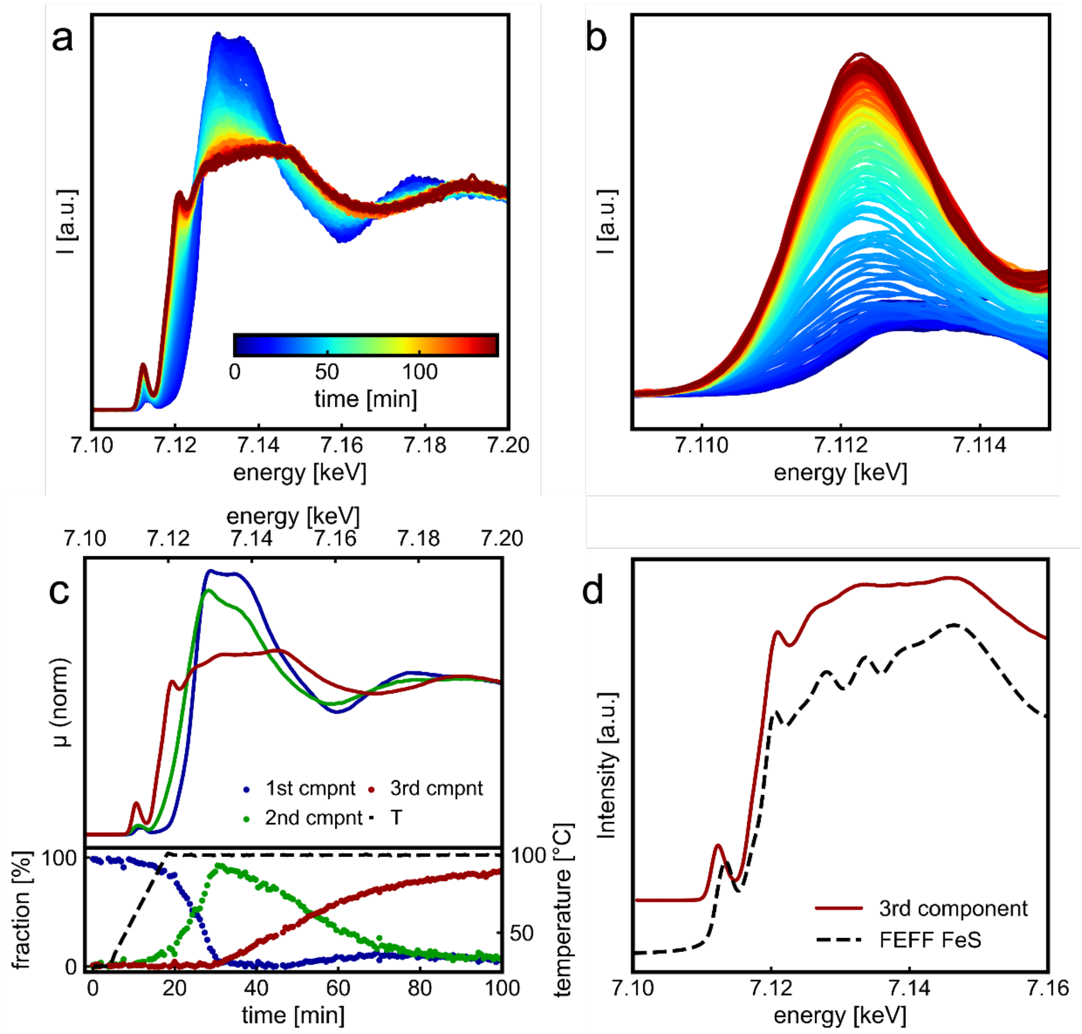

Figure SI8.3.1.2. *In situ* HERFD-XAS data (a) of the FeS reaction in toluene at a reaction temperature of 100°C. The pre-edge region (b) shows an overall increase during this reaction, suggesting the transition from octahedral coordination of iron in $Fe(acac)_3$ to tetrahedral coordination of iron in FeS throughout the reaction. MCR-ALS analysis reveals the presence of three individual contributions, which show the spectral shape of $Fe(acac)_3$ (blue), $[Fe(acac)_2(BA)_2]$ (green), and FeS (red), respectively.

8.3.2 Synthesis of Fe_3S_4 in benzyl alcohol

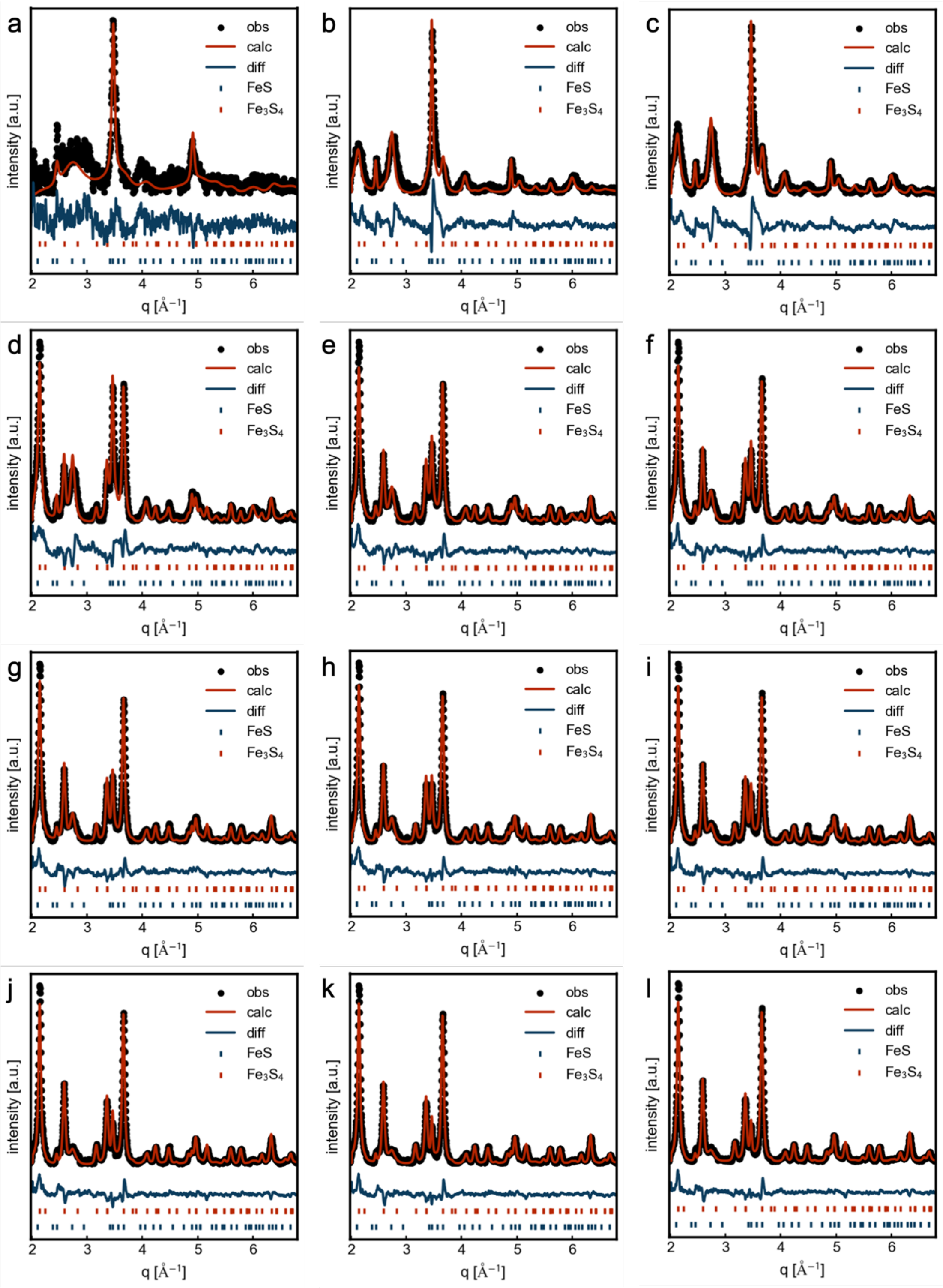

Figure 8.3.2.1 Sequential Rietveld refinement of the synthesis of Fe_3S_4 at 180 °C at **(a)** 10min, **(b)** 13 min, **(c)** 14 min, **(d)** 16 min, **(e)** 18 min, **(f)** 19 min, **(g)** 20 min, **(h)** 21 min, **(i)** 23 min, **(j)** 25 min, **(k)** 26 min, and **(l)** 27 min reaction time.

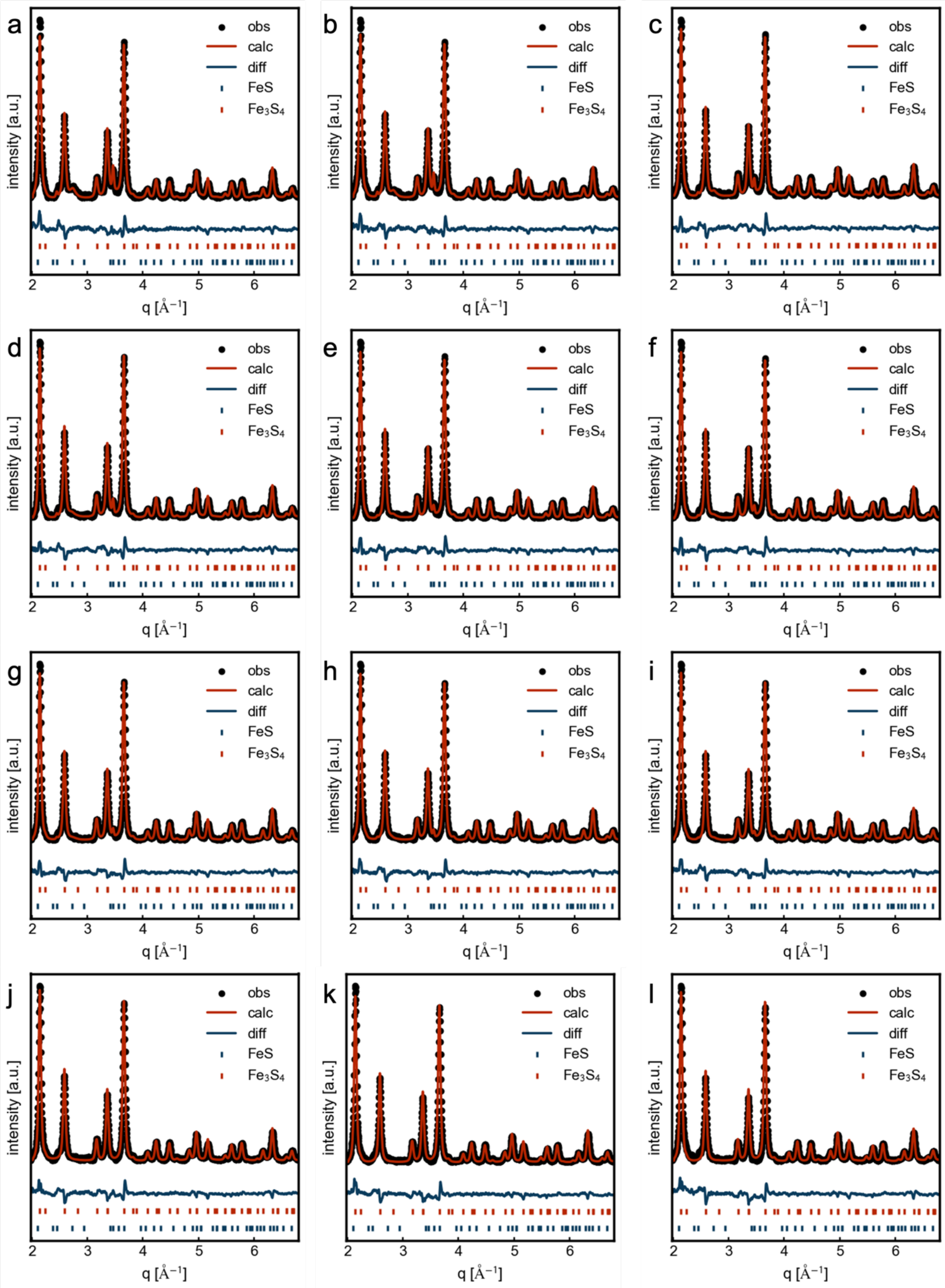

Figure 8.3.2.2 Sequential Rietveld refinement of the synthesis of Fe_3S_4 at 180°C at **(a)** 30 min, **(b)** 34 min, **(c)** 36 min, **(d)** 38 min, **(e)** 39 min, **(f)** 41 min, **(g)** 42 min, **(h)** 44 min, **(i)** 45 min, **(j)** 47 min, **(k)** 49 min, and **(l)** 52 min reaction time.

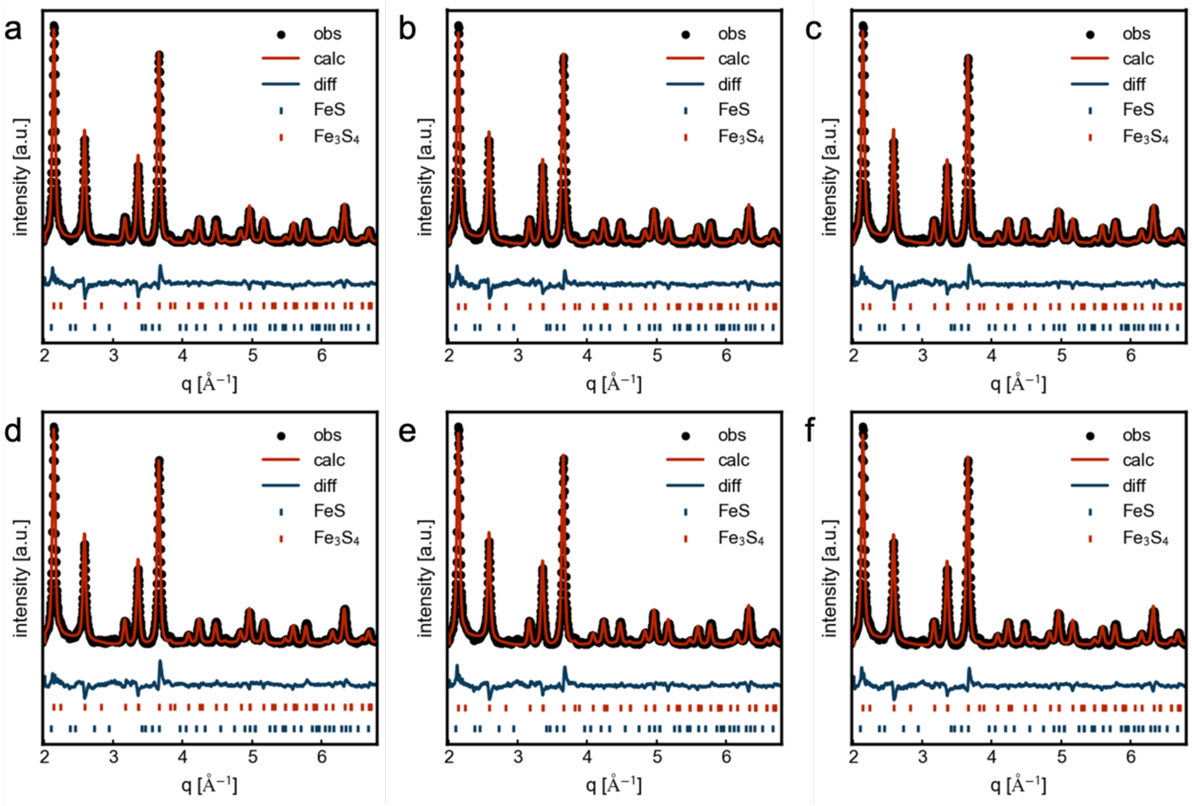

Figure 8.3.2.3. Sequential Rietveld refinement of the synthesis of Fe_3S_4 at 180 °C at **(a)** 52 min, **(b)** 59 min, **(c)** 62 min, **(d)** 66 min, **(e)** 71 min, and **(f)** 75 min reaction time.

Table. 8.3.2.1. Sequential Rietveld refinement results at different reaction times. The refined size of the FeS crystallites at a low fraction of FeS became unreasonable due to the limitation of this analysis.

Time (min)	fraction Fe_3S_4 (%)	fraction FeS (%)	size Fe_3S_4 (nm)	equatorial size FeS (nm)	axial size FeS (nm)	Rw (%)
10	0	100	-	1	13	51.3
13	3	97	14.3	3	72	50.7
14	5	95	15	3	37	40.8
15	24	76	17.1	3	55	45.4
16	38	62	18.3	4	40	36.9
18	53	47	17.5	3	37	29.6
19	58	42	16.8	3	51	29.9
20	62	38	18.2	3	56	29.8
21	65	35	16.8	3	58	30.1
23	67	33	17.1	2	63	27.3
25	68	32	18.5	2	55	37.2
26	74	26	17.8	2	112	25.6
27	76	24	17.4	2	87	25.0
30	82	18	17.9	3	94	24.6
34	87	13	18.6	3	62	24.6
36	91	9	19.4	3	54	23.8
38	90	10	20	2	780	24.9
39	94	6	19.8	3	1000	22.6
41	94	6	19.8	3	1000	21.9
42	95	5	19.8	2	1000	21.2
44	94	6	20	2	1000	20.8
45	97	3	20.3	3	1000	24.4
47	100	0	20.8	-	-	28.4
49	100	0	20.2	-	-	25.8
52	100	0	21.3	-	-	35.3
55	100	0	21.8	-	-	27.2
59	100	0	21.1	-	-	24.9
62	100	0	22.4	-	-	25.2
66	100	0	22.6	-	-	30.5
71	100	0	22.8	-	-	26.4
75	100	0	21.9	-	-	26.1

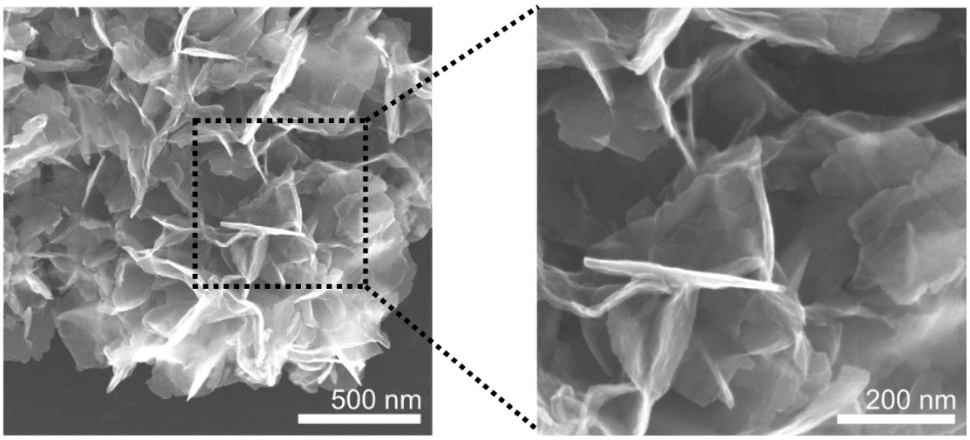

Figure 8.3.2.4. SEM images of the final product (Fe_3S_4 nanocrystals) show a platelet-like morphology.

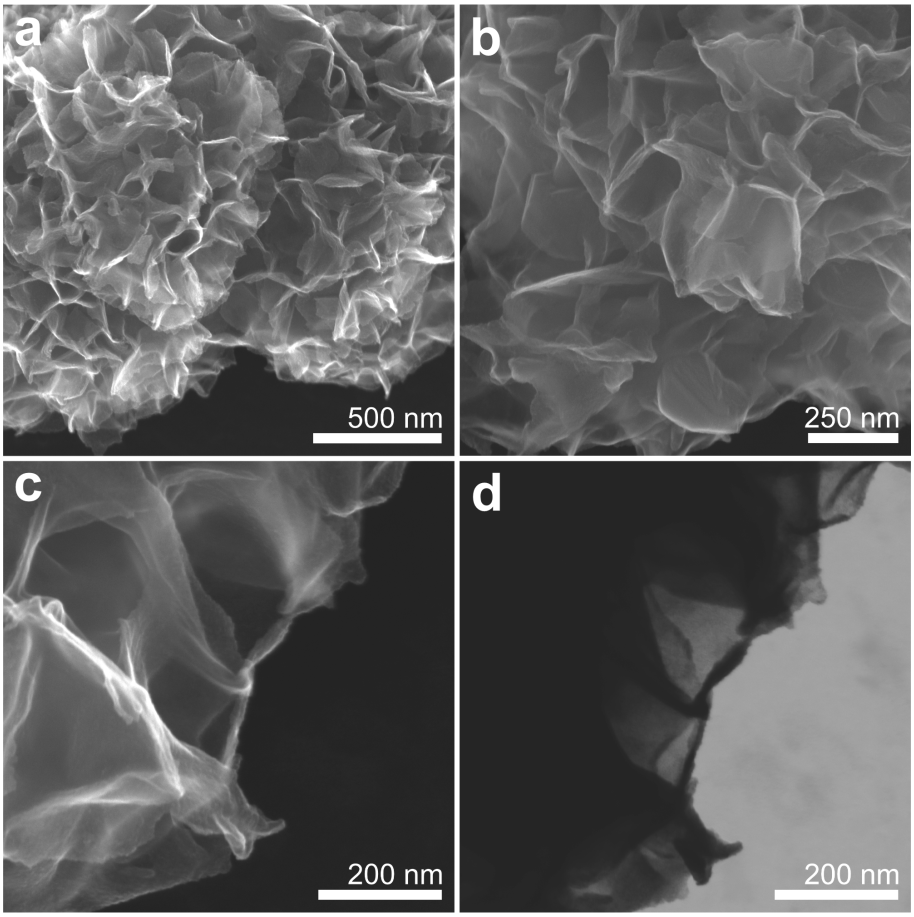

Figure 8.3.2.5. SEM **(a-c)**, and STEM **(d)** images of the final product (mixture of 61 % FeS and 39 % Fe_3S_4) at 140 °C. The SEM images were acquired and provided by Dr. Cecilia Zito.

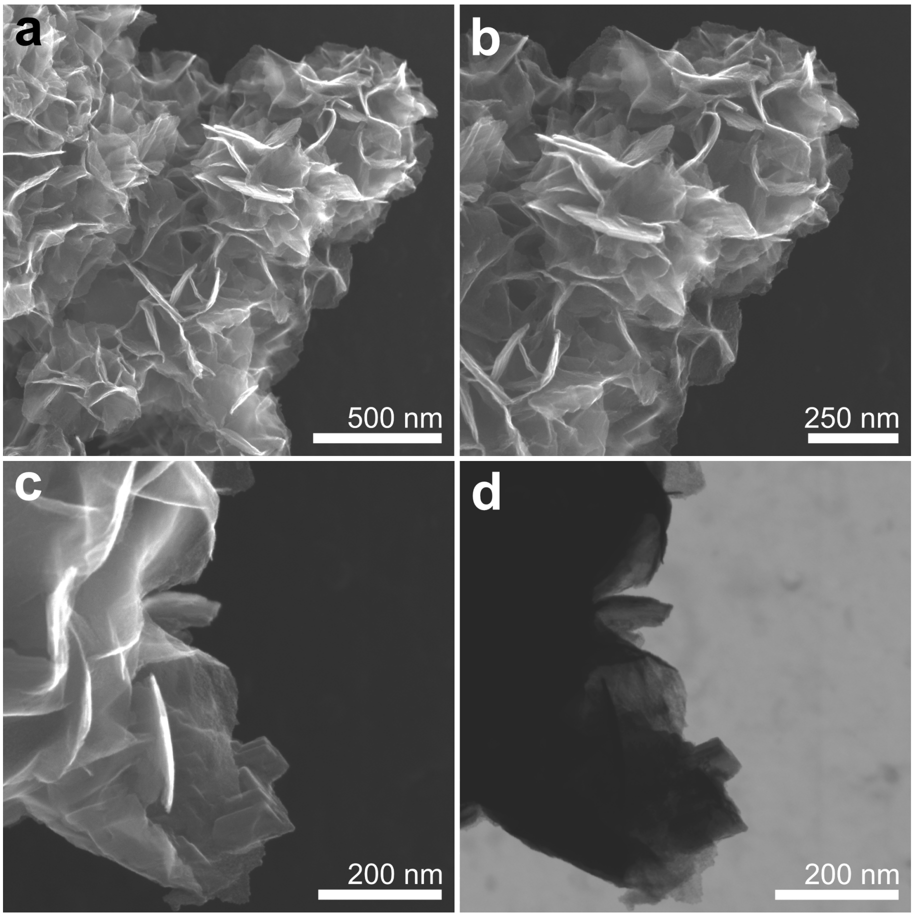

Figure 8.3.2.6. SEM **(a-c)**, and STEM **(d)** images of the final product (mixture of 7 % FeS and 93 % Fe_3S_4) at 160 °C.

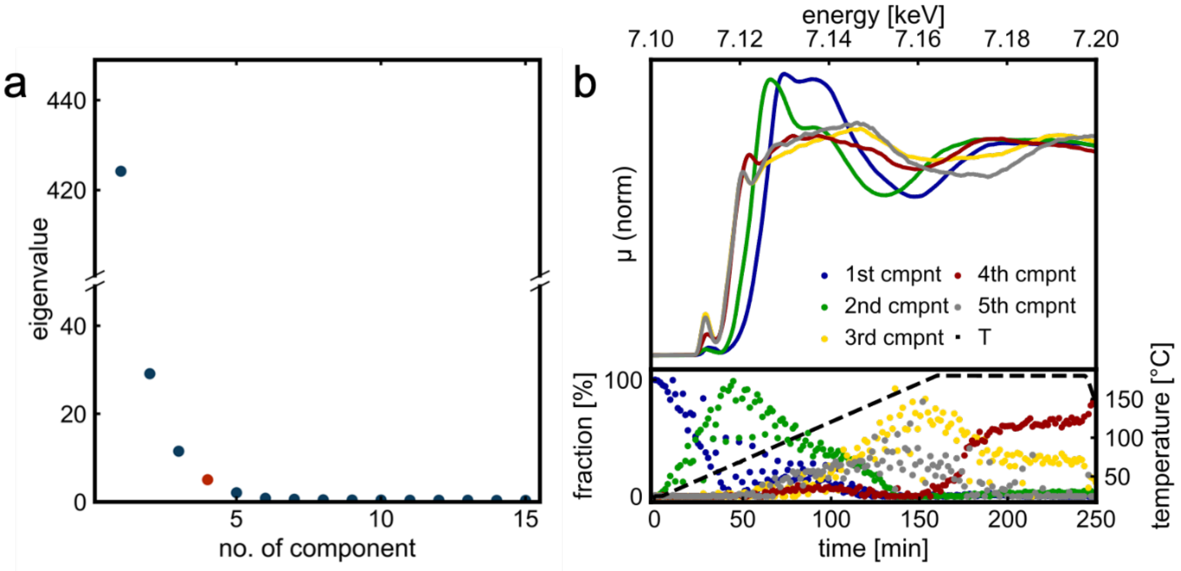

Figure 8.3.2.7. Scree plot of eigenvalues **(a)** suggests four components present during the *in situ* reaction. The linear behavior of eigenvalues corresponds to noise. To rule out the possibility of five components in the *in situ* run, we performed an MCR-ALS analysis with five

components **(b),** revealing that a 5th component strongly correlates in concentration profile and line shape with the 3rd component (FeS).

Table. 8.3.2.2. Fitting parameters of MCR-ALS analysis.

fitting error (%)	0.58
R^2	99.997
σ	0.0062

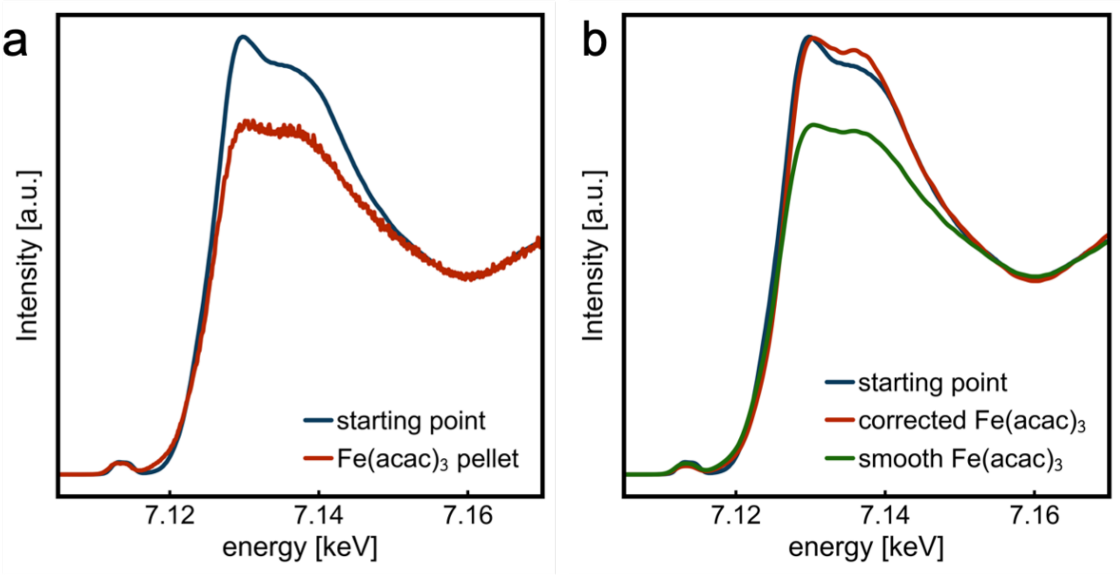

Figure 8.3.2.8. (a) experimental HERFD-XAS spectra of the reaction solution (blue), compared to a $Fe(acac)_3$ pellet (red). The spectral line shape matches, while the onset in the pellet appeared broader and the whiteline less intense. These differences are potentially based on increased self-absorption of the pellet. **(b)** smoothening and self-absorption correction can match the intensity of the whiteline of the reaction solution with the $Fe(acac)_3$ pellet.

Table. 8.3.2.3. Input parameters for the FEFF09 calculations of XANES (left) and vtc-XES data (right).

EDGE K	EDGE K
S02 1.0	S02 1.0
CONTROL 1 1 1 1 1 1	CONTROL 1 1 1 1 1 1
PRINT 1 0 0 0 0 3	PRINT 1 0 0 0 0 3
COREHOLE FSR	SCF 6 1 100 0.2 1
MULTIPOLE 2 0	COREHOLE RPA
SETEDGE	MULTIPOLE 2 0
EGRID	XES 7120 7085 0.25
e_grid -15 120.0 0.5	EXCHANGE 5 0 0.2 -1
EXCHANGE 0 1 0 -1	SETEDGE
LDOS -20 30 0.5	LDOS -40 0 0.2
XANES 10 0.05 0.05	REAL
FMS 9 0	

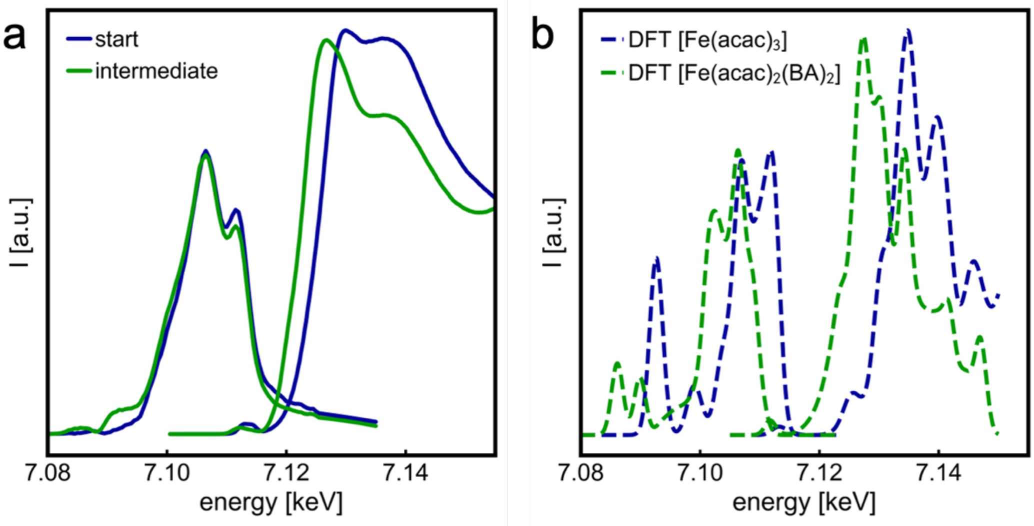

Figure 8.3.2.9. (a) Recovered HERFD-XAS spectra by MRC-ALS of the first and second components, and vtc-XES data at the start of the reaction and at around 40 min reaction time, where the second component is the dominant species in the reaction as determined by MCR-ALS. **(b)** Calculated XAS and XES spectra with DFT of a molecular unit of Fe(acac)$_3$ and of the [Fe(acac)$_2$(BA)$_2$] complex.

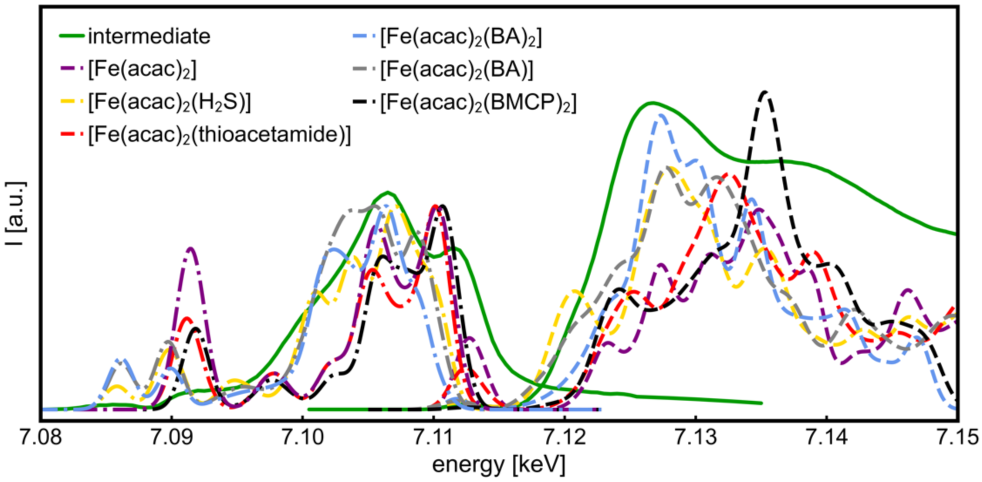

Figure 8.3.2.10. Experimental vtc-XES and HERFD-XAS data of the first intermediate, compared with DFT calculation of possible iron acetylacetonate structures coordinated with H_2S, thioacetamide, benzyl alcohol (BA), and benzyl mercaptan (BMCP).

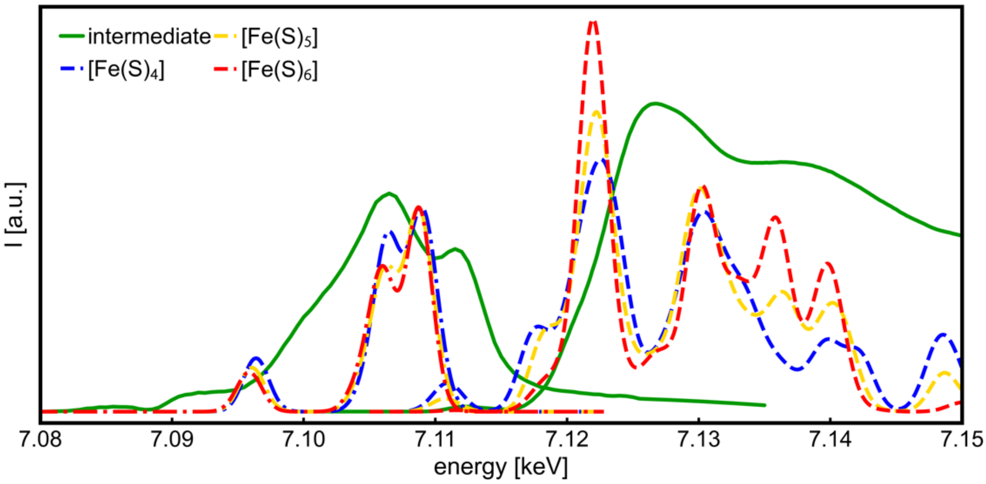

Figure 8.3.2.11. experimental vtc-XES and HERFD-XAS data of the first intermediate, compared with DFT calculation of tetrahedral FeS, pyramidal FeS, and octahedral FeS molecular cutouts.

Table. 8.3.2.4. ORCA input files for structural optimization and vtc-XES (left) and HERFD-XAS analysis (right).

```
!RKS B3LYP TightOpt TightSCF ZORA-def2-TZVP ZORA
!FREQ Largeprint Printbasis
%PAL NPROCS 16 END
%maxcore 20000
%xes
CoreOrb 0
OrbOp 0
end

…
```

```
!RKS B3LYP TightSCF ZORA-def2-TZVP D3BJ RIJCOSX ZORA
!Normalprint MOREAD
%maxcore 10000
%moinp "/orca_XES.gbw"
%tddft
orbwin[0]= 0,0,-1,-1 doquad true
nroots 300
maxdim 50
end
…
```

8.4 Supporting Information: Kβ RIXS of Zn references

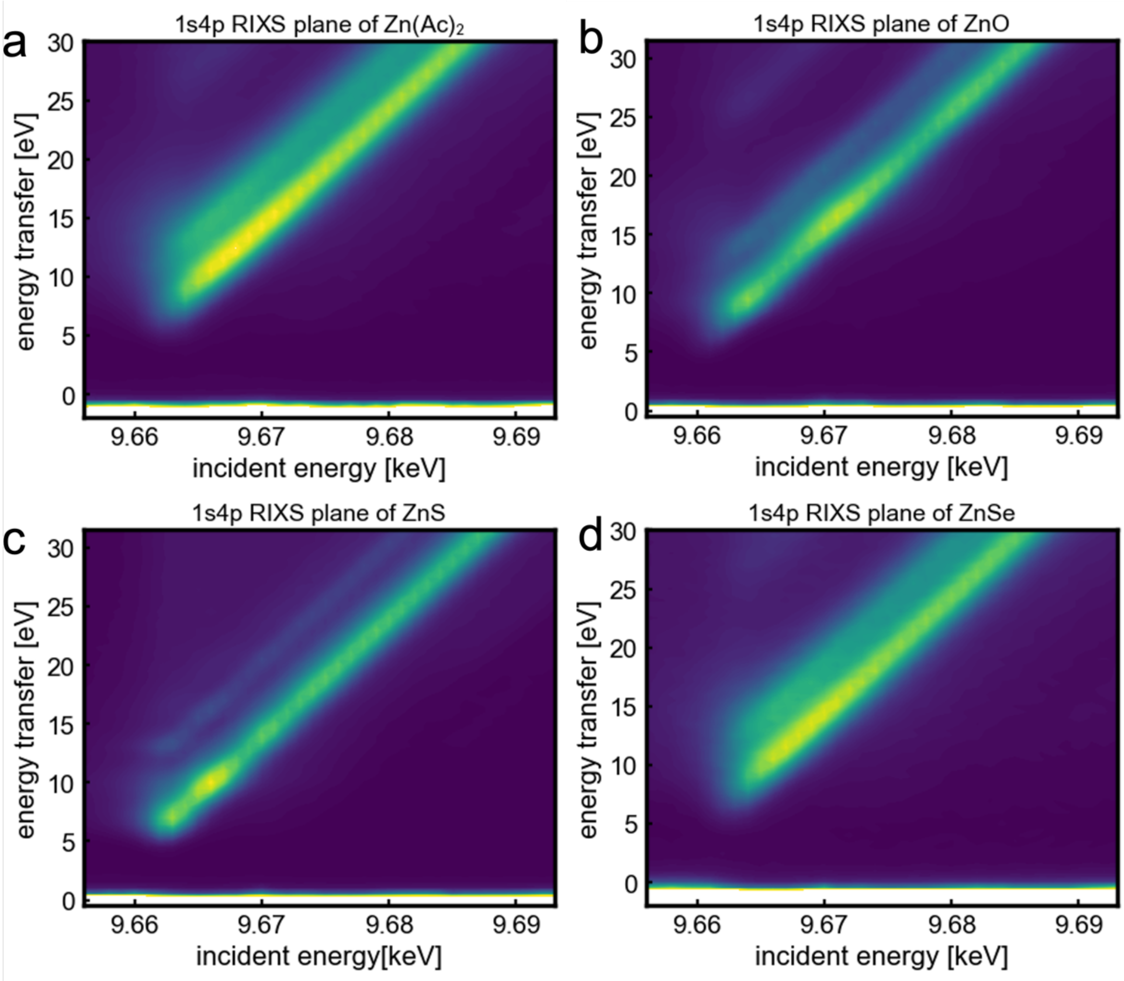

Figure 8.4.1. experimental Kβ RIXS maps of Zn(Ac)$_2$, (**a**, Sigma Aldrich 383317), ZnO (**b**, Sigma Aldrich 544906), ZnS (**c**, Sigma Aldrich 244627) and ZnSe (**d**).

Bibliography

(1) Alivisatos, A. P. Semiconductor Clusters, Nanocrystals, and Quantum Dots. *Science* **1996**, *271* (5251), 933-937. DOI: doi:10.1126/science.271.5251.933.

(2) Weller, H. Quantized Semiconductor Particles: A novel state of matter for materials science. *Advanced Materials* **1993**, *5* (2), 88-95. DOI: https://doi.org/10.1002/adma.19930050204.

(3) Empedocles, S. A.; Bawendi, M. G. Quantum-confined stark effect in single CdSe nanocrystallite quantum dots. *Science* **1997**, *278* (5346), 2114-2117.

(4) Yi, G.-C.; Wang, C.; Park, W. I. ZnO nanorods: synthesis, characterization and applications. *Semiconductor science and technology* **2005**, *20* (4), S22.

(5) Pérez-Juste, J.; Pastoriza-Santos, I.; Liz-Marzán, L. M.; Mulvaney, P. Gold nanorods: synthesis, characterization and applications. *Coordination chemistry reviews* **2005**, *249* (17-18), 1870-1901.

(6) Butler, S. Z.; Hollen, S. M.; Cao, L.; Cui, Y.; Gupta, J. A.; Gutiérrez, H. R.; Heinz, T. F.; Hong, S. S.; Huang, J.; Ismach, A. F.; et al. Progress, Challenges, and Opportunities in Two-Dimensional Materials Beyond Graphene. *ACS Nano* **2013**, *7* (4), 2898-2926. DOI: 10.1021/nn400280c.

(7) Cox, P. A. *Transition metal oxides: an introduction to their electronic structure and properties*; Oxford university press, 2010.

(8) Tokura, Y.; Nagaosa, N. Orbital physics in transition-metal oxides. *science* **2000**, *288* (5465), 462-468.

(9) Wang, H.; Li, J.; Li, K.; Lin, Y.; Chen, J.; Gao, L.; Nicolosi, V.; Xiao, X.; Lee, J.-M. Transition metal nitrides for electrochemical energy applications. *Chemical Society Reviews* **2021**, *50* (2), 1354-1390.

(10) Peng, X.; Yan, Y.; Jin, X.; Huang, C.; Jin, W.; Gao, B.; Chu, P. K. Recent advance and prospectives of electrocatalysts based on transition metal selenides for efficient water splitting. *Nano Energy* **2020**, *78*, 105234.

(11) Lu, T.; Dong, S.; Zhang, C.; Zhang, L.; Cui, G. Fabrication of transition metal selenides and their applications in energy storage. *Coordination Chemistry Reviews* **2017**, *332*, 75-99.

(12) Feng, W.; Pang, W.; Xu, Y.; Guo, A.; Gao, X.; Qiu, X.; Chen, W. Transition metal selenides for electrocatalytic hydrogen evolution reaction. *ChemElectroChem* **2020**, *7* (1), 31-54.

(13) Xu, X.; Liu, W.; Kim, Y.; Cho, J. Nanostructured transition metal sulfides for lithium ion batteries: progress and challenges. *Nano Today* **2014**, *9* (5), 604-630.

(14) Harris, S.; Chianelli, R. Catalysis by transition metal sulfides: A theoretical and experimental study of the relation between the synergic systems and the binary transition metal sulfides. *Journal of Catalysis* **1986**, *98* (1), 17-31.

(15) Thomson, J. W.; Nagashima, K.; Macdonald, P. M.; Ozin, G. A. From Sulfur−Amine Solutions to Metal Sulfide Nanocrystals: Peering into the Oleylamine−Sulfur Black Box. *Journal of the American Chemical Society* **2011**, *133* (13), 5036-5041. DOI: 10.1021/ja1109997.

(16) Makuła, P.; Pacia, M.; Macyk, W. How To Correctly Determine the Band Gap Energy of Modified Semiconductor Photocatalysts Based on UV–Vis Spectra. *The Journal of Physical Chemistry Letters* **2018**, *9* (23), 6814-6817. DOI: 10.1021/acs.jpclett.8b02892.

(17) Christiansen, T. L.; Cooper, S. R.; Jensen, K. M. Ø. There's no place like real-space: elucidating size-dependent atomic structure of nanomaterials using pair distribution function analysis. *Nanoscale Advances* **2020**, *2* (6), 2234-2254, 10.1039/D0NA00120A. DOI: 10.1039/D0NA00120A.

(18) Lafuerza, S.; Retegan, M.; Detlefs, B.; Chatterjee, R.; Yachandra, V.; Yano, J.; Glatzel, P. New reflections on hard X-ray photon-in/photon-out spectroscopy. *Nanoscale* **2020**, *12* (30), 16270-16284.

(19) Bauer, M. HERFD-XAS and valence-to-core-XES: new tools to push the limits in research with hard X-rays? *Physical Chemistry Chemical Physics* **2014**, *16* (27), 13827-13837, 10.1039/C4CP00904E. DOI: 10.1039/C4CP00904E.

(20) Kuzmin, A.; Chaboy, J. EXAFS and XANES analysis of oxides at the nanoscale. *IUCrJ* **2014**, *1* (6), 571-589.

(21) Billinge, S. J. L.; Levin, I. The Problem with Determining Atomic Structure at the Nanoscale. *Science* **2007**, *316* (5824), 561-565. DOI: doi:10.1126/science.1135080.

(22) Glatzel, P. A.-M., R.; Sokaras, D. Hard X-Ray Photon-in/Photon-out Spectroscopy: Instrumentation, Theory and Applications. In *X-Ray Absorption and X-Ray Emission Spectroscopy*, 2016; pp 125-153.

(23) Derelli, D. Investigating Nanostructured Materials by Multi-modal in situ X-ray Methods. Staats-und Universitätsbibliothek Hamburg Carl von Ossietzky, 2024.

(24) Grote, L. Imaging nanomaterials in solution–A multimodal approach using in situ X-ray ptychography, spectroscopy and scattering. Staats-und Universitätsbibliothek Hamburg Carl von Ossietzky, 2022.

(25) Joo, J.; Na, H. B.; Yu, T.; Yu, J. H.; Kim, Y. W.; Wu, F.; Zhang, J. Z.; Hyeon, T. Generalized and Facile Synthesis of Semiconducting Metal Sulfide Nanocrystals. *Journal of the American Chemical Society* **2003**, *125* (36), 11100-11105. DOI: 10.1021/ja0357902.

(26) Pauling, L. On the Stability of the S₈ Molbcule and the Structure of Fibrous Sulfur. *Proceedings of the National Academy of Sciences* **1949**, *35* (9), 495-499. DOI: doi:10.1073/pnas.35.9.495.

(27) Davis, R. E.; Nakshbendi, H. F. Sulfur in Amine Solvents. *Journal of the American Chemical Society* **1962**, *84* (11), 2085-2090. DOI: 10.1021/ja00870a017.

(28) Levi, T. G. G. *Gazzetta chimica Italiana*; Società chimica italiana, 1930.

(29) Hodgson, W. G.; Buckler, S. A.; Peters, G. Free Radicals in Amine Solutions of Elemental Sulfur. *Journal of the American Chemical Society* **1963**, *85* (5), 543-546. DOI: 10.1021/ja00888a012.

(30) Olsen, F. P.; Sasaki, Y. Reactions of sulfur with benzylamine. *Journal of the American Chemical Society* **1970**, *92* (12), 3812-3813. DOI: 10.1021/ja00715a059.

(31) Sasaki, Y.; Olsen, F. P. Reactions of Benzylamine with Sulfur. *Canadian Journal of Chemistry* **1971**, *49* (2), 283-293. DOI: 10.1139/v71-047.

(32) Mori, K.; Nakamura, Y. Reaction of sulfur compounds activated by amines. II. Reaction of sulfur and some aliphatic primary amines. *The Journal of Organic Chemistry* **1971**, *36* (20), 3041-3042. DOI: 10.1021/jo00819a030.

(33) LaMer, V. K.; Dinegar, R. H. Theory, Production and Mechanism of Formation of Monodispersed Hydrosols. *Journal of the American Chemical Society* **1950**, *72* (11), 4847-4854. DOI: 10.1021/ja01167a001.

(34) Sugimoto, T. Preparation of monodispersed colloidal particles. *Advances in Colloid and Interface Science* **1987**, *28*, 65-108. DOI: https://doi.org/10.1016/0001-8686(87)80009-X.

(35) Gibbs, J. W. On the equilibrium of heterogeneous substances. *American Journal of Science* **1878**, *3* (96), 441-458.

(36) Peng, X.; Wickham, J.; Alivisatos, A. P. Kinetics of II-VI and III-V Colloidal Semiconductor Nanocrystal Growth: “Focusing” of Size Distributions. *Journal of the American Chemical Society* **1998**, *120* (21), 5343-5344. DOI: 10.1021/ja9805425.

(37) de Mello Donegá, C.; Liljeroth, P.; Vanmaekelbergh, D. Physicochemical Evaluation of the Hot-Injection Method, a Synthesis Route for Monodisperse Nanocrystals. *Small* **2005**, *1* (12), 1152-1162. DOI: https://doi.org/10.1002/smll.200500239.

(38) Kwon, S. G.; Hyeon, T. Formation Mechanisms of Uniform Nanocrystals via Hot-Injection and Heat-Up Methods. *Small* **2011**, *7* (19), 2685-2702. DOI: https://doi.org/10.1002/smll.201002022.

(39) Murray, C. B.; Norris, D. J.; Bawendi, M. G. Synthesis and characterization of nearly monodisperse CdE (E = sulfur, selenium, tellurium) semiconductor nanocrystallites. *Journal of the American Chemical Society* **1993**, *115* (19), 8706-8715. DOI: 10.1021/ja00072a025.

(40) Talapin, D. V.; Rogach, A. L.; Kornowski, A.; Haase, M.; Weller, H. Highly Luminescent Monodisperse CdSe and CdSe/ZnS Nanocrystals Synthesized in a Hexadecylamine−Trioctylphosphine Oxide−Trioctylphospine Mixture. *Nano Letters* **2001**, *1* (4), 207-211. DOI: 10.1021/nl0155126.

(41) Kwon, S. G.; Hyeon, T. Colloidal Chemical Synthesis and Formation Kinetics of Uniformly Sized Nanocrystals of Metals, Oxides, and Chalcogenides. *Accounts of Chemical Research* **2008**, *41* (12), 1696-1709. DOI: 10.1021/ar8000537.

(42) Sun, S.; Murray, C. B.; Weller, D.; Folks, L.; Moser, A. Monodisperse FePt Nanoparticles and Ferromagnetic FePt Nanocrystal Superlattices. *Science* **2000**, *287* (5460), 1989-1992. DOI: doi:10.1126/science.287.5460.1989.

(43) Park, J.; An, K.; Hwang, Y.; Park, J.-G.; Noh, H.-J.; Kim, J.-Y.; Park, J.-H.; Hwang, N.-M.; Hyeon, T. Ultra-large-scale syntheses of monodisperse nanocrystals. *Nature Materials* **2004**, *3* (12), 891-895. DOI: 10.1038/nmat1251.

(44) Timonen, J. V. I.; Seppälä, E. T.; Ikkala, O.; Ras, R. H. A. From Hot-Injection Synthesis to Heating-Up Synthesis of Cobalt Nanoparticles: Observation of Kinetically Controllable Nucleation. *Angewandte Chemie International Edition* **2011**, *50* (9), 2080-2084. DOI: https://doi.org/10.1002/anie.201005600.

(45) Jana, N. R.; Chen, Y.; Peng, X. Size- and Shape-Controlled Magnetic (Cr, Mn, Fe, Co, Ni) Oxide Nanocrystals via a Simple and General Approach. *Chemistry of Materials* **2004**, *16* (20), 3931-3935. DOI: 10.1021/cm049221k.

(46) Kwon, S. G.; Piao, Y.; Park, J.; Angappane, S.; Jo, Y.; Hwang, N.-M.; Park, J.-G.; Hyeon, T. Kinetics of Monodisperse Iron Oxide Nanocrystal Formation by “Heating-Up” Process. *Journal of the American Chemical Society* **2007**, *129* (41), 12571-12584. DOI: 10.1021/ja074633q.

(47) Pan, D.; Wang, Q.; An, L. Controlled synthesis of monodisperse nanocrystals by a two-phase approach without the separation of nucleation and growth processes. *Journal of Materials Chemistry* **2009**, *19* (8), 1063-1073, 10.1039/B810972A. DOI: 10.1039/B810972A.

(48) Gebauer, D.; Wolf, S. E. Designing Solid Materials from Their Solute State: A Shift in Paradigms toward a Holistic Approach in Functional Materials Chemistry. *Journal of the American Chemical Society* **2019**, *141* (11), 4490-4504. DOI: 10.1021/jacs.8b13231.

(49) Ruiz-Agudo, E.; Burgos-Cara, A.; Ruiz-Agudo, C.; Ibañez-Velasco, A.; Cölfen, H.; Rodriguez-Navarro, C. A non-classical view on calcium oxalate precipitation and the role of citrate. *Nature Communications* **2017**, *8* (1), 768. DOI: 10.1038/s41467-017-00756-5.

(50) Lee, J.; Yang, J.; Kwon, S. G.; Hyeon, T. Nonclassical nucleation and growth of inorganic nanoparticles. *Nature Reviews Materials* **2016**, *1* (8), 16034. DOI: 10.1038/natrevmats.2016.34.

(51) Loiudice, A.; Buonsanti, R. Reaction intermediates in the synthesis of colloidal nanocrystals. *Nature Synthesis* **2022**, *1* (5), 344-351. DOI: 10.1038/s44160-022-00056-x.

(52) Simon, P.; Bahrig, L.; Baburin, I. A.; Formanek, P.; Röder, F.; Sickmann, J.; Hickey, S. G.; Eychmüller, A.; Lichte, H.; Kniep, R.; et al. Interconnection of Nanoparticles within 2D Superlattices of PbS/Oleic Acid Thin Films. *Advanced Materials* **2014**, *26* (19), 3042-3049. DOI: https://doi.org/10.1002/adma.201305667.

(53) Li, D.; Nielsen, M. H.; Lee, J. R. I.; Frandsen, C.; Banfield, J. F.; De Yoreo, J. J. Direction-Specific Interactions Control Crystal Growth by Oriented Attachment. *Science* **2012**, *336* (6084), 1014-1018. DOI: doi:10.1126/science.1219643.

(54) Sturm, E. V.; Cölfen, H. Mesocrystals: structural and morphogenetic aspects. *Chemical Society Reviews* **2016**, *45* (21), 5821-5833, 10.1039/C6CS00208K. DOI: 10.1039/C6CS00208K.

(55) Cölfen, H.; Antonietti, M. Mesocrystals: Inorganic Superstructures Made by Highly Parallel Crystallization and Controlled Alignment. *Angewandte Chemie International Edition* **2005**, *44* (35), 5576-5591. DOI: https://doi.org/10.1002/anie.200500496.

(56) Gebauer, D.; Kellermeier, M.; Gale, J. D.; Bergström, L.; Cölfen, H. Pre-nucleation clusters as solute precursors in crystallisation. *Chemical Society Reviews* **2014**, *43* (7), 2348-2371, 10.1039/C3CS60451A. DOI: 10.1039/C3CS60451A.

(57) Loh, N. D.; Sen, S.; Bosman, M.; Tan, S. F.; Zhong, J.; Nijhuis, C. A.; Král, P.; Matsudaira, P.; Mirsaidov, U. Multistep nucleation of nanocrystals in aqueous solution. *Nature Chemistry* **2017**, *9* (1), 77-82. DOI: 10.1038/nchem.2618.

(58) Wolf, S. L. P.; Caballero, L.; Melo, F.; Cölfen, H. Gel-Like Calcium Carbonate Precursors Observed by in situ AFM. *Langmuir* **2017**, *33* (1), 158-163. DOI: 10.1021/acs.langmuir.6b03974.

(59) Jehannin, M.; Rao, A.; Cölfen, H. New Horizons of Nonclassical Crystallization. *Journal of the American Chemical Society* **2019**, *141* (26), 10120-10136. DOI: 10.1021/jacs.9b01883.

(60) Als-Nielsen, J.; McMorrow, D. *Elements of Modern X-ray Physics*; Wiley, 2011.

(61) Egami, T.; Billinge, S. J. L. *Underneath the Bragg Peaks: Structural Analysis of Complex Materials*; Elsevier Science, 2003.

(62) Glatzel, P.; Juhin, A. X-ray Absorption and Emission Spectroscopy. *Local Structural Characterisation: Inorganic Materials Series* **2013**, 89-171.

(63) Neese, F. The ORCA program system. *WIREs Computational Molecular Science* **2012**, *2* (1), 73-78. DOI: https://doi.org/10.1002/wcms.81.

(64) Cutsail Iii, G. E.; DeBeer, S. Challenges and Opportunities for Applications of Advanced X-ray Spectroscopy in Catalysis Research. *ACS Catalysis* **2022**, *12* (10), 5864-5886. DOI: 10.1021/acscatal.2c01016.

(65) Klemeyer, L.; Gröne, T. L. R.; Zito, C. d. A.; Vasylieva, O.; Gumus Akcaalan, M.; Harouna-Mayer, S. Y.; Caddeo, F.; Steenbock, T.; Hussak, S.-A.; Kesavan, J. K.; et al. Utilizing High X-ray Energy Photon-In Photon-Out Spectroscopies and X-ray Scattering to Experimentally Assess the Emergence of Electronic and Atomic Structure of ZnS Nanorods. *Journal of the American Chemical Society* **2024**. DOI: 10.1021/jacs.4c10257.

(66) Holden, W. M.; Hoidn, O. R.; Ditter, A. S.; Seidler, G. T.; Kas, J.; Stein, J. L.; Cossairt, B. M.; Kozimor, S. A.; Guo, J.; Ye, Y. A compact dispersive refocusing Rowland circle X-ray emission spectrometer for laboratory, synchrotron, and XFEL applications. *Review of Scientific Instruments* **2017**, *88* (7).

(67) Senf, F.; Eggenstein, F.; Peatman, W. Simple, constant length Rowland circle monochromators for undulator radiation. *Review of scientific instruments* **1992**, *63* (1), 1326-1329.

(68) Glatzel, P.; Harris, A.; Marion, P.; Sikora, M.; Weng, T.-C.; Guilloud, C.; Lafuerza, S.; Rovezzi, M.; Detlefs, B.; Ducotte, L. The five-analyzer point-to-point scanning crystal spectrometer at

ESRF ID26. *Journal of Synchrotron Radiation* **2021**, *28* (1), 362-371. DOI: doi:10.1107/S1600577520015416.

(69) Rosa, A. D.; Garbarino, G.; Rodrigues, J.; Mijit, E.; Jacobs, J.; Bugnazet, D.; Pasternak, S.; Berruyer, G.; Moyne, A.; Clavel, C. New opportunities for high pressure X-ray absorption spectroscopy at ID24-DCM and BM23 with the Extremely Brilliant Source of the ESRF. *High Pressure Research* **2024**, *44* (3), 248-276.

(70) de Groot, F. M. F.; Glatzel, P.; Bergmann, U.; van Aken, P. A.; Barrea, R. A.; Klemme, S.; Hävecker, M.; Knop-Gericke, A.; Heijboer, W. M.; Weckhuysen, B. M. 1s2p Resonant Inelastic X-ray Scattering of Iron Oxides. *The Journal of Physical Chemistry B* **2005**, *109* (44), 20751-20762. DOI: 10.1021/jp054006s.

(71) Van Bokhoven, J. A.; Lamberti, C. *X-ray absorption and X-ray emission spectroscopy: theory and applications*; John Wiley & Sons, 2016.

(72) Kvashnina, K. O.; Scheinost, A. C. A Johann-type X-ray emission spectrometer at the Rossendorf beamline. *Journal of Synchrotron Radiation* **2016**, *23* (3), 836-841. DOI: doi:10.1107/S1600577516004483.

(73) Cutsail III, G. E.; Banerjee, R.; Zhou, A.; Que Jr, L.; Lipscomb, J. D.; DeBeer, S. High-resolution extended X-ray absorption fine structure analysis provides evidence for a longer Fe··· Fe distance in the Q intermediate of methane monooxygenase. *Journal of the American Chemical Society* **2018**, *140* (48), 16807-16820.

(74) Lima, F. A.; Bjornsson, R.; Weyhermüller, T.; Chandrasekaran, P.; Glatzel, P.; Neese, F.; DeBeer, S. High-resolution molybdenum K-edge X-ray absorption spectroscopy analyzed with time-dependent density functional theory. *Physical Chemistry Chemical Physics* **2013**, *15* (48), 20911-20920.

(75) Bjornsson, R.; Lima, F. A.; Spatzal, T.; Weyhermueller, T.; Glatzel, P.; Bill, E.; Einsle, O.; Neese, F.; DeBeer, S. Identification of a spin-coupled Mo (III) in the nitrogenase iron–molybdenum cofactor. *Chemical Science* **2014**, *5* (8), 3096-3103.

(76) Kowalska, J. K.; Henthorn, J. T.; Van Stappen, C.; Trncik, C.; Einsle, O.; Keavney, D.; DeBeer, S. X-ray Magnetic Circular Dichroism Spectroscopy Applied to Nitrogenase and Related Models: Experimental Evidence for a Spin-Coupled Molybdenum (III) Center. *Angewandte Chemie International Edition* **2019**, *58* (28), 9373-9377.

(77) Kuciakowski, J.; Kmita, A.; Lachowicz, D.; Wytrwal-Sarna, M.; Pitala, K.; Lafuerza, S.; Koziej, D.; Juhin, A.; Sikora, M. Selective magnetometry of superparamagnetic iron oxide nanoparticles in liquids. *Nanoscale* **2020**, *12* (31), 16420-16426, 10.1039/D0NR02866E. DOI: 10.1039/D0NR02866E.

(78) Chakraborty, U.; Bügel, P.; Fritsch, L.; Weigend, F.; Bauer, M.; Jacobi von Wangelin, A. Planar Iron Hydride Nanoclusters: Combined Spectroscopic and Theoretical Insights into Structures and Building Principles. *ChemistryOpen* **2021**, *10* (2), 265-271. DOI: https://doi.org/10.1002/open.202000307.

(79) Bergmann, U.; Horne, C. R.; Collins, T. J.; Workman, J. M.; Cramer, S. P. Chemical dependence of interatomic X-ray transition energies and intensities – a study of Mn Kβ″ and Kβ2,5 spectra. *Chemical Physics Letters* **1999**, *302* (1), 119-124. DOI: https://doi.org/10.1016/S0009-2614(99)00095-0.

(80) McCubbin Stepanic, O.; Ward, J.; Penner-Hahn, J. E.; Deb, A.; Bergmann, U.; DeBeer, S. Probing a Silent Metal: A Combined X-ray Absorption and Emission Spectroscopic Study of Biologically Relevant Zinc Complexes. *Inorganic Chemistry* **2020**, *59* (18), 13551-13560. DOI: 10.1021/acs.inorgchem.0c01931.

(81) Johst, F.; Rebmann, J.; Werners, H.; Klemeyer, L.; Kopula Kesavan, J.; Koziej, D.; Strelow, C.; Bester, G.; Mews, A.; Kipp, T. Exciton–Phonon Coupling in Single ZnCdSe-Dot/CdS-Rod Nanocrystals with Engineered Band Gaps from Type-II to Type-I. *ACS Photonics* **2024**, *11* (9), 3741-3749. DOI: 10.1021/acsphotonics.4c00931.

(82) Lee, N.; Petrenko, T.; Bergmann, U.; Neese, F.; DeBeer, S. Probing Valence Orbital Composition with Iron Kβ X-ray Emission Spectroscopy. *Journal of the American Chemical Society* **2010**, *132* (28), 9715-9727. DOI: 10.1021/ja101281e.

(83) Lancaster, K. M.; Roemelt, M.; Ettenhuber, P.; Hu, Y.; Ribbe, M. W.; Neese, F.; Bergmann, U.; DeBeer, S. X-ray emission spectroscopy evidences a central carbon in the nitrogenase iron-molybdenum cofactor. *Science* **2011**, *334* (6058), 974-977.

(84) Spatzal, T.; Aksoyoglu, M.; Zhang, L.; Andrade, S. L.; Schleicher, E.; Weber, S.; Rees, D. C.; Einsle, O. Evidence for interstitial carbon in nitrogenase FeMo cofactor. *Science* **2011**, *334* (6058), 940-940.

(85) Lancaster, K. M.; Hu, Y.; Bergmann, U.; Ribbe, M. W.; DeBeer, S. X-ray spectroscopic observation of an interstitial carbide in NifEN-bound FeMoco precursor. *Journal of the American Chemical Society* **2013**, *135* (2), 610-612.

(86) Rees, J. A.; Bjornsson, R.; Kowalska, J. K.; Lima, F. A.; Schlesier, J.; Sippel, D.; Weyhermüller, T.; Einsle, O.; Kovacs, J. A.; DeBeer, S. Comparative electronic structures of nitrogenase FeMoco and FeVco. *Dalton Transactions* **2017**, *46* (8), 2445-2455.

(87) Fritsch, L.; Rehsies, P.; Barakat, W.; Estes, D. P.; Bauer, M. Detection and Characterization of Hydride Ligands in Copper Complexes by Hard X-Ray Spectroscopy. *Chemistry – A European Journal* **2024**, *30* (36), e202400357. DOI: https://doi.org/10.1002/chem.202400357.

(88) Pushkar, Y.; Long, X.; Glatzel, P.; Brudvig, G. W.; Dismukes, G. C.; Collins, T. J.; Yachandra, V. K.; Yano, J.; Bergmann, U. Direct Detection of Oxygen Ligation to the Mn4Ca Cluster of Photosystem II by X-ray Emission Spectroscopy. *Angewandte Chemie International Edition* **2010**, *49* (4), 800-803.

(89) Smolentsev, G.; Soldatov, A. V.; Messinger, J.; Merz, K.; Weyhermüller, T.; Bergmann, U.; Pushkar, Y.; Yano, J.; Yachandra, V. K.; Glatzel, P. X-ray emission spectroscopy to study ligand valence orbitals in Mn coordination complexes. *Journal of the American Chemical Society* **2009**, *131* (36), 13161-13167.

(90) Mathe, Z.; Pantazis, D. A.; Lee, H. B.; Gnewkow, R.; Van Kuiken, B. E.; Agapie, T.; DeBeer, S. Calcium valence-to-core X-ray emission spectroscopy: A sensitive probe of oxo protonation in structural models of the oxygen-evolving complex. *Inorganic Chemistry* **2019**, *58* (23), 16292-16301.

(91) Lassalle-Kaiser, B.; Boron III, T. T.; Krewald, V.; Kern, J.; Beckwith, M. A.; Delgado-Jaime, M. U.; Schroeder, H.; Alonso-Mori, R.; Nordlund, D.; Weng, T.-C. Experimental and computational X-ray emission spectroscopy as a direct probe of protonation states in oxo-bridged MnIV dimers relevant to redox-active metalloproteins. *Inorganic chemistry* **2013**, *52* (22), 12915-12922.

(92) Pollock, C. J.; DeBeer, S. Insights into the Geometric and Electronic Structure of Transition Metal Centers from Valence-to-Core X-ray Emission Spectroscopy. *Accounts of Chemical Research* **2015**, *48* (11), 2967-2975. DOI: 10.1021/acs.accounts.5b00309.

(93) Castillo, R. G.; Hahn, A. W.; Van Kuiken, B. E.; Henthorn, J. T.; McGale, J.; DeBeer, S. Probing Physical Oxidation State by Resonant X-ray Emission Spectroscopy: Applications to Iron Model Complexes and Nitrogenase. *Angewandte Chemie* **2021**, *133* (18), 10200-10209.

(94) Pollock, C. J.; Grubel, K.; Holland, P. L.; DeBeer, S. Experimentally quantifying small-molecule bond activation using valence-to-core X-ray emission spectroscopy. *Journal of the American Chemical Society* **2013**, *135* (32), 11803-11808.

(95) Cutsail III, G. E.; Gagnon, N. L.; Spaeth, A. D.; Tolman, W. B.; DeBeer, S. Valence-to-Core X-ray Emission Spectroscopy as a Probe of O− O Bond Activation in Cu2O2 Complexes. *Angewandte Chemie International Edition* **2019**, *58* (27), 9114-9119.

(96) Lu, T.-T.; Weng, T.-C.; Liaw, W.-F. X-Ray Emission Spectroscopy: A Spectroscopic Measure for the Determination of NO Oxidation States in Fe–NO Complexes. *Angewandte Chemie International Edition* **2014**, *53* (43), 11562-11566. DOI: https://doi.org/10.1002/anie.201407603.

(97) Phu, P. N.; Gutierrez, C. E.; Kundu, S.; Sokaras, D.; Kroll, T.; Warren, T. H.; Stieber, S. C. E. Quantification of Ni–N–O Bond Angles and NO Activation by X-ray Emission Spectroscopy. *Inorganic chemistry* **2020**, *60* (2), 736-744.

(98) Giordanino, F.; Borfecchia, E.; Lomachenko, K. A.; Lazzarini, A.; Agostini, G.; Gallo, E.; Soldatov, A. V.; Beato, P.; Bordiga, S.; Lamberti, C. Interaction of NH3 with Cu-SSZ-13 catalyst: a complementary FTIR, XANES, and XES study. *The journal of physical chemistry letters* **2014**, *5* (9), 1552-1559.

(99) Lomachenko, K. A.; Borfecchia, E.; Negri, C.; Berlier, G.; Lamberti, C.; Beato, P.; Falsig, H.; Bordiga, S. The Cu-CHA deNO x catalyst in action: temperature-dependent NH3-assisted selective catalytic reduction monitored by operando XAS and XES. *Journal of the American Chemical Society* **2016**, *138* (37), 12025-12028.

(100) Bergmann, U.; Kern, J.; Schoenlein, R. W.; Wernet, P.; Yachandra, V. K.; Yano, J. Using X-ray free-electron lasers for spectroscopy of molecular catalysts and metalloenzymes. *Nature Reviews Physics* **2021**, *3* (4), 264-282.

(101) Gilbert, T. L. Hohenberg-Kohn theorem for nonlocal external potentials. *Physical Review B* **1975**, *12* (6), 2111-2120. DOI: 10.1103/PhysRevB.12.2111.

(102) Kohn, W.; Sham, L. Density functional theory. In *Conference Proceedings-Italian Physical Society*, 1996; Editrice Compositori: Vol. 49, pp 561-572.

(103) Bickelhaupt, F. M.; Baerends, E. J. Kohn-Sham density functional theory: predicting and understanding chemistry. *Reviews in computational chemistry* **2000**, 1-86.

(104) Ernzerhof, M.; Scuseria, G. E. Assessment of the Perdew–Burke–Ernzerhof exchange-correlation functional. *The Journal of chemical physics* **1999**, *110* (11), 5029-5036.

(105) Stampfl, C.; Van de Walle, C. G. Density-functional calculations for III-V nitrides using the local-density approximation and the generalized gradient approximation. *Physical Review B* **1999**, *59* (8), 5521.

(106) Perdew, J. P.; Burke, K.; Ernzerhof, M. Generalized gradient approximation made simple. *Physical review letters* **1996**, *77* (18), 3865.

(107) Tirado-Rives, J.; Jorgensen, W. L. Performance of B3LYP density functional methods for a large set of organic molecules. *Journal of chemical theory and computation* **2008**, *4* (2), 297-306.

(108) Théry, V.; Rinaldi, D.; Rivail, J. L.; Maigret, B.; Ferenczy, G. G. Quantum mechanical computations on very large molecular systems: The local self-consistent field method. *Journal of computational chemistry* **1994**, *15* (3), 269-282.

(109) Neese, F.; Wennmohs, F.; Becker, U.; Riplinger, C. The ORCA quantum chemistry program package. *The Journal of Chemical Physics* **2020**, *152* (22). DOI: 10.1063/5.0004608 (acccessed 11/20/2024).

(110) Head, J. D.; Zerner, M. C. A Broyden—Fletcher—Goldfarb—Shanno optimization procedure for molecular geometries. *Chemical physics letters* **1985**, *122* (3), 264-270.

(111) Weigend, F. Accurate Coulomb-fitting basis sets for H to Rn. *Physical chemistry chemical physics* **2006**, *8* (9), 1057-1065.

(112) Schröder, H.; Hühnert, J.; Schwabe, T. Evaluation of DFT-D3 dispersion corrections for various structural benchmark sets. *The Journal of chemical physics* **2017**, *146* (4).

(113) Neese, F. An improvement of the resolution of the identity approximation for the formation of the Coulomb matrix. *Journal of computational chemistry* **2003**, *24* (14), 1740-1747.

(114) Neese, F.; Wennmohs, F.; Hansen, A.; Becker, U. Efficient, approximate and parallel Hartree–Fock and hybrid DFT calculations. A 'chain-of-spheres' algorithm for the Hartree–Fock exchange. *Chemical Physics* **2009**, *356* (1), 98-109. DOI: https://doi.org/10.1016/j.chemphys.2008.10.036.

(115) Kossmann, S.; Neese, F. Efficient structure optimization with second-order many-body perturbation theory: The RIJCOSX-MP2 method. *Journal of chemical theory and computation* **2010**, *6* (8), 2325-2338.

(116) Derelli, D.; Caddeo, F.; Frank, K.; Krötzsch, K.; Ewerhardt, P.; Krüger, M.; Medicus, S.; Klemeyer, L.; Skiba, M.; Ruhmlieb, C.; et al. Photodegradation of CuBi2O4 Films Evidenced by Fast Formation of Metallic Bi using Operando Surface-sensitive X-ray Scattering. *Angewandte Chemie International Edition* **2023**, *62* (43), e202307948. DOI: 10.1002/anie.202307948.

(117) Juhas, P.; Davis, T.; Farrow, C. L.; Billinge, S. J. L. PDFgetX3: a rapid and highly automatable program for processing powder diffraction data into total scattering pair distribution functions. *Journal of Applied Crystallography* **2013**, *46* (2), 560-566. DOI: doi:10.1107/S0021889813005190.

(118) Farrow, C. L.; Billinge, S. J. L. Relationship between the atomic pair distribution function and small-angle scattering: implications for modeling of nanoparticles. *Acta Crystallographica Section A* **2009**, *65* (3), 232-239. DOI: doi:10.1107/S0108767309009714.

(119) Aalling-Frederiksen, O.; Pittkowski, R. K.; Anker, A. S.; Quinson, J.; Klemeyer, L.; Frandsen, B. A.; Koziej, D.; Jensen, K. M. Ø. Effect of solvothermal synthesis parameters on the crystallite size and atomic structure of cobalt iron oxide nanoparticles. *Nanoscale Advances* **2024**, *6* (23), 5939-5948, 10.1039/D4NA00590B. DOI: 10.1039/D4NA00590B.

(120) Derelli, D.; Frank, K.; Grote, L.; Mancini, F.; Dippel, A.-C.; Gutowski, O.; Nickel, B.; Koziej, D. Direct Synthesis of CuPd Icosahedra Supercrystals Studied by In Situ X-Ray Scattering. *Small* **2024**, *20* (32), 2311714. DOI: https://doi.org/10.1002/smll.202311714.

(121) Li, T.; Senesi, A. J.; Lee, B. Small Angle X-ray Scattering for Nanoparticle Research. *Chemical Reviews* **2016**, *116* (18), 11128-11180. DOI: 10.1021/acs.chemrev.5b00690.

(122) Koziej, D. Revealing Complexity of Nanoparticle Synthesis in Solution by in Situ Hard X-ray Spectroscopy—Today and Beyond. *Chemistry of Materials* **2016**, *28* (8), 2478-2490. DOI: 10.1021/acs.chemmater.6b00486.

(123) Wang, J.; Hsu, C.-S.; Wu, T.-S.; Chan, T.-S.; Suen, N.-T.; Lee, J.-F.; Chen, H. M. In situ X-ray spectroscopies beyond conventional X-ray absorption spectroscopy on deciphering dynamic configuration of electrocatalysts. *Nature Communications* **2023**, *14* (1), 6576. DOI: 10.1038/s41467-023-42370-8.

(124) Friebel, D.; Miller, D. J.; Nordlund, D.; Ogasawara, H.; Nilsson, A. Degradation of Bimetallic Model Electrocatalysts: An In Situ X-Ray Absorption Spectroscopy Study. *Angewandte Chemie International Edition* **2011**, *50* (43), 10190-10192. DOI: https://doi.org/10.1002/anie.201101620.

(125) Merte, L. R.; Behafarid, F.; Miller, D. J.; Friebel, D.; Cho, S.; Mbuga, F.; Sokaras, D.; Alonso-Mori, R.; Weng, T.-C.; Nordlund, D.; et al. Electrochemical Oxidation of Size-Selected Pt Nanoparticles Studied Using in Situ High-Energy-Resolution X-ray Absorption Spectroscopy. *ACS Catalysis* **2012**, *2* (11), 2371-2376. DOI: 10.1021/cs300494f.

(126) Kleymenov, E.; Sa, J.; Abu-Dahrieh, J.; Rooney, D.; van Bokhoven, J. A.; Troussard, E.; Szlachetko, J.; Safonova, O. V.; Nachtegaal, M. Structure of the methanol synthesis catalyst determined by in situHERFD XAS and EXAFS. *Catalysis Science & Technology* **2012**, *2* (2), 373-378, 10.1039/C1CY00277E. DOI: 10.1039/C1CY00277E.

(127) Friebel, D.; Mbuga, F.; Rajasekaran, S.; Miller, D. J.; Ogasawara, H.; Alonso-Mori, R.; Sokaras, D.; Nordlund, D.; Weng, T.-C.; Nilsson, A. Structure, Redox Chemistry, and Interfacial Alloy Formation in Monolayer and Multilayer Cu/Au(111) Model Catalysts for CO2 Electroreduction. *The Journal of Physical Chemistry C* **2014**, *118* (15), 7954-7961. DOI: 10.1021/jp412000j.

(128) Gao, D.; Sinev, I.; Scholten, F.; Arán-Ais, R. M.; Divins, N. J.; Kvashnina, K.; Timoshenko, J.; Roldan Cuenya, B. Selective CO2 Electroreduction to Ethylene and Multicarbon Alcohols via Electrolyte-Driven Nanostructuring. *Angewandte Chemie International Edition* **2019**, *58* (47), 17047-17053. DOI: https://doi.org/10.1002/anie.201910155.

(129) Friebel, D.; Bajdich, M.; Yeo, B. S.; Louie, M. W.; Miller, D. J.; Sanchez Casalongue, H.; Mbuga, F.; Weng, T.-C.; Nordlund, D.; Sokaras, D.; et al. On the chemical state of Co oxide electrocatalysts during alkaline water splitting. *Physical Chemistry Chemical Physics* **2013**, *15* (40), 17460-17467, 10.1039/C3CP52981A. DOI: 10.1039/C3CP52981A.

(130) Hung, S.-F.; Chan, Y.-T.; Chang, C.-C.; Tsai, M.-K.; Liao, Y.-F.; Hiraoka, N.; Hsu, C.-S.; Chen, H. M. Identification of Stabilizing High-Valent Active Sites by Operando High-Energy Resolution Fluorescence-Detected X-ray Absorption Spectroscopy for High-Efficiency Water Oxidation. *Journal of the American Chemical Society* **2018**, *140* (49), 17263-17270. DOI: 10.1021/jacs.8b10722.

(131) Morgan, L. M.; Loche, D.; Corrias, A.; Hayama, S.; Mountjoy, G. Using Ex Situ and In Situ HERFD-XANES to Reveal the Superior Oxidation and Reduction Cycling of Ceria Nanocubes Dispersed in Silica Aerogel. *The Journal of Physical Chemistry C* **2023**, *127* (39), 19554-19562. DOI: 10.1021/acs.jpcc.3c03785.

(132) Grote, L.; Zito, C. A.; Frank, K.; Dippel, A.-C.; Reisbeck, P.; Pitala, K.; Kvashnina, K. O.; Bauters, S.; Detlefs, B.; Ivashko, O.; et al. X-ray studies bridge the molecular and macro length scales during the emergence of CoO assemblies. *Nature Communications* **2021**, *12* (1), 4429. DOI: 10.1038/s41467-021-24557-z.

(133) Staniuk, M.; Hirsch, O.; Kränzlin, N.; Böhlen, R.; van Beek, W.; Abdala, P. M.; Koziej, D. Puzzling Mechanism behind a Simple Synthesis of Cobalt and Cobalt Oxide Nanoparticles: In Situ Synchrotron X-ray Absorption and Diffraction Studies. *Chemistry of Materials* **2014**, *26* (6), 2086-2094. DOI: 10.1021/cm500090r.

(134) Harouna-Mayer, S. Y.; Kesavan, J. K.; Caddeo, F.; Belgardt, L.; Hsu, C.-S.; Klemeyer, L.; Kipping, L.; Akcaalan, M. G.; Groene, T. R. L.; Koeppen, A. Cation-site Disordered Cu3PdN Nanoparticles for Hydrogen Evolution Electrocatalysis. **2024**.

(135) Chen, Z.-G.; Cheng, L.; Xu, H.-Y.; Liu, J.-Z.; Zou, J.; Sekiguchi, T.; Lu, G. Q.; Cheng, H.-M. ZnS Branched Architectures as Optoelectronic Devices and Field Emitters. *Advanced Materials* **2010**, *22* (21), 2376-2380. DOI: 10.1002/adma.200903643.

(136) Zeng, X.; Pramana, S. S.; Batabyal, S. K.; Mhaisalkar, S. G.; Chen, X.; Jinesh, K. B. Low temperature synthesis of wurtzite zinc sulfide (ZnS) thin films by chemical spray pyrolysis.

Physical Chemistry Chemical Physics **2013**, *15* (18), 6763-6768, 10.1039/C3CP43470B. DOI: 10.1039/C3CP43470B.

(137) Lange, T.; Reichenberger, S.; Ristig, S.; Rohe, M.; Strunk, J.; Barcikowski, S.; Schlögl, R. Zinc sulfide for photocatalysis: White angel or black sheep? *Progress in Materials Science* **2022**, *124*, 100865. DOI: 10.1016/j.pmatsci.2021.100865.

(138) Hao, X.; Wang, Y.; Zhou, J.; Cui, Z.; Wang, Y.; Zou, Z. Zinc vacancy-promoted photocatalytic activity and photostability of ZnS for efficient visible-light-driven hydrogen evolution. *Applied Catalysis B: Environmental* **2018**, *221*, 302-311. DOI: 10.1016/j.apcatb.2017.09.006.

(139) Mróz, K.; Kobielusz, M.; Orzeł, Ł.; Macyk, W. Spectroscopic and Spectroelectrochemical Studies on Redox Properties of Zinc Sulfide and Their Consequences on Photocatalytic Activity. *The Journal of Physical Chemistry C* **2023**, *127* (35), 17366-17376. DOI: 10.1021/acs.jpcc.3c04298.

(140) Boercker, J. E.; Woodall, D. L.; Cunningham, P. D.; Placencia, D.; Ellis, C. T.; Stewart, M. H.; Brintlinger, T. H.; Stroud, R. M.; Tischler, J. G. Synthesis and Characterization of PbS/ZnS Core/Shell Nanocrystals. *Chemistry of Materials* **2018**, *30* (12), 4112-4123. DOI: 10.1021/acs.chemmater.8b01421.

(141) Ji, B.; Koley, S.; Slobodkin, I.; Remennik, S.; Banin, U. ZnSe/ZnS Core/Shell Quantum Dots with Superior Optical Properties through Thermodynamic Shell Growth. *Nano Letters* **2020**, *20* (4), 2387-2395. DOI: 10.1021/acs.nanolett.9b05020.

(142) Fang, X.; Wu, L.; Hu, L. ZnS Nanostructure Arrays: A Developing Material Star. *Advanced Materials* **2011**, *23* (5), 585-598. DOI: 10.1002/adma.201003624.

(143) Rajaitha, P. M.; Hajra, S.; Sahu, M.; Mistewicz, K.; Toroń, B.; Abolhassani, R.; Panda, S.; Mishra, Y. K.; Kim, H. J. Unraveling highly efficient nanomaterial photocatalyst for pollutant removal: a comprehensive review and future progress. *Materials Today Chemistry* **2022**, *23*, 100692. DOI: 10.1016/j.mtchem.2021.100692.

(144) Scott, S. D.; Barnes, H. L. Sphalerite-wurtzite equilibria and stoichiometry. *Geochimica et Cosmochimica Acta* **1972**, *36* (11), 1275-1295. DOI: 10.1016/0016-7037(72)90049-X.

(145) Li, Y.; Tan, W.; Wu, Y. Phase transition between sphalerite and wurtzite in ZnS optical ceramic materials. *Journal of the European Ceramic Society* **2020**, *40* (5), 2130-2140. DOI: 10.1016/j.jeurceramsoc.2019.12.045.

(146) Sekhar Tiwary, C.; Srivastava, C.; Kumbhakar, P. Onset of sphalerite to wurtzite transformation in ZnS nanoparticles. *Journal of Applied Physics* **2011**, *110* (3). DOI: 10.1063/1.3622625 (acccessed 6/11/2024).

(147) Dai, L.; Lesyuk, R.; Karpulevich, A.; Torche, A.; Bester, G.; Klinke, C. From Wurtzite Nanoplatelets to Zinc Blende Nanorods: Simultaneous Control of Shape and Phase in Ultrathin ZnS Nanocrystals. *The Journal of Physical Chemistry Letters* **2019**, *10* (14), 3828-3835. DOI: 10.1021/acs.jpclett.9b01466.

(148) Yu, J. H.; Joo, J.; Park, H. M.; Baik, S.-I.; Kim, Y. W.; Kim, S. C.; Hyeon, T. Synthesis of Quantum-Sized Cubic ZnS Nanorods by the Oriented Attachment Mechanism. *Journal of the American Chemical Society* **2005**, *127* (15), 5662-5670. DOI: 10.1021/ja044593f.

(149) Li, Y.; Li, X.; Yang, C.; Li, Y. Ligand-Controlling Synthesis and Ordered Assembly of ZnS Nanorods and Nanodots. *The Journal of Physical Chemistry B* **2004**, *108* (41), 16002-16011. DOI: 10.1021/jp0489018.

(150) Zhao, Y.; Zhang, Y.; Zhu, H.; Hadjipanayis, G. C.; Xiao, J. Q. Low-Temperature Synthesis of Hexagonal (Wurtzite) ZnS Nanocrystals. *Journal of the American Chemical Society* **2004**, *126* (22), 6874-6875. DOI: 10.1021/ja048650g.

(151) Ludi, B.; Olliges-Stadler, I.; Rossell, M. D.; Niederberger, M. Extension of the benzyl alcohol route to metal sulfides: “nonhydrolytic” thio sol–gel synthesis of ZnS and SnS2. *Chemical Communications* **2011**, *47* (18), 5280-5282. DOI: 10.1039/C1CC10856E.

(152) Islam, H.-U.; Roffey, A.; Hollingsworth, N.; Bras, W.; Sankar, G.; De Leeuw, N. H.; Hogarth, G. Understanding the role of zinc dithiocarbamate complexes as single source precursors to ZnS nanomaterials. *Nanoscale Advances* **2020**, *2* (2), 798-807, 10.1039/C9NA00665F. DOI: 10.1039/C9NA00665F.

(153) Ströh, J.; Hess, T.; Ohrt, L.; Fritzsch, H.; Etter, M.; Dippel, A. C.; Nyamen, L. D.; Terraschke, H. Detailed insights into the formation pathway of CdS and ZnS in solution: a multi-modal in situ characterisation approach. *Physical Chemistry Chemical Physics* **2023**, *25* (6), 4489-4500, 10.1039/D2CP02707K. DOI: 10.1039/D2CP02707K.

(154) Zhai, X.; Zhang, X.; Chen, S.; Yang, W.; Gong, Z. Oleylamine as solvent and stabilizer to synthesize shape-controlled ZnS nanocrystals with good optical properties. *Colloids and Surfaces A: Physicochemical and Engineering Aspects* **2012**, *409*, 126-129. DOI: 10.1016/j.colsurfa.2012.05.047.

(155) Tzitzios, V.; Dimos, K.; Lelidis, I.; Boukos, N. K.; Wadi, V. S.; Basina, G.; Nounesis, G.; Alhassan, S. M. Sulfur–oleyl amine platelet derivatives with liquid crystalline behavior. *RSC Advances* **2018**, *8* (72), 41480-41483, 10.1039/C8RA08325H. DOI: 10.1039/C8RA08325H.

(156) Ramya, S.; Nataraj, D.; Krishnan, S.; Premkumar, S.; Thrupthika, T.; Sangeetha, A.; Senthilkumar, K.; Thangadurai, T. D. Aggregation induced emission behavior in oleylamine acetone system and its application to get improved photocurrent from In2S3 quantum dots. *Scientific Reports* **2020**, *10* (1), 19712. DOI: 10.1038/s41598-020-76703-0.

(157) DeBeer, D. K. a. S. Application of Modern X-ray Spectroscopy in Chemistry—Beyond Studying the Oxidation State. *Chemistry of Materials* **2017**, *29* (17), 7051-7053. DOI: 10.1021/acs.chemmater.7b03455.

(158) Hirsch, O.; Kvashnina, K. O.; Luo, L.; Süess, M. J.; Glatzel, P.; Koziej, D. High-energy resolution X-ray absorption and emission spectroscopy reveals insight into unique selectivity of La-based nanoparticles for CO₂. *Proceedings of the National Academy of Sciences* **2015**, *112* (52), 15803-15808. DOI: doi:10.1073/pnas.1516192113.

(159) Glatzel, P.; Bergmann, U. High resolution 1s core hole X-ray spectroscopy in 3d transition metal complexes—electronic and structural information. *Coordination Chemistry Reviews* **2005**, *249* (1), 65-95. DOI: 10.1016/j.ccr.2004.04.011.

(160) Thomas, S. A.; Mishra, B.; Myneni, S. C. B. High Energy Resolution-X-ray Absorption Near Edge Structure Spectroscopy Reveals Zn Ligation in Whole Cell Bacteria. *The Journal of Physical Chemistry Letters* **2019**, *10* (10), 2585-2592. DOI: 10.1021/acs.jpclett.9b01186.

(161) Estevenon, P.; Amidani, L.; Bauters, S.; Tamain, C.; Bodensteiner, M.; Meurer, F.; Hennig, C.; Vaughan, G.; Dumas, T.; Kvashnina, K. O. From Molecular Oxo-Hydroxo Ce Clusters to Crystalline CeO2. *Chemistry of Materials* **2023**, *35* (4), 1723-1734. DOI: 10.1021/acs.chemmater.2c03456.

(162) Gallo, E.; Glatzel, P. Valence to Core X-ray Emission Spectroscopy. *Advanced Materials* **2014**, *26* (46), 7730-7746. DOI: 10.1002/adma.201304994.

(163) Ravel, B.; Newville, M. ATHENA, ARTEMIS, HEPHAESTUS: data analysis for X-ray absorption spectroscopy using IFEFFIT. *Journal of Synchrotron Radiation* **2005**, *12* (4), 537-541. DOI: 10.1107/S0909049505012719.

(164) Grote, L.; Seyrich, M.; Döhrmann, R.; Harouna-Mayer, S. Y.; Mancini, F.; Kaziukenas, E.; Fernandez-Cuesta, I.; A. Zito, C.; Vasylieva, O.; Wittwer, F.; et al. Imaging Cu2O nanocube

hollowing in solution by quantitative in situ X-ray ptychography. *Nature Communications* **2022**, *13* (1), 4971. DOI: 10.1038/s41467-022-32373-2.

(165) Gerber, E.; Romanchuk, A. Y.; Pidchenko, I.; Amidani, L.; Rossberg, A.; Hennig, C.; Vaughan, G. B. M.; Trigub, A.; Egorova, T.; Bauters, S.; et al. The missing pieces of the PuO2 nanoparticle puzzle. *Nanoscale* **2020**, *12* (35), 18039-18048, 10.1039/D0NR03767B. DOI: 10.1039/D0NR03767B.

(166) Yoko, A.; Omura, Y.; Ninomiya, K.; Nishibori, M.; Fujita, T.; Kasai, H.; Nishibori, E.; Chiba, N.; Seong, G.; Tomai, T.; et al. Fusion Growth and Extraordinary Distortion of Ultrasmall Metal Oxide Nanoparticles. *Journal of the American Chemical Society* **2024**, *146* (23), 16324-16331. DOI: 10.1021/jacs.4c05106.

(167) Hirsch, O.; Kvashnina, K.; Willa, C.; Koziej, D. Hard X-ray Photon-in Photon-out Spectroscopy as a Probe of the Temperature-Induced Delocalization of Electrons in Nanoscale Semiconductors. *Chemistry of Materials* **2017**, *29* (4), 1461-1466. DOI: 10.1021/acs.chemmater.6b05218.

(168) Kvashnina, K. O.; Kowalski, P. M.; Butorin, S. M.; Leinders, G.; Pakarinen, J.; Bès, R.; Li, H.; Verwerft, M. Trends in the valence band electronic structures of mixed uranium oxides. *Chemical Communications* **2018**, *54* (70), 9757-9760, 10.1039/C8CC05464A. DOI: 10.1039/C8CC05464A.

(169) Gilbert, B.; Frandsen, C.; Maxey, E. R.; Sherman, D. M. Band-gap measurements of bulk and nanoscale hematite by soft x-ray spectroscopy. *Physical Review B* **2009**, *79* (3), 035108. DOI: 10.1103/PhysRevB.79.035108.

(170) Liu, C.-Y.; Feng, P.; Ruotsalainen, K.; Bauer, K.; Decker, R.; Kusch, M.; Siewierska, K. E.; Pietzsch, A.; Haase, M.; Lu, Y.; et al. Role of La 5p in Bulk and Quantum-Confined Solids Probed by the La 5p54f1 3D1 Excitonic Final State of Resonant Inelastic X-ray Scattering. *The Journal of Physical Chemistry C* **2023**, *127* (23), 11111-11118. DOI: 10.1021/acs.jpcc.3c02011.

(171) Suzuki, H.; Minola, M.; Lu, Y.; Peng, Y.; Fumagalli, R.; Lefrançois, E.; Loew, T.; Porras, J.; Kummer, K.; Betto, D.; et al. Probing the energy gap of high-temperature cuprate superconductors by resonant inelastic x-ray scattering. *npj Quantum Materials* **2018**, *3* (1), 65. DOI: 10.1038/s41535-018-0139-7.

(172) He, H. A new monoclinic polymorph of anhydrous zinc acetate. *Acta Crystallographica Section E* **2006**, *62* (12), m3291-m3292. DOI: doi:10.1107/S1600536806046678.

(173) Kavčič, M.; Žitnik, M.; Bučar, K.; Mihelič, A.; Štuhec, M.; Szlachetko, J.; Cao, W.; Alonso Mori, R.; Glatzel, P. Separation of Two-Electron Photoexcited Atomic Processes near the Inner-Shell Threshold. *Physical Review Letters* **2009**, *102* (14), 143001. DOI: 10.1103/PhysRevLett.102.143001.

(174) Hoszowska, J.; Dousse, J. C.; Szlachetko, J.; Kayser, Y.; Cao, W.; Jagodziński, P.; Kavčič, M.; Nowak, S. H. First Observation of Two-Electron One-Photon Transitions in Single-Photon K-Shell Double Ionization. *Physical Review Letters* **2011**, *107* (5), 053001. DOI: 10.1103/PhysRevLett.107.053001.

(175) Pankin, I. A.; Polozhentsev, O. E.; Soldatov, M. A.; Bugaev, A. L.; Tsaturyan, A.; Lomachenko, K. A.; Guda, A. A.; Budnyk, A. P.; Lamberti, C.; Soldatov, A. V. Investigation of the nanoscale two-component ZnS-ZnO heterostructures by means of HR-TEM and X-ray based analysis. *Journal of Solid State Chemistry* **2018**, *262*, 264-272. DOI: 10.1016/j.jssc.2018.03.008.

(176) Jaumot, J.; Gargallo, R.; de Juan, A.; Tauler, R. A graphical user-friendly interface for MCR-ALS: a new tool for multivariate curve resolution in MATLAB. *Chemometrics and Intelligent Laboratory Systems* **2005**, *76* (1), 101-110. DOI: 10.1016/j.chemolab.2004.12.007.

(177) de Juan, A.; Jaumot, J.; Tauler, R. Multivariate Curve Resolution (MCR). Solving the mixture analysis problem. *Analytical Methods* **2014**, *6* (14), 4964-4976, 10.1039/C4AY00571F. DOI: 10.1039/C4AY00571F.

(178) Rama Krishna, M. V.; Friesner, R. A. Quantum confinement effects in semiconductor clusters. *The Journal of Chemical Physics* **1991**, *95* (11), 8309-8322. DOI: 10.1063/1.461258 (acccessed 6/11/2024).

(179) Madelung, O. *Semiconductors: data handbook*; Springer Science & Business Media, 2004.

(180) Cárdenas, J. R.; Bester, G. Atomic effective pseudopotentials for semiconductors. *Physical Review B* **2012**, *86* (11), 115332. DOI: 10.1103/PhysRevB.86.115332.

(181) Zirkelbach, F.; Prodhomme, P. Y.; Han, P.; Cherian, R.; Bester, G. Large-scale atomic effective pseudopotential program including an efficient spin-orbit coupling treatment in real space. *Physical Review B* **2015**, *91* (7), 075119. DOI: 10.1103/PhysRevB.91.075119.

(182) Kumar, S.; Bui, H.; Bester, G. Empirical band-gap correction for LDA-derived atomic effective pseudopotentials. *Computational Condensed Matter* **2024**, *40*, e00917. DOI: 10.1016/j.cocom.2024.e00917.

(183) Karpulevich, A.; Bui, H.; Antonov, D.; Han, P.; Bester, G. Nonspherical atomic effective pseudopotentials for surface passivation. *Physical Review B* **2016**, *94* (20), 205417. DOI: 10.1103/PhysRevB.94.205417.

(184) Bester, G. Electronic excitations in nanostructures: an empirical pseudopotential based approach. *Journal of Physics: Condensed Matter* **2009**, *21* (2), 023202. DOI: 10.1088/0953-8984/21/2/023202.

(185) Karpulevich, A.; Bui, H.; Wang, Z.; Hapke, S.; Palencia Ramírez, C.; Weller, H.; Bester, G. Dielectric response function for colloidal semiconductor quantum dots. *The Journal of Chemical Physics* **2019**, *151* (22). DOI: 10.1063/1.5128334 (acccessed 7/24/2024).

(186) Pässler, R.; Griebl, E.; Riepl, H.; Lautner, G.; Bauer, S.; Preis, H.; Gebhardt, W.; Buda, B.; As, D. J.; Schikora, D.; et al. Temperature dependence of exciton peak energies in ZnS, ZnSe, and ZnTe epitaxial films. *Journal of Applied Physics* **1999**, *86* (8), 4403-4411. DOI: 10.1063/1.371378 (acccessed 9/17/2024).

(187) Koziej, D., Kopula Kesavan, J., Klemeyer, L., Rebber, M. N., Sani Harouna-Mayer, & Gröne, T. L. R. In situ photon-in photon-out spectroscopy measurements on ultra-small Cu3N nanoparticles. *European Synchrotron Radiation Facility* **2025**. DOI: 10.15151/ESRF-ES-657465136.

(188) Zito, C. D. A., Koziej, D., Caddeo, F., Kopula Kesavan, J., Klemeyer, L., Aaling-Frederiksen, O., Gröne, T. L. R., & Liu, X. Investigating the cooridnation of PtAg Nanoclusters in ZIF-8 by in situ HERFD-XANES studies. *European Synchrotron Radiation Facility* **2025**. DOI: 10.15151/ESRF-ES-819999907.

(189) Zito, C. D. A., Koziej, D., Kesavan, J. K., Klemeyer, L., Akcaalan, M. G., Hussak, S.A., & Gröne, T. L. R. in situ photon-in-photon-out spectroscopic studies with high temporal, spatial and energy resolution during emergence of transition metal su. *European Synchrotron Radiation Facility* **2026**. DOI: 10.15151/ESRF-ES-1022934512.

(190) Derelli, D.; Frank, K.; Grote, L.; Mancini, F.; Dippel, A.-C.; Gutowski, O.; Nickel, B.; Koziej, D. Direct Synthesis of CuPd Icosahedra Supercrystals Studied by In Situ X-Ray Scattering. *Small n/a* (n/a), 2311714. DOI: 10.1002/smll.202311714.

(191) Haas, S.; Sun, X.; Conceicao, A. L. C.; Horbach, J.; Pfeffer, S. The new small-angle X-ray scattering beamline for materials research at PETRA III: SAXSMAT beamline P62. *Journal of Synchrotron Radiation* **2023**, *30* (6), 1156-1167. DOI: 10.1107/S1600577523008603.

(192) Mortensen, D. R.; Seidler, G. T.; Kas, J. J.; Govind, N.; Schwartz, C. P.; Pemmaraju, S.; Prendergast, D. G. Benchmark results and theoretical treatments for valence-to-core x-ray emission spectroscopy in transition metal compounds. *Physical Review B* **2017**, *96* (12), 125136. DOI: 10.1103/PhysRevB.96.125136.

(193) Rehr, J. J.; Kas, J. J.; Vila, F. D.; Prange, M. P.; Jorissen, K. Parameter-free calculations of X-ray spectra with FEFF9. *Physical Chemistry Chemical Physics* **2010**, *12* (21), 5503-5513, 10.1039/B926434E. DOI: 10.1039/B926434E.

(194) Newville, M. Larch: An Analysis Package for XAFS and Related Spectroscopies. *Journal of Physics: Conference Series* **2013**, *430* (1), 012007. DOI: 10.1088/1742-6596/430/1/012007.

(195) Harris, C. R.; Millman, K. J.; van der Walt, S. J.; Gommers, R.; Virtanen, P.; Cournapeau, D.; Wieser, E.; Taylor, J.; Berg, S.; Smith, N. J.; et al. Array programming with NumPy. *Nature* **2020**, *585* (7825), 357-362. DOI: 10.1038/s41586-020-2649-2.

(196) Virtanen, P.; Gommers, R.; Oliphant, T. E.; Haberland, M.; Reddy, T.; Cournapeau, D.; Burovski, E.; Peterson, P.; Weckesser, W.; Bright, J.; et al. SciPy 1.0: fundamental algorithms for scientific computing in Python. *Nature Methods* **2020**, *17* (3), 261-272. DOI: 10.1038/s41592-019-0686-2.

(197) Neese, F. Software update: The ORCA program system—Version 5.0. *WIREs Computational Molecular Science* **2022**, *12* (5), e1606. DOI: 10.1002/wcms.1606.

(198) Hanwell, M. D.; Curtis, D. E.; Lonie, D. C.; Vandermeersch, T.; Zurek, E.; Hutchison, G. R. Avogadro: an advanced semantic chemical editor, visualization, and analysis platform. *Journal of Cheminformatics* **2012**, *4* (1), 17. DOI: 10.1186/1758-2946-4-17.

(199) Kieffer, J.; Wright, J. P. PyFAI: a Python library for high performance azimuthal integration on GPU. *Powder Diffraction* **2013**, *28* (S2), S339-S350. DOI: 10.1017/S0885715613000924 From Cambridge University Press Cambridge Core.

(200) Toby, B. H.; Von Dreele, R. B. GSAS-II: the genesis of a modern open-source all purpose crystallography software package. *Journal of Applied Crystallography* **2013**, *46* (2), 544-549. DOI: 10.1107/S0021889813003531.

(201) *SASView webpage*. https://www.sasview.org (accessed 2023 05.10.2023).

(202) Vrugt, J. A.; Ter Braak, C. J. F. DREAM_(D): an adaptive Markov Chain Monte Carlo simulation algorithm to solve discrete, noncontinuous, and combinatorial posterior parameter estimation problems. *Hydrol. Earth Syst. Sci.* **2011**, *15* (12), 3701-3713. DOI: 10.5194/hess-15-3701-2011.

(203) Buriak, J. M.; Akinwande, D.; Artzi, N.; Brinker, C. J.; Burrows, C.; Chan, W. C. W.; Chen, C.; Chen, X.; Chhowalla, M.; Chi, L.; et al. Best Practices for Using AI When Writing Scientific Manuscripts. *ACS Nano* **2023**, *17* (5), 4091-4093. DOI: 10.1021/acsnano.3c01544.

(204) Klemeyer, L.; Caddeo, F.; Gröne, T. L.; Harouna-Mayer, S. Y.; Jessen, B.; Zito, C. A.; Kesavan, J. K.; Dippel, A.-C.; Saldaña, F. I.; Mathon, O. Spatially Resolved In Situ HERFD-XANES studies of ZnS Nanoparticle Synthesis at the Water-Toluene Interface. **2025**.

(205) Brust, M.; Walker, M.; Bethell, D.; Schiffrin, D. J.; Whyman, R. Synthesis of thiol-derivatised gold nanoparticles in a two-phase Liquid–Liquid system. *Journal of the Chemical Society, Chemical Communications* **1994**, (7), 801-802, 10.1039/C39940000801. DOI: 10.1039/C39940000801.

(206) Corthey, G.; Rubert, A. A.; Picone, A. L.; Casillas, G.; Giovanetti, L. J.; Ramallo-López, J. M.; Zelaya, E.; Benitez, G. A.; Requejo, F. G.; José-Yacamán, M.; et al. New Insights into the Chemistry of Thiolate-Protected Palladium Nanoparticles. *The Journal of Physical Chemistry C* **2012**, *116* (17), 9830-9837. DOI: 10.1021/jp301531n.

(207) He, L.; Dong, T. Multiple synthesis routes for atomically precise noble metal nanoclusters. *CrystEngComm* **2024**, *26* (30), 3998-4016, 10.1039/D4CE00488D. DOI: 10.1039/D4CE00488D.

(208) Castro, E. G.; Salvatierra, R. V.; Schreiner, W. H.; Oliveira, M. M.; Zarbin, A. J. Dodecanethiol-stabilized platinum nanoparticles obtained by a two-phase method: synthesis, characterization, mechanism of formation, and electrocatalytic properties. *Chemistry of Materials* **2010**, *22* (2), 360-370.

(209) Hofmann, D. M.; Fairbrother, D. H.; Hamers, R. J.; Murphy, C. J. Two-Phase Synthesis of Gold–Copper Bimetallic Nanoparticles of Tunable Composition: Toward Optimized Catalytic CO2 Reduction. *ACS Applied Nano Materials* **2019**, *2* (6), 3989-3998. DOI: 10.1021/acsanm.9b00904.

(210) Pan, D.; Zhao, N.; Wang, Q.; Jiang, S.; Ji, X.; An, L. Facile Synthesis and Characterization of Luminescent TiO2 Nanocrystals. *Advanced Materials* **2005**, *17* (16), 1991-1995. DOI: https://doi.org/10.1002/adma.200500479.

(211) Yang, S.; Gao, L. Controlled Synthesis and Self-Assembly of CeO2 Nanocubes. *Journal of the American Chemical Society* **2006**, *128* (29), 9330-9331. DOI: 10.1021/ja063359h.

(212) Friderichs, C.; Zotov, N.; Mader, W. Synthesis of Monodisperse SrTi1–ZrO3 Nanocubes in Oleate by a Two-Phase Solvothermal Method. *European Journal of Inorganic Chemistry* **2015**, *2015* (2), 288-295. DOI: https://doi.org/10.1002/ejic.201402724.

(213) Yin, X.; Wang, Y.; Jacobs, R.; Shi, Y.; Szlufarska, I.; Morgan, D.; Wang, X. Massive Vacancy Concentration Yields Strong Room-Temperature Ferromagnetism in Two-Dimensional ZnO. *Nano Letters* **2019**, *19* (10), 7085-7092. DOI: 10.1021/acs.nanolett.9b02581.

(214) Zhao, N.; Nie, W.; Mao, J.; Yang, M.; Wang, D.; Lin, Y.; Fan, Y.; Zhao, Z.; Wei, H.; Ji, X. A General Synthesis of High-Quality Inorganic Nanocrystals via a Two-Phase Method. *Small* **2010**, *6* (22), 2558-2565. DOI: https://doi.org/10.1002/smll.201001218.

(215) Wang, X.; Sun, Z.; Shao, C.; Boye, D. M.; Zhao, J. A facile and general approach to polynary semiconductor nanocrystals via a modified two-phase method. *Nanotechnology* **2011**, *22* (24), 245605. DOI: 10.1088/0957-4484/22/24/245605.

(216) Nguyen, T.-D. From formation mechanisms to synthetic methods toward shape-controlled oxide nanoparticles. *Nanoscale* **2013**, *5* (20), 9455-9482, 10.1039/C3NR01810E. DOI: 10.1039/C3NR01810E.

(217) Heuer-Jungemann, A.; Feliu, N.; Bakaimi, I.; Hamaly, M.; Alkilany, A.; Chakraborty, I.; Masood, A.; Casula, M. F.; Kostopoulou, A.; Oh, E.; et al. The Role of Ligands in the Chemical Synthesis and Applications of Inorganic Nanoparticles. *Chemical Reviews* **2019**, *119* (8), 4819-4880. DOI: 10.1021/acs.chemrev.8b00733.

(218) Zhuang, Z.; Peng, Q.; Zhang, B.; Li, Y. Controllable Synthesis of Cu2S Nanocrystals and Their Assembly into a Superlattice. *Journal of the American Chemical Society* **2008**, *130* (32), 10482-10483. DOI: 10.1021/ja803644g.

(219) Pan, D.; Jiang, S.; An, L.; Jiang, B. Controllable Synthesis of Highly Luminescent and Monodisperse CdS Nanocrystals by a Two-Phase Approach under Mild Conditions. *Advanced Materials* **2004**, *16* (12), 982-985. DOI: https://doi.org/10.1002/adma.200400010.

(220) Wang, Q.; Pan, D.; Jiang, S.; Ji, X.; An, L.; Jiang, B. A New Two-Phase Route to High-Quality CdS Nanocrystals. *Chemistry – A European Journal* **2005**, *11* (13), 3843-3848. DOI: https://doi.org/10.1002/chem.200400993.

(221) Pan, D.; Wang, Q.; Jiang, S.; Ji, X.; An, L. Synthesis of Extremely Small CdSe and Highly Luminescent CdSe/CdS Core–Shell Nanocrystals via a Novel Two-Phase Thermal Approach. *Advanced Materials* **2005**, *17* (2), 176-179. DOI: https://doi.org/10.1002/adma.200401425.

(222) Fang, X.; Bando, Y.; Liao, M.; Gautam, U. K.; Zhi, C.; Dierre, B.; Liu, B.; Zhai, T.; Sekiguchi, T.; Koide, Y.; et al. Single-Crystalline ZnS Nanobelts as Ultraviolet-Light Sensors. *Advanced Materials* **2009**, *21* (20), 2034-2039. DOI: https://doi.org/10.1002/adma.200802441.

(223) Wang, X.; Xie, Z.; Huang, H.; Liu, Z.; Chen, D.; Shen, G. Gas sensors, thermistor and photodetector based on ZnS nanowires. *Journal of Materials Chemistry* **2012**, *22* (14), 6845-6850.

(224) Zhang, C.; Xie, Y.; Deng, H.; Tumlin, T.; Zhang, C.; Su, J.-W.; Yu, P.; Lin, J. Monolithic and Flexible ZnS/SnO2 Ultraviolet Photodetectors with Lateral Graphene Electrodes. *Small* **2017**, *13* (18), 1604197. DOI: https://doi.org/10.1002/smll.201604197.

(225) Miao, X.; Tongay, S.; Petterson, M. K.; Berke, K.; Rinzler, A. G.; Appleton, B. R.; Hebard, A. F. High Efficiency Graphene Solar Cells by Chemical Doping. *Nano Letters* **2012**, *12* (6), 2745-2750. DOI: 10.1021/nl204414u.

(226) Zhu, B.; Lin, B.; Zhou, Y.; Sun, P.; Yao, Q.; Chen, Y.; Gao, B. Enhanced photocatalytic H2 evolution on ZnS loaded with graphene and MoS2 nanosheets as cocatalysts. *Journal of Materials Chemistry A* **2014**, *2* (11), 3819-3827, 10.1039/C3TA14819J. DOI: 10.1039/C3TA14819J.

(227) Bao, L.; Ali, S.; Dai, C.; Zeng, Q.; Zeng, C.; Jia, Y.; Liu, X.; Wang, P.; Ren, X.; Yang, T.; et al. A Full-Spectrum ZnS Photocatalyst with Gradient Distribution of Atomic Copper Dopants and Concomitant Sulfur Vacancies for Highly Efficient Hydrogen Evolution. *ACS Nano* **2024**, *18* (7), 5878-5889. DOI: 10.1021/acsnano.3c12773.

(228) Brayek, A.; Chaguetmi, S.; Ghoul, M.; Assaker, I. B.; Souissi, A.; Mouton, L.; Beaunier, P.; Nowak, S.; Mammeri, F.; Chtourou, R. Photoelectrochemical properties of nanocrystalline ZnS discrete versus continuous coating of ZnO nanorods prepared by electrodeposition. *RSC advances* **2016**, *6* (37), 30919-30927.

(229) Kurnia, F.; Ng, Y. H.; Tang, Y.; Amal, R.; Valanoor, N.; Hart, J. N. ZnS Thin Films for Visible-Light Active Photoelectrodes: Effect of Film Morphology and Crystal Structure. *Crystal Growth & Design* **2016**, *16* (5), 2461-2465. DOI: 10.1021/acs.cgd.5b01590.

(230) Jana, S.; Srivastava, B. B.; Pradhan, N. A Controlled Growth Process To Design Relatively Larger Size Semiconductor Nanocrystals. *The Journal of Physical Chemistry C* **2013**, *117* (2), 1183-1188. DOI: 10.1021/jp310783a.

(231) Xu, H.; Sommer, S.; Broge, N. L. N.; Gao, J.; Iversen, B. B. The Chemistry of Nucleation: In Situ Pair Distribution Function Analysis of Secondary Building Units During UiO-66 MOF Formation. *Chemistry – A European Journal* **2019**, *25* (8), 2051-2058. DOI: https://doi.org/10.1002/chem.201805024.

(232) Dippel, A.-C.; Gutowski, O.; Klemeyer, L.; Boettger, U.; Berg, F.; Schneller, T.; Hardtdegen, A.; Aussen, S.; Hoffmann-Eifert, S.; Zimmermann, M. v. Evolution of short-range order in chemically and physically grown thin film bilayer structures for electronic applications. *Nanoscale* **2020**, *12* (24), 13103-13112, 10.1039/D0NR01847C. DOI: 10.1039/D0NR01847C.

(233) Egami, T.; Billinge, S. J. *Underneath the Bragg peaks: structural analysis of complex materials*; Elsevier, 2003.

(234) Rosa, A. D.; Garbarino, G.; Rodrigues, J. E.; Mijit, E.; Jacobs, J.; Bugnazet, D.; Pasternak, S.; Berruyer, G.; Moyne, A.; Clavel, C.; et al. New opportunities for high pressure X-ray absorption spectroscopy at ID24-DCM and BM23 with the Extremely Brilliant Source of the ESRF. *High Pressure Research* **2024**, *44* (3), 248-276. DOI: 10.1080/08957959.2024.2364281.

(235) Klemeyer, L.; Gröne, T. L. R.; Zito, C. d. A.; Vasylieva, O.; Gumus Akcaalan, M.; Harouna-Mayer, S. Y.; Caddeo, F.; Steenbock, T.; Hussak, S.-A.; Kesavan, J. K.; et al. Utilizing High X-ray Energy Photon-In Photon-Out Spectroscopies and X-ray Scattering to Experimentally Assess

the Emergence of Electronic and Atomic Structure of ZnS Nanorods. *Journal of the American Chemical Society* **2024**, *146* (49), 33475-33484. DOI: 10.1021/jacs.4c10257.

(236) Neese, F. Software update: the ORCA program system, version 4.0. *WIREs Computational Molecular Science* **2018**, *8* (1), e1327. DOI: https://doi.org/10.1002/wcms.1327.

(237) Ishioka, T.; Murata, A.; Kitagawa, Y.; Nakamura, K. T. Zinc(II) Acetate Dihydrate. *Acta Crystallographica Section C* **1997**, *53* (8), 1029-1031. DOI: https://doi.org/10.1107/S0108270197004484.

(238) Yano, J.; Yachandra, V. K. X-ray absorption spectroscopy. *Photosynthesis Research* **2009**, *102* (2), 241-254. DOI: 10.1007/s11120-009-9473-8.

(239) Fornasini, P. Introduction to X-Ray Absorption Spectroscopy. In *Synchrotron Radiation: Basics, Methods and Applications*, Mobilio, S., Boscherini, F., Meneghini, C. Eds.; Springer Berlin Heidelberg, 2015; pp 181-211.

(240) Guglieri Rodríguez, C. Zinc K-edge X-ray Absorption Study of ZnO-Based Magnetic Semiconductors. In *Relationship Between Structure and Magnetic Behaviour in ZnO-Based Systems*, Guglieri Rodríguez, C. Ed.; Springer International Publishing, 2015; pp 67-96.

(241) Lefèvre, I.; Vogel-Mikuš, K.; Arčon, I.; Lutts, S. How do roots of the metal-resistant perennial bush Zygophyllum fabago cope with cadmium and zinc toxicities? *Plant and Soil* **2016**, *404* (1), 193-207. DOI: 10.1007/s11104-016-2834-0.

(242) Guda, A. A.; Guda, S. A.; Martini, A.; Kravtsova, A. N.; Algasov, A.; Bugaev, A.; Kubrin, S. P.; Guda, L. V.; Šot, P.; van Bokhoven, J. A.; et al. Understanding X-ray absorption spectra by means of descriptors and machine learning algorithms. *npj Computational Materials* **2021**, *7* (1), 203. DOI: 10.1038/s41524-021-00664-9.

(243) Zhang, H.; Banfield, J. F. Identification and Growth Mechanism of ZnS Nanoparticles with Mixed Cubic and Hexagonal Stacking. *The Journal of Physical Chemistry C* **2009**, *113* (22), 9681-9687. DOI: 10.1021/jp902499a.

(244) Gilbert, B.; Frazer, B. H.; Zhang, H.; Huang, F.; Banfield, J. F.; Haskel, D.; Lang, J. C.; Srajer, G.; Stasio, G. D. X-ray absorption spectroscopy of the cubic and hexagonal polytypes of zinc sulfide. *Physical Review B* **2002**, *66* (24), 245205. DOI: 10.1103/PhysRevB.66.245205.

(245) Wintersteller, S.; Yarema, O.; Kumaar, D.; Schenk, F. M.; Safonova, O. V.; Abdala, P. M.; Wood, V.; Yarema, M. Unravelling the amorphous structure and crystallization mechanism of GeTe phase change memory materials. *Nature Communications* **2024**, *15* (1), 1011. DOI: 10.1038/s41467-024-45327-7.

(246) Dippel, A.-C.; Jensen, K. M. O.; Tyrsted, C.; Bremholm, M.; Bojesen, E. D.; Saha, D.; Birgisson, S.; Christensen, M.; Billinge, S. J. L.; Iversen, B. B. Towards atomistic understanding of polymorphism in the solvothermal synthesis of ZrO2 nanoparticles. *Acta Crystallographica Section A* **2016**, *72* (6), 645-650. DOI: doi:10.1107/S2053273316012675.

(247) Tyrsted, C.; Lock, N.; Jensen, K. M. O.; Christensen, M.; Bojesen, E. D.; Emerich, H.; Vaughan, G.; Billinge, S. J. L.; Iversen, B. B. Evolution of atomic structure during nanoparticle formation. *IUCrJ* **2014**, *1* (3), 165-171. DOI: doi:10.1107/S2052252514006538.

(248) La Porta, F. A.; Andrés, J.; Li, M. S.; Sambrano, J. R.; Varela, J. A.; Longo, E. Zinc blende versus wurtzite ZnS nanoparticles: control of the phase and optical properties by tetrabutylammonium hydroxide. *Physical Chemistry Chemical Physics* **2014**, *16* (37), 20127-20137, 10.1039/C4CP02611J. DOI: 10.1039/C4CP02611J.

(249) Persson, K. Materials Data on ZnS (SG:216) by Materials Project. **2014**. DOI: 10.17188/1187297.

(250) Rickard, D.; Luther, G. W. Chemistry of Iron Sulfides. *Chemical Reviews* **2007**, *107* (2), 514-562. DOI: 10.1021/cr0503658.

(251) Roberts, A. P.; Chang, L.; Rowan, C. J.; Horng, C. S.; Florindo, F. Magnetic properties of sedimentary greigite (Fe3S4): An update. *Reviews of Geophysics* **2011**, *49* (1).

(252) Hartmann, F.; Etter, M.; Cibin, G.; Groß, H.; Kienle, L.; Bensch, W. Understanding sodium storage properties of ultra-small Fe3S4 nanoparticles – a combined XRD, PDF, XAS and electrokinetic study. *Nanoscale* **2022**, *14* (7), 2696-2710, 10.1039/D1NR06950K. DOI: 10.1039/D1NR06950K.

(253) Guo, S.-P.; Li, J.-C.; Xiao, J.-R.; Xue, H.-G. Fe3S4 nanoparticles wrapped in an rGO matrix for promising energy storage: outstanding cyclic and rate performance. *ACS applied materials & interfaces* **2017**, *9* (43), 37694-37701.

(254) Li, G.; Zhang, B.; Yu, F.; Novakova, A. A.; Krivenkov, M. S.; Kiseleva, T. Y.; Chang, L.; Rao, J.; Polyakov, A. O.; Blake, G. R.; et al. High-Purity Fe3S4 Greigite Microcrystals for Magnetic and Electrochemical Performance. *Chemistry of Materials* **2014**, *26* (20), 5821-5829. DOI: 10.1021/cm501493m.

(255) Huang, D.-D.; Li, S.; Wu, Y.-P.; Wei, J.-H.; Yi, J.-W.; Ma, H.-M.; Zhang, Q.-C.; Liu, Y.-L.; Li, D.-S. In situ synthesis of a Fe3S4/MIL-53(Fe) hybrid catalyst for an efficient electrocatalytic hydrogen evolution reaction. *Chemical Communications* **2019**, *55* (31), 4570-4573, 10.1039/C9CC01433K. DOI: 10.1039/C9CC01433K.

(256) Santos-Carballal, D.; Roldan, A.; Dzade, N. Y.; De Leeuw, N. H. Reactivity of CO2 on the surfaces of magnetite (Fe3O4), greigite (Fe3S4) and mackinawite (FeS). *Philosophical Transactions of the Royal Society A: Mathematical, Physical and Engineering Sciences* **2018**, *376* (2110), 20170065.

(257) Wu, M.; Tse, J. S.; Pan, Y. Electronic structures of greigite (Fe3S4): A hybrid functional study and prediction for a Verwey transition. *Scientific Reports* **2016**, *6* (1), 21637. DOI: 10.1038/srep21637.

(258) Devey, A. J.; Grau-Crespo, R.; de Leeuw, N. H. Electronic and magnetic structure of ${\text{Fe}}_{3}{\text{S}}_{4}$: $\text{GGA}+\text{U}$ investigation. *Physical Review B* **2009**, *79* (19), 195126. DOI: 10.1103/PhysRevB.79.195126.

(259) Lyubutin, I.; Starchikov, S.; Lin, C.-R.; Lu, S.-Z.; Shaikh, M. O.; Funtov, K.; Dmitrieva, T.; Ovchinnikov, S.; Edelman, I.; Ivantsov, R. Magnetic, structural, and electronic properties of iron sulfide Fe 3 S 4 nanoparticles synthesized by the polyol mediated process. *Journal of nanoparticle research* **2013**, *15*, 1-13.

(260) Bairan Espano, J. R.; Macdonald, J. E. Phase Control in the Synthesis of Iron Sulfides. *Journal of the American Chemical Society* **2023**, *145* (34), 18948-18955. DOI: 10.1021/jacs.3c05653.

(261) Lennie, A. R.; England, K. E.; Vaughan, D. J. Transformation of synthetic mackinawite to hexagonal pyrrhotite: A kinetic study. *American Mineralogist* **1995**, *80* (9-10), 960-967.

(262) Westre, T. E.; Kennepohl, P.; DeWitt, J. G.; Hedman, B.; Hodgson, K. O.; Solomon, E. I. A Multiplet Analysis of Fe K-Edge 1s → 3d Pre-Edge Features of Iron Complexes. *Journal of the American Chemical Society* **1997**, *119* (27), 6297-6314. DOI: 10.1021/ja964352a.

(263) Ferrari, A.; Braibanti, A.; Bigliardi, G. Refinement of the crystal structure of NiCl2 and of unit-cell parameters of some anhydrous chlorides of divalent metals. *Acta Crystallographica* **1963**, *16* (8), 846-847.

(264) Stout, J.; Reed, S. A. The crystal structure of mnf2, fef2, cof2, nif2 and znf2. *Journal of the American Chemical Society* **1954**, *76* (21), 5279-5281.

(265) Burbridge, C.; Goodgame, D. SPEKTRALUNTERSUCHUNGEN VON OKTAEDRISCHEN EISEN (II)-KOMPLEXEN MIT STICKSTOFF-DONATOREN. *Chemischer Informationsdienst. Organische Chemie* **1970**, *1* (42), no-no.

(266) Miller, L. L.; Jacobson, R. A.; Chen, Y.-S.; Kurtz, D. Structure of hexakis (N-methylimidazole-N') iron (II) tetraphenylborate dichloromethane solvate. *Acta Crystallographica Section C: Crystal Structure Communications* **1989**, *45* (3), 527-529.

(267) Price, D. Static and dynamic crystal-field effects in ferrous fluosilicate. *Canadian journal of physics* **1987**, *65* (10), 1280-1293.

(268) Montgomery, H.; Morosin, B.; Natt, J.; Witkowska, A. t.; Lingafelter, E. The crystal structure of Tutton's salts. VI. Vanadium (II), iron (II) and cobalt (II) ammonium sulfate hexahydrates. *Acta Crystallographica* **1967**, *22* (6), 775-780.

(269) Bjornsson, R. *ORCA Inout Library*. 2013. https://sites.google.com/site/orcainputlibrary/home?authuser=0 (accessed 2024 16.04.).

9 Acknowledgments

This research was supported by the European Research Council (LINCHPIN project, grant no. 818941) and the Graduate School “Nanohybrid” (funding ID 408076438). Furthermore, I acknowledge DESY (Hamburg, Germany), a member of the Helmholtz Association, for the provision of experimental facilities. Parts of this research were carried out at PETRA III using beamlines P07 and P21.1 and P62 and at ESRF using beamlines ID26 and ID24 under proposals MA5353, MA5366 and HC-4929. [187-189]

I would like to take this opportunity to express my gratitude to the many people who supported me during my Ph.D. studies. First, I want to thank my master’s students, Brian Jessen and Tjark L.R. Gröne, for their support, passion, and time in addressing all the challenges that arose while working on the synthesis of ZnS and Fe_3S_4 nanomaterials.

I was fortunate to work with two outstanding scientists, Dr. Cecilia Zito and Dr. Francesco Caddeo, on writing and structuring the research articles presented in this thesis. Your kind and honest feedback enabled me to enhance my writing and draw conclusions about ongoing projects.

I would also like to thank Dr. Jagadesh Kopula Kesavan for engaging in extensive and productive discussions about X-ray spectroscopy and always providing a second opinion on my findings. I also want to thank Olga Vasylieva for introducing me to ZnS synthesis at the beginning of my work and Melike Gumus Akcaalan for all the support in designing and producing the sample environment for the experiments.

Sani Harouna-Mayer, Marvin Skiba, and Sarah Alexandra Hussak, you were my daily support at work. I cherished all our discussions, including those about science, and I feel extremely fortunate to have had you around during my time at CHyN. I would like to thank Andrea Köppen for the supply of many HRTEM pictures.

I would like to thank Dr. Ann-Christin Dippel, Dr. Xiao Sun, and Dr. Wolfgang Calibe from DESY for countless hours of friendly beamtime, allowing me to double-check my claims, develop hypotheses, and obtain supplementary data. Ann-Christin, I am very grateful for the extensive discussions on background subtraction, data processing, and interpretation.

I would also like to thank Dr. Pieter Glatzel, Dr. Olivier Mathon, and Prof. Dr. Marcin Sikora for hosting me during my time at ESRF (Grenoble, France) and Solaris (Krakow, Poland) and for providing me with essential hands-on knowledge about X-ray spectroscopy.

I also want to thank Dr. Antonia Freibert for introducing me to ORCA calculations and Martin Stieben for providing computational support in executing the calculations.

I want to express my gratitude to Dr. Torben Steenbock, Surender Kumar, and Prof. Dr. Gabriel Bester for their support in simulating band gaps and assisting in the relaxation of complexes.

I also want to acknowledge all members of the Koziej lab for their continuous support during numerous beam times, taking shifts, and helping to acquire the data presented.

I want to thank also all my collaborators, Dr. Lizhen Chen, Dr. Marvin Skiba, Dr. Ferdinand Otto, Dr. Davide Derelli, Dr. Olivia Aaling-Frederiksen, Florian Johst, Dr. Jannik Rebmann, Dr. Tobias Kipp, Prof. Dr. Alf Mews, Prof. Dr. Indranath Chakraborty, Prof. Dr. Wolfgang Parak, who allowed me to explore new scientific fields and expand my comfort zone in materials research.

In the end, I would like to express my deepest thanks to the most important person in my scientific journey, Prof. Dr. Dorota Koziej, for igniting my passion for X-ray scattering and spectroscopy and for the immense support since October 2017, which has shaped me into the scientist I am today.

10 Table of Figures and Tables

11 List of abbrevations

AEPs	atomic effective pseudopotentials
BA	benzyl alcohol
CEE	constant emission energy
CIE	constant incident energy
COSX	chain of spheres
CTE	constant transfered energy
DFT	density functional theory
DOS	density of states
ESR	electron spin resonance
FFT	fast fourier transformation
GGA	generalized gradient approximation
HDA	hexadecylamine
HERFD-XAS	high energy resolution fluorescence detected X-ray absorption spectroscopy
HF	Hartree-Fock
HOMO	highest occupied molecule orbital
HRTEM	high resolution transmission electron microsope
LDA	local density approximation
LUMO	lowest occupied molecule orbital
MCR-ALS	multi curve resolution alternated least square
NC	nanocluster
NMR	nuclear magnetic resonance
NP	nanoparticle
OA	oleylamine
ODA	octadecylamine
OEC	oxygen evolving complex
PDF	atomic pair distribution function
PXRD	powder X-ray diffraction
QDs	quantum dots
QM	quantum mechanical
RI	resolution-of-the-identity
RKS	restricted Kohn-Sham
RXES	resonant X-ray emission spectroscopy
s-ZnS	sphalerite zinc sulfide
SAXS	small angle X-ray scattering
SCF	self consitent field
SOA	oleylthioamide
SP	single particle
TDDFT	time-dependend density fuctional theory
TS	total scattering

TZVP	triple-zeta quality
vtc-XES	valence-to-core X-ray emission spectroscopy
w-ZnS	wurtzite zinc sulfide
XAS	X-ray absorption spectroscopy
XFEL	X-ray free electron laser
XMCD	X-ray magnetic circular dichroism
ZORA	zeroth-order regular approximation

12 Curriculum Vitae

Education

04/2021 – est. 2025	**University of Hamburg**, Hamburg, Germany Dr. rer. nat. in Physics
10/2018 – 03/2021	**University of Hamburg**, Hamburg, Germany M.Sc. in Nanoscience
10/2015 – 09/2018	**University of Hamburg**, Hamburg, Germany B.Sc. in Nanoscience
08/2011 – 01/2015	**Berufliche Schule Chemie, Pharmazie, Agrarwirtschaft Hamburg**, Hamburg, Germany Certificated Chemical-technical assistant
10/2012 – 08/2014	**Gymnasium Altona**, Hamburg, Germany Abitur

Working experiences

04/2021 – 12/2024	**University of Hamburg**, Hamburg, Germany Research associate, Group of Dorota Koziej
01/2023 – 05/2023	**European Synchrotron Radiation Facility (ESRF)**, Grenoble, France Visiting scientist at ID24/ID26
01/2022 –	**B.A.C.H. UG (haftungsbeschränkt)**, Hamburg, Germany Co-Chief Executive Officer
10/2020 – 04/2021	**University of Hamburg**, Hamburg, Germany Teacher for exercises in experimental physics, Ulrike Frühling
10/2020 – 12/2020	**Max Planck Insitute for Chemical Energy Conversion**, Mühlheim a.d. Ruhr, Germany Visiting scientist at Subgroup of Olaf Rüdiger, Group of Serena de Beer
11/2019 – 03/2021	**Deutschen Elektronen Synchrotron (DESY)**, Hamburg, Germany Young research fellow at P07/P21, Group of Oliver Seek
04/2019 – 09/2019	**Northwestern University**, Evanston, USA Pre-doctoral fellow, Group of Jiaxing Huang

11/2018 – 04/2019	**Deutschen Elektronen Synchrotron (DESY)**, Hamburg, Germany Young research fellow at P07/P21, Group of Oliver Seek
06/2015 – 09/2015	**GBA Gesellschaft für Bioanalytik GmbH**, Hamburg, Germany Chemical-technical assistant, Department GC-MS

Awards & Scholarships

01/2024	**Certificate of Intercultural Competences (CIC)** – distinction for my voluntary commitment in welcoming international students to Hamburg and my participation in intercultural training.
08/2021	**Teaching price** – Best teacher for exercise classes in the Department of Physics in SoSe 21
08/2019	**McCormick Stipend** – scholarship by Robert McCormick school of Engineering and Applied Science, Northwestern University
04/2019	**Hamburglobal** – scholarship by University of Hamburg

13 List of publications:

Evolution of short-range order in chemically and physically grown thin film bilayer structures for electronic applications. Ann-Christin Dippel, Olof Gutowski, Lars Klemeyer, Ulrich Boettger, Fenja Berg, Theodor Schneller, Alexander Hardtdegen, Stephan Aussen, Susanne Hoffmann-Eifert and Martin v. Zimmermann, ***Nanoscale***, 2020,12, 13103-13112

Geometry-Dependent Thermal Reduction of Graphene Oxide Solid. Lars Klemeyer, Hun Park and Jiaxing Huang, ***ACS Materials Lett.*** 2021, 3, 5, 511–515

Structural Analysis and Intrinsic Enzyme Mimicking Activities of Ligand-Free PtAg Nanoalloys. Lizhen Chen, Lars Klemeyer, Mingbo Ruan, Xin Liu, Stefan Werner, Weilin Xu, Andrea Koeppen, Robert Bücker, Marta Gallego Gonzalez, Dorota Koziej, Wolfgang J. Parak and Indranath Chakraborty, ***Small,*** 2023, 19, 2206772.

Photodegradation of $CuBi_2O_4$ Films Evidenced by Fast Formation of Metallic Bi using Operando Surface-sensitive X-ray Scattering. Davide Derelli, Francesco Caddeo, Kilian Frank, Kilian Krötzsch, Patrick Ewerhardt, Marco Krüger, Sophie Medicus, Lars Klemeyer, Marvin Skiba, Charlotte Ruhmlieb, Olof Gutowski, Ann-Christin Dippel, Wolfgang J. Parak, Bert Nickel, Dorota Koziej, ***Angew. Chem. Int. Ed.*** 2023, 62, e202307948.

Exciton–Phonon Coupling in Single ZnCdSe-Dot/CdS-Rod Nanocrystals with Engineered Band Gaps from Type-II to Type-I. Florian Johst, Jannik Rebmann, Hans Werners, Lars Klemeyer, Jagadesh Kopula Kesavan, Dorota Koziej, Christian Strelow, Gabriel Bester, Alf Mews, and Tobias Kipp, ***ACS Photonics,*** 2024 11 (9), 3741-3749

Effect of solvothermal synthesis parameters on the crystallite size and atomic structure of cobalt iron oxide nanoparticles. Olivia Aalling-Frederiksen, Rebecca K Pittkowski, Andy S Anker, Jonathan Quinson, Lars Klemeyer, Benjamin A Frandsen, Dorota Koziej, Kirsten MØ Jensen, ***Nanoscale Adv.*** 2024, 6, 5939-5948

Utilizing High X-ray Energy Photon-In Photon-Out Spectroscopies and X-ray Scattering to Experimentally Assess the Emergence of Electronic and Atomic Structure of ZnS Nanorods. Lars Klemeyer, Tjark LR Gröne, Cecilia de Almeida Zito, Olga Vasylieva, Melike Gumus Akcaalan, Sani Y Harouna-Mayer, Francesco Caddeo, Torben Steenbock, Sarah-Alexandra Hussak, Jagadesh Kopula Kesavan, Ann-Christin Dippel, Xiao Sun, Andrea Köppen, Viktoriia A Saveleva, Surender Kumar, Gabriel Bester, Pieter Glatzel, Dorota Koziej, ***J. Am. Chem. Soc.*** 2024

Cation-site Disordered Cu3PdN Nanoparticles for Hydrogen Evolution Electrocatalysis. Sani Yusuf Harouna-Mayer, Jagadesh Kopula Kesavan, Francesco Caddeo, Lian Belgardt, Chia-Shuo Hsu, Lars Klemeyer, Lizzi Kipping, Melike Gumus Akcaalan, Tjark Raphael Leon Groene, Andrea Koeppen, Olivier Mathon, Ann-Christin Dippel, Dorota Koziej, ***ChemRxiv***, 2024

Spatially Resolved In Situ HERFD-XANES studies of ZnS Nanoparticle Synthesis at the Water-Toluene Interface. Lars Klemeyer, Francesco Caddeo, Tjark L.R. Gröne, Sani Y. Harouna-Mayer, Brian Jessen, Cecilia A. Zito, Jagadesh Kopula Kesavan, Ann-Christin Dippel, Fernando Igoa Saldaña, Olivier Mathon, Pieter Glatzel, Dorota Koziej, ***ChemRxiv***, 2025

14 Eidesstattliche Versicherung

Hiermit versichere ich an Eides statt, die vorliegende Dissertationsschrift selbst verfasst und keine anderen als die angegebenen Hilfsmittel und Quellen benutzt zu haben.

Sofern im Zuge der Erstellung der vorliegenden Dissertationsschrift generative Künstliche Intelligenz (gKI) basierte elektronische Hilfsmittel verwendet wurden, versichere ich, dass meine eigene Leistung im Vordergrund stand und dass eine vollständige Dokumentation aller verwendeten Hilfsmittel gemäß der Guten wissenschaftlichen Praxis vorliegt. Ich trage die Verantwortung für eventuell durch die gKI generierte fehlerhafte oder verzerrte Inhalte, fehlerhafte Referenzen, Verstöße gegen das Datenschutz- und Urheberrecht oder Plagiate.

Hamburg, den 27.02.2025

Datum

Unterschrift der Doktorandin / des Doktoranden